EXCITATION AND PHOTOIONIZATION OF LASER-COOLED ATOMS IN THE AC-DRIVEN MAGNETO-OPTICAL TRAP (AC-MOT), USING RESONANT AND NON-RESONANT RADIATION

A THESIS

SUBMITTED TO THE UNIVERSITY OF MANCHESTER FOR THE DEGREE OF DOCTOR OF PHILOSOPHY (PhD) IN THE FACULTY OF SCIENCE AND ENGINEERING

2014

JOHN CHIDOWEREM AGOMUO

SCHOOL OF PHYSICS AND ASTRONOMY

Contents

Final Word Count: 66861

List of Figures

List of Tables

ABSTRACT

Candidate's Names: John Agomuo

Degree Title: PhD

Thesis Title: Excitation And Photoionization Of Laser-Cooled Atoms In The AC Driven Magneto-Optical Trap (AC-MOT), Using Resonant And Non-Resonant Radiation.

Date: 19/12/2014

Results of experiments involving the manipulation of atoms using laser radiation are presented. A high-density trap of potassium atoms was created using an AC-driven magneto-optical trap (AC-MOT), loaded from a Zeeman-slowed atomic beam. The AC-MOT was operated in a pulsed mode, with a trapping laser that was detuned by -4Γ, where Γ is the natural line-width of the trapping transition. Under these conditions, the AC-MOT trapped an average of $3.63 \pm 0.02 \times 10^8 atoms$, which were cooled to a mean temperature of $275\mu K \pm 33\mu K$.

Using the AC-MOT, the absolute photoionization cross-section of cold potassium atoms was determined using ionizing laser radiation at $450.4\ nm$ obtained from a high-power diode laser. The measured photoionization cross-section from the $4^2P_{3/2}$ excited state was obtained by measuring the loss rate and the lifetime of the AC-MOT during the loading and decay processes. Using these methods, the cross section was determined to be $1.49 \pm 0.13\ Mb$, and $2.38 \pm 0.18\ Mb$ respectively.

Precise energy levels of high-n Rydberg states of potassium have also been measured using stepwise-excitation of the trapped atoms, with the intermediate state being the $4^2P_{1/2}$ state that was excited by resonant laser radiation at 389,286,368.12 MHz. Excitation from the $4^2P_{1/2}$ state to the $n^2S_{1/2}$ states was carried out using blue radiation from a dye laser, for transitions to Rydberg states with principal quantum numbers ranging from n = 18 to ~ 200. For excitation to the $n^2D_{3/2}$ states, transitions up to Rydberg states with n ranging from 18 to 167 were studied. Due to the strong interaction between Rydberg atoms, the measured energy levels deviated from their predicted theoretical values at high principal quantum numbers ($n \geq 130$ for the S-states, and $n \geq 100$ for the D-states). For principal quantum numbers greater than these values, the spectral lines were found to both broaden and shift in energy, and new features in the Rydberg spectra were observed. These new features have been attributed to the dipole-forbidden $n^2P_{1/2}$ and $n^2P_{3/2}$ states, which cannot be excited directly by the laser. These states must hence be excited due to interplay between the highly excited Rydberg atoms that is occurring due to their large effective size and close proximity in the AC-MOT.

DECLARATION

I declare that no portion of the work referred to in the thesis has been submitted in support of an application for another degree or qualification of this or any other university or other institute of learning.

Copyright

Acknowledgements

My study in Manchester has been very rewarding and is as a dream come true. It would not have been possible, but for the help and support I got from many people to whom I owe many thanks.

First and foremost, I thank my Supervisor Prof Andrew, J Murray for giving me the opportunity to work within his research group, and for his guidance and support during the research and writing of this thesis. I have been inspired by his enthusiasm and dedication to research. Without his help and encouragements, it would have been more difficult to come to where I am. Many thanks go to my adviser, Dr Mark Dickenson for his help and support. I would like to thank Prof George King and Prof Phil Dawson for their words of encouragement.

Many thanks go also to other members of the research group who also helped me at various stages of this work. In particular, I want to thank Dr Matthew Harvey for putting me through the experimental setup, and the workings of the AC-MOT. Matthew also wrote most of the Labview codes used during this work and assisted me in many other ways. Others include Dr Martyn Hussey, Dr Kate Nixon, Dr Alex Knight-Percival, Dr Sarah Jhumka, James Pursehouse, and Mike Jones, to whom I owe many thanks for their help and encouragements. Without them the lab would have been boring.

Without time and fund this achievement would have been impossible, and so I want to thank the management and staff of the Nigerian Defence Academy (NDA) Kaduna, Nigeria for granting me the leave to undertake this study. Many thanks go to the management and staff of the Tertiary Education Trust Fund (TETFund), Nigeria for providing most of the fund needed for this study.

I received many assistance from family and friends to whom I am very grateful. They include my brothers James, Chinedum, and my sisters Eberechi and Beatrice and their families. My appreciation equally goes to my mother in-law and her family for their encouragements and supports. I also thank my good friend Sunday Uko and his family,

and the pastors and members of Stockport Christian Fellowship, and Amazing Grace Christian Assembly Kaduna for their prayers, help and encouragements.

I share this success with my wife Sarah, and my two boys Jonathan and Joseph for their love, patience and support throughout the duration of this study. I am very blessed.

Above all, my profound thanks and gratitude go to Almighty God for giving me good health and strength to undertake this study.

DEDICATION

To the loving memory

Of my late brother

Christopher.

List of Publication

1. Andrew James Murray, Martyn Hussey, Alex Knight-Percival, Sarah Jhumka, Kate L Nixon, Matthew Harvey and John Agomuo, *Electron impact ionization and excitation studies of laser prepared atomic targets.* Journal of Physics: Conference Series **388** (2012).

CHAPTER ONE

Introduction

1.0 Introduction

Since the first demonstration of the magneto-optical trap (MOT) of neutral atoms by Raab et al [1], the MOT has evolved into a powerful and flexible technique for cooling and trapping different atomic species. The MOT in its simplest form uses a combination of optical molasses force and magnetic field to cool and confine atoms in space, thereby producing a high density of cold atomic samples, which can then form targets for further investigation. Atoms have been cooled to temperatures of a few micro- or nano-Kelvin [2]. At these temperatures, single atomic models break down, and the quantum nature of matter and the associated interactions between the atoms becomes important. The low temperature (equivalent to a low energy) of atoms implies that:

- The de Broglie wavelength of scattering atoms is larger than the chemical bond length, and so wavelike effects like interference and resonance become important.
- The Doppler width of transitions is narrower than the natural line-width of dipole transitions, and so can often be ignored.
- The collisional interaction time becomes larger at these temperatures, which allows interactions with weak potentials to become significant. At collisional timescale longer than the atomic radiative lifetime, these collisional processes become sensitive to external radiation.

Hence the use of cold atoms in atomic spectroscopy has increased the sensitivity of measurements, resulting in high-resolution spectroscopy and precision measurements.

A new type of MOT driven by an alternating current, the AC-MOT, was invented and developed by the atomic physics group in Manchester, and this has the potential to combine cold-atom physics and charge particle collision physics in one experiment. The

research detailed in this thesis was therefore aimed at exploring some applications of the AC-MOT to cold collision studies. These involved the trapping of potassium atoms in the AC-MOT, and subsequent photo-ionization of the trapped atoms. This then allowed the absolute photoionization cross-section of cold potassium atoms to be determined. The trapped atoms were further used as a target for stepwise spectroscopy of cold Rydberg states. This work has resulted in new measurements of the energy levels of different Rydberg states, with principal quantum number $n = 18$ up to $n{\sim}200$. The work presented in this thesis therefore had the following specific objectives;

(i) Modification of the atomic beam oven to make this simpler to operate
(ii) Creation of an ensemble of cold potassium atoms in the AC-MOT.
(iii) Characterization of the trap in terms of density, number of trapped atoms, temperature and the loading and decay lifetimes.
(iv) Electron scattering studies of the cold and trapped atoms as targets.
(v) Photo-ionization studies of the trapped atoms.
(vi) To enhance the excited state population in order to improve the photo-ionization yield for subsequent experiments.
(vii) To carry out a stepwise spectroscopic study of highly excited cold Rydberg atoms of potassium.

1.1 Laser Cooling Of Neutral Atoms

From kinetic theory, the average velocity of atoms in a gas is proportional to the square root of the gas temperature, and is inversely proportional to the mass of the atom. At room temperature the velocity of most atoms is of the order of several hundreds of meters per second. The relative motion of the atoms hinders a detailed study and precise measurement of the interactions between atoms, or between atoms and charged particles and photons due to the variation of the Doppler profile associated with their motion. Energetic collision between atoms tends to complicate the system dynamics and hence mask quantum effects. To make precise measurement on the individual or collective properties of atoms, the atoms hence need to be slowed down.

One of the means of slowing atoms is to refrigerate the gas (i.e. reduce the temperature of the gas), but even at 77K (the temperature of liquid nitrogen), nitrogen molecules are still moving with speeds of about 150m/s. At 4 Kelvin (the temperature at which helium condenses), the helium atoms have a speed ≈ 90m/s. To reduce the temperature of the gas by refrigeration to a point where the speed of the atoms is below 1m/s would mean that

any gas in equilibrium (other than spin-polarized atomic hydrogen) would undergo condensation, with a vapour pressure so low that virtually no atoms would be in the gaseous phase. Hence prior to atom cooling techniques, all studies of free atoms were carried out with high velocity targets [3]. The desire for a new technique to reduce motional effects for spectroscopy was a major motivation for the cooling of both neutral atoms and ions. It is now possible to optically slow or cool atoms to temperatures of a fraction of a micro Kelvin, and trap them at relatively high densities. The technique of optical cooling, trapping and manipulation of neutral atoms and particles therefore provides a unique means of controlling the dynamics of these particles [4].

1.1.1 Review of Laser Cooling and Trapping

Early astronomers had observed the momentum property of light. They attributed the existence of comet tails (which always point away from the sun) to radiation pressure from light emitted by the sun. Maxwell gave a quantitative explanation of this phenomenon in his theory of electromagnetism [5]. This prediction was later verified by Lebedev, Nichols and Hull in 1903 [6, 7], in an experiment using a torsional balance to qualitatively measure the radiation pressure resulting from the deflection of a silvered glass plate.

Einstein in 1906 predicted the existence of photons [8], and in 1917 showed that light can be considered as being made up of particles (later called photons), which carry momentum h/λ [9], where h is Planck's constant and λ is the radiation wavelength. In 1924, de Broglie extended this idea to matter. He associated to a particle with mass m and velocity v a wave with wavelength $\lambda_{dB} = \frac{h}{mv}$, where λ_{dB} is the de Broglie wavelength.

The absorption and emission of photons by an atom results in momentum transfer between the particles. As stated above, this is the basis for laser cooling and trapping of atoms. Frisch in 1933 demonstrated this effect in an experiment in which an atomic beam of sodium was deflected by light from a sodium lamp [10]. Following the invention of the laser in the 1960's with its narrow line-width and high power, new fields of research in atomic physics have hence emerged that exploit these processes.

The idea of manipulating or deflecting atomic beams using lasers was first proposed by Ashkin in 1970 [11]. This was demonstrated in 1972 by Picque and Vialle [12] and Schieder et al [13], with the deflection of atomic beams using lasers. Following this, Wineland et al, [14] and Hänsch et al [15] suggested the use of laser light to slow down (cool) and trap atoms. The first laser cooling experiment was reported in 1978 in which a

cloud of magnesium ions was laser-cooled in a Penning trap [16]. Also reported was the cooling of trapped barium ions [17]. While trapping ions was possible because of the large ion trap depth (>300K), it was not possible for neutral atoms at the time because of their low trap depth of only a few Kelvin [18]. Trapping neutral atoms therefore requires a means of compressing the velocity spread of the atoms to an acceptable velocity so that trapping can occur.

By 1978 several proposals for cooling and trapping neutral atoms had been suggested. In addition to the radiation trap that had been suggested by Wineland, Hänsch and co-workers [14,15], magnetic traps were also proposed. The first suggestion for magnetic traps was made in 1963 [19] as an extension to the focussing of atomic beams demonstrated by Vauthier in 1949 [20]. In 1978, a further suggestion that a magnetic field could be used to trap atoms emerged when Kugler et al [18] succeeded in the confinement of cold neutrons in a toroidal superconducting magnetic ring. In these experiments the interaction of the neutrons' magnetic moment with the applied magnetic field created the confinement. These magnetic traps are based on the Stern-Gerlach experiment in 1924, which demonstrated the mechanical action of an inhomogeneous magnetic field on neutral atoms that have a magnetic moment [21].

The first experimental observation of the cooling of neutral atoms using lasers was reported by Balykin et al in 1979 [23] when they successfully slowed an atomic beam of sodium from a mean velocity of approximately 1100m/s to about 900m/s the resulting atomic beam having a velocity spread of only ≈23m/s. The high mean velocity of the resulting beam was attributed to Doppler shifting of the slowing atoms out of resonance with the cooling laser. Shortly after, Proden J V et al [23] added a magnetic gradient field to compensate for the changing Doppler shift, so as to keep the atoms in resonance with the cooling laser beam as they slowed down. This technique varied the resonant frequency of the atoms to balance the Doppler effect, by exploiting the Zeeman effect (the shift in an atom's energy levels due to an applied magnetic field).

In these experiments a tapered magnetic field was used to Zeeman shift the resonance frequency of the atoms along the full length of the slowing region, thus keeping the atoms in resonance with the cooling laser beam as they reduced in velocity. This cooling method was later referred to as *Zeeman slowing*. Phillips et al in 1982 successfully cooled a beam of sodium atoms with a Zeeman slower [24], and sodium atoms were first brought to rest with a Zeeman slower in 1985 [25].

Several other attempts were made to compensate for this changing Doppler shift, including rapid changes to the frequency of the laser (chirping). This method succeeded in slowing the sodium atoms to a velocity of about 600m/s [26]. Sodium was finally stopped using this method in 1985 [27, 28]. These successes made in laser cooling with both the laser chirping and Zeeman slower methods meant that attempts to efficiently load a neutral atom trap became possible.

Chu et al. in 1985 extended the laser cooling of neutral atoms to three dimensions in an experiment where pairs of counter-propagating laser beams were used to dampen the motion of neutral sodium atoms in all directions [28]. The arrangement of lasers in this experiment was termed a 3-D 'optical molasses', in analogy to describing the motion of atoms to that of particles moving through a thick viscous fluid. Since the force only dampened the atomic motion and did not have a spatial dependence, the atoms were not trapped in the molasses, and so slowly diffused out of the interaction region defined by the counter-propagating laser beams. The first successful trapping of neutral atoms was reported in 1985 by Migdall et al [30]. In their experiment, a Zeeman slowed atomic beam of sodium was used to load a magnetic trap. The trap consisted of an inhomogeneous magnetic field produced by a pair of coils in an anti-Helmholtz configuration. This configuration produces a magnetic quadrupole field which is zero at the centre and which increases in magnitude from the centre. The magnetic trap had a depth of approximately 17 mK, which corresponds to capture velocity of 3.5 m/s. This low capture velocity made it difficult to load the trap and so a complicated system of pulsed laser beams and magnetic fields was required to load their trap. A few years later in 1987 a new hybrid trap known as the magneto-optical trap (MOT) was demonstrated by Raab *et al.* [1]. This MOT employed both magnetic and radiation fields (a 3D optical molasses), and had a trap depth of ≈400 mK, corresponding to a capture velocity of ≈20 m/s. In the MOT the magnetic field does not directly contribute to the restoring force, and hence the trap requires field gradients 100 times smaller than is required for a purely magnetic trap. Since that time the MOT has proven to be a robust trap in terms of power matching of the laser beams and in terms of the purity requirements for their polarisation, and so has become the principal mechanism that is now used for the production of cold atoms for atomic physics experiments and for other applications.

1.1.2 The AC-MOT

Although the MOT has proven to be a robust source of cold atoms, which can form cold targets for further investigation, its application to low energy electron impact ionization and photoionization has been hindered by the requirement to eliminate the magnetic fields

prior to an interaction occurring. This is more critical with collisions involving low energy electrons, or where there is a need to extract the electrons produced during collision.

A new type of atom trap – the AC driven magneto optical trap (AC-MOT) which eliminates these difficulties [31] was recently invented by our group.

The AC-MOT has the advantage that for an appropriate choice of drive to the MOT coil, the magnetic **B**-field generated by eddy currents in the surrounding conductors can be eliminated when the MOT current is switched to zero [31]. The **B**-field can be accurately controlled and so charged particle experiments can be carried out around 500 times faster than is possible with the conventional MOT (now referred to in this thesis as a DC-MOT). With the development of the AC-MOT, the difficulties in reducing the magnetic field to an acceptable level for charged particle interactions with the cold atom cloud were eliminated; hence collision experiments with cold (trapped) atoms can now be routinely performed to measure different scattering cross sections using low energy electrons. These AC techniques have opened up the possibility of performing new experiments using cold atoms. In particular, it now becomes possible to routinely combine the fields of cold atom physics and charged particle collision physics, which adds significant advantages to each.

The development of these laser cooling and trapping techniques has opened up a new rich area of possible experiments and applications. With these techniques it became possible to create ultra-cold and very dense samples of neutral atoms. It equally enables the study of wave particle duality of matter and the creation of Bose Einstein condensates (BEC) and atom lasers, (an atomic analogue of the laser) [32, 33]. In addition to these fundamental applications, laser cooling and trapping has become important in the accurate determination of physical constants [34], in atomic clocks and for quantum computing [35, 36]. Recently, laser cooling and trapping techniques have been applied to the measurement of fundamental electron-atom scattering [37] and photoionization processes [38]. This has doubled the precision of measurements of scattering cross sections from previous methods.

1.2 Photoionization of cold atoms

The interaction of electromagnetic radiation with matter is a basic process in nature, and so the study of photoionization cross sections is of significant relevance in a number of applied areas of science and technology. Such areas include space science and

astrophysics, plasma physics, atmospheric science, radiation protection, laser design and lighting technology. Photoionization cross-sections from the ground state of various atoms have been studied extensively [40, 41]. Significant progress in both theory and experiment has also been made from the excited state of a number of alkali metal [42, 43, 44].

Following the first experiment on the use of trapped atoms as targets in the determination of photoionization cross-sections as reported by TP Dinneem et al [38], similar experiments have been conducted to measure photoionization cross sections from excited states of different atoms [45 - 49]. While there are available data on the photoionization cross-section of several alkali targets [50] as measured using trapped atoms, the photoionization cross-section of potassium using trapped atoms in a MOT has not yet been reported. Another motivation besides the demonstration of the application of the AC-MOT in collision studies was the desire for sources of cold electrons, so the experiments described in this thesis also serve as a platform to test the possibility of adapting the AC-MOT as a photo-ionization source of cold electrons. Indeed, this is currently being studied in a new experimental apparatus by our group.

1.2.1 Review of Photoionization of Atoms

The first experimental determination of the photoionization cross section from the first excited state of potassium (4P) was reported by Nygaard et al [42], where a two-step photoionization process was used. The measured cross-section was compared with the work of Moskvin [51], obtained using the quantum defect method for calculating photoionization cross-sections. Using the single-electron model and a parametric central potential, Aymar et al [41] computed the photoionization cross-section of some alkali metals, including potassium. Other methods, including atomic beam and laser saturation techniques, have been used by different groups to determine the photoionization cross section of different alkali metal targets [52, 54].

Following the formulation of an empirical relation to determine the photoionization cross-section [44], several groups have used this relation to determine absolute photoionization cross-sections [55-57]. Later Petrov et al [58] reported the partial and total photoionization cross-section of potassium using a configuration-interaction technique, and discussed the effect of polarization of the atomic core by the valence electron. They also presented the photoionization cross-section from the $4^2P_{3/2}$ state of potassium using three selected photon energies. Amin et al in 2007 [59], reported new measurements of the absolute photoionization cross-section from the 4p, 5d and 7s excited states of potassium. Recently

Zatsarinny and Tayal [40], used the Dirac-based B-spline R-matrix method to calculate the photoionization cross-section of potassium from the 4s ground state and the 4p, 5s-7s, and 3d-5d excited states.

Following the advancement in laser cooling techniques, Dinneem et al [38], pioneered the use of cold, trapped, and excited atoms in a MOT to determine absolute photoionization cross-sections. Cold rubidium atoms confined in the MOT were exposed to ionizing radiation, and the subsequent decrease in the trap fluorescence was measured. The difference in the trap fluorescence in the presence of the ionizing laser and in it's absence was used to determine an absolute photoionization cross-section. Similar trap loss techniques have also been used to measure cross-sections of excited P and D states of Rb, Cs, Na, Mg, and Li [45, 46, 47, 60, 61], as well as the 5s state of Rb [62]. In the present work, a similar technique is used to determine the photoionization cross-section from the $4^2P_{3/2}$ excited state of cold, trapped and excited potassium using the AC-MOT.

1.3 Cold Rydberg atom spectroscopy

In recent years there has been a renewed interest in the study of Rydberg atoms because of their potential application in quantum information measurements. The advancement in laser cooling and trapping techniques has enabled a new perspective in the study of Rydberg atoms, with the emphasis being shifted to the study of cold Rydberg atoms. The low kinetic energy of cold atoms has allowed the observation of strong interactions between Rydberg atoms to be made [62, 63]. Several studies of cold Rydberg atoms using different alkali metals have been reported, apart from potassium [64-69].

The present work was motivated by the desire to extend the study of ultra-cold Rydberg studies to potassium, as trapped in the AC-MOT. From the available NIST data, only energy level measurements for transitions to high-n Rydberg states with principal quantum number $n \leq 46$ have so far been reported for this target. Several quantum defects for potassium and rubidium have been measured by [70], using a millimetre wave-doubled spectroscopy technique. The quantum defects determined using this technique only allowed interpolation of the energy levels for states with high quantum number n. It is therefore useful to make a direct measurement of these energy levels over a larger range of n, using a more precise technique. The present work was hence again motivated by the need to obtain data for energy levels of Rydberg states with $n > 46$, so as to provide high-accuracy energy level data for a significant number of new Rydberg states of potassium.

1.3.1 Review of Cold Rydberg atoms spectroscopy

The study of Rydberg atoms dates back to the nineteenth century, with the observation of high-lying energy levels of hydrogen in the Balmer series [71], and these data became the key experimental basis for Bohr's atomic theory. Interest in these Rydberg systems is linked to their large dipole moment, which offers various opportunities to explore different phenomena which are inaccessible in other physical systems. These include the manipulation of Rydberg particles with small electric field gradients [72] and the possibility of controlling the interaction between two Rydberg particles at a macroscopic distance [73]. The strong and long-range inter-particle interaction of Rydberg atoms makes it possible to study complex quantum systems with full control of their dynamics. This then offers an efficient tool for quantum engineering, especially for entanglement studies of neutral particles [74].

Rydberg atoms have been extensively studied for their exaggerated properties such as their giant size ($\sim 1\mu m$ for $n \sim 100$), which scales as n^2 in terms of Bohr's atomic radius a_0. Energy levels of atomic transitions of various elements have been measured for Rydberg atoms using Doppler-free two-photon absorption spectroscopy [75, 76 and 77]. Lorenzen et al [78] further measured the nS and nD energy levels of ^{39}K for principal quantum number $7 \leq n \leq 46$, using this Doppler-free two-photon absorption technique. Recent advancements in laser cooling and trapping has opened up a new perspective in the study of Rydberg atoms, that of *cold* Rydberg atoms [71]. With cold atoms, the motion of the target can be neglected within the time scale of the excitation process, and so the atoms can be regarded as a 'frozen' Rydberg gas [79]. Several different new effects have been discovered in cold Rydberg atoms. These include the many-body diffusion of the excitation profile due to dipole-dipole energy transfer [63, 64], population of high angular momentum states through free charges [80], and the spontaneous formation and recombination of ultra-cold plasmas [81, 82].

1.4 Overview of the Experiments Described in this Thesis

In achieving the overall aim of this research, several different studies and experiments were carried out. In this section a brief overview of this work is given.

A. Re-designing of the atomic beam oven. The efficient loading of the AC-MOT via the Zeeman slower relies heavily on the ability of the atomic beam

oven to emit a well-collimated high-flux atomic beam. To achieve this, the atomic beam oven was modified. These modifications involved the conversion of the former oven (a complex recirculating oven) into a simpler effusive design. This made the oven easier to operate, and eliminated the need for an oil bath for the condensation pipe (in the old oven). The thermo-coax heating cable and the power and thermocouple wires were also re-wired in these modifications. Different mounting configurations aimed at making the oven easier to align with the Zeeman slower beam were also attempted, however these were ultimately abandoned due to outgassing problems with the mounts.

B. **Setting up the necessary optics**. A major component of every laser cooling and trapping experiment is designing the optical setup. Since many of the components from the previous cold atom experiments had been changed, a new optical setup was designed. This involved the re-calibration of the laser locking and detuning system, and realignment of all the laser beams required to produce an AC-MOT.

C. **Creating an AC-MOT of potassium**. With the atomic beam oven and optics operational, the next was to create a trap of cold potassium in the AC-MOT. The vacuum system was first cleaned and baked to create an ultra-high vacuum, as was necessary to produce a sustainable MOT. The Zeeman slower was reassessed, and the power supplies modified so that it was possible to control the Zeeman slower remotely via the main control programme on the PC. The oven was then tested and characterised to produce an atomic beam, and the quarter wave plate axes determined for their correct handedness to create a MOT. Following successful implementation of the AC-MOT, this was then characterized to determine the number of atoms that were trapped, and the lifetime of the MOT.

D. **Electron impact ionization of the cold atoms.** The formation and optimization of the MOT provided the required cold atoms for an investigation of the ion detector which was to be used for the new experiments. To test the operation of the ion detector in preparation for these new photoionization experiments, electron impact ionization experiments were initially carried out using the trapped atoms as targets. These experiments used an existing electron gun in the MOT chamber, and produced time of flight spectra for ionization by

electron impact of the cold potassium atoms as a function of the incident electron energy.

E. **Direct photoionization of cold-trapped atoms**. Following these electron impact ionization experiments, new measurements were taken for direct photoionization of trapped and excited atoms using radiation from a high-power diode laser. By monitoring the fluorescence from the trapped atoms, the effect of the ionizing laser on the trap loading rate and the trap lifetime were determined. From these measurements, the absolute photoionization cross-section for radiation at ~450 nm from excited potassium atoms in the $4^2P_{3/2}$ state was calculated.

F. **Excitation to high-n Rydberg states.** The final experiments described in this thesis followed the commissioning of a new tuneable dye laser operating in the blue region of the electromagnetic spectrum. These experiments used stepwise spectroscopy to study ultra-cold Rydberg states of potassium in the AC-MOT. Atoms were excited to states with principal quantum numbers ranging from $18 \leq n \leq 200$. This experiment further demonstrated the applicability of the AC-MOT in studies with charged particles.

1.5 Layout of the Thesis

This thesis is divided into eight chapters. This chapter has presented a brief introduction to the thesis, and has highlighted the various objectives of this study. It also contained a review of the recent development in the areas of laser cooling and trapping, photoionization and Rydberg atom spectroscopy. In chapter two, a brief overview of the interaction of light with matter is given, with particular attention given to the quantum electrodynamics (QED) treatment of potassium in a laser field. Chapter three discusses the mechanisms of laser cooling and trapping, which includes the nature of light forces and the techniques of Zeeman slowing of neutral atoms. A detailed description of the experimental apparatus used in the experiments, excluding some additional components used during the experiments on photoionization and Rydberg atom spectroscopy is then given in chapter four. In this chapter most of the apparatus is described, including the atomic beam source, the vacuum system and the optical setup.

In chapter five the description of the AC-MOT and its use in the trapping of neutral potassium is presented. Here the characteristics of the trap are discussed in terms of the

number of trapped atoms, the temperature of the atomic cloud and the trap lifetime. In chapter six the direct photoionization of cold potassium atoms in the AC-MOT using a high power diode laser is described. The results of these measurements of the absolute photoionization cross-sections are then discussed. Chapter seven then discusses the stepwise spectroscopy of cold Rydberg atom of potassium from the first excited state. Energy level data for Rydberg states with principal quantum numbers between $n = 18$ and $n{\sim}200$ are presented here.

Chapter eight summarises the results of this work, and suggests several possible future investigations, especially in the field of cold Rydberg atom spectroscopy. At the end of each chapter is a list of useful references.

References

[1] Raab, E. L., M. Prentiss, Alex Cable, Steven Chu, and D. E. Pritchard. *Trapping of neutral sodium atoms with radiation pressure*. Physical Review Letters 59, no. 23 (1987): 2631.

[2] Steane, A. M., and C. J. Foot. *"Laser cooling below the Doppler limit in a magneto-optical trap."* EPL (Europhysics Letters) 14, no. 3 (1991): 231.

[3] Phillips William, D. *"Laser cooling and trapping of atoms."* Rev. Mod. Phys 70 (1998): 721-741.

[4] Ashkin, Arthur. *"Optical trapping and manipulation of neutral particles using lasers."* Proceedings of the National Academy of Sciences 94, no. 10 (1997): 4853-4860.

[5] Maxwell, James Clerk. *"A Treatise on Electricity and Magnetism, i and ii."* (1873).

[6] Lebedev, P. N. *"Experimental examination of light pressure."* Nuovo Cimento 15, no. 195 (1883): 195.

[7] Nichols, E. F., and G. F. Hull. *"The pressure due to radiation.(second paper.)."* Physical Review (Series I) 17, no. 1 (1903): 26.

[8] Einstein, A. (1906). *A new determination of molecular dimensions.* Ann. Phys, 19(2), 289-306.

[9] Einstein, A. (1917). *On the quantum mechanics of radiation.* Physikalische Zeitschrift, 18, 121-128.

[10] Frisch, R. *"Experimental demonstration of Einstein's radiation recoil."* Z. Phys 86 (1933): 42.

[11] Ashkin, A. (1970). *Acceleration and trapping of particles by radiation pressure.* Physical Review Letters, 24(4), 156.

[12] Picqué, J-L., and J-L. Vialle. *"Atomic-beam deflection and broadening by recoils due to photon absorption or emission."* Optics Communications 5, no. 5 (1972): 402-406.

[13] Schieder, R., H. Walther, and L. Wöste. *"Atomic beam deflection by the light of a tunable dye laser."* Optics Communications 5, no. 5 (1972): 337-340.

[14] Hänsch, T. W., & Schawlow, A. L. (1975). *Cooling of gases by laser radiation.* Optics Communications, 13(1), 68-69.

[15] Wineland, D. J., and H. G. Dehmelt. *"Principles of the stored ion calorimeter." Journal of Applied Physics 46.2 (1975): 919-930.*

[16] Wineland, D. J., R. E. Drullinger, and F. L. Walls. *"Radiation-pressure cooling of bound resonant absorbers."* Physical Review Letters 40.25 (1978): 1639.

[17] Neuhauser, W., M. Hohenstatt, P. Toschek, and H. Dehmelt. *"Optical-sideband cooling of visible atom cloud confined in parabolic well."* Physical Review Letters 41, no. 4 (1978): 233-236.

[18] Kügler, K-J., W. Paul, and U. Trinks. *"A magnetic storage ring for neutrons."* Physics Letters B 72, no. 3 (1978): 422-424.

[19] Heer, C. V. *"Feasibility of Containment of quantum magnetic dipoles."* Review of Scientific Instruments 34.5 (1963): 532-537.

[20] Vauthier, R. *"Focusing Properties and Resolving Power of a Magnetic Field Limited by Parallel Planes."* Compt. rend. 229 (1949).

[21] Weinert, Friedel. *"Stern—Gerlach Experiment."* Compendium of Quantum Physics. Springer Berlin Heidelberg, 2009. 746-750.

[22] Balykin, V. I., Letokhov, V. S., & Mushin, V. I. (1979). *Observation of the cooling of free sodium atoms in a resonance laser field with a scanning frequency.* JETP lett, 29(10), 560-564.

[23] Prodan, J. V., Phillips, W. D., & Metcalf, H. (1982). *Laser production of a very slow monoenergetic atomic beam.* Physical Review Letters, 49(16), 1149.

[24] Phillips, W D., and Metcalf. H. *"Laser deceleration of an atomic beam."* Physical Review Letters 48.9 (1982): 596.

[25] Prodan, J., Migdall, A., Phillips, W. D., So, I., Metcalf, H., & Dalibard, J. (1985). *Stopping atoms with laser light*. Physical Review Letters, 54(10), 992.

[26] Prodan, J. V., & Phillips, W. D. (1984). *Chirping the light—fantastic? Recent NBS atom cooling experiments.* Progress in Quantum Electronics, 8(3), 231-235.

[27] Blatt, R., W. Ertmer, and J. L. Hall. *"Cooling of an atomic beam with frequency-sweep techniques."* Progress in Quantum Electronics 8, no. 3 (1984): 237-248.

[28] Ertmer, W., R. Blatt, J. L. Hall, and M. Zhu. *"Laser manipulation of atomic beam velocities: Demonstration of stopped atoms and velocity reversal."* Physical Review Letters 54, no. 10 (1985): 996.

[29] Chu, S., Hollberg, L., Bjorkholm, J. E., Cable, A., & Ashkin, A. (1985). *Three-dimensional viscous confinement and cooling of atoms by resonance radiation pressure.* Physical Review Letters, 55(1), 48.

[30] Migdall, A. L., Prodan, J. V., Phillips, W. D., Bergeman, T. H., & Metcalf, H. J. (1985). *First observation of magnetically trapped neutral atoms.* Physical Review Letters, 54(24), 2596.

[31] Harvey, M., & Murray, A. J. (2008). *Cold atom trap with zero residual magnetic field: The ac magneto-optical trap.* Physical Review Letters, 101(17), 173201.

[32] Anderson, M. H., Ensher, J. R., Matthews, M. R., Wieman, C. E., & Cornell, E. A. (1995). *Observation of Bose-Einstein condensation in a dilute atomic vapor*. Science, 269(5221), 198-201.

[33] Davis, K. B., Mewes, M. O., Andrews, M. V., Van Druten, N. J., Durfee, D. S., Kurn, D. M., & Ketterle, W. (1995). *Bose-Einstein condensation in a gas of sodium atoms.* Physical Review Letters, 75(22), 3969.

[34] Kasevich, M., & Chu, S. (1991). *Atomic interferometry using stimulated Raman transitions.* Physical Review Letters, 67(2), 181.

[35] Gibble, K., & Chu, S. (1993). *Laser-cooled Cs frequency standard and a measurement of the frequency shift due to ultracold collisions.* Physical Review Letters, 70(12), 1771.

[36] Monroe, C., Meekhof, D. M., King, B. E., Itano, W. M., & Wineland, D. J. (1995). *Demonstration of a fundamental quantum logic gate.* Physical Review Letters, 75(25), 4714.

[37] Schappe, R. S., P. Feng, L. W. Anderson, C. C. Lin, and T. Walker. *"Electron collision cross-sections measured with the use of a magneto-optical trap."* EPL (Europhysics Letters) 29, no. 6 (1995): 439.

[38] Dinneen, T. P., Wallace, C. D., Tan, K. Y. N., & Gould, P. L. (1992). *Use of trapped atoms to measure absolute photoionization cross sections.* Optics letters, 17(23), 1706-1708.

[40] Zatsarinny, O., and S. S. Tayal. *"Photoionization of potassium atoms from the ground and excited states."* Physical Review A 81.4 (2010): 043423.

[41] Aymar, M., E. Luc-Koenig, and F. Combet Farnoux. *"Theoretical investigation on photoionization from Rydberg states of lithium, sodium and potassium."* Journal of Physics B: Atomic and Molecular Physics 9, no. 8 (1976): 1279.

[42] Nygaard, Kaare J., Robert J. Corbin, and J. Daniel Jones. *Two-step photoionization of potassium atoms*. Physical Review A 17, no. 4 (1978): 1543

[43] Barrientos, C., & Martin, I. (1988). *Oscillator strength distribution in the alkaline-earth elements.* Canadian journal of physics, 66(1), 29-33.

[44] Burkhardt, C. E., Libbert, J. L., Xu, J., Leventhal, J. J., & Kelley, J. D. (1988). *Absolute measurement of photoionization cross sections of excited atoms: Application to determination of atomic beam densities.* Physical review A, 38(11), 5949.

[45] Duncan, B. C., Sanchez-Villicana, V., Gould, P. L., & Sadeghpour, H. R. (2001). *Measurement of the Rb ($5D_{5/2}$) photoionization cross-section using trapped atoms.* Physical Review A, 63(4), 043411.

[46] Gabbanini, C., Gozzini, S., & Lucchesini, A. (1997). *Photoionization cross section measurement in a Rb vapor cell trap.* Optics communications, 141(1), 25-28.

[47] Maragò, O., Ciampini, D., Fuso, F., Arimondo, E., Gabbanini, C., & Manson, S. T. (1998). *Photoionization cross sections for excited laser-cooled cesium atoms.* Physical Review A, 57(6), R4110.

[48] Gabbanini, C., Fioretti, A., Lucchesini, A., Gozzini, S., & Mazzoni, M. (2000). *Cold rubidium molecules formed in a magneto-optical trap.* Physical Review Letters, 84(13), 2814.

[50] Amin, N., Mahmood, S., Anwar-ul-Haq, M., & Baig, M. A. (2006). *Measurement of the 4d-photoionization cross section via two-photon and two-step excitation in sodium.* Journal of Quantitative Spectroscopy and Radiative Transfer, 102(2), 269-276.

[51] Moskvin, Yu V. *"Photoionization of atoms and recombination of ions in the vapors of alkali metals."* Optical Spectroscopy.(USSR)(English Transl.) 15 (1963).

[52] Ambartzumian, R. V., Furzikov, N. P., Letokhov, V. S., & Puretsky, A. A. (1976). *Measuring photoionization cross-sections of excited atomic states.* Applied physics, 9(4), 335-337.

[53] Heinzmann, U., Schinkowski, D., & Zeman, H. D. (1977). *Comment on measuring photoionization cross sections of excited atomic states.* Applied physics, 12(1), 113-113.

[54] Duong, H. T., J. Pinard, and J-L. Vialle. *"Experimental separation and study of the two partial photoionisation cross sections σ3p, s and σ3p, d from the 3p state of sodium."* Journal of Physics B: Atomic and Molecular Physics 11, no. 5 (1978): 797.

[55] He, L. W., Burkhardt, C. E., Ciocca, M., Leventhal, J. J., & Manson, S. T. (1991). *Absolute cross sections for the photoionization of the 6s6p P excited state of barium.* Physical Review Letters, 67(16), 2131.

[56] Willke, B., and M. Kock. *"Photoionization cross sections from the Ba (6s6p) $^1P_1°$ state."* Physical Review A 43, no. 11 (1991): 6433.

[57] Mende, W., Bartschat, K., & Kock, M. (1995). *Near-threshold photoionization from the Sr I (5s5p) 1Po1 state.* Journal of Physics B: Atomic, Molecular and Optical Physics, 28(12), 2385.

[58] Petrov, I. D., Sukhorukov, V. L., Leber, E., & Hotop, H. (2000). *Near threshold photoionization of excited alkali atoms Ak (np)(Ak= Na, K, Rb, Cs; n= 3-6).* The

European Physical Journal D-Atomic, Molecular, Optical and Plasma Physics, 10(1), 53-65.

[59] Amin, N., Mahmood, S., Haq, S. U., Kalyar, M. A., Rafiq, M., & Baig, M. A. (2008). *Measurements of photoionization cross sections from the 4p, 5d and 7s excited states of potassium.* Journal of Quantitative Spectroscopy and Radiative Transfer, 109(5), 863-872.

[60] Patterson, B. M., Takekoshi, T., & Knize, R. J. (1999). *Measurement of the photoionization cross section of the 6 P 3/2 state of cesium.* Physical Review A, 59(3), 2508.

[61] Wippel, V., C. Binder, W. Huber, L. Windholz, M. Allegrini, F. Fuso, and E. Arimondo. *"Photoionization cross-sections of the first excited states of sodium and lithium in a magneto-optical trap."* The European Physical Journal D-Atomic, Molecular, Optical and Plasma Physics 17, no. 3 (2001): 285-291.

[62] Lowell, J. R., Northup, T., Patterson, B. M., Takekoshi, T., & Knize, R. J. (2002). *Measurement of the photoionization cross section of the 5 S 1/2 state of rubidium.* Physical Review A, 66(6), 062704.

[63] Anderson, W. R., Veale, J. R., & Gallagher, T. F. (1998). *Resonant dipole-dipole energy transfer in a nearly frozen Rydberg gas.* Physical Review Letters, 80(2), 249.

[64] Mourachko, I., Comparat, D., De Tomasi, F., Fioretti, A., Nosbaum, P., Akulin, V. M., & Pillet, P. (1998). *Many-body effects in a frozen Rydberg gas.* Physical Review Letters, 80(2), 253.

[65] Farooqi, S. M., Tong, D., Krishnan, S., Stanojevic, J., Zhang, Y. P., Ensher, J. R Estrin A S, Boisseau C, Cote R,Eyler E E & Gould, P. L. (2003). *Long-range molecular resonances in a cold Rydberg gas.* Physical Review Letters, 91(18), 183002.

[66] Vogt, T., Viteau, M., Zhao, J., Chotia, A., Comparat, D., & Pillet, P. (2006). *Dipole blockade at Förster resonances in high resolution laser excitation of Rydberg states of cesium atoms.* Physical review letters, 97(8), 083003.

[67] McGeoch, M. W., Schlier, R. E., & Chawla, G. K. (1988). *Associative ionization with cold Rydberg lithium atoms.* Physical Review Letters, 61(18), 2088.

[68] Li, W., Mourachko, I., Noel, M. W., & Gallagher, T. F. (2003). *Millimeter-wave spectroscopy of cold Rb Rydberg atoms in a magneto-optical trap: Quantum defects of the ns, np, and nd series.* Physical Review A, 67(5), 052502.

[69] Beterov, I. I., Tretyakov, D. B., Ryabtsev, I. I., Ekers, A., & Bezuglov, N. N. (2007*). Ionization of sodium and rubidium n S, n P, and n D Rydberg atoms by blackbody radiation.* Physical Review A, 75(5), 052720.

[70] Lorenzen, C. J., & Niemax, K. (1983). *Quantum Defects of the* $n^2P_{1/2,\ 3/2}$ *Levels in* ^{39}K *I and* ^{85}Rb *I.* Physica Scripta, 27(4), 300.

[71] Gallagher, Thomas F. *Rydberg atoms*. Vol. 3. Cambridge University Press, 2005.

[72] Hogan, S. D., and F. Merkt. *"Demonstration of three-dimensional electrostatic trapping of state-selected Rydberg atoms."* Physical Review Letters 100, no. 4 (2008): 043001.

[73] Gallagher, T. F., & Pillet, P. (2008). *Dipole–dipole interactions of Rydberg atoms.* Advances in Atomic, Molecular, and Optical Physics, 56, 161-218.

[74] Saffman, M., Walker, T. G., & Mølmer, K. (2010). *Quantum information with Rydberg atoms.* Reviews of Modern Physics, 82(3), 2313.

[75] Lee, S. A., Stoicheff, B. P., Helmcke, J., & Hall, J. L. (1978). *Doppler-free two-photon transitions to Rydberg levels: convenient, useful, and precise reference wavelengths for dye lasers.* Optics letters, 3(4), 141-143.

[76] Stoicheff, B. P., & Weinberger, E. (1979). *Doppler-free two-photon absorption spectrum of rubidium.* Canadian Journal of Physics, 57(12), 2143-2154.

[77] Pendrill, L. R., Delande, D., & Gay, J. C. (1979). *Quantum defect and fine-structure measurements of P, D, F and G Rydberg states of atomic caesium.* Journal of Physics B: Atomic and Molecular Physics, 12(20), L603.

[78] Lorenzen, C. J., Niemax, K., & Pendrill, L. R. (1981). *Precise measurements of< ^{39}K nS and nD energy levels with an evaluated wavemeter*. Optics Communications, 39(6), 370-374.

[79] Singer, K., Reetz-Lamour, M., Amthor, T., Marcassa, L. G., & Weidemüller, M. (2004). *Suppression of excitation and spectral broadening induced by interactions in a cold gas of Rydberg atoms*. Physical Review Letters, 93(16), 163001.

[80] Dutta, S. K., Feldbaum, D., Walz-Flannigan, A., Guest, J. R., & Raithel, G. (2001). *High-angular-momentum states in cold Rydberg gases*. Physical Review Letters, 86(18), 3993.

[81] Robinson, M. P., Tolra, B. L., Noel, M. W., Gallagher, T. F., & Pillet, P. (2000). *Spontaneous evolution of Rydberg atoms into an ultracold plasma*. Physical Review Letters, 85(21), 4466.

[82] Gallagher, T. F., Pillet, P., Robinson, M. P., Laburthe-Tolra, B., & Noel, M. W. (2003). *Back and forth between Rydberg atoms and ultracold plasmas.* JOSA B, 20(5), 1091-1097.

CHAPTER TWO

Theoretical Background

2.0 Introduction

In the experiments described in this thesis, lasers are used to manipulate atoms leading to the slowing, trapping, excitation and ionization of potassium atoms. This chapter gives an overview of the target element (potassium), and the theory behind the interactions of light with matter. Special attention is given to the dynamics of atoms in a laser field, which is vital in understanding the techniques of laser cooling, trapping and photoionization of neutral atoms. First a summary of the properties of atomic potassium relevant to laser cooling and trapping is given, followed by a general treatment of the interaction of light with matter. Next the interactions of light with neutral atoms, with particular focus on the quantum mechanical treatment of atoms in a laser field is given, and a summary of the derivation of the equations governing the motion and behavior of atoms in such fields is presented.

2.1 Potassium

Potassium is an alkali metal element with three naturally occurring isotopes namely: ^{39}K (93.23%) ^{40}K (0.012%) and ^{41}K (6.72%). Potassium has one electron in the outer shell, which makes it chemically very reactive. Unlike other alkali metals, the nuclear magnetic moments of its isotopes are comparatively small; this leads to correspondingly small hyperfine splitting of the excited states, as shown in figure 2.1. This small splitting informed the approach employed in the cooling and trapping of ^{39}K in the AC-MOT as described in this thesis.

2.1.1 Fine and Hyperfine structure of ^{39}K

The fine structure of atoms originates from the coupling of the orbital angular momentum **L** of the electrons and the magnetic moment associated with its spin **S** with corresponding quantum numbers *L* and *S*. The total angular momentum is given by:

$$\mathbf{J} = \mathbf{L} + \mathbf{S} \tag{2.1}$$

where **J** has associated quantum number J, known as the total electron angular momentum quantum number. The values of J range from $|L - S| \leq J \leq L + S$. The electronic ground state of ^{39}K is the $4^2S_{1/2}$ state with $L=0$ and $S=1/2$, and therefore $J = 1/2$. For the first excited state, $L=1$ and $S=1/2$, and so J can take on values $1/2$ or $3/2$. These correspond to the states $4^2P_{1/2}$ and $4^2P_{3/2}$ respectively. Because of the fine structure interaction, the $4^2P_{1/2}$ and $4^2P_{3/2}$ excited states have different energies, therefore excitation to the first excited P-state results in two spectral lines, the D_1 ($4^2S_{1/2} \rightarrow 4^2P_{1/2}$) and the D_2 ($4^2S_{1/2} \rightarrow 4^2P_{3/2}$) lines, which are resonant at around 770.1 nm and 766.7 nm respectively, (see figure 2.1).

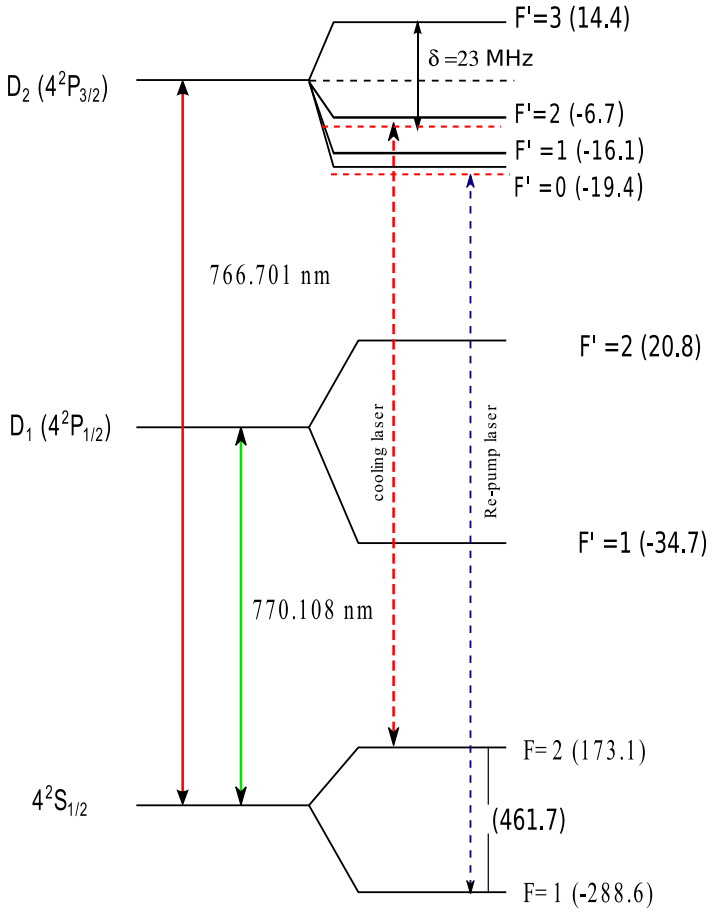

Fig2.1: Energy level diagram of ^{39}K showing the fine and hyperfine structure. The $4^2S_{1/2}$ ground state has two sub-energy levels separated by ~461.7 MHz. The first excited P-state has two spectral lines D_1 ($4^2P_{1/2}$) and D_2 ($4^2P_{3/2}$), which are resonant at around 770.1 nm and 766.7 nm respectively. The trapping laser is locked to the $4^2P_{1/2} \rightarrow 4^2P_{3/2}$ transition red detuned by 23 MHz (red dashed line) and the blue dashed line indicates the re-pump frequency.

The interaction between the nuclear spin **I** and the total electronic angular momentum **J** is the origin of the hyperfine structure of atoms. The total angular momentum (including nuclear spin) is denoted by $\boldsymbol{F}$ and is given by:

$$\mathbf{F} = \mathbf{J} + \mathbf{I} \tag{2.2}$$

The values of the corresponding quantum number F associated with $\mathbf{F}$, lies between $|J - I| \leq F \leq J + I$ (in integer steps), where I is the nuclear spin quantum number corresponding to **I.** For ^{39}K, the nuclear spin quantum number $I = 3/2$, and therefore, $F = 1, and\ 2$ for the ground state. For the $4^2P_{1/2}$ excited state, $F' = 1, and\ 2$, while for the $4^2P_{3/2}$ excited state, F takes values 0,1,2 and 3 as shown in fig 2.1.

The total shift in the energy level due to the hyperfine structure is given by [1]:

$$\Delta E_{hyp} = \frac{1}{2}hAK + hB\frac{\frac{3}{2}K(K+1) - 2I(I+1)J(J+1)}{2I(2I-1)2J(J-1)}\ Joule \tag{2.3}$$

where $K = F(F+1) - I(I+1) - J(J+1)$, and h is the Planck's constant.

A is the magnetic-dipole coupling constant and B is the electric-quadruple coupling constant. The hyperfine splitting of the ground state and the $4^2P_{1/2}$ excited state are determined only by the magnetic-dipole interaction, since the electric-quadruple interaction is only present for states with $I, J \geq 1$. The hyperfine constants are obtained from experiments, and are unique for each element and state. For the ground and excited states of ^{39}K shown in fig 2.1, the hyperfine constants are listed in table 2.1[1].

States	**A (MHz)**	**B (MHz)**
$4^2S_{1/2}$	230.859860 [21]	-
$4^2P_{1/2}$	28.848	-
$4^2P_{3/2}$	6.077	2.875

Table 2.1: The hyperfine constants of the ground and first excited states of ^{39}K. The constant B is only present for states with $I, J \geq 1$.

In the experiment described here, the $4^2S_{1/2}$ ground state and the $4^2P_{3/2}$ excited state are used in cooling and trapping of potassium because this provides the largest damping force [2]. The F=1and F=2 hyperfine splitting of the ground state is separated by $\sim 462\ MHz$, while the F′=0 and

F′=3 excited state hyperfine splitting are separated by only $\sim 33\ MHz$ as shown in the energy level diagram in figure 2.1.

The trapping transition at $\approx 766.7\ nm$ has an excited state lifetime of 26.37 ns, which corresponds to a natural line-width of 6.035 MHz. The small splitting of the excited state, which is of the order of the natural line-with, makes it difficult to resolve individual sub-states. This results in the overlapping of different states, and excitation to any of the first excited sub-states is accompanied by unavoidable excitation to other sub-states. The excited atoms can then decay to other states, which are not resonant with the trapping transition. This makes effective laser cooling and trapping of ^{39}K more difficult than it is for some alkali metals like rubidium with the $5S_{1/2}$ ground state splitting separated by ~ 3 GHz, and the $5P_{3/2}$ splitting separated by ~200 MHz.

2.1.2 The Selection Rules.

The basic process of laser cooling involves the absorption and emission of photons, which results in the transfer of momentum from the laser field to the atom. Slowing an atom from a thermal velocity requires photons to be scattered tens of thousands of time in an excitation-decay cycle, (for potassium about 45 thousand interactions are required for the condition used in this experiment). It is therefore important that the atom remains in states which are accessible to the cooling laser.

The selection rule for the allowed transitions requires the conservation of both energy and angular momentum of the system made up of atom and photon, as well as the linear momentum and the parity. This implies that absorption of photons must be accompanied by a corresponding change of the projection of the angular momentum of the atom along the quantization axis.

The selection rule is such that the absorption of a right hand circular polarized, σ^+ photon must cause the projection of angular momentum to change by $\Delta m = +1$, whereas the absorption of left hand polarized, σ^- photon must cause a change by $\Delta m = -1$ [2]. Absorption of a linear polarized π, light will result in $\Delta m = 0$ for a quantization axis along the direction of the laser field. Since the angular momentum of the photon is $\hbar$, the absorption and emission of photons must obey the selection rule $\Delta F = 0, \pm 1$. This means that atoms in the F′=3 excited state can only decay to the F=2 ground state, but atoms in the F′=1 or F′=2 can decay to either the F=1 or F=2 ground states. To ensure that atoms remain accessible to the laser field, the slowing and trapping lasers are circular polarized to pump the atoms into a two-level system, where excitation and decay are restricted to discrete eigenstates, in this case the F=2→F′=3 transition cycle as shown in figure 2.2.

Excitations to the F′=3 excited state from the F=2 ground state are accompanied by unavoidable excitation to the F′=2 excited state due to the close hyperfine splitting between F′=3 and F′=2 excited states. From the F′=2 excited state, atoms can decay to the F=1 ground state, which are not accessible to the cooling laser beam because of the narrow line-width of the laser, and so there would be a depletion of the F=2 ground state due to optical pumping. With no intervention, the cooling process would come to an abrupt end due to loss of atoms to the non-resonant state.

In this experiment, the cooling laser is red detuned by $\sim 23\ MHz$ with respect to the F=2→F′=3 transition, which enhances the depletion of the F=2 ground state due to an increased rate of excitation to the F′=2 state (since the cooling laser is brought close to resonance with the F=2→F′=2 transition by the detuning). To counteract the depletion of the F=2 ground state and sustain the cooling process, a second laser beam at a different frequency is necessary. This second laser beam referred to as the re-pump laser, cycles the atoms back into the F=2 ground state. The re-pump frequency is increased by $441\ MHz$ (the ground state hyperfine splitting (462 MHz) minus the separation F′=2 and F′=3 excited state levels (21 MHz)).

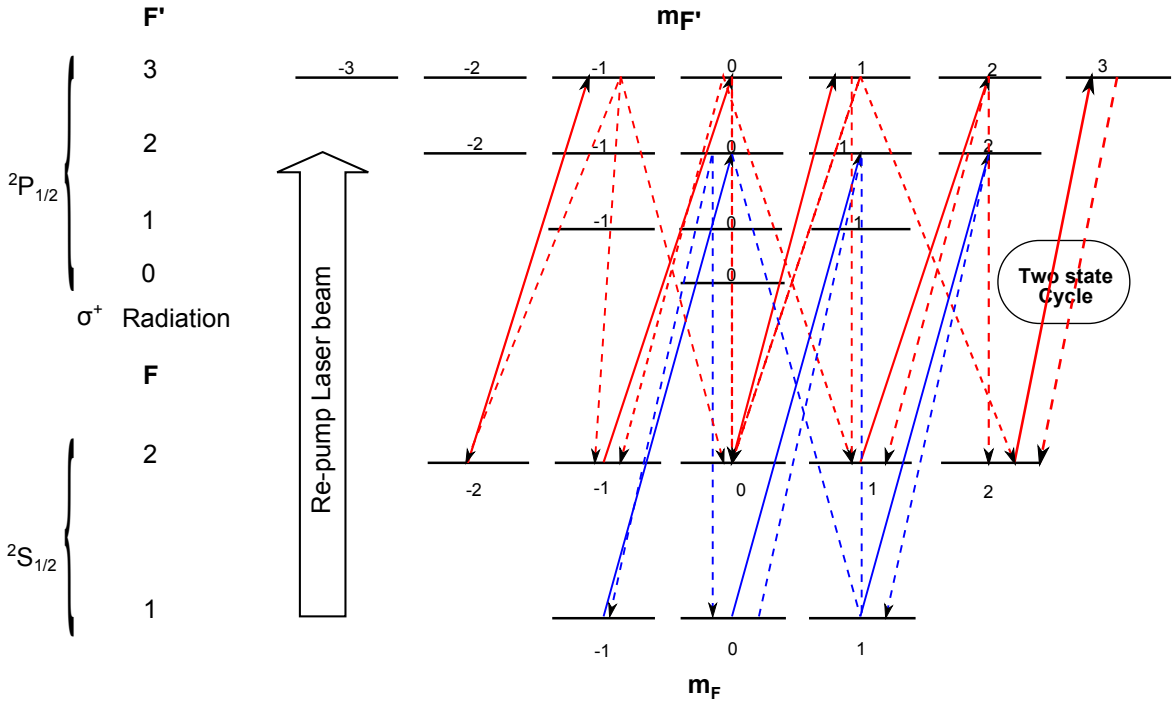

Fig 2.2: Creating a two level system with the use of circular polarized radiation. Two laser frequencies (the main laser shown in red and the re-pump beam shown in blue) are required to effectively cool and trap ^{39}K. Due to the small hyperfine splitting, the main laser (resonant with the F=2→ F′=3 transition) can excite atoms to states other than the F′=3 state, leading to a loss of atoms that are accessible using this laser. The re-pump laser beam re-pumps atoms that are in the F=1 ground state back to the excited state so that they can continue to participate in the trapping cycle. The thick lines and dashed lines indicate excitation and decay paths respectively.

2.1.3 Hyperfine Zeeman Splitting

In the absence of a magnetic field, the atomic sub-levels m_F are degenerate, but this degeneracy is lifted in the presence of a magnetic field. This is due to the interaction between the magnetic moment of the atom and the external magnetic field, which results in the splitting of the energy levels. This then shifts the resonant frequency for the absorption of σ^- and σ^+ polarized light. The shift in energy ΔE for a state with quantum number F is given by [3]

$$\Delta E = g_F \mu_B B m_F \tag{2.4}$$

where g_F is the hyperfine Landé g-factor, μ_B is the Bohr magneton, B is the magnitude of the applied magnetic field and m_F is the magnetic quantum number.

This shift is only linear for magnetic fields low enough to keep the nuclear spin I, and the total electron angular momentum J, strongly coupled. The Landé g-factor is given by

$$g_F = g_J \frac{F(F+1) + J(J+1) - I(I+1)}{2F(F+1)} \tag{2.5}$$

where

$$g_J = 1 + \frac{J(J+1) + S(S+1) - L(L+1)}{2J(J+1)} \tag{2.6}$$

The factors J, L and S are the orbital, spin and total electron angular momentum quantum numbers. For ^{39}K, the nuclear spin $I = 3/2$ and the electron spin is $S = 1/2$. As stated above, the $4^2P_{3/2}$ excited state has $L = 1,\ J = 3/2$ and the $4^2S_{1/2}$ has $L = 0,\ J = 1/2$. The shift in excitation frequency $\Delta\omega$ from resonance, between two energy sub-levels E_1 and E_2 is according to equation 2.4 then given by

$$\Delta\omega = \frac{\mu_B B}{\hbar}(g_2 m_{F'} - g_1 m_F) \tag{2.7}$$

For the F=2→F′=3 transition cycle shown in fig 2.2, the F=2, $m_F = 2$ ground state has the Landé g-factor $g_1 = 1/2$, and the excited state F′=3, m_F=3 has Landé g-factor $g_2 = 2/3$. This results in a frequency shift of 1.40 MHz/G of applied magnetic field for this transition. This hyperfine Zeeman splitting is illustrated in figure 2.3.

The Zeeman Effect is exploited in several parts of the experiment discussed here, namely:

- The laser locking system, where a DC magnetic field is applied to Zeeman-shift the energy levels of potassium atoms in the vapor cell; thereby giving an appropriate detuning to the main laser.
- The Zeeman slower, where the magnetic field along the path of the atoms is varied as the atoms travel down the Zeeman slower flight tube. This shifts the energy levels of the atoms in order to counteract the Doppler shift experienced by the atoms, and by so doing keeps the atoms in resonance with the slowing laser beam.
- The Magneto-Optical Trap, where a non-homogeneous magnetic field, which is zero at the centre but increases in magnitude with distance from this centre, is used to create a restoring force towards the centre of the trap when combined with trapping laser beams. The atoms in the MOT experience an increased Zeeman shift as they move further away from the centre of the trap.

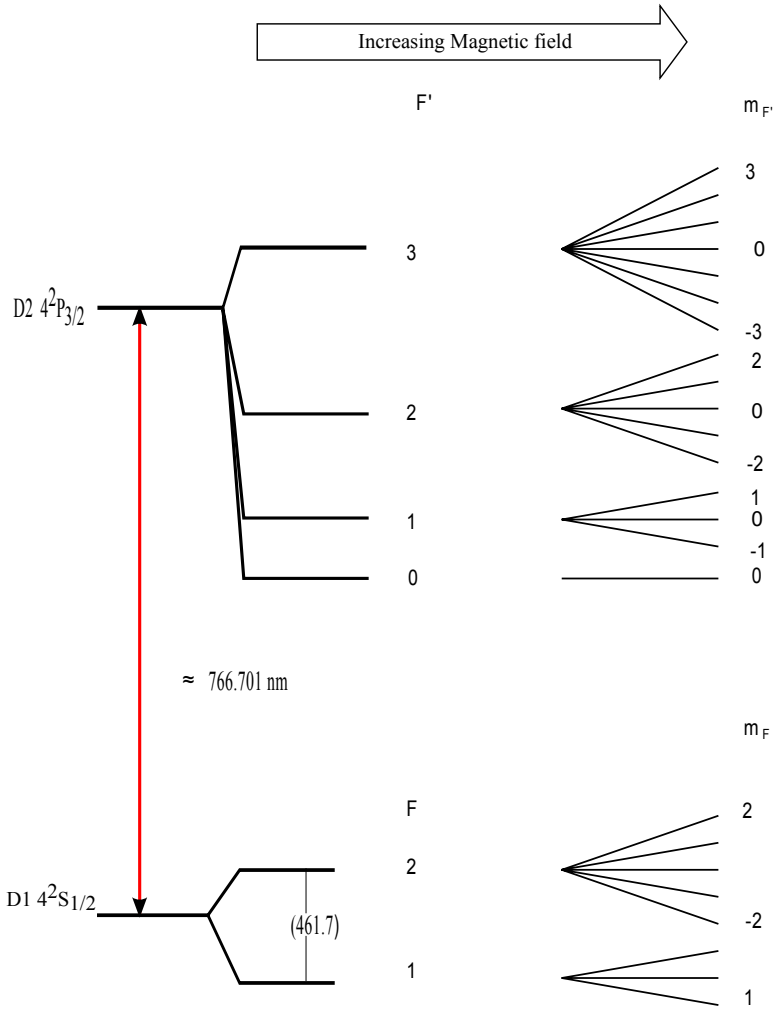

Fig2.3: The hyperfine Zeeman splitting. In the presence of an external magnetic field, the degenerate hyperfine energy levels split into discrete sub-levels. As the magnetic field increases, the excited state sub-levels start to overlap in energy.

2.2 Light – Matter Interaction

Light is an electromagnetic radiation, and when in contact with matter interacts with the atoms of which matter is made of, leading to different phenomena. Einstein in 1917 [4] predicted three different processes result when light of the correct frequency interacts with matter. These are absorption, spontaneous emission, and stimulated emission.

In absorption, an incoming photon interacts with an atom in the ground state, resulting in the disappearance of the photon and the atom being promoted to an excited state. Spontaneous emission occurs when an atom in the excited state decays to a lower state, with no other photon being present. This results in the emission of a photon, and the atom returns to the ground state. The third process (stimulated emission) begins with an atom in the excited state together with a photon, resulting in the emission of a photon from the atom (the photon from the atom being identical to the incident photon), and the atom returning to the ground state. These processes are illustrated in figure 2.4.

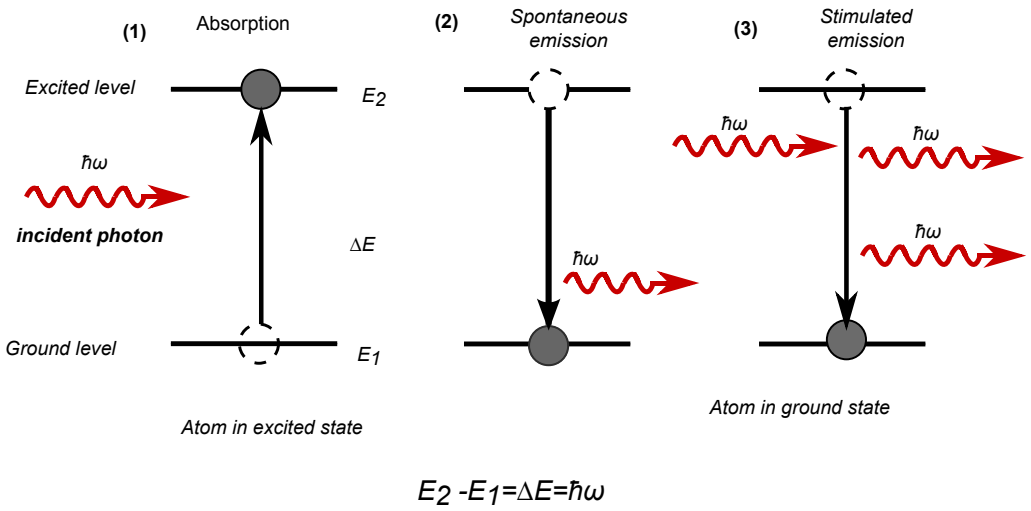

Fig 2.4: Light matter interactions with resonant radiation. (1) An atom originally in the ground state absorbs a photon and is excited. Following excitation, the atom can emit a photon and returns back to the ground state through (2) spontaneous emission, (3) Stimulated emission.

Under ordinary equilibrium conditions, there are more atoms in the ground state than in the excited state in a given medium. Through the process of population inversion of levels, a non-equilibrium distribution of atoms among the excited states can be produced in some materials, so that more atoms are in the excited states than there are in the ground state. In such a medium, light amplification through stimulated emission can be achieved.

2.2.1 Rate of Spontaneous Emission

The transition of an excited atom to the ground state through spontaneous emission is a random process, with the direction of the emitted photon and the time when the emission occurs being both random in nature. As a result, information about the process can be obtained by averaging over a large number of independent measurements of the energy $E = \hbar\omega$ or frequency ω, of the emitted photons and the time delay between excitation and spontaneous decay of the atom. The rate of spontaneous emission Γ from an excited state $|e\rangle$, to the ground state $|g\rangle$ is given by [5],

$$\Gamma = \frac{32\pi^3}{3\hbar\lambda^3}\left|d_{eg}\right|^2 \qquad \{for\ d_{eg} \neq 0\} \tag{2.8}$$

where λ is the wavelength of radiation from the transition $e \rightarrow g$, and $|d_{eg}|$ is the expectation value of the transition dipole moment operator $\hat{\mathbf{d}} = \mathrm{e}_j\mathbf{r_j}$ given by [2],

$$d_{eg} = \langle e|\mathbf{d}|g\rangle = e_j \int \psi_e{}^*(r_j)\boldsymbol{r_j}\psi_g(r_j)\,\boldsymbol{dr}_j \tag{2.9}$$

ψ_e and ψ_g are the wavefunctions describing the states $|e\rangle$and $|g\rangle$ respectively. e_j is the electronic charge, and $\mathbf{r_j}$ is the radius vector of the electron.

2.2.2 Rate of Stimulated emission and Absorption

Unlike spontaneous emission, stimulated emission occurs in the direction of the incident radiation. The rate of stimulated transitions depends on the intensity of the radiation.

The rate of stimulated emission per unit intensity is given by [5],

$$Q = \frac{8\pi}{c\hbar^2\Delta\omega_0}|\varepsilon.\boldsymbol{d}|^2 \tag{2.10}$$

where c is the speed of light, ε is the electromagnetic field polarization, $\boldsymbol{d}$ is the dipole matrix elements of the atomic transition, and $\Delta\omega_0$ is the full width at half maximum of the atomic line width. For atoms whose line width is entirely due to spontaneous emission (where there is no collision or Doppler effects), $\Delta\omega_0 = \Gamma$, the rate of spontaneous emission. This is equal to the inverse of the excited state lifetime τ, and is called the natural width of the transition.

$$\Gamma = \frac{1}{\tau} \tag{2.11}$$

Equation 2.10 can then be written as,

$$Q = \frac{8\pi}{c\hbar^2\Gamma}|\varepsilon.\boldsymbol{d}|^2 \tag{2.12}$$

Using equation 2.8, a relationship between the rate of stimulated and spontaneous emission is obtained.

$$Q = \frac{3\lambda^3}{2\pi ch}\,\frac{|\varepsilon.\boldsymbol{d}|^2}{d^2} \tag{2.13}$$

$\frac{|\varepsilon.\boldsymbol{d}|^2}{d^2}$ can be written as $\left|\varepsilon.\hat{\boldsymbol{d}}\right|^2$, where $\hat{\boldsymbol{d}}$ is the unit vector along the dipole moment $\boldsymbol{d}$. The quantity $\left|\varepsilon.\hat{\boldsymbol{d}}\right|^2$, which contains the dipole selection rule information for the given transition, takes values between zero and unity. For a two level atom, $\left|\varepsilon.\hat{\boldsymbol{d}}\right|^2 = 1$ [5], and the rate of stimulated emission per unit intensity can then be written for a pure two state atom as;

$$Q = \frac{3\lambda^3}{2\pi ch} \tag{2.14}$$

2.2.3 Evolution of Population of States-The Rate Equations for a Two Level System

Assuming light tuned exactly to the atomic resonance is incident on a system with only one ground state and one excited state – a two-level system. Populations transfer between the states then occurs only through the processes of stimulated and spontaneous transitions, the rate equation describing the transfer of atoms to each state being given by [6]

$$\dot{N}_e = -QIN_e + QIN_g - \Gamma N_e\,, \tag{2.15}$$

$$\dot{N}_g = QIN_e - QIN_g + \Gamma N_e\,, \tag{2.16}$$

where N_e *and* N_g are the excited state and ground state population densities respectively, Q is the rate of stimulated emission per unit intensity, I is the light intensity and Γ is the

rate of spontaneous emission. The first two terms of equations 2.15 and 2.16 describe the rate at which atoms are lost from the excited state and added to the ground state through stimulated emission and the third term relates to the spontaneous emission. Equation 2.15 means that the excited state population changes for three reasons at three different rates: at the rate of $-QIN_e$ because of induced emission, at the rate of QIN_g due to absorption, and at the rate of $-\Gamma N_e$ due to spontaneous emission. A similar interpretation applies to equation 2.16, except that the term $+\Gamma N_e$ represents the rate at which atoms are added to the ground state because of spontaneous decay.

Under steady state conditions, equations 2.15 and 2.16 equate to zero

$$-QIN_e + QIN_g - \Gamma N_e = QIN_e - QIN_g + \Gamma N_e = 0 \tag{2.17}$$

For a closed system,

$$N_e + N_g = N \tag{2.18}$$

where N is the total number of atoms in the system.

Substituting for N_g in equation 2.17 using 2.18, and rearranging leads to equation 2.19

$$2QIN_e + \Gamma N_e = QIN \tag{2.20}$$

The total number of atoms in the excited state N_e in the steady state then becomes:

$$N_e = \frac{QI}{2QI + \Gamma} N \tag{2.20}$$

Equation 2.20, implies that as $I \longrightarrow \infty$, $N_e \longrightarrow \frac{1}{2}N$, indicating that no more than half the number of atoms can be pumped to the excited state.

As stated above for a pure two level system, $\left|\varepsilon.\hat{\boldsymbol{d}}\right|^2 = 1$. At the saturation intensity, one quarter of the atoms in the system will be in the excited state (intensity $I = I_0$ [5]), and so, equation 2.20 can be written as,

$$N_e = \frac{QI_0}{2QI_0 + \Gamma} N = \frac{1}{4}N \tag{2.21}$$

So that

$$I_0 = \frac{\Gamma}{2Q} \tag{2.22}$$

This equation implies the intensity of radiation that saturates a given transition depends on both rates of transition.

Putting equation 2.14 into equation 2.22, yields

$$I_0 = \frac{\pi hc\Gamma}{3\lambda^3} \tag{2.23}$$

This gives the saturation intensity in terms of the rate of spontaneous decay (excited state lifetime) of the transition and the laser wavelength. From equation 2.22, the rate of stimulated emission can then be written as,

$$\mathrm{Q} = \frac{\Gamma}{2I_0} \tag{2.24}$$

Substituting this into equations 2.15 and 2.16, the evolution of the state as the light field interacts with the system can be described by the rate equations;

$$\dot{N}_e = -\frac{I}{2I_0}\Gamma\left(N_e - N_g\right) - \Gamma N_e \tag{2.25}$$

$$\dot{N}_g = \frac{I}{2I_0}\Gamma\left(N_e - N_g\right) + \Gamma N_e \tag{2.26}$$

Defining the saturation parameter S_0 as,

$$S_0 = \frac{I}{I_0} \tag{2.27}$$

and noting that $N_e + N_g = N \equiv constant$, the rate equations can be written as

$$\dot{N}_e = -(\Gamma + S_0\Gamma)N_e(t) + \frac{S_0}{2}\Gamma N \tag{2.28}$$

Equation 2.28 has a solution;

$$N_e(t) = \left[N_0 - \frac{1}{2}\frac{S_0\Gamma N}{\Gamma(S_0+1)}\right]e^{-\Gamma(S_0+1)t} + \frac{1}{2}\frac{S_0\Gamma N}{\Gamma(S_0+1)}, \tag{2.29}$$

where N_0 is the excited state population at time $t = 0$.

If there is no radiation field ($I = 0 \Rightarrow S_0 = 0$), equation 2.21 reduces to

$$N_e(t) = N_0 e^{-\Gamma t} \tag{2.30}$$

This means that the excited state population decays purely in an exponential manner.

With a laser of low intensity ($I \lll I_0 \Rightarrow S_0 \lll 1$), and all the atoms initially in the ground state, the excited state population increases as

$$N_e(t) = \frac{S_0 N}{2}(1 - e^{-\Gamma t}), \tag{2.31}$$

and after a time Γ^{-1} reaches a very small steady state population $\frac{S_0 N}{2} \lll N$.

In a strong laser field ($I \ggg I_0 \Rightarrow S_0 \ggg 1$), the equation reduces to

$$N_e(t) = \left[N_0 - \frac{N}{2}\right] e^{-\Gamma S_0 t} + \frac{N}{2}, \quad \rightarrow \frac{N}{2} \tag{2.32}$$

Equation 2.32 implies that even at high laser power, it is not possible to have more than half the atoms in the excited state (at least for a two level system), as has been noted previously. These rate equations can be extended to multilevel atoms by adding terms to take account of stimulated and spontaneous emission for each additional state.

2.3 Quantum Electrodynamics Treatment of Atom In A Laser Field

The description of the interaction of an atom with a coherent light source is complex, particularly for atoms with energy levels consisting of manifolds of degenerate and near degenerate states, as is the case with potassium. The interaction transfers information from the ground to the excited state in a coherent manner hence it is important to consider the influence of any dephasing on the signal due to spontaneous emission. The use of rate equations as illustrated above, do not include the coherent nature of the light source except those implied in the Einstein coefficients. In the semi-classical approach, while the atom is quantized, the laser field is left un-quantized. This approach has been adopted by several authors [7].

A more rigorous and complete model for the description of atom-laser interactions is the Quantum Electrodynamics (QED) model, where both the laser field and the atomic system are quantized. In this model, the coupling of the atomic system with the field is described by an interaction Hamiltonian containing both atomic and field operators, making it possible to derive the coupling coefficients directly from the evolution of the system under

the influence of this Hamiltonian. In doing this, the time evolution of the atomic matrix element under electric dipole interactions with a coherent light field is described in terms of creation and annihilation operators.

Although the derivation of this QED model was not part of the work described in this thesis, it is useful to highlight some aspects of this interaction, which are relevant to laser cooling and trapping. Therefore only a brief description is given here, with a summary of the equations of motion which have been derived by previous researchers.

The interaction of atoms and laser radiation described in this work is based on the QED model developed by J. R. Ackerhalt and J. H. Eberly (1974) [8], for a two level system. This was extended to a three-level atom by Whitley et al [9]. The derivation of the general equations describing the interaction is based on the work of Farrell et al [10]. This model was modified [11] to incorporate a mechanism to take into account a second laser mode in the double-mode excitation scheme for sodium. N.Strohmaier [12] made an attempt to extend the double-mode excitation model to potassium, and incorporated the effect of an applied magnetic field by adding effective detunings to the 24 sub-levels of the potassium ground and first excited state. In deriving the equations of motion presented here, a two level system is assumed for simplicity, with the interaction only being with a single mode of the laser field.

2.3.1 Density Matrix Representation of the Atomic Operator

In quantum mechanics, the state vector $|\Psi\rangle$, provides all information about a pure state, which can be determined (except the overall phase) by performing measurements corresponding to a complete set of commuting observables. The time evolution of a quantum system can be described by the time dependent Schrödinger equation

$$i\hbar\frac{\partial}{\partial t}\Psi = \widehat{\boldsymbol{H}}\Psi \tag{2.33}$$

where $\widehat{H}$ is a Hamiltonian and Ψ is the wavefunction for the system.

The interaction of the laser field with an atom leaves the atom in a mixed state with different probabilities p_i of being in a given state $|\Psi_i\rangle$. For example, a two level atom in the excited state has a probability to remain in the excited state, or it can transit to the ground state by spontaneous emission of a photon. This interaction can be described by the density operator ρ, given by [13]

$$\rho = \sum_i p_i \, |\Psi_i\rangle\langle\Psi_i| \tag{2.34}$$

Considering a free atom (in a pure state), the density operator can be written as

$$\rho = |\Psi\rangle\langle\Psi| \tag{2.35}$$

or as an $n \times n$ matrix in the energy representation, where n is the number of wavefunctions that span the Hilbert space. In terms of a complete orthonormal set of basis $\{\psi_i\}$, the wavefunction can be written as

$$|\Psi\rangle = \sum_i^n c_i \, |\psi_i\rangle \tag{2.36}$$

Hence the density matrix elements in this representation are given by:

$$\rho_{ij} = \langle\psi_i|\rho|\psi_j\rangle = \langle\psi_i|\Psi\rangle\langle\Psi|\,\psi_j\rangle = c_i c_j^* \tag{2.37}$$

Some properties of the density operator include;

- The Density operator is an Hermitian operator so that $\rho_{ij} = \rho_{ji}^*$
- The density operator is usually normalized: Tr $(\rho) = 1$

The time evolution of the density operator is given by the Liouville-Neumann equation [13].

$$i\hbar \frac{d}{dt}\rho = [H, \rho] = H\rho - \rho H, \tag{2.38}$$

For a two-level atom with only one ground state and one excited state, ρ can be written as

$$\rho = \begin{pmatrix} \rho_{11} & \rho_{21} \\ \rho_{12} & \rho_{22} \end{pmatrix} = \begin{pmatrix} c_1 {c_1}^* & c_2 {c_1}^* \\ c_1 {c_2}^* & c_2 {c_2}^* \end{pmatrix} \tag{2.39}$$

ρ_{11} and ρ_{22} represent the populations of the states $|1\rangle$ and $|2\rangle$ respectively, while the off diagonal elements ρ_{12} and ρ_{21} defines the optical coherences (phase relationship) between the states as a result of interaction with the laser field. For a normalized population,

$$\rho_{11} + \rho_{22} = 1 \tag{2.40}$$

2.3.2 Derivation of the General Expression for the Interaction Hamiltonian

An atom in a laser field is coupled on the one hand with the laser field and on the other hand to all other modes of the radiation field, which initially do not contain photons and which form the quantum vacuum field [14]. Considering only the laser–atom coupling, the total Hamiltonian of the interaction can be written as:

$$H = H_A + H_F + H_{AL} \tag{2.41}$$

where, H_A is the free atomic Hamiltonian, H_F, the free field Hamiltonian, and H_{AL} is the laser-atom interaction Hamiltonian.

In deriving the expressions describing the interaction between and atom and the laser field, the following assumptions are made:

- Only electric dipole interactions are considered, since magnetic dipole interactions (which are the next most likely interaction process) are ~10^5 times less likely and the magnetic dipole moment is by a factor of $\approx {}^{1}/_{137}$ smaller than the electric dipole moment [15]. This is referred to as the *electric dipole approximation.*
- The effects of radiation trapping and collisional induced transitions are neglected.
- The laser intensities are low enough to neglect non-linear effects.
- The rotating wave approximation is adopted, which consist of neglecting the anti-resonant terms in the interaction Hamiltonian [14]
- The states are normally ordered to allow for vacuum effects [6].
- The initial upper state is set to zero and the lower state is uniformly populated.
- The laser radiation is tuned to be near resonance with the allowed transition.

2.3.2.1 The Free Field Hamiltonian

Under the above approximations, the free field Hamiltonian is given by

$$H_F = \hbar \sum_{\lambda} \omega_\lambda a_\lambda^\dagger a_\lambda \tag{2.42}$$

The electromagnetic field has been expanded on the complete set of plane wave modes with wavenumber $\boldsymbol{k}$, frequency $\boldsymbol{c}|\boldsymbol{k}|$ and polarization $\boldsymbol{\epsilon}$, (specified by the mode λ) where $a_\lambda^\dagger$ and a_λ are the creation and annihilation operators of a photon in the mode λ. The operators obeys the commutation relations [16]

$$[a_\lambda, a_{\lambda'}^\dagger] = a_\lambda a_{\lambda'}^\dagger - a_{\lambda'}^\dagger a_\lambda = \delta_{\lambda\lambda'}$$

$$a_\lambda^\dagger a_{\lambda'}^\dagger + a_{\lambda'}^\dagger a_\lambda^\dagger = 0$$

$$a_\lambda a_{\lambda'} - a_{\lambda'} a_\lambda = 0 \tag{2.43}$$

2.3.2.2 The Free Atomic Hamiltonian

For a two-level atom with one excited state $|e\rangle$, and one ground state $|g\rangle$, the state are separated by an energy interval

$$E_e - E_g = \hbar\omega_{eg} \tag{2.44}$$

ω_{eg} is the atomic transition frequency, E_e and E_g are the excited and ground state energies of the atom respectively.

The atomic operator σ_{eg} is of the form

$$\sigma_{eg} = |g\rangle\langle e| \tag{2.45}$$

where $|g\rangle$ and $|e\rangle$ are the states of the atomic system [8]. The expectation value of the atomic operator is related to the density operator by

$$\rho_{ge} = \rho^*{}_{eg} = \langle g|\rho|e\rangle = \langle g|\psi\rangle\langle\psi|e\rangle = (\langle\psi|g\rangle\langle e|\psi\rangle)^* = \langle\sigma_{eg}\rangle = c_g c_e^* \tag{2.46}$$

The free atom Hamiltonian is given by

$$H_A = \sum_n E_n \sigma_{nn} = \sum_n \hbar\omega_n |\mathrm{n}\rangle\langle\mathrm{n}| \tag{2.47}$$

where $|n\rangle$ is the eigenstate of the system with corresponding energy E_n, as in equation 2.44.

2.3.2.3 The Laser-Atom Interaction Hamiltonian

The Hamiltonian H_{AL} represents the coupling between the atomic dipole moment $\boldsymbol{d}$ and the electric field component of the laser field $\boldsymbol{E}$, and is given by

$$H_{AL} = \boldsymbol{d} \cdot \boldsymbol{E} \tag{2.48}$$

The dipole matrix element $\boldsymbol{d}$ of the atomic transition is given by;

$$\boldsymbol{d} = \sum_{g} |g\rangle\langle g|\, \boldsymbol{d} \sum_{e} |e\rangle\langle e| = \sum_{ge} \langle g|\boldsymbol{d}|e\rangle\, |g\rangle\langle e| = \sum_{ge} d_{ge}\, |g\rangle\langle e| = \sum_{ge} d_{ge}\, \sigma_{ge} \tag{2.49}$$

where use has been made of the closure relations

$$\sum_{g} |g\rangle\langle g| = 1 \tag{2.50}$$

and as before, $d_{ge} = \langle g|\boldsymbol{d}|e\rangle$ is the dipole matrix elements between the states $|g\rangle$ and $|e\rangle$

Considering only the non-zero elements of $\boldsymbol{d}$, (for transition between the ground and excited states) gives

$$|d| = \sum_{eg} (d_{eg}\, \sigma_{eg} + d_{ge}\sigma_{ge}) \tag{2.51}$$

The electromagnetic field operator of the radiation $\boldsymbol{E}$, is given (in the Schrödinger picture) by [17]

$$\boldsymbol{E} = i \sum_{\lambda} \sqrt{\frac{\hbar\omega_{\lambda}}{2\epsilon_0 V}}\, \boldsymbol{\varepsilon}_{\lambda} \left(a_{\lambda} exp^{(i\boldsymbol{k}\cdot\boldsymbol{r})} - a_{\lambda}^{\dagger} exp^{(-i\boldsymbol{k}\cdot\boldsymbol{r})}\right) \tag{2.52}$$

$\boldsymbol{\varepsilon}_{\lambda}$ is the unit polarization vector of the laser mode, $\boldsymbol{k}$ is the wave vector and V is the interaction volume supporting the field. The position of the centre of mass of the atom with respect to the point where the electric field is evaluated is denoted by $\boldsymbol{r}$

Combining equations 2.51 and 2.52, the interaction Hamiltonian becomes

$$H_{AL} = \sum_{e}\sum_{g} (d_{eg}\, \sigma_{eg} + d_{ge}\sigma_{ge}) \cdot i \sum_{\lambda} \sqrt{\frac{\hbar\omega_{\lambda}}{2\epsilon_0 V}}\, \boldsymbol{\varepsilon}_{\lambda} \left(a_{\lambda} exp^{(i\boldsymbol{k}\cdot\boldsymbol{r})} - a_{\lambda}^{\dagger} exp^{(-i\boldsymbol{k}\cdot\boldsymbol{r})}\right) \tag{2.53}$$

This expression can be written as

$$H_{AL} = \hbar \sum_{e}\sum_{g}\sum_{\lambda} \left(G_{eg}^{\lambda}\sigma_{eg} + G_{ge}^{\lambda}\sigma_{ge}\right)\left(a_{\lambda} exp^{(i\boldsymbol{k}\cdot\boldsymbol{r})} - a_{\lambda}^{\dagger} exp^{(-i\boldsymbol{k}\cdot\boldsymbol{r})}\right) \tag{2.54}$$

where G_{eg}^{λ} is the coupling coefficient between the field mode and the ground and excited states given by

$$G_{eg}^{\lambda} = -i \sum_{\lambda} \sqrt{\frac{\omega_{\lambda}}{2\hbar\epsilon_0 V}}\, \boldsymbol{\varepsilon}_{\lambda} \cdot d_{ge} \tag{2.55}$$

Multiplying out equation 2.54, four kinds of interaction processes can be seen:

1. $\sigma_{ge} a_{\lambda}$: - a ground state electron excited to the upper state with the annihilation of a photon (absorption).
2. $\sigma_{eg} a_{\lambda}$: - an electron in the excited state is shifted to the ground state and a photon is annihilated.
3. $\sigma_{ge} a_{\lambda}^{\dagger}$: - an electron is excited from the ground state to the upper state and a photon is created.
4. $\sigma_{eg} a_{\lambda}^{\dagger}$: - an electron in the excited state is shifted to the ground state and a photon is created.

Processes 2 and 3, which are non-energy- conserving, are omitted because they contribute only to the rapidly oscillating processes [17].

Consider only atoms moving in the direction of the laser propagation chosen to be z-direction, so that $\boldsymbol{k} \cdot \boldsymbol{r} = kz = \frac{\boldsymbol{2\pi}}{\boldsymbol{\lambda}} z$. The atom laser interaction Hamiltonian is then given as

$$H_{AL} = \hbar \sum_{e} \sum_{g} \sum_{\lambda} \left(G_{ge}^{\lambda} \sigma_{ge} a_{\lambda} + G_{eg}^{\lambda *} a_{\lambda}^{\dagger} \sigma_{eg} \right) exp^{(ikz)} \tag{2.56}$$

Although the field and atomic operator commute at this stage, normal ordering has been introduced. That means keeping the field creation operators to the left of the atomic operators and the field annihilation operators to the right of the atomic operator. Further in the derivation this commutation becomes invalid due to additional approximations that are made, and at this time the normal ordering becomes relevant so as to simplify the calculations.

2.3.3 The General Equations of Motion

In the Heisenberg representation, the equation of motion of an operator $\boldsymbol{A}$ is given by

$$\frac{d\boldsymbol{A}}{dt} = -\frac{i}{\hbar}[\boldsymbol{A}, H] \tag{2.57}$$

where H is the total Hamiltonian of the system. Starting from this representation, the time evolution of the field and atomic operators can be derived.

2.3.3.1 Equation of Motion of the Field Operator

From equation 2.57, the equation of motion for the field operator a_{λ} is given by

$$\dot{a}_{\lambda} = -\frac{i}{\hbar}[a_{\lambda}, H_F + H_{AL}] \tag{2.58}$$

where H_A has been omitted since it commutes with a_{λ}. Hence

$$\dot{a}_{\lambda} = -\frac{i}{\hbar}([a_{\lambda}, H_F] + [a_{\lambda}, H_{AL}]) \tag{2.59}$$

Substituting equations 2.42 and 2.56 into 2.59 yields (upon simplification) that

$$\dot{a}_{\lambda} = -i\omega_{\lambda} a_{\lambda} - ie^{-ikz} \sum_{e} \sum_{g} G_{eg}^{\lambda\ *} \sigma_{ge} \tag{2.60}$$

Solving this first order differential equation gives [14]

$$a_{\lambda}(t) = a_{\lambda}(0)e^{-i\omega_{\lambda} t} - ie^{-ikz} \sum_{e} \sum_{g} G_{eg}^{\lambda\ *} \int_{0}^{t} \sigma_{ge}\,(t')e^{-i\omega_{\lambda}(t-t')}dt' \tag{2.61}$$

Similarly, the Hermitian conjugate equation for $a_{\lambda}^{\dagger}$ is given by

$$a_{\lambda}^{\dagger}(t) = a_{\lambda}^{\dagger}(0)e^{i\omega_{\lambda} t} + ie^{ikz} \sum_{e} \sum_{g} G_{eg}^{\lambda} \int_{0}^{t} \sigma_{eg}\,(t')e^{i\omega_{\lambda}(t-t')}dt' \tag{2.62}$$

From equations 2.61 and 2.62, the field operator has two parts. The first term depends on the initial condition and a time dependent oscillatory part. The second term, which depends on the atomic operator, describes the radiative coupling of the field to the atomic transition.

2.3.3.2 Equation of Motion of the Atomic Operator

The equation of motion of the atomic operator is given by

$$\dot{\sigma}_{eg} = -\frac{i}{\hbar}\left[\sigma_{eg}, H\right] = -\frac{i}{\hbar}\left[\sigma_{eg}, H_A + H_{AL}\right] \tag{2.63}$$

where the field has been omitted since it commutes with the atomic operator. Since the only allowed transitions are between the upper and lower states, $G^{\lambda}_{ee'} = G^{\lambda}_{gg'} = 0$, where $G^{\lambda}_{ee'}$ designates transition from $e \to e$ and $G^{\lambda}_{gg'}$ designates transition from $g \to g$. Using the orthogonality relation [18]

$$\sigma_{kl}\sigma_{mn} = \sigma_{kn}\delta_{lm} \tag{2.64}$$

where the Kronecker delta function is given by;

$$\langle m|n\rangle = \delta_{mn} \tag{2.65}$$

Such that;

$$\delta_{mn} = \begin{cases} 0, & m \neq n \\ 1, & m = n \end{cases}$$

The equation of motion then becomes

$$\dot{\sigma}_{eg} = i\omega_{eg}\sigma_{eg} - i\sum_{\lambda}\sum_{e'} G^{\lambda^*}_{e'g}\, a^{\dagger}_{\lambda} exp^{(-i\boldsymbol{kz})}\sigma_{ee'} + i\sum_{\lambda}\sum_{g'} G^{\lambda^*}_{eg'}\, a^{\dagger}_{\lambda} exp^{(-i\boldsymbol{kz})}\sigma_{g'g} \tag{2.66}$$

where ω_{eg} is the atomic transition frequency given by equation 2.44. Substituting for $a^{\dagger}_{\lambda}$ into equation 2.66 then gives

$$\begin{aligned}
\dot{\sigma}_{eg} &= i\omega_{eg}\sigma_{eg} \\
&- i\sum_{\lambda}\sum_{e'} G^{\lambda^*}_{e'g}\, a^{\dagger}_{\lambda}(0) e^{(i\omega_{\lambda} t - kz)}\sigma_{ee'} \\
&+ i\sum_{\lambda}\sum_{g'} G^{\lambda^*}_{eg'}\, a^{\dagger}_{\lambda}(0) e^{(i\omega_{\lambda} t - kz)}\sigma_{g'g} \\
&+ i\sum_{\lambda}\sum_{e'} G^{\lambda^*}_{e'g}\left(\sum_{e''}\sum_{g'} G^{\lambda}_{e''g'}\int_0^t \sigma_{e''g'}(t') e^{i\omega_{\lambda}(t-t')} dt'\right)\sigma_{ee'} \\
&- i\sum_{\lambda}\sum_{g'} G^{\lambda^*}_{eg'}\left(\sum_{e'}\sum_{g'} G^{\lambda}_{e'g''}\int_0^t \sigma_{e'g''}(t') e^{i\omega_{\lambda}(t-t')} dt'\right)\sigma_{g'g}
\end{aligned} \tag{2.67}$$

In the integrals in equation 2.67, the exponential term oscillates at optical frequencies resulting in destructive interference. In the derivation of the equations of motion of the atomic operator detailed in [12], the atomic operator is assumed to evolve as though they are not coupled to the field within a time interval $t \approx t'$ and is put outside the integral. This is known as the harmonic approximation.

The integral in equation 2.67, is then written as [12]

$$\sum_{\lambda} \int_0^t \sigma_{e'g''}(t') e^{i\omega_\lambda (t-t')} dt' = \sum_{\lambda} \sigma_{e'g''}(t) \int_0^t e^{i\omega_\lambda (t-t')} dt' \tag{2.68}$$

This approximation is valid for time intervals much shorter than the timescale for radiative interactions, such as Rabi oscillation and spontaneous emission.

For a freely evolving atomic operator (independent of the interaction),

$$\begin{aligned} \dot{\sigma_{eg}} &= -\frac{i}{\hbar}[\sigma_{eg}, H_A] \\ &= -i(\omega_g - \omega_e)\sigma_{eg} \Rightarrow \int_{t'}^{t} \frac{d\sigma_{eg}}{\sigma_{eg}} = -i(\omega_g - \omega_e) \int_{t'}^{t} dt \\ \therefore \sigma_{eg}(t') &= \sigma_{eg}(t) e^{i(\omega_g - \omega_e)(t-t')} \end{aligned} \tag{2.69}$$

Substituting for $\sigma_{eg}(t')$ in equation 2.67, and using the orthogonality relation gives

$$\begin{aligned} &\dot{\sigma_{eg}} \\ &= i\omega_{eg}\sigma_{eg} - i \sum_{\lambda} \sum_{e'} G^{\lambda^*}_{e'g} a^{\dagger}_{\lambda}(0) e^{(i\omega_\lambda t - kz)} \sigma_{ee'} \\ &+ i \sum_{\lambda} \sum_{g'} G^{\lambda^*}_{eg'} a^{\dagger}_{\lambda}(0) e^{(i\omega_\lambda t - kz)} \sigma_{g'g} \\ &- i \sum_{\lambda} \sum_{e'} \sum_{g'} G^{\lambda^*}_{eg'} G^{\lambda}_{e'g'} \int_0^t e^{i(\omega_\lambda + \omega_{g'} - \omega_{e'})(t-t')} dt' \, \sigma_{e'g} \end{aligned} \tag{2.70}$$

Evaluating the integral as $t \to \infty$ and for laser frequency near resonance,

$$\int_0^t e^{i\omega_\lambda + \omega_e - \omega_g (t-t')} dt'$$

$$= e^{i(\omega_\lambda+\omega_g-\omega_e)t}\int_0^t e^{-i(\omega_\lambda+\omega_g-\omega_e)t'}dt' \xrightarrow{t\to\infty} \pi\delta(\omega_\lambda+\omega_g-\omega_e) \qquad (2.71)$$

Where $\delta(\omega_\lambda+\omega_g-\omega_e)$ is a Dirac delta function [10].

Under the above approximations the time derivative of the atomic operator is given by

$$\begin{aligned}\dot{\sigma}_{eg} &= i\omega_{eg}\sigma_{eg}\\ &-i\sum_\lambda\sum_{e'} G^{\lambda^*}_{e'g}\, a^\dagger_\lambda(0)e^{i(\omega_\lambda t-kz)}\sigma_{ee'}\\ &+i\sum_\lambda\sum_{g'} G^{\lambda^*}_{eg'}\, a^\dagger_\lambda(0)e^{i(\omega_\lambda t-kz)}\sigma_{g'g}\\ &-\sum_\lambda\sum_{g'}\sum_{e'} G^{\lambda^*}_{eg'}G^{\lambda}_{e'g'}\,\pi\delta\left(\omega_\lambda+\omega_{g'}-\omega_{e'}\right)\sigma_{e'g}\end{aligned} \qquad (2.72)$$

Similarly, starting with the Heisenberg equation, the general equation for the ground and excited states matrix element for the atomic operator are given by [18]:

$$\begin{aligned}\dot{\sigma}_{gg'} &= i\omega_{gg'}\sigma_{gg'}\\ &+i\sum_\lambda\sum_{e} G^{\lambda}_{eg}\,\sigma_{eg'}\, a_\lambda(0)e^{-i(\omega_\lambda t-kz)}\\ &-i\sum_\lambda\sum_{e} G^{\lambda^*}_{eg'}\, a^\dagger_\lambda(0)e^{i(\omega_\lambda t-kz)}\sigma_{eg}\\ &+\sum_\lambda\sum_{e}\sum_{e'} G^{\lambda^*}_{eg'}G^{\lambda}_{e'g}\,\pi\delta\left(\omega_\lambda+\omega_g-\omega_{e'}\right)\sigma_{e'e}\\ &+\sum_\lambda\sum_{e}\sum_{e'} G^{\lambda}_{eg}G^{\lambda^*}_{e'g'}\,\pi\delta\left(\omega_\lambda+\omega_{g'}-\omega_{e'}\right)\sigma_{ee'}\end{aligned} \qquad (2.73)$$

$$\dot{\sigma}_{ee'} = i\omega_{ee'}\sigma_{ee'}$$

$$-i\sum_{\lambda}\sum_{g} G^{\lambda}_{e'g}\,\sigma_{eg}\,a_{\lambda}(0)e^{-i(\omega_{\lambda}t-kz)}$$

$$+i\sum_{\lambda}\sum_{g} G^{\lambda^*}_{e'g}\,a^{\dagger}_{\lambda}(0)e^{i(\omega_{\lambda}t-kz)}\sigma_{ge'}$$

$$-\sum_{\lambda}\sum_{g}\sum_{e''} G^{\lambda^*}_{e''g}G^{\lambda}_{e'g}\,\pi\delta\left(\omega_{\lambda}+\omega_{g}-\omega_{e''}\right)\sigma_{ee''}$$

$$-\sum_{\lambda}\sum_{g}\sum_{e''} G^{\lambda}_{e''g}G^{\lambda^*}_{eg}\,\pi\delta\left(\omega_{\lambda}+\omega_{g}-\omega_{e''}\right)\sigma_{e''e'} \qquad (2.74)$$

In equations 2.72 - 2.74, the first term represents the free evolution of the atomic operator, the second and third terms are related to stimulated emission and absorption, and the last terms (the triple sum) relate to atomic relaxation due to the interaction with the field that leads to spontaneous emission.

In order to obtain the expectation values, the rotating wave approximation is applied to equations 2.72 – 2.74, and the rapidly oscillating terms (oscillations at optical frequencies) removed. This transforms the atomic operators σ_{ij} into slowly varying operators χ_{ij} [9]:

$$\chi_{ee'}=\sigma_{ee'}, \qquad \chi_{gg'},=\sigma_{gg'}, \qquad \chi_{eg}=\sigma_{eg}e^{-i(\omega_L t-k_L z)} \qquad (2.75)$$

And so the time derivatives

$$\dot{\sigma}_{ee'} = \quad \dot{\chi}_{ee'}$$

$$\dot{\sigma}_{gg'} = \quad \dot{\chi}_{gg'}$$

$$\frac{d\sigma_{eg}}{dt} = \frac{d\chi_{eg}}{dt}e^{i(\omega_L t-k_L z)} + i\omega_L\sigma_{eg}e^{i(\omega_L t-k_L z)} + ik_L v\sigma_{eg}e^{i(\omega_L t-k_L z)}$$

$$= \quad \dot{\chi}_{eg}e^{i(\omega_L t-k_L z)} + \chi_{eg}i(\omega_L-k_L v_z)e^{i(\omega_L t-k_L z)} \qquad (2.76)$$

Substituting these equations into equations 2.72-2.74, the equations of motion then becomes

$$\langle\ \dot{\chi}_{eg}\rangle\ = i(\omega_{eg}-(\omega_L+k_L v_z))\langle\chi_{eg}\rangle$$

$$-i\sum_{\lambda}\sum_{e'} G^{\lambda^*}_{e'g}\,a^{\dagger}_{\lambda}(0)e^{i[(\omega_{\lambda}-\omega_L)t-(k_{\lambda}-k_L)z]}\langle\chi_{ee'}\rangle$$

$$+i\sum_{\lambda}\sum_{g'} G_{eg'}^{\lambda^*}\, a_{\lambda}^{\dagger}(0)e^{i[(\omega_\lambda-\omega_L)t-(k_\lambda-k_L)z]}\langle\chi_{gg'}\rangle$$

$$-\sum_{\lambda}\sum_{g'}\sum_{e'} G_{eg'}^{\lambda^*}G_{e'g'}^{\lambda}\,\pi\delta\big(\omega_\lambda+\omega_{g'}-\omega_{e'}\big)\langle\chi_{ee'}\rangle \qquad (2.77)$$

$$\langle\dot{\chi}_{gg'}\rangle = i\omega_{gg'}\langle\chi_{gg'}\rangle$$

$$+i\sum_{\lambda}\sum_{e} G_{eg}^{\lambda}\, a_{\lambda}(0)e^{-i[(\omega_\lambda-\omega_L)t-(k_\lambda-k_L)z]}\langle\chi_{eg'}\rangle$$

$$-i\sum_{\lambda}\sum_{e} G_{eg'}^{\lambda^*}\, a_{\lambda}^{\dagger}(0)e^{-i[(\omega_L-\omega_\lambda)t-(k_L-k_\lambda)z]}\langle\chi_{ge}\rangle$$

$$+\sum_{\lambda}\sum_{e}\sum_{e'} G_{eg'}^{\lambda^*}G_{e'g}^{\lambda}\,\pi\delta\big(\omega_\lambda-(\omega_{e'}-\omega_g)\big)\langle\chi_{e'e}\rangle$$

$$+\sum_{\lambda}\sum_{e}\sum_{e'} G_{eg}^{\lambda}G_{e'g'}^{\lambda^*}\,\pi\delta\big(\omega_\lambda-(\omega_{e'}-\omega_{g'})\big)\langle\chi_{ee'}\rangle \qquad (2.78)$$

$$\langle\dot{\chi}_{ee'}\rangle = i\omega_{ee'}\langle\chi_{ee'}\rangle$$

$$-i\sum_{\lambda}\sum_{g} G_{e'g}^{\lambda}\, a_{\lambda}(0)e^{-i[(\omega_\lambda-\omega_L)t-(k_\lambda-k_L)z]}\langle\chi_{eg}\rangle$$

$$+i\sum_{\lambda}\sum_{g} G_{e'g}^{\lambda^*}\, a_{\lambda}^{\dagger}(0)e^{i(\omega_\lambda-\omega_L)t-(k_\lambda-k_L)z}\langle\chi_{ge'}\rangle$$

$$-\sum_{\lambda}\sum_{g}\sum_{e''} G_{e''g}^{\lambda^*}G_{e'g}^{\lambda}\,\pi\delta\big(\omega_\lambda-(\omega_{e''}-\omega_g)\big)\langle\chi_{ee''}\rangle$$

$$-\sum_{\lambda}\sum_{g}\sum_{e''} G_{e''g}^{\lambda}G_{eg}^{\lambda^*}\,\pi\delta\big(\omega_\lambda-(\omega_{e''}-\omega_g)\big)\langle\chi_{e''e'}\rangle \qquad (2.79)$$

where $\langle\chi_{ij}\rangle$ are expectation values. The expectation values of the slowly varying operators are related to the density matrix elements by

$$\langle\chi_{ij}\rangle = \langle\psi|i\rangle\langle j|\psi\rangle = (\langle i|\psi\rangle\langle\psi|j\rangle)^* = \rho_{ij}^* = \rho_{ji} \qquad (2.80)$$

Using equation 2.80, equations 2.77 - 2.79 can hence be written in terms of the density matrix elements for the system.

2.3.3.3 The Two-Level System Approximation

Starting with the above steps, the equations of motion for the system can be derived. For potassium, this will result in 576 coupled differential equations that must be solved simultaneously. Details of the derivation of the atom-laser coupling and the optical coherences are available in [12, 18]. For computational ease, the system is here approximated by a simpler two-level model as was detailed earlier in this chapter. In laser cooling and trapping, this two level model gives sufficient insight into how the atoms behave in a laser radiation field. As noted, using circular polarized light the system will rapidly evolve into a two level system, and hence in this work the interaction of potassium atoms with the cooling laser is approximated to that of a two level interaction.

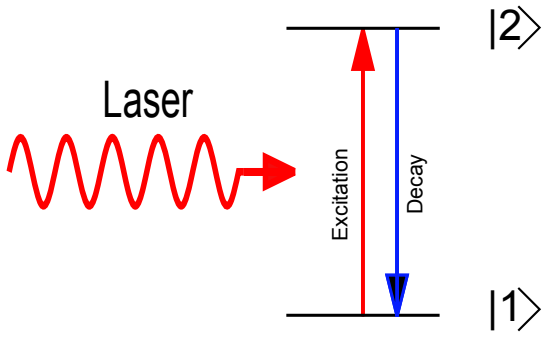

Fig 2.5: The action of a resonant laser on a two level system. This atom is excited from state $|1\rangle$ *to state* $|2\rangle$ *and can only decay back to state* $|1\rangle$.

The final set of equations summarized for a two level system with only one ground and excited state can be derived from equations 2.77 to 2.80, and these are given by:

$$\dot{\rho_{ee}} = -i\omega_{ee}\rho_{ee} - \frac{1}{\tau}\rho_{ee} + i\Omega_1(\rho_{eg} - \rho_{ge}) \tag{2.81}$$

$$\dot{\rho_{gg}} = -i\omega_{gg}\rho_{gg} + \frac{1}{\tau}\rho_{ee} + i\Omega_1(\rho_{ge} - \rho_{eg}) \tag{2.82}$$

$$\dot{\rho_{eg}} = -i(\omega_{eg} - \omega_l)\rho_{eg} - \frac{1}{2\tau}\rho_{eg} + i\Omega_1(\rho_{ee} - \rho_{gg}) \tag{2.83}$$

$$\dot{\rho_{ge}} = +i(\omega_{eg} - \omega_l)\rho_{ge} - \frac{1}{2\tau}\rho_{eg} - i\Omega_1(\rho_{ee} - \rho_{gg}) \tag{2.84}$$

where $\Omega_1$is known as the half Rabi frequency for the laser mode, ω_{eg} is the transition frequency between the states $|e\rangle\ and\ |g\rangle$, and ω_l is the laser frequency. Noting that $\omega_{jj} = \omega_j - \omega_j = 0$, the first term in equations 2.81 and 2.82 vanishes, and the above equations reduce to:

$$\dot{\rho_{ee}} = -\frac{1}{\tau}\rho_{ee} + i\Omega_1(\rho_{eg} - \rho_{ge}) \tag{2.85}$$

$$\dot{\rho_{gg}} = +\frac{1}{\tau}\rho_{ee} - i\Omega_1(\rho_{eg} - \rho_{ge}) \tag{2.86}$$

$$\dot{\rho_{eg}} = -i\delta\rho_{eg} - \frac{1}{2\tau}\rho_{eg} + i\Omega_1(\rho_{ee} - \rho_{gg}) \tag{2.87}$$

$$\dot{\rho_{ge}} = +i\delta\rho_{ge} - \frac{1}{2\tau}\rho_{eg} - i\Omega_1(\rho_{ee} - \rho_{gg}) \tag{2.88}$$

Where $\delta = \omega_{eg} - \omega_l$ is the laser detuning from resonance.

For a normalized population,

$$\rho_{ee} + \rho_{gg} = 1 \tag{2.89}$$

Under steady state conditions, $\dot{\rho_{ee}} = \dot{\rho_{gg}} = \dot{\rho_{eg}} = \dot{\rho_{ge}} = 0$, and the steady state equations for the two level system are then given by:

$$\frac{1}{\tau}\rho_{ee} - i\frac{\Omega}{2}(\rho_{eg} - \rho_{ge}) = 0 \tag{2.90}$$

$$-\left(i\delta + \frac{1}{2\tau}\right)\rho_{eg} + i\frac{\Omega}{2}(\rho_{ee} - \rho_{gg}) = 0 \tag{2.91}$$

$$\left(\frac{1}{2\tau} - i\delta\right)\rho_{eg} - i\frac{\Omega}{2}(\rho_{gg} - \rho_{ee}) = 0 \tag{2.92}$$

Where $\Omega = 2\Omega_1$, is the full Rabi frequency. From equation 2.90 the excited state is

$$\rho_{ee} = i\tau\frac{\Omega}{2}(\rho_{eg} - \rho_{ge}) \tag{2.93}$$

From equations 2.91 and 2.92, the optical coherences ρ_{eg} and ρ_{ge} in terms of the ground and excited states populations are given by:

$$\rho_{eg} = \frac{i\Omega}{2\left(\frac{1}{2\tau} + i\delta\right)}\left(\rho_{ee} - \rho_{gg}\right) \tag{2.94}$$

$$\rho_{ge} = \frac{i\Omega}{2\left(\frac{1}{2\tau} - i\delta\right)}\left(\rho_{gg} - \rho_{ee}\right) \tag{2.95}$$

Substituting these equations into equation 2.93 then gives

$$\rho_{ee} = \frac{\Omega^2}{4}(1 - 2\rho_{ee})\left(\frac{1}{\left(\frac{\Gamma^2}{4} + \delta^2\right)}\right) \tag{2.96}$$

Where the spontaneous emission rate $\Gamma = {}^{1}/_{\tau}$. Re-arranging the above equation for ρ_{ee}, gives the excited state population as;

$$\rho_{ee} = \frac{\Omega^2}{4\delta^2 + \Gamma^2 + 2\Omega^2}$$

$$= \frac{\Omega^2}{\Gamma^2}\left(\frac{1}{1 + \frac{2\Omega^2}{\Gamma^2} + \frac{4\delta^2}{\Gamma^2}}\right) \tag{2.97}$$

Similar expression can be obtained for the ground state population ρ_{gg} since

$\rho_{gg} = 1 - \rho_{ee}$.

The on resonance saturation parameter S_0 is defined as:

$$S_0 = \frac{2\Omega^2}{\Gamma^2} = \frac{I}{I_0}, \tag{2.98}$$

and the saturation parameter is given by:

$$S = \frac{S_0}{1 + \frac{2\delta^2}{\Gamma^2}} \tag{2.99}$$

The saturation parameter is related to the laser intensity according to equations 2.24 and 2.27.

The excited state population can therefore be written as:

$$\rho_{ee} = \frac{S_0/2}{1 + S_0 + \left(\frac{2\delta}{\Gamma}\right)^2} = \frac{S}{2(1+S)} \tag{2.100}$$

Hence, when $S \gg 1$, both ρ_{ee} and ρ_{gg} tend toward $\frac{1}{2}$ which implies that the population of the excited state cannot be more than half of the number of atoms in the system, as has been noted previously.

2.4 Atomic Spectral Line and Broadening Mechanisms

The absorption and emission of light does not occur at a single frequency (spectral lines are not infinitely narrow), but occurs over a range of frequencies with a finite width described by the line-width. Different mechanisms affect the observed atomic transition lines. In a system where different broadening processes are likely, the spectral line profile is a complex function made up of all the individual contributions.

2.4.1 Natural line-width

The excited state has a finite lifetime τ, after which it decays into a lower energy state by spontaneous emission. This introduces an uncertainty in the measurement of the transition energy. From the Heisenberg uncertainty principle,

$$\Delta E \Delta \mathrm{t} \cong \hbar \tag{2.101}$$

$$\hbar \Delta\omega \cong \frac{\hbar}{\Delta t} \tag{2.102}$$

$$\Delta\omega = \frac{1}{\tau} \tag{2.103}$$

where $\Delta t = \tau$. The line profile due to the natural line-width is hence given by a Lorentzian function [20]

$$I(\omega) = \frac{\Gamma}{4\pi^2} \frac{1}{\Delta^2 + \left(\Gamma/4\pi\right)^2} \tag{2.104}$$

where $\Delta = \omega - \omega_0$.

For atoms whose line-width is purely due to spontaneous emission, the natural line-width is equal to the rate of spontaneous emission Γ. The $4^2S_{1/2}$ to $4^2S_{3/2}$ transition of potassium

have an excited state lifetime of 26.37 ns [19], which results in a natural line-width of 6.035 MHz.

2.4.2 Doppler (Thermal) Line-width

The thermal motion of absorbing atoms leads to a change in the absorbed frequency due to the Doppler effect. For an atom moving relative to an observer with velocity v, the Doppler shifted frequency ω as measured by the observer is given by

$$\omega = \omega_0 \left(1 + \frac{v}{c}\right) \tag{2.105}$$

where c is the speed light and ω_0 is the centroid frequency of the transition. Thus the Doppler shift in frequency is given by

$$\Delta\omega = \omega - \omega_0 = \omega_0 \left(\frac{v}{c}\right) \tag{2.106}$$

For a Maxwellian distribution of atomic velocity (as occurs in an atomic beam), the velocity distribution is given by

$$P(v)dv = \sqrt{\frac{m}{2\pi k_B T}}\, exp^{-\left(\frac{mv^2}{2k_B T}\right)} dv \tag{2.107}$$

Where m is the mass of the atom and T is the temperature of the atomic gas. From equation 2.106:

$$v = c\left(\frac{\omega - \omega_0}{\omega_0}\right) \tag{2.108}$$

So that

$$dv = \frac{c}{\omega_0} d\omega \tag{2.109}$$

Substituting equations 2.108 and 2.109 into equation 2.107 then gives the distribution function in terms of the Doppler shift.

$$P(\omega)d\omega = \sqrt{\frac{mc}{2\pi k_B T {\omega_0}^2}}\, exp^{-\left(\frac{mc^2\Delta\omega^2}{2k_B T\omega_0{}^2}\right)} d\omega \tag{2.110}$$

This is a Gaussian function with a full width at half maximum (FWHM) given by

$$\Delta\omega_D = \omega_0 \sqrt{\frac{8k_B T}{mc^2} \ln 2} \tag{2.111}$$

$$= \frac{2}{\lambda_0} \sqrt{\frac{2k_B T}{m} \ln 2} \tag{2.112}$$

The line profile due to Doppler broadening is hence given by a Gaussian function

$$\varphi(\omega) = \frac{1}{\Delta\omega_D \sqrt{\pi}} exp - \left(\frac{\Delta\omega^2}{\Delta\omega_D{}^2} \right) \tag{2.113}$$

For radiation emitted by an ensemble of atoms distributed over a range velocities, (as is the case with the atoms emitted by the oven at emission temperature), the Doppler shift determines the broadening of the spectral lines of the transition. This is known as Doppler broadening. For potassium at room temperature, the Doppler width $\Delta\omega_D = 796\, MHz$, and at a typical oven temperature of 473K as used in these experiments, $\Delta\omega_D = 1.01\, GHz$.

2.4.3 Power Broadening

Power broadening occurs when the absorption of a photon followed by stimulated emission does not contribute to the scattering force. At laser intensities larger than the saturation intensity, there is a higher probability for stimulated emission to occur and so the atoms spend less time in the excited state resulting in the broadening of the spectral lines. For a two level atom, the total scattering rate of photons from the laser field is given by [13].

$$\Gamma_p = \Gamma \rho_{ee} \tag{2.114}$$

Using equation 2.100, gives

$$\Gamma_p = \frac{\Gamma \frac{S_0}{2}}{1 + S_0 + \left(\frac{2\delta}{\Gamma} \right)^2} \tag{2.115}$$

The above equation can be rewritten as

$$\Gamma_p = \left(\frac{S_0}{1+S_0}\right)\left(\frac{\Gamma/_2}{1+\left(\frac{2\delta}{\Gamma\sqrt{1+S_0}}\right)^2}\right) \tag{2.116}$$

so that

$$\Gamma_p = \left(\frac{S_0}{1+S_0}\right)\left(\frac{\Gamma/_2}{1+\left(\frac{2\delta}{\Gamma'}\right)^2}\right) \tag{2.117}$$

Where

$$\Gamma' = \Gamma\sqrt{1+S_0} \tag{2.118}$$

is referred to as the power broadening line-width [13].

The power (rate of absorption of energy) spectrum is then given by the normalized Lorentzian function [23]

$$I(\Delta) = \frac{\Gamma'/_{4\pi^2}}{\Delta^2 + (\Gamma'/4\pi)^2} \tag{2.119}$$

The plot of equation 2.119 for different values of S_0 shown in figure 2.6 indicates a reduction in the absorption rate due to enhanced rate of stimulated emission. The broadening effect becomes obvious for $S_0 > 1$.

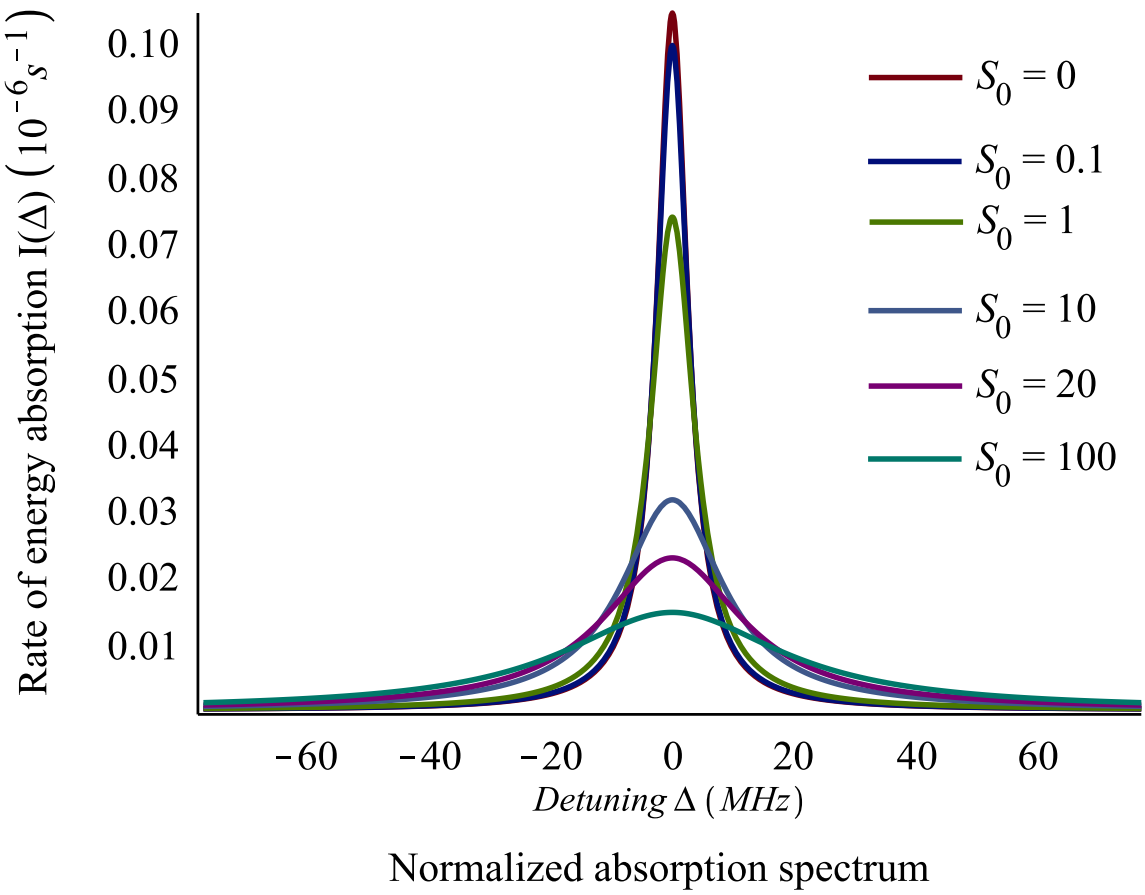

Fig 2.6: Energy absorption spectrum of a two level atom with increasing laser radiation intensity as a function of the detuning Δ showing the power-broadened line-width. As the intensity increases, the spectral width broadens (as evident for $S_0 > 1$) because the atom spends less time in the excited state and so enhances the probability of stimulated emission.

2.4.4 Collisional (Pressure) Broadening

Collisional broadening of atomic spectral lines originates from the distortion of electron energy level due to frequent collision between atoms. The magnitude of collisional or pressure broadening effects depends on the frequency at which collision occur, the temperature (thermal velocity of the atoms) and the density of the atomic cloud. Since atoms are coupled to each other in the radiation field, a photon emitted by one atom can be absorbed by another atom in the lower energy level, or it may induce the emission of a photon from another atom in the upper energy level. These processes result in a decrease in the excited state lifetime, and thus broaden the spectrum as shown in figure 2.6. As in the case of natural linewidth and power broadening, the collisional broadening line profile is also Lorentzian given by

$$I(\Delta) = \frac{\Gamma'/4\pi^2}{\Delta^2 + (\Gamma'/4\pi)^2} \tag{2.120}$$

In this case $\Gamma' = \Gamma + 2\omega_{col}$ where Γ is the natural line-width of the excited state and ω_{col} the frequency of collision, is given by [24]

$$\omega_{col} = v_{th} N \sigma_{col} \tag{2.121}$$

where v_{th} is the thermal velocity of the atom, N is the density of the atomic cloud and σ_{col} is the collision cross section.

2.5 Conclusion

This chapter has highlighted some of the theory behind the experiments described in this thesis. An overview of the relevant properties of atomic potassium, including the hyperfine states and the effect of a magnetic field is given. The QED treatment of the dynamics of the interaction of an atom in a laser field, with particular attention to the time evolution of the different states for a two level atom has been briefly discussed. Finally the processes that lead to the broadening of the atomic spectral lines as observed in some aspects of the experiments are described. In the next chapter, a detailed description of the mechanism of slowing and trapping potassium atom in the experiment is given.

References

[1] Das, Dipankar, and Vasant Natarajan. *High-precision measurement of hyperfine structure in the D lines of alkali atoms.* Journal of Physics B: Atomic, Molecular and Optical Physics 41.3 (2008): 035001.

[2] V.S Letokhov. *Laser control of Atoms and molecules*. Oxford University press New York 2011.

[3] Kerckhoff, J. A., et al. *A frequency stabilization method for diode lasers utilizing low-field Faraday polarimetry*. Review of scientific instruments 76.9 (2005): 093108.

[4] A. Einstein: *On the quantum theory of radiation*; Phys.ZS 18 (1917)

[5] Dunning, Frank B., and Randall G. Hulet. *Atomic, Molecular, and Optical Physics: Atoms and Molecules: Volume 29B:* Academic Press, 1996.

[6] L Allen and J.H Eberly, *Optical resonance and two-level Atoms*. John Wiley & sons New York 1975

[7] McClelland, J. J., and M. H. Kelley. *Detailed look at aspects of optical pumping in sodium*. Physical Review A 31.6 (1985): 3704.

[8] Ackerhalt, J. R., and J. H. Eberly. *Quantum electrodynamics and radiation reaction: nonrelativistic atomic frequency shifts and lifetimes*. Physical Review D 10.10 (1974): 3350.

[9] Whitley, Richard Morgan, and C. R. Stroud Jr. *Double optical resonance*. Physical Review A 14.4 (1976): 1498.

[10] Farrell, P. M., W. R. MacGillivray, and M. C. Standage. *Quantum- electrodynamic calculation of hyperfine-state populations in atomic sodium.* Physical Review A 37.11 (1988): 4240.

[11] M Shurgalin, *Electron scattering from optically prepared 3P state of Sodium*; PhD thesis, Griffith University 1998.

[12] N Strohmaier, *Magneto optical trapping of ^{39}K from a Zeeman-slowed atomic beam;* MPhil thesis, University of Manchester 2005.

[13] Metcalf, Harold J, and Peter Van der Straten. *Laser cooling and trapping*. Springer, 1999.

[14] C. Cohen-Tannuodji. *Lecture notes on atomic motion in laser Light.* Collège de France and Département de Physique de l'Ecole Normale Supérieure, Paris France

[15] Svelto, Orazio. *Principles of lasers*. Springer, 2010

[16] A J Murray, *A stepwise electron-photon coincidence experiments on the 6^1P_1 state of Mercury*; Ph.D Thesis, Griffith University, 1989.

[17] Loudon, Rodney. *The quantum theory of light*. Oxford university press, 2000.

[18] M Harvey, *Low energy electron scattering from a pulsed AC-MOT*; PhD thesis, University of Manchester. 2009

[19] Tiecke, T. G. *Properties of potassium*. University of Amsterdam, The Netherlands, Thesis (2010).

[20] Cowan, Robert D. *The theory of atomic structure and spectra*. Vol. 3. Univ of California Press, 1981.

[21] Arimondo, E., M. Inguscio, and P. Violino. *Experimental determinations of the hyperfine structure in the alkali atoms.* Reviews of Modern Physics 49.1 (1977): 31.

[22] Murray, A. J., MacGillivray, W., & Hussey, M. (2008). *Theoretical modeling of resonant laser excitation of atoms in a magnetic field*. Physical Review A, 77(1), 013409.

[23] Citron, M. L., H. R. Gray, C. W. Gabel, and C. R. Stroud Jr. *Experimental study of power broadening in a two-level atom.* Physical Review A 16, no. 4 (1977): 1507.

[24] Williams, D., Wenstrand, D. C., Brockman, R. J., & Curnutte, B. (1971). *Collisional broadening of infra-red absorption lines*. *Molecular Physics*, *20*(5), 769-785.

CHAPTER THREE

Mechanisms of Slowing and Trapping Neutral Atoms

3.0 Introduction

The manipulation of atoms using light forces is based on the momentum transfer, which occurs when an atom absorbs a photon from a laser beam. The absorption of a photon changes the momentum of the atom by $\hbar\boldsymbol{k}$ where $\boldsymbol{k}$ is the wave vector of the incident photon, and the atom recoils. The associated recoil velocity and energy are given by:

$$v_r = \frac{\hbar k}{m} \tag{3.1}$$

$$E_r = \frac{\hbar^2 |k|^2}{2m} \tag{3.2}$$

where m is the mass of the atom.

The absorption of a photon is usually accompanied by the emission of another photon by the atom through spontaneous emission. Since this is a random event (the direction of the emitted photon and the time of its emission are both random), the emission will follow a symmetric pattern with respect to the incident photon [1]. When this process is averaged over many cycles, the momentum contribution due to spontaneous emission averages to zero, and the atom gains a net momentum in the direction of the of the incident photon. In this way, the velocity of the atom is reduced by a factor equal to the recoil velocity after each absorption and emission cycle. Due to the small momentum of a photon, many photon absorption and emission cycle would be required to significantly slow an atomic beam. As an example, to slow a beam of potassium atoms moving with speed of about 600m/s to ~50 m/s, would require about 4.5 x 10^4 interactions with the laser field. Figure

3.1 illustrates how the absorption, followed by the emission process for multiple scattering events leads to the manipulation of atoms.

This chapter focuses on the different mechanisms that are employed in slowing and trapping neutral atoms. These will include the description of the nature of light forces and the technique of Zeeman slowing. It will discuss the concept of optical molasses, which is the basis of the magneto optical trap (MOT), and the prevailing forces in the MOT that confines the atoms in the trap.

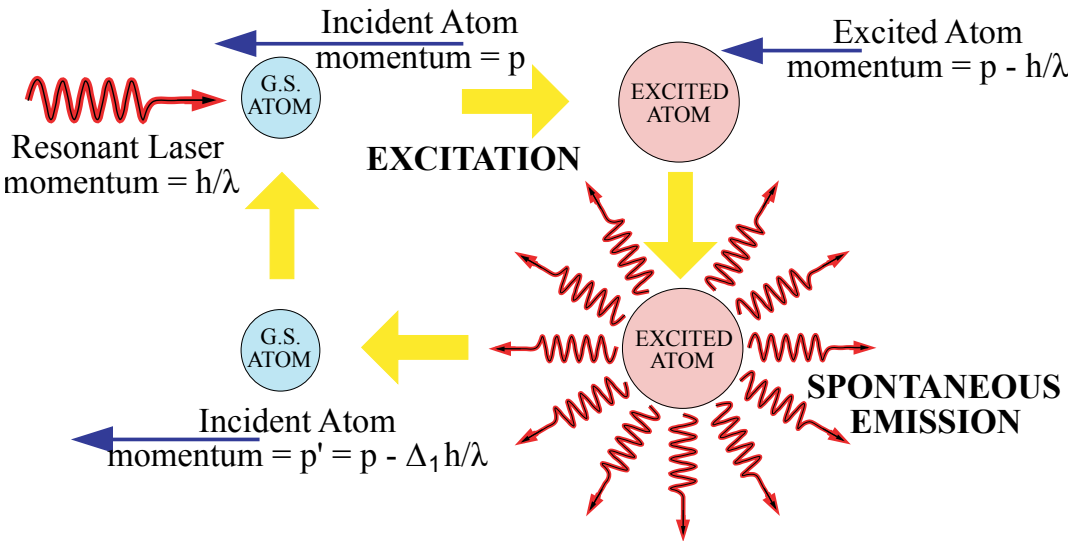

Fig3.1: Laser-atom interaction cycle that leads to laser cooling. The absorption of a resonant laser gives the atom a net momentum kick in the direction of the laser beam. The recoil momentum due to spontaneous emission averages to zero.

3.1 The Nature of Light Forces

As stated above, the light forces originate as a result of momentum transfer between the photon and the atom due to the absorption and emission of photon through the processes of spontaneous and stimulated emission. The forces resulting from these processes differ in nature.

3.1.1 Scattering Force

The light force resulting from spontaneous emission is referred to as the scattering force, radiation pressure, or the light pressure force, and is given by [1]

$$F_{scat} = \Gamma_p \hbar k \tag{3.3}$$

where Γ_p is the total scattering rate defined by equation 2.114. The scattering rate depends on the amount of power available for the excitation, and the rate of spontaneous emission Γ. In terms of the laser detuning δ and the on-resonance saturation parameter S_0 defined by equation 2.98, the scattering force is given by:

$$\Gamma_{scat} = \frac{\Gamma}{2} \frac{S_0}{1 + S_0 + \left(2\delta/\Gamma\right)^2} \tag{3.4}$$

At high intensity where $S_0 \gg 1$, the scattering rate asymptote to a value of $\frac{\Gamma}{2}$, so that the maximum scattering force due to spontaneous emission is

$$F_{max} = \frac{\Gamma \hbar \mathrm{k}}{2} \tag{3.5}$$

This equation implies that increasing the intensity does not increase the force without limit, but rather increases the rate of stimulated emission (which does not contribute to the scattering force).

Considering an atom in motion, the effective detuning will be a function of the atom's velocity. The velocity dependent scattering force (due to a counter-propagating laser beam) acting on an atom moving with a velocity v is hence given by

$$F_{scat} = \frac{\Gamma \hbar \mathrm{k}}{2} \frac{S_0}{1 + S_0 + (2(\delta - k \cdot v)/\Gamma)^2} \tag{3.6}$$

This is a dissipative force, since it is not possible to reverse the process of spontaneous emission, and so the action of this force is not reversible. This force plotted against longitudinal velocity of the atoms has a Lorentzian profile as shown in figure 3.2. Atoms with velocities close to the resonant velocity $v_r = |\delta|/k$, experience a strong force which opposes their motion, and as a result, the scattering force plays an important role in slowing and cooling of atoms because of this dissipative nature.

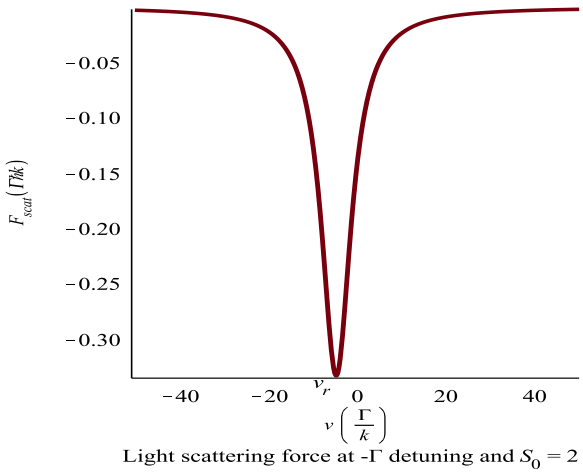

Fig 3.2: Light scattering force plotted for ^{39}K as function of longitudinal velocity of the atoms. Atoms with resonant velocity $v_r \approx -5\frac{\Gamma}{k}$, experience a strong opposing force. The effect of the scattering force is less for atoms with velocities far from v_r.

3.2 Deceleration of Neutral Atoms

To produce a beam of slow atoms whose velocity distribution is within the capture velocity of a MOT, different techniques are adopted.

3.2.1 Slowing With a Counter-Propagating Laser Beam

The scattering force according to equation 3.6, is a velocity selective force, and hence can be used to decelerate a beam of thermal atoms. A red detuned counter-propagating laser beam as illustrated in fig 3.3, creates a light pressure force which effectively slows the atoms whose velocities are close to the resonant velocity $v_r = |\delta|/k$. The deceleration of atoms with velocities far from the resonant velocity is less efficient, see figure 3.2. Therefore, this technique of slowing with a counter-propagating laser field of fixed detuning is most suitable for slowing and cooling atoms moving with velocities close to the resonant velocity. With a laser beam resonant with the D_2 line of ^{39}K, and red-detuned by ~ 3 Γ (typical detuning for the experiments described in this thesis), only atoms with velocity less than $\approx 14\ m/s$ can be slowed using this technique, and also, owing to the small linewidth of the laser, after a small change in velocity, the atoms will have shifted out of resonance with the laser due to the Doppler effect. At the typical oven operating temperature (see section 4.2), less than 0.001% of atoms are likely to be within this velocity, and so a different technique is required to slow sufficient number of atoms down to the capture velocity of the MOT. The two most common techniques for keeping the atoms in resonance with the slowing laser beam are; sweeping (rapidly changing) the laser frequency along the changing Doppler shift of the decelerating atoms (known as frequency chirping) [2-4], and the use of an inhomogeneous magnetic field to vary the atomic resonance frequency to keep the decelerating atoms in resonance with the fixed laser frequency (Zeeman slowing) [1,5,6]. The latter method is used in this experiment, and so is described in more detail.

3.2.2 Zeeman slowing

To effectively slow atoms of varying velocity using the scattering force requires a means of keeping the atoms in resonance with the slowing laser. One way of doing this uses a spatially varying magnetic field to shift the energy levels of the atoms and bring the atoms back into resonance with the slowing laser beam in a technique known as Zeeman slowing. In a Zeeman slower, a circular polarized and counter-propagating laser beam at

fixed detuning is used in combination with a magnetic field that varies along the length of the Zeeman slower to slow the atoms. In the Zeeman slower used in this experiment, the magnetic field is generated by a set of current carrying solenoids wound around the flight tube as described in section 4.3. The magnetic field shifts the energy level of the atoms to keep them in resonance with the cooling laser frequency as the atoms slows down. The schematic diagram of the Zeeman slower technique is shown in fig 3.3

To ensure that atoms of various velocities are slowed, the magnetic field profile is adjusted so that the fastest atoms are in resonance with the laser bean along the entire length of the Zeeman slower as they slow from their initial velocity down to the chosen exit velocity. The slower atoms within the beam profile will travel unaffected down the Zeeman slower until they reach a point along the Zeeman slower where they too become resonant with the slowing laser beam, and thereby enter the slowing cycle.

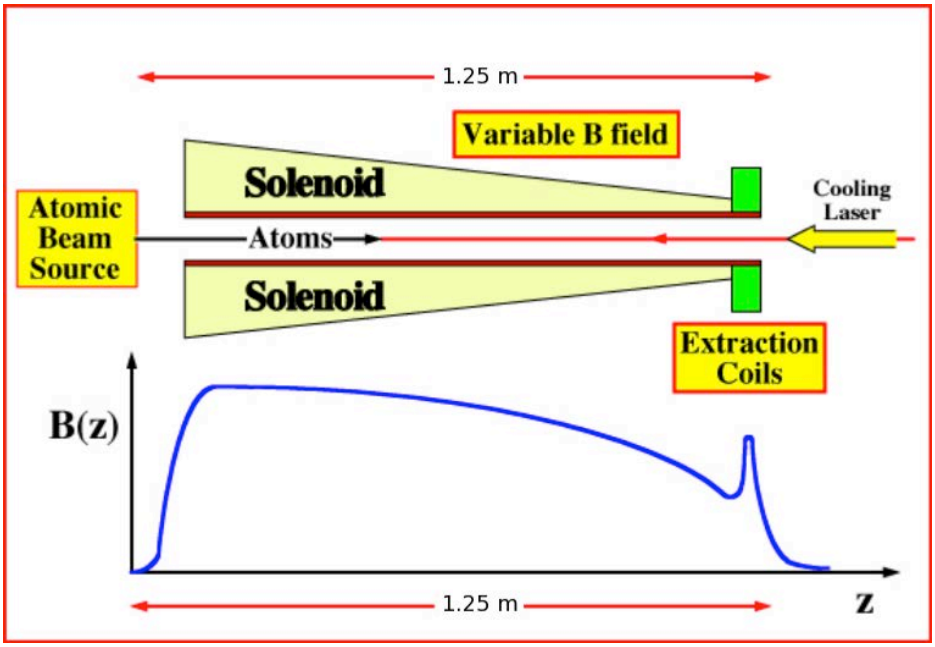

Fig 3.3: Schematic diagram of the Zeeman slower technique. Layers of varying length on the solenoid produce the tapered magnetic field. The extraction coils creates an abrupt magnetic field that decouples the atoms from the cooling laser once they reach the exit of the Zeeman slower.

The magnetic field is tuned in such a way that atoms are optically pumped in to the F=2 ground state of ^{39}K, and so the probability that a slowing atom will be pumped out of the cycling process to a state not resonant with the cooling laser is reduced.

The Zeeman slower not only slows the atoms, but also compresses their velocity spread (cools the atoms) due to the dispersive nature of the scattering force. With this technique,

atoms from the source can be slowed into a beam of atoms with velocities below the capture velocity of the MOT.

From equation 3.5, the maximum acceleration of the atom is given by

$$a_{max} = \frac{F_{max}}{m}$$

$$= \frac{\Gamma \hbar k}{2m}$$

$$= \frac{h}{2m\lambda\tau} \tag{3.7}$$

where m is the mass of a potassium atom, λ is the laser wavelength and $\tau = {}^{1}/_{\Gamma}$.

3.2.2.1 Maximum Initial Velocity

The maximum scattering force is limited by the rate of spontaneous emission Γ, and so increasing the laser intensity beyond saturation has no effect on the scattering force but rather increases the rate of stimulated emission [1]. The maximum deceleration depends on the maximum scattering force, and therefore, there is a minimum stopping distance and a corresponding maximum initial velocity for a given atomic species. The Zeeman slower used in the experiments described here is 1.25 m long; this puts a restriction on the maximum initial velocity of the atoms that can be stopped. Starting from Newton's equations of motion, an expression for the maximum initial velocity of potassium atoms that can be stopped using this Zeeman slower is derived.

$$v_{final}^2 = v_{imax}^2 + 2a_{max}z_0 \tag{3.8}$$

where v_{final} is the final velocity, v_{imax} is the maximum initial velocity of the atoms, and z_0 is the length of the Zeeman slower. If the atoms are stopped, $v_{final} = 0$, and so

$$v_{imax}^2 = 2a_{max}z_0 \tag{3.9}$$

for $a_{max} < 0$ (deceleration).

Using equation 3.7, the maximum initial velocity of atoms that can be brought to rest in the Zeeman slower of this length z_0 is

$$v_{imax} = \sqrt{\frac{hz_0}{m\lambda\tau}} \tag{3.10}$$

With a laser beam resonant with the $4^2S_{1/2}$ to $4^2P_{3/2}$ transition of ^{39}K (766.7012 nm), and the mass of ^{39}K given in kilogram, $(39.1 \times 1.672614 \times 10^{-27} kg)$, and for $\tau = 26.37\ ns$, the maximum initial velocity which can be slowed using this Zeeman slower is $\approx 800\ m/s$.

3.2.2.3 The Magnetic Field Profile of the Zeeman Slower

The magnetic field is profiled to match between the Doppler shift and the Zeeman shifting of decelerating atoms to keep them in resonance with the cooling laser along the length of the Zeeman slower. The shift in frequency due to the influence of the magnetic is given by equation 2.7 as

$$\Delta\omega = \frac{\mu_B B}{\hbar}(g_2 m_{F'} - g_1 m_F) \tag{3.11}$$

For ^{39}K in a two level cycle (F=2→F′=3), the F=2, m_F=2 ground state has the Landé g-factor $g_1 = 1/2$, and the excited state F′=3, m_F=3 has Landé g-factor $g_2 = 2/3$, so the above equation becomes

$$\Delta f = \frac{\mu_B B}{h} \tag{3.12}$$

Equating the Zeeman shift in frequency to the Doppler shift of equation 2.106, gives

$$\frac{\mu_B B}{h} = \frac{v}{\lambda}$$

$$\Rightarrow v = \frac{\mu_B B \lambda}{h} \tag{3.13}$$

The velocity of the decelerating atom at a position z along the Zeeman slower is given by

$$v^2 = v_{imax}^2 - 2az$$

$$\Rightarrow v = \sqrt{v_{imax}^2 - 2az}$$

$$= v_{imax}\sqrt{1 - \frac{2az}{v_{imax}^2}} \tag{3.14}$$

Substituting for v_{imax}^2 using equation 3.9, then gives

$$v = v_{imax}\sqrt{1 - \frac{z}{z_0}} \tag{3.15}$$

Equating equations 3.15 and 3.13, and re-written in term of B and B_{max} which correspond to v and v_{imax}

$$\frac{\mu_B B\lambda}{h} = \frac{\mu_B B_{max}\lambda}{h}\sqrt{1 - \frac{z}{z_0}} \tag{3.16}$$

This equation upon simplification, gives an expression for the magnetic field profile B required to slow down the atoms as

$$B = B_{max}\sqrt{1 - \frac{z}{z_0}} \tag{3.17}$$

where B_{max} is the magnetic field required to bring the atoms moving with maximum slowable initial velocity v_{imax} into resonance with the cooling laser beam as they enter the Zeeman slower, and is given by:

$$B_{max} = \frac{hv_{imax}}{\mu_B\lambda} \tag{3.18}$$

In the Zeeman slower used in the present experiment, the cooling laser beam is blue detuned by δ_z~115 MHz to avoid the interaction of the cooling laser with stationary atoms in the MOT. To compensate for this blue detuning, a uniform bias field B_{bias} is added to the Zeeman slower magnetic field. The modified Zeeman slower magnetic field then is given by:

$$B = B_{bias} + B_{max}\sqrt{1 - \frac{z}{z_0}} \tag{3.19}$$

The value of B_{bias} is obtained using equation 3.13 as

$$B_{bias} = \frac{h\delta_z}{\mu_B} \tag{3.20}$$

Where δ_z is the detuning due to the AOM.

The exit velocity v_{ext} of the atoms is determined by setting a minimum magnetic field B_{min} at the end of the main solenoid Zeeman slower (before the extraction coils), where the atoms can interact with the laser field in the cooling process. This is given by [7]:

$$v_{ext} = \lambda\left(\frac{\mu_B B_{min}}{h} - \delta_z\right) \tag{3.21}$$

3.2.2.4 The Extraction Coils

The Zeeman slower as described above can produce a continuous beam of very slow atoms within the tuning magnetic field, but decoupling these atoms from the magnetic field and the cooling laser is difficult at the low velocity required for the trapping experiments [7]. To effectively extract these atoms at the appropriate capture velocity for the MOT, a set of four coils known as the extraction coils are installed at the exit of the Zeeman slower. These create an abrupt change in the magnetic field needed to decouple the atoms from the slowing process and this prevents them from stopping and returning back into the Zeeman slower. During normal operation, two of these coils are energized in the reverse direction by negative going currents [7]. The combined magnetic field profile produced by the main Zeeman slower solenoids and the extraction coils during normal operation is shown in figure 3.4. A detailed description of the design and operation of the Zeeman slower used in this experiment is given section 4.3.

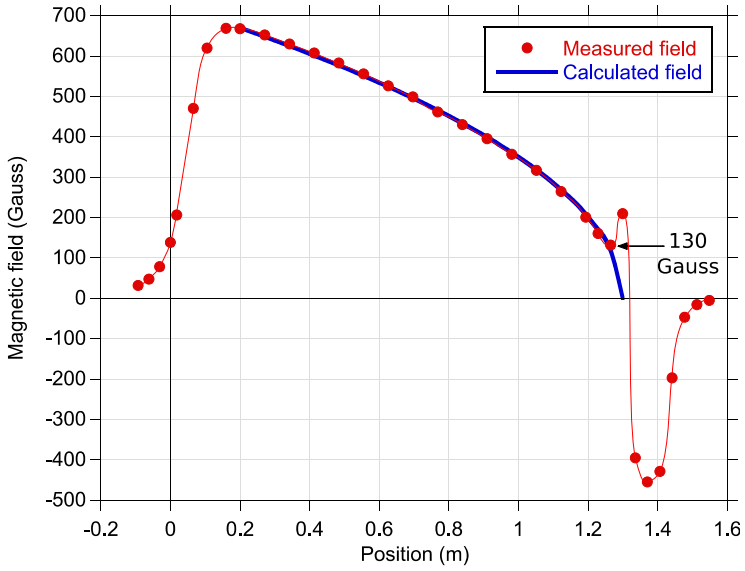

Fig. 3.4: *The magnetic field profile of the Zeeman slower during normal operation. The negative **B**-field gives a very strong detuning to the atoms at the exit, and so decouples them from the cooling process [8]. This allows the atoms to exit the slower effectively at the required velocity.*

3.3 Optical Molasses.

The previous discussions have been restricted to the interaction of an atom with a single laser beam. An atom moving with velocity v and subject to two laser beams in opposite direction will experience a force $F(v)$ due to interaction with both laser beams. This

combination of laser beams with appropriate detuning and polarization can provide a damping force that is proportional to the velocity of the atom, and is referred to as an 'optical molasses' [1]. This term is used because the resulting viscous force not only slows the atoms to very low velocities, but also compresses the velocity spread of the atoms.

3.3.1 One Dimensional Optical Molasses

In a one-dimensional optical molasses, a beam of atoms interacts with two counter-propagating laser beams as illustrated in figure 3.5. If the counter-propagating beams are slightly red detuned with respect to the atomic resonance, the atoms experience a velocity dependent force. A moving atom will 'see' the light from the opposing beam blue shifted in the atomic reference frame, while the beam moving in the same direction as the atom will be further red shifted. This causes the atom to scatter more photons from the right hand beam which is opposing its motion (see figure 3.6) and the atom then slows down.

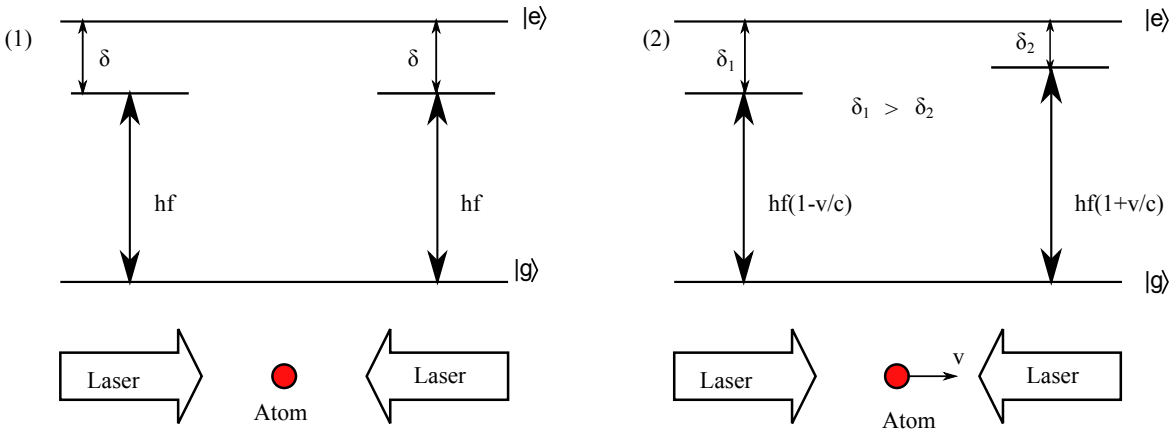

Fig 3.5: Optical molasses in one dimension formed by two counter-propagating laser beam red detuned by same amount δ. (1) The atom is at rest and so has equal probability of scattering photon from each of the laser beam. In (2) the atom is moving with a velocity v towards the right, it is therefore less detuned with respect to the counter-propagating laser beam. It then scatters more photon from the opposing laser beam and is slowed down.

Under this condition, the force opposing the motion will always be larger than the force in the direction of the atom. This technique is referred to as Doppler cooling. The net force on the atom due to its interaction with the two counter-propagating laser beams is given by:

$$F(v) = F_+ + F_-$$

$$= \frac{\Gamma\hbar k}{2} \frac{S_0}{1 + S_0 + (2(\delta - kv)/\Gamma)^2} - \frac{\Gamma\hbar k}{2} \frac{S_0}{1 + S_0 + (2(\delta + kv)/\Gamma)^2} \quad (3.22)$$

where δ is the laser detuning from resonance for a stationary atom, and kv represent the Doppler shift due to the motion of the atom. This approximation is only valid for light intensities low enough that stimulated emission can be neglected. For small v, the force can be expanded in power series of small derivations about $v = 0$ to give

$$F(v) \cong F(0) + v\frac{d}{dv}F(0) + \cdots \tag{3.23}$$

where

$$F(0) = 0 \tag{3.24}$$

and

$$\frac{d}{dv}F(v)$$

$$= \frac{\Gamma\hbar\mathrm{k}S_0}{2}\left(\frac{8(\delta - kv)k}{\Gamma^2(1 + S_0 + (2(\delta - kv)/\Gamma)^2)^2}\right)$$

$$+ \frac{\Gamma\hbar\mathrm{k}S_0}{2}\left(\frac{8(\delta + kv)k}{\Gamma^2(1 + S_0 + (2(\delta + kv)/\Gamma)^2)^2}\right)$$

$$\therefore v\frac{d}{dv}F(0) = \left(\frac{8\delta\hbar k^2 S_0}{\Gamma(1 + S_0 + (2\delta/\Gamma)^2)^2}\right)v \tag{3.25}$$

Neglecting higher powers in the equation on the assumption that $v^4 \ll \left(\frac{\Gamma}{k}\right)^4$, gives the net force on the atom as

$$F(v) \cong \left(\frac{8\delta\hbar k^2 S_0}{\Gamma(1 + S_0 + (2\delta/\Gamma)^2)^2}\right)v = -\alpha v \tag{3.26}$$

where α, the damping factor of the optical molasses is given by

$$\alpha = -\frac{8\delta\hbar k^2 S_0}{\Gamma(1 + S_0 + (2\delta/\Gamma)^2)^2} \tag{3.27}$$

Figure 3.6 illustrates the damping nature of the optical molasses force indicated by the linear regime of the net force. The force has maximum and minimum values when the atom is at resonant with the right and left beams respectively, which is satisfied when $\delta = \pm kv$. Atoms that are moving with initial velocities close to the resonant velocity experiences a damping force varying linearly with velocity. They are therefore captured by the molasses and slowed down to the Doppler cooling limit. The net force loses it linearity at higher detunings.

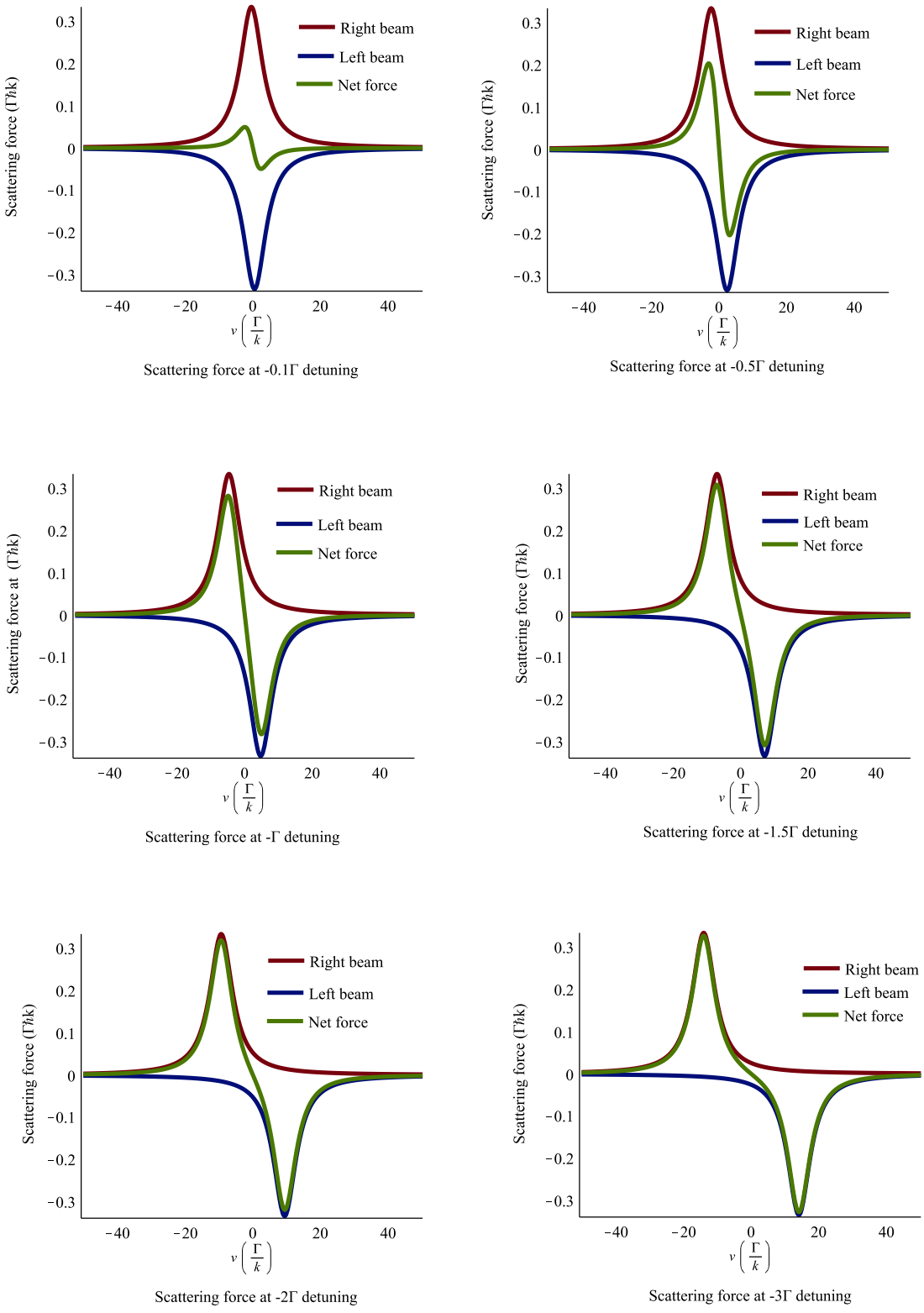

Fig 3.6: 1-D optical molasses force against velocity for various values of detuning. The force acts as a pure damping force over a range of velocity. The linearity of the net force depends on the detuning.

3.3.2 Three Dimensional Optical Molasses

To produce a three-dimensional (3-D) optical molasses, three pair of circular polarized counter propagating laser beams of appropriate detuning are used instead on one, as shown in figure 3.7. In this configuration, the atoms interact with the six counter-propagating laser beams and are slowed wherever they are within the interaction region formed by the overlap of the beams. The beam size defines the interaction region, and for a fixed intensity and detuning, increasing the beam size will lead to an increase in the total number of atoms that can be cooled. In general, this will not lead to increase in the density of the atomic cloud cooled by the molasses, since the density of the atomic cloud in the MOT is limited by collision between trapped atoms.

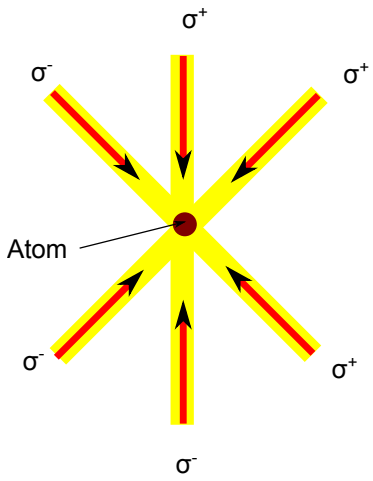

Fig.3.7: 3-D optical molasses formed by three pairs of circular polarized counter-propagating laser beams.

3.3.3 Doppler Cooling Limit

The minimum temperature of the atoms achievable by Doppler cooling, is limited by the loss in momentum of the atom to the resonant photons emitted through each spontaneous emission. This momentum loss has a heating effect on the entire cooling process; the lowest temperature of the atomic cloud is achieved when the Doppler cooling rate and the rate of heating due to random momentum kicks have reached an equilibrium condition.

For each spontaneously emitted photon, the atom will experience a minimum recoil momentum p_r, equal to the momentum of the emitted photon, $\hbar k_r$, where k_r is the photon wavenumber. The corresponding recoil energy is given by

$$E_r = \frac{\hbar^2 k_r^2}{2m}$$

$$\Rightarrow \hbar\omega_r = \frac{\hbar^2 k_r^2}{2m} \tag{3.28}$$

Where ω_r is the recoil frequency of the atom, which is related to its momentum p_r.

For each photon absorbed, the average energy of the atom is given by

$$E_{abs} = \hbar\omega_{abs} \tag{3.29}$$

where $\omega_{abs} = \omega_a + \omega_r$ is the average frequency of each absorption of photon, and ω_a is the atom's transition frequency.

And for each photon emitted, the average energy of the atom is

$$E_{emis} = \hbar\omega_{emis} \tag{3.30}$$

where $\omega_{emis} = \omega_a - \omega_r$ is the average frequency of each emission cycle.

The total energy of the atom after each absorption and emission cycle is

$$E_{abs} - E_{emis} = 2\hbar\omega_r \tag{3.31}$$

This is the average kinetic energy (because of the recoil movement) of the atom after each scattering cycle and equals the average energy lost by the light field. This loss occurs at twice the rate of scattering of photons Γ_p [1], because two beams are involved, and so the rate of heating Γ_h becomes

$$\Gamma_h = 4\hbar\omega_r\Gamma_p \tag{3.32}$$

Under equilibrium condition, the rate of heating will be equal to the rate of cooling $\Gamma_{cool} = F(v) \cdot v$ where $F(v)$ is defined in equation 3.26; and

$\Gamma_{cool} = 4\hbar\omega_r\Gamma_p$

$$\therefore \quad \frac{8\delta\hbar k^2 S_0}{\Gamma(1 + S_0 + (2\delta/\Gamma)^2)^2} v^2 = \frac{4\hbar^2 k_r^2}{2m} \frac{\Gamma\frac{S_0}{2}}{1 + S_0 + (2\delta/\Gamma)^2}$$

$$\Rightarrow \frac{8\delta}{\Gamma(1 + S_0 + (2\delta/\Gamma)^2)} v^2 = \frac{\hbar}{m}\Gamma \tag{3.33}$$

where use has been made of equations 2.115 and 3.28. Rearranging equation 3.33, gives on simplification an expression for the average velocity of the atoms in the steady state.

$$v^2 = \frac{\hbar\Gamma}{8m}\left(\frac{\Gamma}{\delta} + \frac{\Gamma S_0}{\delta} + \frac{4\delta}{\Gamma}\right) \tag{3.34}$$

And so the average kinetic energy in the steady state is given by

$$E_k = \frac{1}{2}mv^2 = \frac{\hbar\Gamma}{8}\left(\frac{\Gamma}{2\delta} + \frac{\Gamma S_0}{2\delta} + \frac{2\delta}{\Gamma}\right) \tag{3.35}$$

At very low laser intensity ($S_0 \approx 0$), the minimum kinetic energy is then given by

$$E_{min} = \frac{\hbar\Gamma}{8}\left(\frac{\Gamma}{2\delta} + \frac{2\delta}{\Gamma}\right) \tag{3.36}$$

This energy is dependent only on the detuning, and so in the steady state, we can calculate the detuning for minimum energy. Hence

$$\frac{d}{d\delta}\frac{\hbar\Gamma}{8}\left(\frac{\Gamma}{2\delta} + \frac{2\delta}{\Gamma}\right) = 0$$

$$\Rightarrow \frac{\hbar\Gamma}{8}\left(-\frac{\Gamma}{2\delta^2} + \frac{2}{\Gamma}\right) = 0 \tag{3.37}$$

Therefore, the minimum energy is reached when the detuning

$$\delta = \frac{\Gamma}{2} \tag{3.38}$$

Using this equation, the minimum kinetic energy of equation 3.36 becomes

$$E_{min} = \frac{\hbar\Gamma}{4} \tag{3.39}$$

The average kinetic energy of the atom is related to its temperature by

$$E_k = \frac{1}{2}k_B T \tag{3.40}$$

From equations 3.39 and 3.40, an expression for the minimum temperature of the system, the Doppler cooling limit T_D is then given as

$$T_D = \frac{\hbar\Gamma}{2k_B} \tag{3.41}$$

where k_B is the Boltzmann constant.

For potassium approximated to a two-level system containing the $4^2S_{1/2}$ ground and $4^2P_{3/2}$ excited states with $\Gamma = 6.035$ MHz, the Doppler cooling limit is here given by $T_D = 146\ \mu K$.

3.4 Magneto Optical Trap

The atoms cooled by the Doppler cooling technique are not trapped (confined) but can within sufficient time diffuse out of the interaction region defined by the overlap of the six laser beams forming the 3-dimensional optical molasses, by a process known as 'random walk' [1]. Several techniques have been developed [9-14], that are used in conjunction with Doppler cooling to confine the atomic ensemble in space. The magneto optical trap (MOT) technique was used in the trapping experiment described in this thesis.

A MOT is a hybrid trap that uses the combination of the light scattering force and an external magnetic field. This technique takes advantage of the dipole magnetic moments of the atoms to manipulate the energy levels, by the application of an external magnetic field. The first confinement of an atomic ensemble using the MOT technique was demonstrated by Raab et al in 1987 [13], where it was used to trap neutral sodium atoms. Later in 1995 [14], the first MOT of potassium was implemented.

A 3-D MOT consists of a 3-D optical molasses and a quadruple magnetic field generated by a pair of coils in an anti-Helmholtz configuration. When equal but opposite currents flow through the coils, the magnitude of the generated magnetic field is zero at the centre of the coils but increases away from the centre as shown in figure 3.8. When the coils are separated by a distance $\sqrt{3}R$, where R is the radius of the coils, the magnitude of the field is approximately linear along any line passing through the centre of the magnetic field [14].

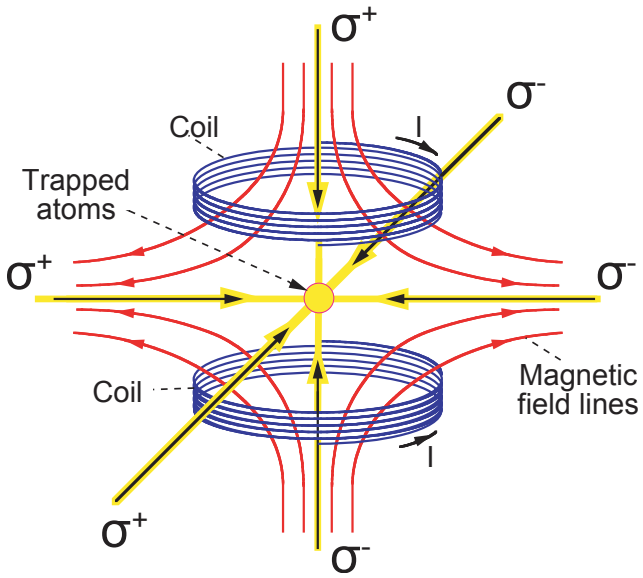

Fig 3.8: 3-D MOT showing the coils in anti-Helmholtz configuration. The optical molasses force is created by 3 pair of counter-propagating and circular polarized laser beams centred on the inhomogeneous magnetic field generated by the current carrying coils.

3.4.1 Basic MOT Operation

Considering an atomic system with a ground state F = 0, with m_F = 0, and an excited state F′ = 1, with three sub-levels $m_{F'}$ = -1, 0, +1 in an external magnetic field, the shift in the excited state energy level due to the Zeeman interaction is given by

$$\Delta E = \mu_B g_e B m_{F'} \tag{3.42}$$

Where μ_B is the Bohr magneton, g_e is the hyperfine Lande-g factor of the excited state, and B is the magnitude of the magnetic field. For a negative B (with respect to the centre of the MOT), the $m_{F'}$ = -1 sub-level will be shifted up in energy, while the $m_{F'}$ = +1 sub-level will be shifted down in energy. To create a MOT, the polarization of the counter-propagating laser beams that form the molasses, are chosen so that the beams interact with the atomic sub-level that is shifted down in energy by the applied magnetic field.

For an atom in a 1-D optical molasses described above, the inhomogeneous magnetic field generated by the MOT coils are shown in figure 3.9.

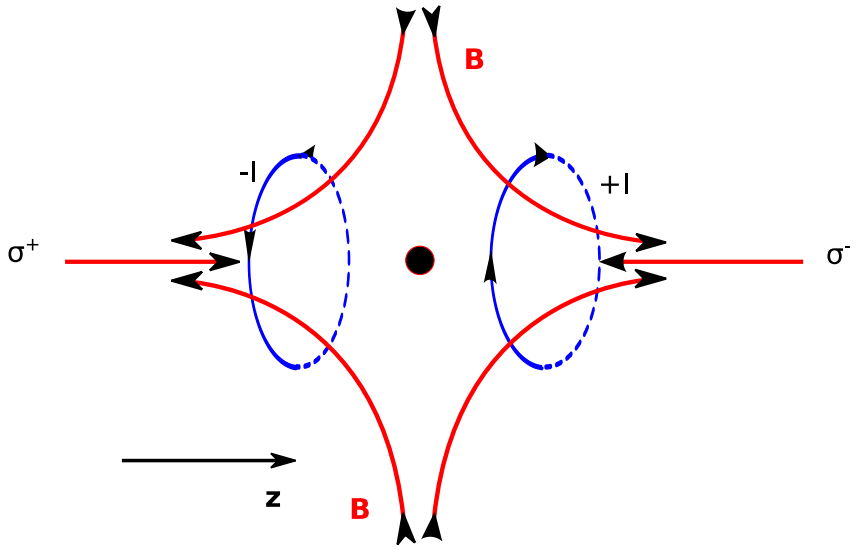

Fig. 3.9: Schematic diagram of a 1-D MOT. The coils carrying equal but opposite currents I, create an inhomogeneous magnetic field which is zero at the centre and which is approximaely linear along the axis defined by the counter-propagating laser beams.

In this case, the field will be linear along the axis z defined by the laser beam, and so

$$B(z) = Az \tag{3.43}$$

where A is the magnetic field gradient. As illustrated in figure 3.10, the magnetic field at the opposite sides of the MOT centre interacts with different classes of atoms, and causes the excited state sub-levels to be Zeeman shifted in energy; on the left side, the $m_{F'}$ = +1

sub-level is shifted down in energy while the $m_{F'}$ = -1 sub-level is shifted up in energy. This bring the atom close to resonance with the counter-propagating σ^+ laser beam, which results in the scattering of more photons from this beam than from the co-propagating σ^- laser beam (see figure 3.10). The $m_{F'}$ = +1 atoms are then pushed back towards the centre of the MOT. On the right side, the $m_{F'}$ = +1 atoms are shifted up in energy, while the $m_{F'}$ = -1 are down in energy, causing them to scatter more photons from the σ^- laser beam, and are also pushed back towards the centre. For atoms at the centre of the MOT where the field is zero, there is no shift in the energy and so all the levels are non-degenerate.

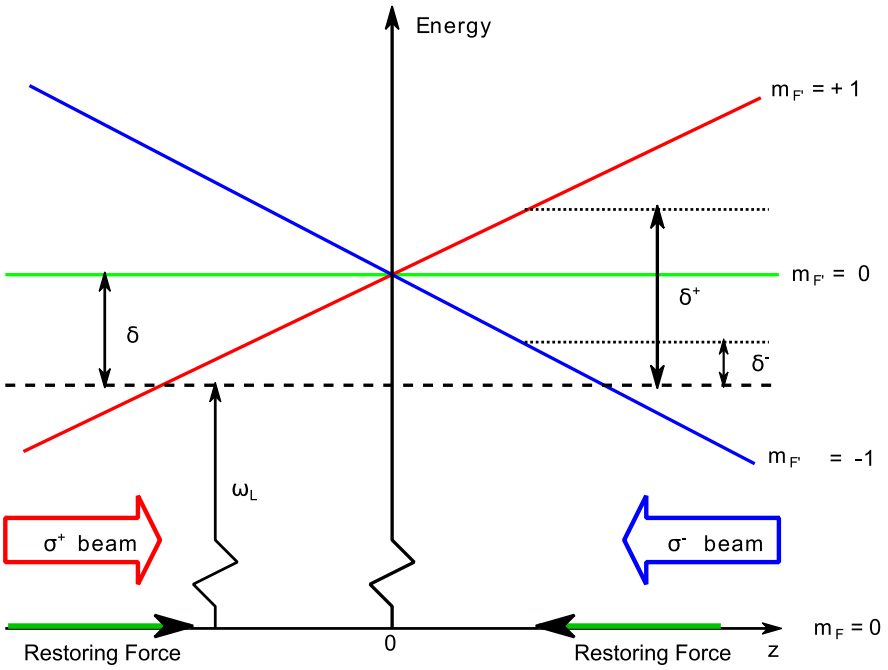

Fig. 3.10: Zeeman shifting of energy sub-levels of an atom in a 1-D MOT. The dashed lines represent the red-detuned trapping laser seen by atoms at rest. On the right, the $m_{F'}$ = -1 sub-level is shifted down in energy by the magnetic field and so interacts strongly with the σ^- laser beam. On the left, the $m_{F'}$ = +1 sub-level is shifted down in energy, and scatters more photons from the σ^+ laser beam. These interactions create a restoring force that pushes the atoms back towards the centre of the MOT.

In effect the magnetic field introduces a spatially dependent restoring force to the scattering force, so that the trap not only cools the atoms but also confines them within the interaction region defined by the counter-propagating laser beams and the quadruple magnetic field. The 1-D MOT can be extended to 3-D by incorporating an appropriate quadruple magnetic field to the 3-D optical molasses described section 3.3.2.

3.4.2 The MOT Magnetic Field

The quadruple magnetic field required to cool and trap neutral atoms in the MOT, was created by two coils carrying opposite current and separated by a distance $s = \sqrt{3}R$ (anti-

Helmholtz configuration), as shown in figure 3.11, where R is the radius of the coils. This creates a field which is zero at the centre point between the coils but which increases in all directions. Along the z-axis, the field gradient is twice as strong as the gradient along both the x and y −axes. At points close to the centre, the field has a constant gradient A, and can be given as [1]

$$\boldsymbol{B} = A\sqrt{x^2 + y^2 + 4z^2} \tag{3.44}$$

In most conventional MOT, the magnetic field is generated by passing currents through the coils. Changes in the magnetic flux in the MOT will induces eddy current in any conducting material in the vicinity of the trap (for instance during switch off); and even when the currents are rapidly switched to zero, the induced eddy currents continue to generate magnetic fields until they are eventually reduced to zero.

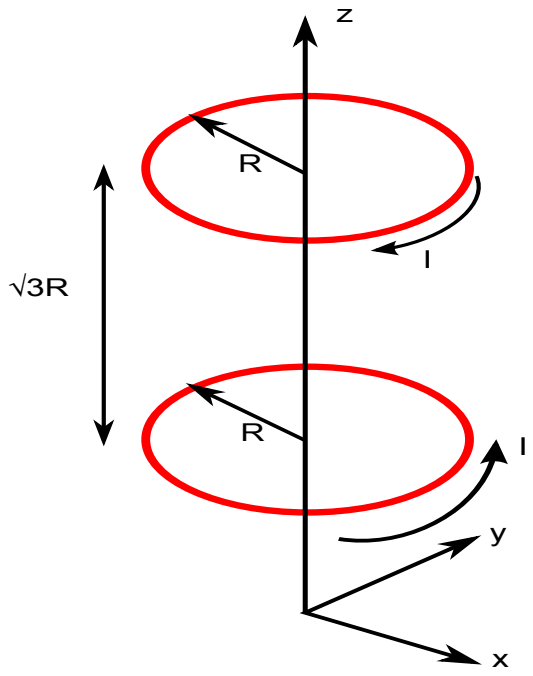

Fig 3.11: Schematics of the Trap coils in anti-Helmholtz configuration.

These magnetic fields due to changes in current become a hindrance for the application of the conventional MOT to collision studies with trapped samples, where the directions of charged particles are of great importance, since these collision studies measure their momenta. In the experiments described in this thesis, ^{39}K was trapped in a new kind of MOT known as the alternating current magneto optical trap – AC-MOT [17]. Details of the AC-MOT and its application are discussed in chapters 5, 6 and 7.

3.4.3 The MOT Forces

Considering a 1-D MOT, the magnetic field from the MOT coils modifies the light scattering force due to Zeeman shifting of the energy levels of the atoms. From equation 3.22, the total scattering force from the 1-D optical molasses is

$$F(v) = F_+ + F_-$$

$$= \frac{\Gamma\hbar\mathrm{k}}{2}\,\frac{S_0}{1+S_0+(2(\delta-kv)/\Gamma)^2} - \frac{\Gamma\hbar\mathrm{k}}{2}\,\frac{S_0}{1+S_0+(2(\delta+kv)/\Gamma)^2} \quad (3.45)$$

The MOT magnetic field introduces a spatial dependence to the effective detuning, and so the force in the MOT can be written as:

$$F_{MOT} = F_+ + F_-$$

$$= \frac{\Gamma\hbar\mathrm{k}}{2}\,\frac{S_0}{1+S_0+(2(\delta-kv+\mu' Az/\hbar)/\Gamma)^2} - \frac{\Gamma\hbar\mathrm{k}}{2}\,\frac{S_0}{1+S_0+(2(\delta+kv-\mu' Az/\hbar)/\Gamma)^2} \quad (3.46)$$

Where $\mu' = \left(g_e m_{F'} - g_g m_F\right)\mu_B$, is the effective magnetic moment of the transition under consideration.

Expanding equation 3.46 in terms of small values of v and z and retaining only the first two terms as in section 3.2.1, the force in the MOT approximates to:

$$F_{MOT} \cong \left(\frac{8\delta\hbar k^2 S_0}{\Gamma(1+S_0+(2\delta/\Gamma)^2)^2}\right)v - \frac{\mu' Az}{\hbar k}\left(\frac{8\delta\hbar k^2 S_0}{\Gamma(1+S_0+(2\delta/\Gamma)^2)^2}\right) \quad (3.47)$$

$$\Leftrightarrow F_{MOT} = -\alpha v - \kappa z \quad (3.48)$$

Where α is defined in equation 3.27 and

$$\kappa = \frac{\mu' A}{\hbar k}\,\alpha \quad (3.49)$$

From equation 3.48, the motion of an atom in the MOT can classically be described as

$$M\frac{d^2z}{dt^2} + \alpha\frac{dz}{dt} + \kappa z = 0$$

$$\Longrightarrow \frac{d^2z}{dt^2} + \frac{\alpha}{M}\frac{dz}{dt} + \frac{\kappa}{M}z = 0$$

$$\therefore \frac{d^2z}{dt^2} + \gamma_{MOT}\frac{dz}{dt} + \omega_{MOT}^2 z = 0 \tag{3.50}$$

where $\gamma_{MOT} = \frac{\alpha}{M}$ and $\omega_{MOT}^2 = \frac{\kappa}{M}$.

This implies that the motion of an atom of mass M in the MOT is equivalent to the motion of a particle of mass M in a damped harmonic oscillator with a damping rate $\gamma_{MOT} = \frac{\alpha}{M}$, the simple harmonic oscillator oscillating at a rate $\omega_{MOT}^2 = \frac{\kappa}{M}$. Since the ratio $\xi = \alpha/2\sqrt{\kappa M}$, (known as the damping ratio) is greater than one, the motion of the atoms in the MOT is over-damped and so decays exponentially towards the centre of the trap with a decay constant α/κ [16], with no oscillation. For a typical potassium MOT with detuning $\delta = -4\Gamma,\ S_0 = 2$ and field gradient $A = 10\ Gcm^{-1}$, the damping rate $\gamma_{MOT} = 54.5\ kHz$, and the oscillation frequency $\omega_{MOT} = 7.6\ kHz$ [8]. It therefore takes approximately $2\ ms$ for the atoms to move to the centre of the trap.

3.5 Trapping of ^{39}K

Although there are 24 sub-energy levels in the $4^2S_{1/2}$ to $4^2P_{3/2}$ transition of ^{39}K, the simple principles based on a two-level atom can still be applied under steady state condition as described in section 2.3.3. The lack of a closed transition in ^{39}K due to the small hyperfine splitting of both the ground and excited state makes effective cooling and trapping more difficult. The overlapping of the Zeeman hyperfine sub-levels (in an external magnetic field) means that some atoms can be excited to other sub-levels besides the F′ = 3 state, which allows the atoms to decay to levels other than the F = 2 ground state as illustrated in figure 2.2. The consequence of this is the reduction in the number of atoms accessible with the trapping laser, which is locked to the F = 2 to F′ = 3 transition. To improve the MOT, two laser frequencies both red detuned by the same amount are required: one resonant with the F = 2 to F′ = 3 transition (the main laser beam), and the other resonant with F = 1 to F′ = 2 transition (the re-pump laser beam). The re-pump laser interacts with the atoms which are originally in the F = 1ground state and those resulting from the decays of atoms from states other than the F′ = 3 excited state, and so brings them back into the trapping transition.

The main and re-pump laser frequencies are separated by $(\sim 441\, MHz)$. This is the difference between the ground state splitting of $\sim 462\, MHz$ and the separation between the F′ = 3 and F′ = 2 $(\sim 21\, MHz)$ excited state hyperfine sub-levels.

3.6 Conclusion

In this chapter, the nature of optical forces and the principle behind the use of laser light to manipulate atoms have been briefly described. It has also discussed the technique of Zeeman slowing, where a magnetic field is used to manipulate the energy levels of atoms in order to bring them into resonance as they slow down. The concept of optical molasses in both 1- and 3-dimensions and their application in Doppler cooling has been discussed. Finally, the operation of a MOT is described. In chapter four, a detailed description of the different component of the experimental apparatus will be presented based upon these principles.

References

[1] Metcalf, Harold J., and Peter Van der Straten. *Laser cooling and trapping*. Springer,1999.

[2] J. Prodan and W. Phillips, *Chirping the light fantastic? — recent NBS atom cooling experiments,* Prog. Quantum Electron. **8**, 231–235 (1984).

[3] W. Ertmer, R. Blatt, J. L. Hall, and M. Zhu, *Laser manipulation of atomic beam velocities: demonstration of stopped atoms and velocity reversal*, Phys. Rev. Lett. **54**, 996–999(1985).

[4] R. Watts and C. Wieman, *Manipulating atomic velocities using diode lasers*, Opt. Lett. **11**, 291–293 (1986)

[5] W. Phillips and H. Metcalf, *Laser deceleration of an atomic beam*, Phys. Rev. Lett. **48**, 596–599 (1982).

[6] J. Prodan, W. Phillips, and H. Metcalf, *Laser production of a very slow monoenergetic atomic beam,* Phys. Rev. Lett. **49**, 1149–1153 (1982).

[7] Barrett, Thomas E., et al. *Slowing atoms with σ-polarized light*. Physical review letters 67.25 (1991): 3483.

[8] M Harvey, *Low energy electron scattering from a pulsed AC-MOT;* PhD thesis, University of Manchester. 2009

[9] Ashkin, Arthur, and James P. Gordon. *Stability of radiation-pressure particle traps: an optical Earnshaw theorem*. Optics letters 8.10 (1983): 511-513.

[10] Chu, Steven, et al. *Three-dimensional viscous confinement and cooling of atoms by resonance radiation pressure*. Physical Review Letters 55.1 (1985): 48.

[11] Gordon, J. P., and A. Ashkin. *Motion of atoms in a radiation trap*. Physical Review A 21.5 (1980): 1606.

[12] Spreeuw, R. J. C., et al. *Demonstration of neutral atom trapping with microwaves*. Physical review letters 72.20 (1994): 3162.

[13] Raab, E. L., Prentiss, M., Cable, A., Chu, S., & Pritchard, D. E. (1987). *Trapping of neutral sodium atoms with radiation pressure*. Physical Review Letters, 59(23), 2631.

[14] Williamson, R. S., and T. Walker. *Magneto-optical trapping and ultracold collisions of potassium atoms*. JOSA B 12.8 (1995): 1393-1397.

[15] Bergeman, T., Gidon Erez, and Harold J. Metcalf. *Magnetostatic trapping fields for neutral atoms*. Physical Review A 35.4 (1987): 1535.

[16] Steane, A. M., and C. J. Foot. *Laser cooling below the Doppler limit in a magneto-optical trap*. EPL (Europhysics Letters) 14.3 (1991): 231.

[17] Harvey, M., & Murray, A. J. *Cold atom trap with zero residual magnetic field: The ac magneto-optical trap*. Physical review letters, 101(17) (2008), 173201.

Chapter Four

Description of the Experimental Apparatus

4.0 Introduction

In this chapter, a description of the experimental apparatus used in this research is given. This includes the setup used to produce an ensemble of cold potassium atoms that form the target for photoionization and other scattering experiments. Components discussed in this chapter include the cold atom source comprising vacuum system, Zeeman slower, atomic beam source shown in figure 4.1, and the optical setup including the main laser and associated locking system used to cool and trap ^{39} K. The MOT coils and the electron optics used in the electron scattering experiment are discussed in chapter five. A description of the laser systems and the pulsing scheme used for the photoionization and cold Rydberg atom study aspect of this work is given in chapter six.

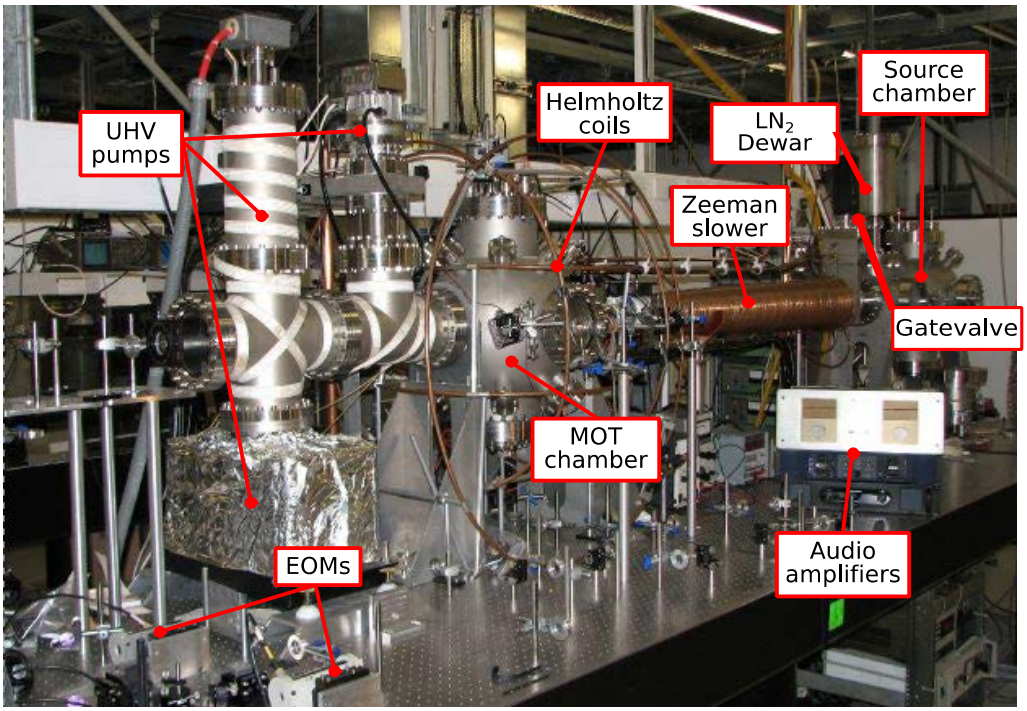

Fig 4.1: Picture of the cold atom source showing various parts of the setup. The electro optic modulators (EOMs) are used for switching the light polarization, as part of the optical setup. Sets of ultra-high vacuum (UHV) pumps were used to create the high vacuum condition in the chamber as required in the experiment. Three sets of Helmholtz coils were used to cancel the earth's magnetic field and magnetic field from the Zeeman slower at the interaction region especially during charged particle experiments.

4.1 The Vacuum System

In order to reduce collisional losses with background gases and extend the lifetime of trapped atoms in the magneto-optical trap (MOT), it is essential that trapping experiments are conducted in a low base pressure enclosure. The vacuum system is therefore designed to operate under ultra-high vacuum (UHV), capable of reaching a base pressure of $\simeq 7\times 10^{-11}\ Torr$. In this apparatus, large metallic vacuum chambers are used, containing both the MOT coils and the charge particle optics used in collision studies. The metallic walls of the chambers minimize the effect of uncontrolled electric field due to electrostatic charging of the surfaces by electrons. As low energy electron impact, photoionization and high-n Rydberg experiments were performed with the cold atoms in the MOT chamber (charged particles are extremely sensitive to even a slight magnetic field), all the chambers and components are made from non-magnetic materials (magnetic field needs to be kept below a few mGauss). The chambers are made from 316L grade stainless steel, which has excellent low out-gassing qualities and extremely low magnetic permeability. All nuts and bolts are made of A4 stainless steel and the chambers are bolted together using copper gaskets held between Conflat^{TM} type knife- edge flanges. The internal metallic components are all made from molybdenum, copper or 310-grade stainless steel. Results from an electron beam experiment [21], indicates that stray field from the walls of the 316 L stainless steel MOT chamber was less than 1mG. Fields above 1mG would cause significant deflection of the electron beam in the chamber.

Figure 4.2 shows the schematic diagram of the vacuum system illustrating different parts of the system.

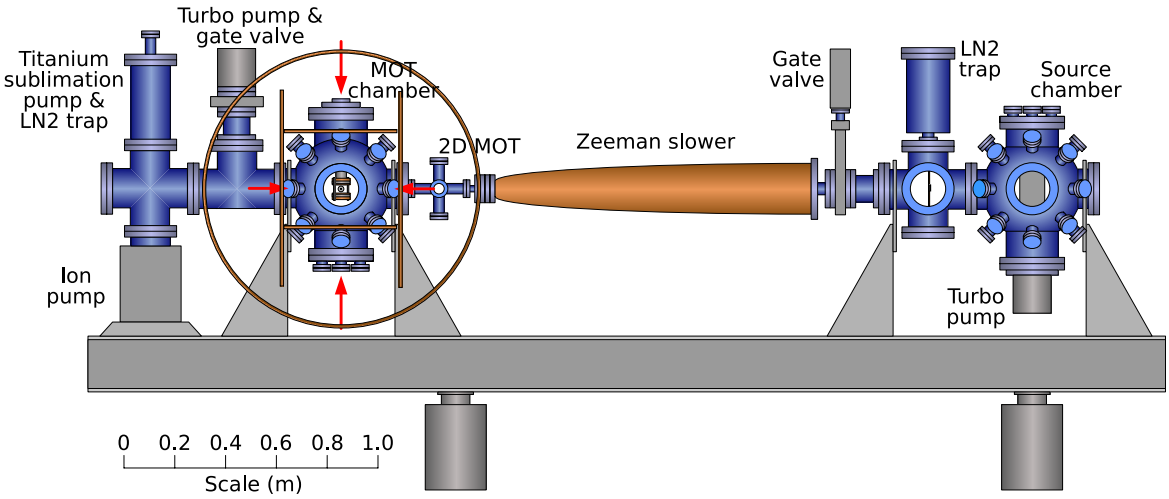

Fig 4.2: *The Vacuum system: (R-L) oven (source chamber), isolation (gate) valve, Zeeman slower, MOT chamber and finally vacuum pump section. The vacuum system is isolated from the supports by ceramic spacers in order to maintain a more even temperature distribution during baking of the system.*

4.1.1 The Atomic Source Chamber

The source chamber contains the oven used to produce an atomic beam of potassium as described in section 4.2. The oven is mounted on the source chamber's upper flange. Also connected to the chamber is an ion vacuum gauge to directly monitor the pressure in the chamber, and an internal heating element used for baking the chamber.

Next to the oven chamber is a six-way cross with 8inch flanges and large windows, which contains the liquid nitrogen (LN_2) cold trap plate, used to reduce the background pressure in the source chamber. This six-way cross is also useful during the alignment of the atomic beam oven, as laser beams can be focused through the windows to probe the atomic beam emanating from the oven. The cold plate (shown in figure 4.3), has a 15 mm aperture to allow the atomic beam to pass through, and at the same time provides a large surface area onto which background gases are trapped. The atomic beam that passes through the aperture then enters the Zeeman slower (described in section 4.3) in which the atomic beam velocity spread is compressed and reduced.

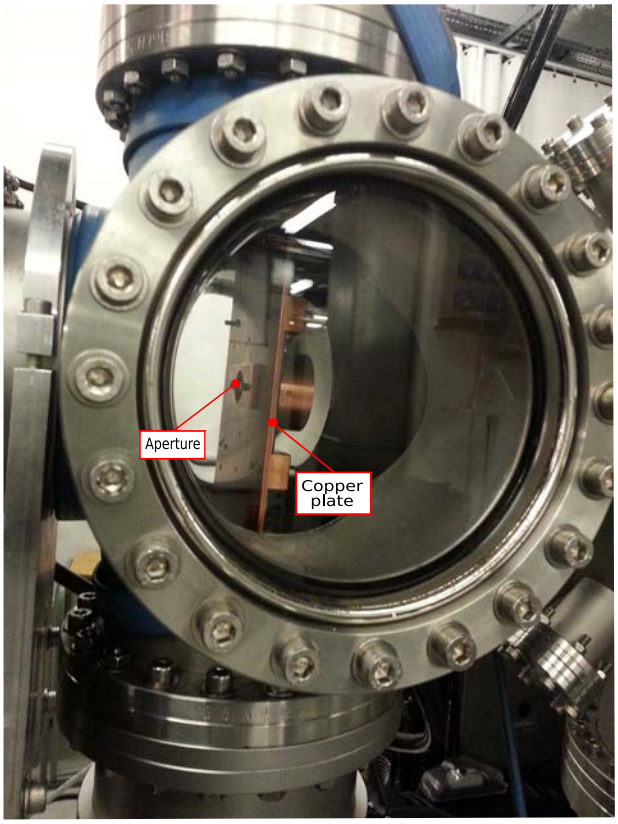

Fig 4.3:The LN2 trap located between the oven chamber and Zeeman slower. It consists of a large copper plate with an aperture which defines the atomic beam that enters the Zeeman slower. The copper plate can be moved up and down the supply pipes (not shown) that contain the liquid nitrogen. In this way, the aperture can be adjusted to coincide with the atomic beam during the alignment of the atomic beam with the slowing laser beam.

The Zeeman slower consists of a 1.25 m long tube with an internal diameter of 36 mm. The tube diameter is stepped down to 20 mm at the exit connected to the MOT chamber. This step helps differentially pump the chambers system so that the pressure in the MOT chamber can be several orders of magnitude lower than the pressure in the source chamber. Through the Zeeman slower, the atomic beam reaches the MOT chamber once the atomic beam has passed. The design and construction of the Zeeman slower is discussed in more details in section 4.3.

The MOT chamber contains the anti-Helmholtz coils used in the magneto-optical trap and the charged particle optics for scattering and collision experiments. Details of the charge particle optics are given in section 5.6 of chapter 5. The MOT chamber also contains an ion gauge for monitoring the pressure and three heating elements for baking the chamber.

To eliminate the earth's magnetic field and cancel the magnetic field from the Zeeman slower penetrating the MOT chamber, three pairs of Helmholtz coils shown in fig 4.1 surrounds the MOT chamber. Cancelling these fields is essential for performing low energy electron impact ionization and high-n Rydberg experiments, which require the magnetic field to be kept below a few mGauss [1]. The Helmholtz coils are controlled by three constant current power supplies.

To achieve the ultra-high vacuum condition needed in the MOT chamber, a titanium sublimation pump, a LN_2 trap, an ion pump, an ion pressure gauge (used to monitor the performance of the vacuum system) and a turbo pump are connected to the vacuum system adjacent to the MOT chamber. At the far end of the chamber is a window to allow the slowing laser beam to pass through the Zeeman slower to the oven.

The vacuum chamber system contains two pneumatically operated Vacuum Generators SoftShut gate-valves. With these it is possible to maintain one side at UHV pressures whilst the other side is at any pressure between atmosphere and UHV. The first valve located between the source chamber and the Zeeman slower is used to isolate the source chamber from the slowing and trapping side of the experiment. This valve also enables the atomic beam to be quickly shut off during experiments involving trapped atoms, and allows either side of the chamber system to be opened for maintenance whilst keeping the other side under vacuum. The second valve is located between the MOT chamber and the turbo-pump and is used to maintain UHV when the turbo-pump is switched off. The base pressure can reach $\sim 7\times10^{-9}$ Torr in the source chamber and $\sim 7\times10^{-11}$ Torr in the MOT chamber when the gate valve between the source chamber and the Zeeman slower is shut. The pressure in the source chamber is limited by out-gassing from the hot oven when at

the emission temperature. When the source chamber gate valve is open and the oven is emitting, the differential pumping of the Zeeman slower flight tube allows the MOT chamber pressure to be maintained in the low 10^{-10} Torr regime.

4.1.2 The Source Chamber Vacuum Pumps

The source chamber is pumped by an air-cooled 360 litre per second Leybold Turbovac 360CSV turbo-molecular pump [2] which is backed by a Varian TriScroll 300 [3] roughing pump. To operate the pumps, the backing pump is switched on first to bring the pressure down to approximately 10^{-2} Torr and then the turbo pump is switched on. In addition to these pumps the LN_2 trap mentioned above aids in reducing the base pressure in the source chamber. The copper plate in the LN_2 trap is cooled by a stainless steel tube containing liquid nitrogen fed from an external dewar. The tubes are connected to the external dewar through Swagelok fittings. The LN_2 trap can reduce the base pressure by a factor of ten. The LN_2 trap was only used after the chambers have been thoroughly baked to remove most of the water vapour from the chamber.

4.1.3 The MOT Chamber Vacuum Pumps

To reach the ultra-high vacuum needed in the MOT chamber, three different pumps are used. An air cooled Varian TV301 turbo-molecular pump [3] with a pumping speed of 250 l/s and a Varian TriScroll 300 [4] roughing pump are connected next to the MOT chamber as shown in figure 4.1. With these pumps the pressure in the chamber can be reduced to $\simeq 10^{-9}$ Torr. To reduce the pressure further, a Varian VacIon ion pump [5], with a pumping speed of 300 l/s is connected to the vacuum chamber. The ion pump can operate at 3, 5 or 7 kV depending on the ultimate vacuum that is required, and can only be activated when the pressure in the chamber is lower than 10^{-6} Torr. In addition, the MOT chamber has a titanium sublimation pump (TSP) consisting a titanium generator ST22 cartridge and a controller unit. This is often used in conjunction with an LN_2 trap. A current of ~60 A flowing for ~60 seconds causes titanium to be sputtered over the walls of the chamber. Background gases are then adsorbed onto the walls. Depending on the pressure, the titanium getter is cycled on every hour [6].

With LN_2 in the Ti:S trap, the pumping speed is increased by a factor of five depending on the prevailing gas in the chamber [7]

As in the source chamber, the backing pump is first switched on to bring the pressure to about 10^{-2} Torr before the turbo pump is switched on. The ion pump is switched on when the pressure has reached 10^{-6} Torr. At this time the TSP can also be switched on.

4.1.4 The Pressure Gauges

For real time monitoring of the pressure in both chambers, two Varian UHV-24 ion gauges [8] are connected to each chamber. The gauges can measure pressure between 10 mTorr and ~5×10^{-11} Torr. The backing pressures are measured by two Varian ConcecTorr gauges [9]. The gauges are controlled by a Varian multi gauge controller [10].

4.1.5 Baking the Vacuum System

To further improve the vacuum condition in the vacuum system, the chambers are baked to remove impurities such as water vapour that adsorb onto the walls of the chamber. Baking is achieved with the built-in heaters in the turbo-pumps and the ion pump, and by any ceramic heaters within the chambers. Three ceramic heaters are in the MOT chamber and one in the source chamber. The ceramic heaters are made from ceramic formers wound with molybdenum wires. About 4 A current through the each heater is required to bake the main chambers. Passing a current of 4 A through the coils of the Zeeman slower also bakes the flight tube of the Zeeman slower. Heating tapes are wound around other part of the system; these tapes require about 190 V_{ac} to heat the system to approximately 150 ℃.

During baking, all windows are covered with thin Aluminium foil to prevent stress fractures and retain the heat. The chambers are mounted on supports via ceramic spacers in order to prevent cold spots. Due to the large surface area of the chambers and the fairly low baking temperature ~170 ℃ in the chambers, baking can take several weeks to achieve 10^{-11} Torr in the MOT chamber. This relatively low temperature is necessary as the outgassing performance of the Kapton coating of the MOT coils winding will permanently degrade at temperature above 200 ℃. This then limits the baking temperature in the MOT. To minimize water adsorption onto the walls of the vacuum system when brought up to atmospheric pressure, the system is filled with nitrogen gas rather than air. Noble gases such as argon can be used when the source chamber side is brought to atmospheric pressure in readiness for opening, to carry out maintenance or refilling of the oven. This prevents oxidation of the potassium and helps prevent buildup of water vapour.

Noble gases are not used in the MOT chamber since noble gases are pumped inefficiently by ion and titanium sublimation pumps [7]. When baking the source chamber it is necessary to disconnect the chilled water supply to the condensation chamber (see section 4.2), to prevent it acting as a cold trap inside the chamber.

4.2 The Atomic Beam Source

The work on potassium described in this thesis, requires a potassium atomic beam, which in this experiment is emitted from an effusive oven. The atomic beam oven originally installed in the chamber was a recirculating oven designed by Paul Cooper [11]. The design was based on the works of Smee [12], Patel [13] and Hickey [14]. Due to difficulties getting the oven to operate properly in recirculating mode (which it was originally designed to operate), some modifications were made to the oven design in this work. The oven was redesigned to operate as a simple effusive oven and not be recirculating. A detailed description of the unmodified oven is given in [11] hence only a brief description will be given here, with highlights on the modifications made to the oven in this work. The oven is designed to operate under UHV condition inside the source chamber and produce a narrow beam of potassium atoms, which can be aimed along the Zeeman slower to the MOT chamber with minimal waste. A schematic diagram of the oven is shown in fig 4.4. The different parts that made up the oven are as follows:

The crucible - this holds up to 10g of solid potassium. Thermocoax heating cables wound around its body heat the crucible to a temperature of about 200 ℃.

The Ascending Pipe - Vaporised potassium rises up this pipe. The ascending pipe is heated to a temperature of about 235 ^{o}C by a copper block, which has Thermocoax heaters inserted along its length.

The First Aperture The vaporised potassium then passes through this 1 mm diameter aperture. This aperture has Thermocoax, heaters wound around it that heats it to a temperature of about 250^{o}C.

The Condensation Chamber is kept at a constant temperature of about 20 ℃ by running chilled water through it, see fig 4.4. Here any of the potassium from the aperture, which does not make it through the second aperture, is condensed back to solid form and so is retained in the chamber. The second aperture forms one of the walls of the condensation chamber.

The Second Aperture with a diameter of 2mm is located a distance of 40 mm from the first aperture. The atoms that pass through this aperture form an atomic beam. Only atoms in the centre of the emission cone pass through the defining aperture at the cold trap, and it is these that pass down through the Zeeman slower to the MOT chamber.

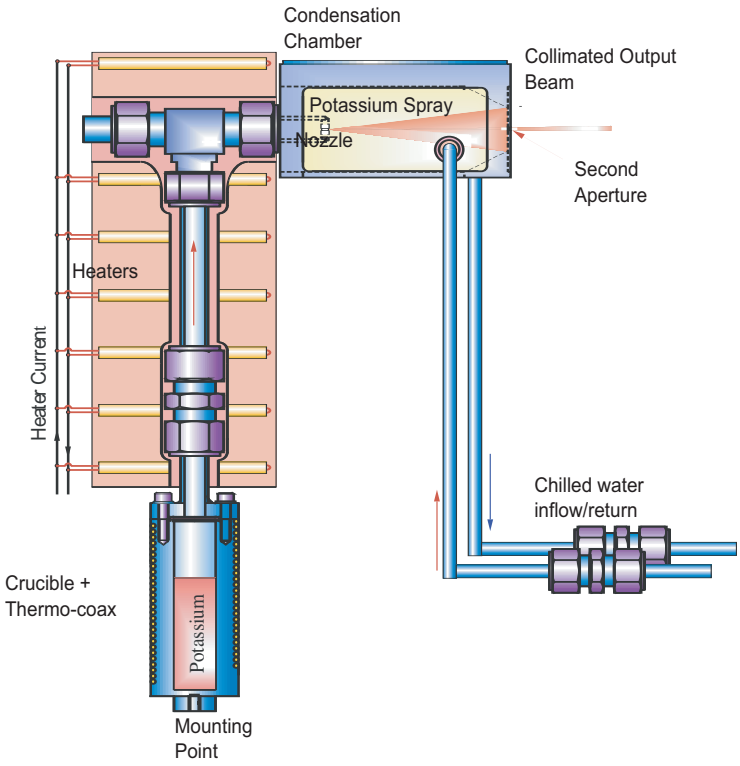

Fig 4.4: An illustration of the atomic beam oven used in this experiment. Temperatures of the different parts are measured by thermocouples (not shown). Potassium is vaporized in the crucible and rises up the heated ascending pipe. The vapour then sprays out of the first aperture and is collimated by the second aperture to form the atomic beam. Potassium spray which did not pass through the second aperture then sticks to the walls of the condensation chamber, which is at the temperature of the chilled water.

4.2.1 Mounting the Oven

The oven has to be mounted in such a way to allow precise alignment of the atomic beam. This is necessary to maximize the flux reaching the trapping region in the MOT chamber. Several different mounting configurations were tried during these experiments.

In the first configuration, the oven was mounted on a steel disc held in place by a mirror mount, which served as a tilt adjuster. With two steel brackets this assembly was bolted to a circular plates attached to the lower end of a rotary adjuster, as shown in figure 4.5.

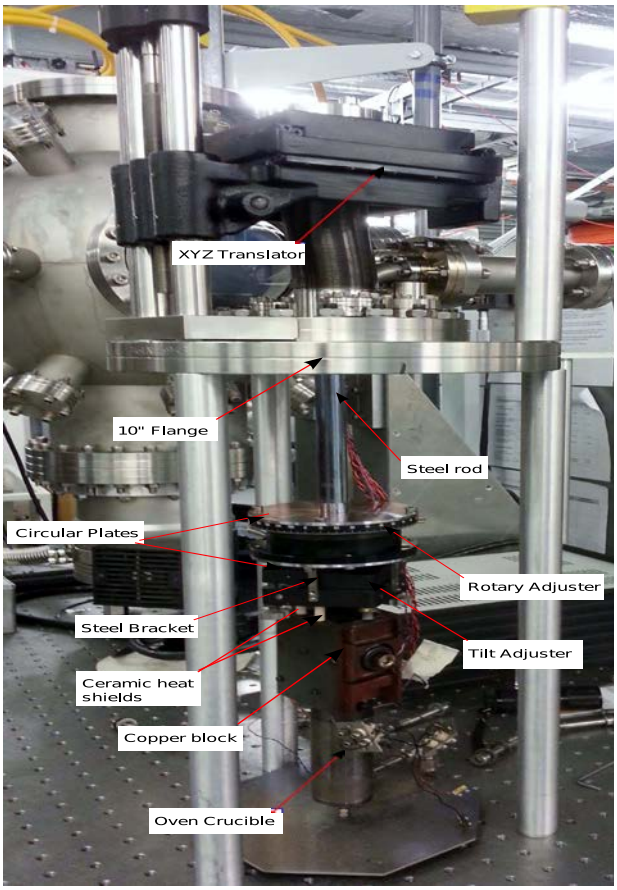

Fig 4.5: A picture of the oven assembly mounted with a rotary and tilt adjuster. Oven alignment in the XYZ plane can done while the chamber is under vacuum

This arrangement was then mounted to a steel rod with a circular plate bolted to the top end of the rotary adjuster. This assembly was then bolted onto an XYZ translator attached to the 10” flange as shown in figure 4.5. The XYZ translator’s adjuster were external to the chamber, while the rotary and tilt adjusters were housed in the vacuum chamber. During testing, this design was found to outgas such that UHV pressures could not be reached. This design was then abandoned.

In the second attempt, the oven was coupled to the steel disc with steel studding in ceramic heat shields and mounted via the rod to the XYZ translator, as shown in fig 4.6. Although there was no out gassing with this configuration, and the oven could be adjusted in the XYZ plane, the tilt angles were not guaranteed due to flexing of the support studding. This hence leads to imprecise adjustments of the atomic beam, and so this configuration was also abandoned.

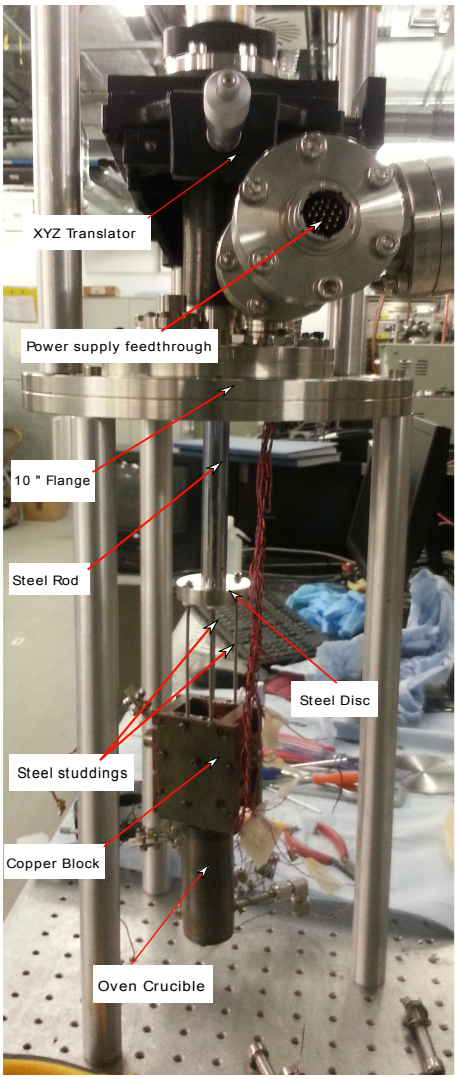

Fig 4.6: A photograph of the oven assembly mounted off four steel studding and an XYZ translator. Oven alignment in the XYZ plane can be done while the chamber is under vacuum.

The final mounting configuration was similar to that described in [11]. This is a more robust stand built entirely with 316-grade stainless steel and has a rugged construction with no discernible flexibility to eliminate inaccuracy, as shown in fig 4.7. This stand has adjustable screws, which are useful during the alignment of the oven. A disadvantage of this arrangement is that the alignment must be set before the source chamber is closed and evacuated. However, since the more flexible designs discussed above did not work reliably, it was this configuration that was finally adopted.

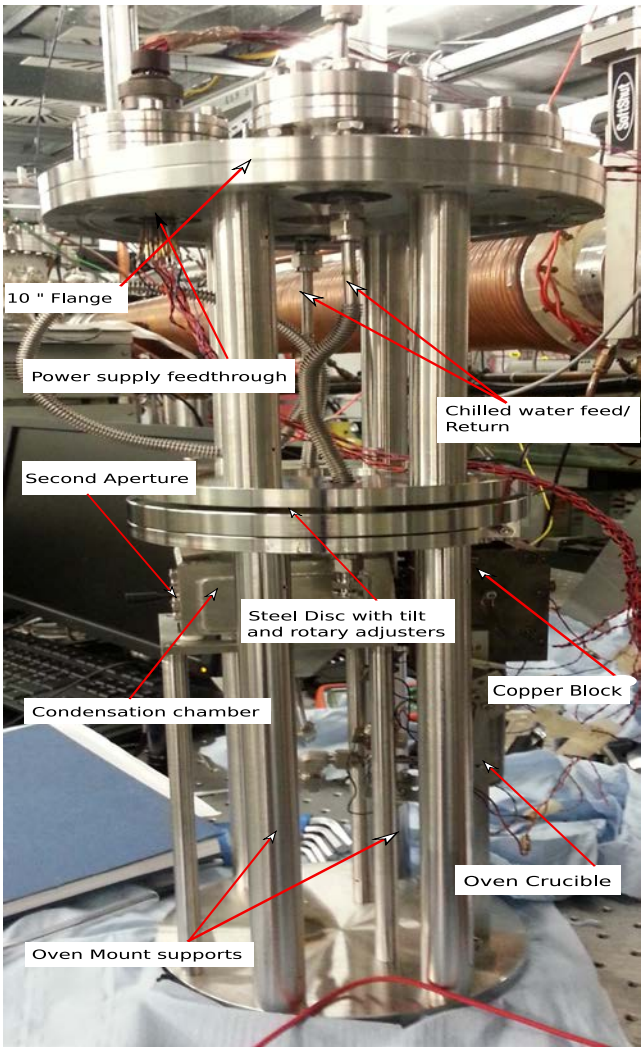

Fig 4.7: A photograph of the oven assembly mounted off the 10" flange. The atomic beam can be correctly aimed by adjusting the height and angle of the stand.

4.2.2 Oven Characteristics

For a ballistic atomic beam, the distance between the second aperture and third apertures (located at the cold trap) and their diameters define the beam divergence. With the second and third apertures of diameters 2 mm and 15 mm respectively, separated by 500 mm, the atomic beam divergence is $\approx 4^{o}$. Since the MOT coils are about 2m away from the oven, the atomic beam would naturally spread to ≈150 mm diameter at this distance. Although the atomic beam was further collimated with the converging Zeeman slower beam, the actual diameter was limited by the 20 mm diameter of the Zeeman slower at the MOT chamber end. Despite the large beam divergence, the atomic flux reaching the MOT chamber is still sufficient to rapidly load the MOT.

It is important to know the velocity distribution of the atomic beam because the tuning of the Zeeman slower magnetic field is dependent on the maximum velocity of the atoms to

be slowed. The speed probability distribution of the atoms effusing from a thin walled aperture differs slightly from the 3D Maxwell-Boltzmann distribution (the distribution of velocity inside the oven) and is given by: [11]

$$P(v) = 2\left(\frac{m}{2k_BT}\right)^2 v^3 e^{-\frac{mv^2}{2k_BT}} \tag{4.1}$$

where v is the speed of the atoms**,** T is their temperature in Kelvin, k_B is Boltzmann constant, m is the mass of the atom, and $P(v)$ is the speed probability density. The speed probability distribution for atoms emitted from the oven at 473K (typical oven operating temperature), calculated from equation 4.1 is shown in figure 4.8. The flux of atoms Φ from an oven with two thin apertures of radii r_1 and r_2 separated by a distance d is given by [11]

$$\Phi \approx \frac{\pi r_1^2 P}{4k_BT}\sqrt{\frac{8k_BT}{\pi m}}\left(\frac{r_1 + r_2}{d}\right)^2 \tag{4.2}$$

where P is the vapour pressure in the oven, and T is the temperature of the oven. The vapour pressure P is related to the oven temperature by

$$\log_{10} P = aT^{-1} + c \tag{4.3}$$

where a and c are constants. Using equation 4.2, the flux of potassium atoms from the oven at temperature of 473K is $\approx 1.1 \times 10^{14}$ atoms/s, where use has been made of the values for a and c ($-4512K$ and 9.448 respectively), obtained by Honig and Kramer [15].

4.2.3 The Oven Operation and Settings

The oven is powered by three constant current power supplies consisting of a 60 V 2 A supply for the crucible, a 75 V, 2 A supply for the copper block and a 30 V, 2 A supply for the first aperture. The oven operation commences by gradually heating different parts, beginning with the first aperture, then the copper block. This avoids blockage of the nozzle leading to the first aperture.

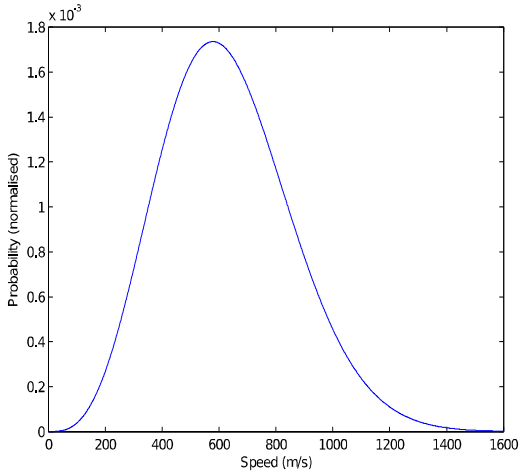

Fig 4.8: The speed probability distribution of potassium atoms emitted by the oven at 473K.

The aperture, copper block (which heats the ascending pipe) and the crucible are thermally coupled such that, heating the aperture and copper block to their standby temperatures naturally heats the crucible to its standby temperature as shown in table 4.1.

Oven part	**Current setting (A)**	**Temperature (℃)**
Crucible	0.00	140
Copper block	0.40	200
First Aperture	0.65	220
Condensation chamber	Chilled water	20

Table 4.1: Oven setting when on standby.

At standby temperature, the potassium in the crucible is fully melted and the oven is always left at these settings even when not in use. This reduces the impact of out gassing due to impurities in the charge and keeps the oven in a state of readiness so that emission temperature can be attained in $\simeq 60$ minutes. During normal operation only the crucible temperature need be adjusted (increased), this brings the other parts to full operating temperatures as given in table 4.2. When the oven temperature is quoted in this thesis, this refers to the temperature of the crucible. The oven starts emitting atoms at ~ 155 ℃ $(\sim 430K)$ and can be operated at temperature up to ~ 330 ℃ $(\sim 600K)$. The oven was normally operated at 200 ℃ during experiments conducted in this work. This temperature was chosen as it was found that higher emission temperatures caused an increase in MOT chamber pressure without an increase in MOT loading rate.

Oven part	Current setting (A)	Temperature (℃)
Crucible	0.20	200
Copper block	0.50	220
First Aperture	0.65	250
Condensation chamber	Chilled water	20

Table 4.2: Oven operating setting.

If there was a need to shut down the oven, it had to be kept at the standby setting for at least 12 hours to prevent potassium blocking the aperture which cools faster than the copper block and crucible. After this cooling process, the copper block heaters could be switched off, followed by the aperture heaters.

4.3 The Zeeman Slower

One of the limitations of the laser cooling of sodium atoms reported by Balykin et al in 1979 [16], was the high mean velocity of the sodium atoms, which was attributed to the Doppler shifting (the apparent change in the atomic energy levels due to the motion of the atoms) of the slowed atoms out of resonance with the cooling laser beam. Also the oven such as the one used in this experiment emits atoms with a Maxwellian velocity distribution with half-width of 200-300m/s and corresponding Doppler width of 300-400MHz. To overcome these problems, Phillips and Metcalf [17] incorporated a magnetic field gradient to compensate for the changing Doppler shift and to keep the atoms in resonance with the cooling laser as they slow down, in addition to compressing the velocity spread. This technique is known as Zeeman slowing. A Zeeman slower therefore uses the combination of a circularly polarized, counter propagating laser beams and a spatially varying magnetic field to slow the atoms to the required velocity. The maximum capture velocity of a typical magneto-optical trap is ≈ 40 m/s [18]. In the absence of laser cooling, less than 0.0025 % of an atomic beam of potassium leaving the oven at 473 K would be within the $0 - 40$ m/s velocity range (see fig 4.8), and therefore a ‘hot’ atomic beam is unsuitable for loading the MOT with the efficiency required for the experiments described in this thesis.

For the present work, a source of cold potassium atoms is therefore required for the magneto-optical trapping phase of the experiment, since it provides a continuous supply of atoms that are within the capture velocity of the magneto-optical trap.

Another advantage of loading a MOT using a Zeeman slower instead of loading the MOT from a background vapour is that the vapour pressure of the oven does not limit the vacuum in the trapping chamber. Further, the flux of a slow atomic beam is many orders of magnitude higher than the trappable flux from a background-vapour loaded MOT. Under this condition, the MOT in these experiments was loaded in less than 3seconds. Another important benefit of loading the MOT via the Zeeman slower is the possibility of switching off the atomic beam at will by simply shutting the gate valve, thereby interrupting the atomic beam entering the slower. The above benefits make this technique most suitable for collision experiments.

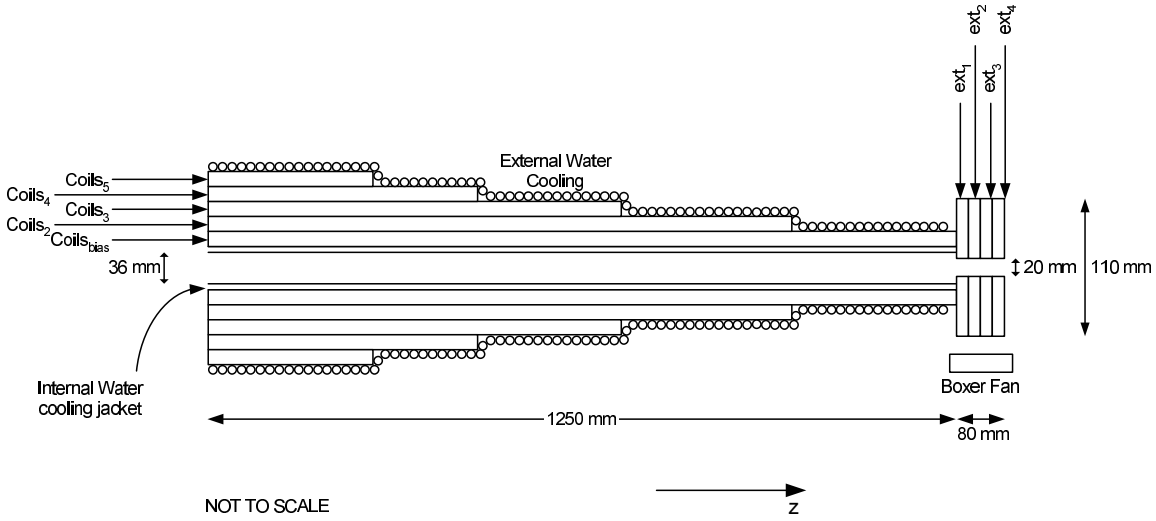

Fig 4.9: A schematic showing the winding of the Zeeman slower solenoids. The slower is made from a 1.25m long stainless steel flight tube. The flight tube has an internal water cooling channel. The solenoid made up five layers of separate windings and the extraction section made up of four additional solenoids. The nine separate windings allow for accurate tuning of the magnetic field.

4.3.1 Construction of the Zeeman Slower

The design and construction of the Zeeman slower used in this work is described in more detail in [11], so only a brief description will be given here.

The Zeeman slower is made from approximately 3.5 km of 3.55 × 1.25 mm rectangular cross section aluminum wire, coated in Nomex insulation [19] and arranged in five layers of decreasing lengths as shown in figure 4.9, such that the current can be set independently

for fine-tuning of the magnetic field profile. This wire has a high maximum temperature specification (475 K) and small volume compared with plastic insulated wires. The flight tube is 1.25 m long and is made from two tubes welded together to provide a channel for water-cooling. At the source chamber end, the internal diameter is 36 mm and at the extraction end the internal diameter is 20 mm. The different internal diameters at each end of the flight tube are helpful in pumping the MOT chamber. Since large amounts of heat (1.5 kW) are dissipated in the coils of the Zeeman slower, water-cooling is employed both inside and outside the coils. The inner water channel is housed in the double walled, Conflat flanged Zeeman slower flight tube. An additional water-cooling jacket made from 8 mm OD copper tubing is wound on top of the solenoid to provide additional cooling.

The stainless steel flight tube around which the solenoid is wound was custom made by Vacuum Generators [20], including a jacket for the flow of chilled cooling water.

Each of the five main solenoid windings and the extractions coils has a resistance of approximately 5.5Ω and 0.3Ω, respectively and are powered separately by constant current power supplies built at the Physics and Astronomy electronics workshop. The innermost winding, which is used to create a homogenous magnetic field that compensates for the detuning of the slowing laser beam (see section 4.3.2), is referred to as the bias solenoid. The other four main solenoids create the spatially varying magnetic field profile (described by equation 4.2) needed to tune the atomic levels along the beam path. Tuning these fields (by adjusting the current flowing through each coil) provide the appropriate Doppler shift along the path of the moving atom. The power supply for the bias solenoid can provide 20A at 60V. The supplies for the other four main coils can provide 15A at 60V, while the supply for the extraction coil can provide 20A at 10V [21]

As the slowing atoms arrive at the end of the Zeeman slower, an abrupt change in the magnetic field is needed to rapidly shift the atoms out of resonance with the slowing laser beam. This abrupt change in the magnetic field profile prevents the atoms from stopping and turning around inside the Zeeman slower, by decoupling them from the slowing process.

To achieve this, four set of coils known as the extraction coils are placed at the end of the main Zeeman slower solenoids. The extraction coils are constructed from ≈190 turns of 2 mm diameter circular cross section copper wire and are air-cooled. For the present Zeeman slower, four coils are used to set the extraction field, which gives strong detuning to the atoms from the slowing laser when they arrive at the end of the main solenoids. The magnetic field profile generated by each of the main solenoids and the extraction coils

when a current of 1 A flows through them are shown in figures 4.10 and 4.11 respectively. The first of these coils (with a positive current in table 4.3) increases the magnetic field sharply to accomplish this detuning, and the atoms then stop absorbing light from the slowing laser and propagate freely [22]. The other set of coils with reverse currents generate fields in the opposite direction, which results in a large magnetic field gradient between the coils and so prevents the atoms from scattering much light when they go through resonance. Details of the profile are given below.

4.3.2 The Magnetic Field Profile of the Zeeman Slower

A detailed derivation of the magnetic field profile needed in conjunction with a σ^+ circular polarized laser beam to cool and slow an atomic beam of potassium in the Zeeman slower can be found in [11, 21]. The resulting equations reproduced in section 3.2 are;

$$B = B_{bias} + B_{max}\sqrt{1 - \frac{z}{z_0}} \tag{4.2}$$

where B_{bias} is the magnetic field required to compensate for the detuning, δ, of the cooling laser beam and is given by;

$$B_{bias} = \frac{h\delta}{\mu_B} \tag{4.3}$$

where μ_B is the Bohr magneton, B_{max} is the magnetic field needed to compensate for the Doppler shift of the fastest atoms moving with velocity v_{max} and is given by;

$$B_{max} = \frac{hv_{max}}{\mu_B \lambda} \tag{4.4}$$

and λ is the wavelength of the laser beam.

The minimum magnetic field value B_{min} at the end of the Zeeman slower main solenoids, (before extraction) where the atoms can interact with the laser field in the cooling process defines the extraction velocity v_{ext}, which is given by

$$v_{ext} = \lambda\left(\frac{\mu_B B_{min}}{h} - \delta\right) \tag{4.5}$$

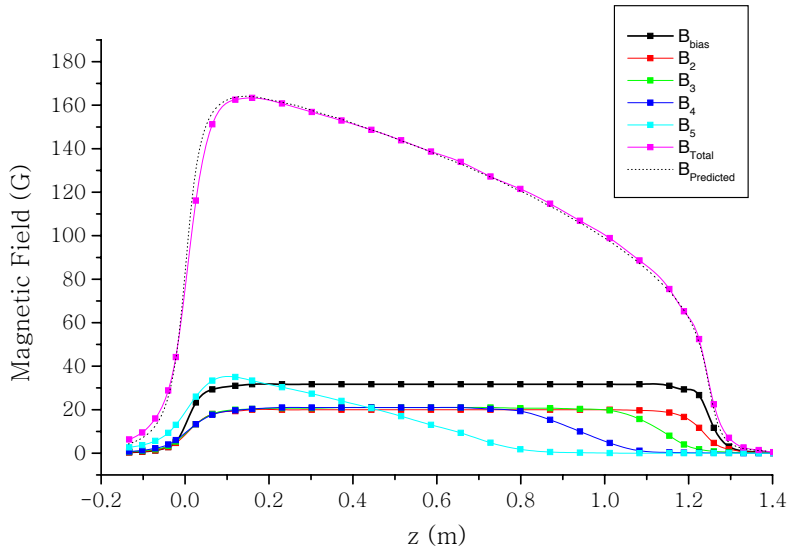

Fig 4.10: The measured magnetic field profile for each section of the Zeeman slower when a current of 1 A flows through each of the five main solenoids.

From equation 4.5, it can be seen that the extraction velocity can be selected by varying the minimum magnetic field, the laser detuning or both. With a laser beam locked to $F = 2 \rightarrow F' = 3$ transition for potassium, detuned by $+115\,MHz$, and B_{min} of 130 $Gauss$, the extraction velocity is $\cong 51\,m/s$.

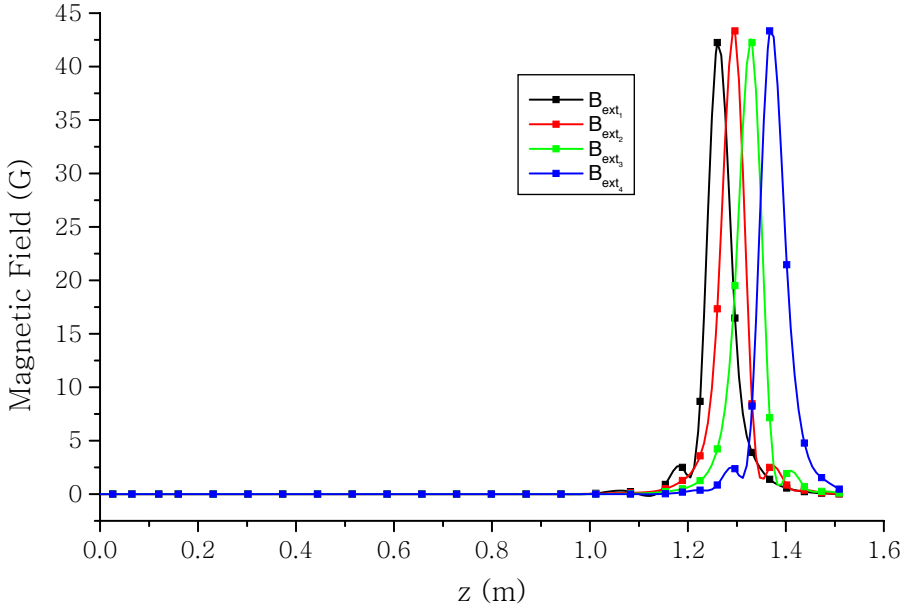

Fig 4.11: The measured magnetic field profile for each of the extraction coils of the Zeeman slower at a current of 1 A

4.3.3 The Cooling Laser and Bias Field

Atoms in the atomic beam are slowed down by interaction with a counter-propagating laser beam- the slowing laser. Since this beam will pass through the trapping region, it is tuned off resonance with respect to stationary atoms, so that the beam appear 'invisible' to the trapped atom in the trap region, minimizing the interaction between the slowing laser beam and stationary trapped atoms. This is achieved by passing the main beam through an AOM set to shift the beam by +115 MHz (blue detuned). A full description on the generation of the slowing beam as well the trapping beams is given in section 4.5 on the optical setup. To partially compensate for the divergence of the atomic beam, the slowing beam is expanded to a diameter of 20 mm (as it enter the vacuum chamber) and then focused to about 1 mm at the exit of the oven. The convergence of the laser beam provides some collimation of the atomic beam due to the reduction of its transverse momentum [23]. The slowing beam as well as the trapping beams is circular polarized by passing it through a quarter wave plate before entering the experiment. This is to ensure there is an appropriate Zeeman shifting of the energy levels, and to pump the atoms into a two level system. As mentioned above, a bias magnetic field is added to the Zeeman slower magnetic field to compensate for the detuning of the slowing laser beam.

4.3.4 Zeeman Slower Optimal Current Settings

The final exit velocity of the atoms from the Zeeman slower depends on the oven temperature and the Zeeman slower's magnetic field profile. The Zeeman slower's current settings (which determine the value of B_{min}) used in this work are given in table 4.3. A full description of the procedure to determine the velocity distribution of the Zeeman slower is given in [21]. Under these conditions, atoms travelling with velocities below 625 m/s are slowed to a minimum velocity of $\cong 51\, m/s$ according to equation 4.5. The intensity of the slowing beam at the exit of the Zeeman slower is ~ 30 mW/cm^2 which is well above the saturation intensity (1.77 mW/cm^2), and hence the atoms are likely to be further slowed down due to power broadening, (see section 3.2).

Winding	I_{bias}	I_1	I_2	I_3	I_4	Ext_1	Ext_2	Ext_3	Ext_4
Current (A)	0	7.64	6.8	6.4	7.4	11	-11.06	-10.9	-10.9

Table 4.3: Zeeman slower optimal current settings with oven at 200 ℃*. The bias coil* (I_{bias}) *and the coil through which the current* I_1 flows *are wound on the same length of the Zeeman slower so it was not necessary to use both at the same time.*

The magnetic field profile generated by these settings is shown in figure 4.12. In addition to providing the magnetic field that decouples the atoms from the slowing process, the other three coils operating at negative currents counteract the magnetic field generated by the main Zeeman slower coils. This reduces the magnetic field from the Zeeman slower permeating into the MOT chamber.

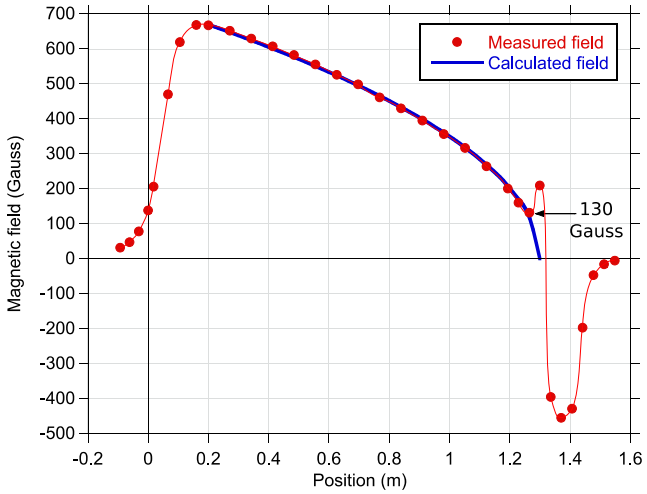

Fig 4.12: Magnetic field profile of the Zeeman slower generated with the above setting. These setting are used with the oven operating at 473K (200 ℃).

4.4 The Coherent Laser System

The laser system used to generate all cooling and trapping laser beams used in these experments consists of a continuous wave Coherent MBR-110 Ti:Sapphire (Ti:S) tunable ring laser [24] pumped by a 10.5W Coherent Verdi V10 Nd:YVO_4 laser [24] operating at 532nm. The Ti:S crystal allows the MBR-110 to tune continuously from 700 nm to 1000 nm. Trapping potassium-39 requires a coherent laser radiation at a wavelength of 766.7011 nm. This corresponds to the $4^2S_{1/2}$ (F=2) to $4^2P_{3/2}$ (F′=3) transition. At this wavelength, the power output of the coherent MBR-110 is approximately 1.2 W. Figure 4.13 shows the layout of the coherent laser system and the laser locking system. A glass slide is used to split off approximately 50 mW from the beam which is then directed into a Burleigh WA-1500 wave-meter. Approximately 20 mW of the beam is sent (using a beam picker from Thorlab) to the laser locking system described below. The $4^2S_{1/2}$ (F=2) to $4^2P_{3/2}$ (F′=3) transition for potassium is close to one of the absorption lines of oxygen, this makes the laser very unstable. The laser cavity was therefore filled with dry nitrogen (N_2) gas to displace the oxygen in the cavity before the laser can be locked to this transition.

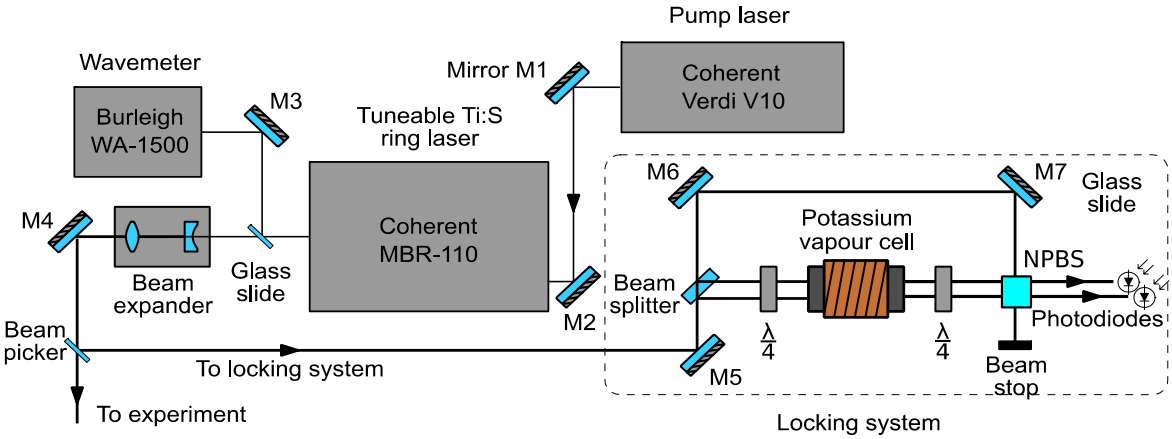

Fig.4.13: The layout of the main laser system. The laser system used in this experiment consists of a Coherent Verdi V10 pump laser, a Coherent MBR-110 Ti-sapphire continuous wave laser, tunable between 700 nm and 1000 nm, a Burleigh wavemeter and a Doppler-free saturated absorption based laser locking system used to lock the laser frequency to the desired trapping transition of potassium. At the 766.7 nm used in this experiment, the laser outputs ~ 1W. A glass slide is used to direct ~50 mW of laser light into the wavemeter for real time monitoring of the laser wavelength. A beam picker is used to direct 20 mW of laser light into the locking system

In brief, the laser system works as follows. The pump laser beam is focussed and steered by mirrors so that it enters the cavity at mirror M1 as shown in figure 4.14. The beam then passes through the Ti:S crystal and cavity optics via mirrors M2, M3 and M4. Mirror M4 returns the beam to mirror M1 and also acts as the output coupler. The Coherent system contains a number of frequency control systems to keep the laser operating at a constant frequency and in a single mode, as shown in figure 4.14. The inbuilt stability and locking system of the Coherent MBR-110 laser are controlled by the following optics:

1. **The birefringent filter:** This provides a coarse adjustment of the laser frequency across the entire frequency range of the laser.
2. **An intra-cavity thin etalon:** This feature ensures single frequency operation and, by rotating the etalon, allows finer tuning of the laser frequency. When the etalon - lock function is engaged, the transmission frequency of the etalon is locked to the frequency of the laser and mode hopping of the laser is reduced.
3. **The Brewster angled glass plates:** There two Brewster angled plates within the laser cavity which allows the laser frequency to be tuned even more precisely. When these plates are rotated, the optical path length within the laser is adjusted. The use of two such plates ensures that the laser beam path does not alter. A piezo controlled mirror, which forms part of the cavity, automatically adjusts to prevent mode hops. A fraction of the light produced by the laser is directed into a temperature controlled and hermetically sealed Invar - stabilized reference cavity. Fine adjustment of the laser frequency can then be made by adjusting the length of

the reference cavity using a long extension piezo, whilst maintaining a lock to the reference cavity fringes. Strain gauges are used to monitor the length of the reference cavity. The servo-lock function of the control electronics locks the laser to one of the fringes produced by the reference cavity by adjusting the Brewster angled plates.

Despite these control systems, the frequency of the laser still drifts at a rate of ≈ 100 kHz/s, which is not stable enough for long-term trapping experiments. It is therefore necessary to further control the laser using an external locking system.

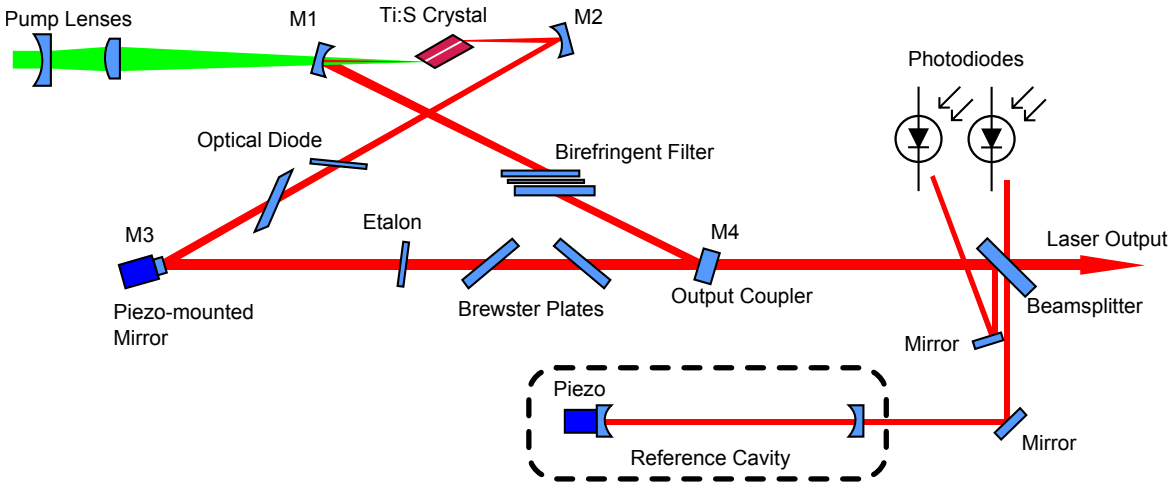

Fig. 4.14: The MBR-110 schematic showing the ring setup, the Ti:Sapphire crystal and the in-built stability systems used to control the laser frequency.

4.5 The External Laser Locking System

To ensure the stability of the laser system and to maintan a drift of less than 1 MHz during normal experiments (which may last for several hours), an external locking system is required. The laser locking system used in this experiment is based on the Doppler–free saturated absorption spectroscopy described by Hänsch et al [26].

Absorption spectroscopy obtains spectroscopic information about a target by monitoring the wavelengths of light it absorbs. Absorption spectroscopy works by passing a probe laser beam through an atomic vapour and measuring its intensity. The use of an atomic vapour poses some problems because the atoms are moving with a spread of velocities, so the absorption signal is Doppler broadened.

In Doppler free absorption spectroscopy, two laser beams passing through an atomic sample, comprising of a pump beam and a probe beam, produce the spectrum. The intensity of the pump beam is much greater than that of the probe. In the absence of a

pump beam, a Doppler broadened absorption profile is expected as the probe laser frequency scans across the central resonance frequency of the atomic transition. This broad profile makes it difficult to accurately determine where the line centre is. The presence of the pump beam, however, allows the central frequency to be determined by saturated absorption, and so the resolution is limited only by the natural linewidth of the transition.

The principle behind this is as follows. When the laser is off-resonance, the two beams excite two different classes of atoms; those that are moving towards or away from the laser direction at a certain velocity so as to Doppler shift the atoms into resonance with the respective beam. The absorption dip for each of the beams will then occur at different wavelengths since the beams are counter-propagating and thus are selecting atoms of different velocities. As the laser is tuned to the centre of the resonance peak, both the probe beam and pump beam interact with the same class of atom - those that have a zero velocity component parallel to the beams. The high intensity of the pump beam excites nearly 50% of atoms in this class - i.e. it saturates the sample. This results in a reduction in the absorption of the probe beam at the central frequency with a full width at half maximum (FWHM) equal to the natural half-width.

A detailed description of the design of the original setup can be found in [11]. As an improvement to this technique [21], a second probe beam is made to pass through the atomic vapour without overlapping with the pump beam as shown in figure 4.15. The signal from the probe beam can then be subtracted from the reference beam signal (saturated absorption signal) to leave just the Doppler-free absorption peaks. This means that the signal is less affected by variations in the laser power output.

The natural linewidth of the $4^2P_{3/2}$ state of potassium is $\sim 6.035\ MHz$ which is on the order of the excited state hyperfine splittings for potassium-39. At 360 K, the Doppler full width at half maximum (FWHM) is 850 MHz [21]. This exceeds the ground state hyperfine splitting, and there are also nearby pairs of ground state crossover resonances for each isotope. These features are due to moving atoms whose Doppler shifts equal half the frequency difference between transitions. This gives rise to six overlapping features for each hyperfine ground state of the ^{39}K isotope [27]. The overlap between various transitions and the close hyperfine splitting of the $4^2P_{3/2}$ excited state of potassium ($\sim 33\ MHz$) makes it difficult to resolve individual hyperfine levels, (see figure 2.1).

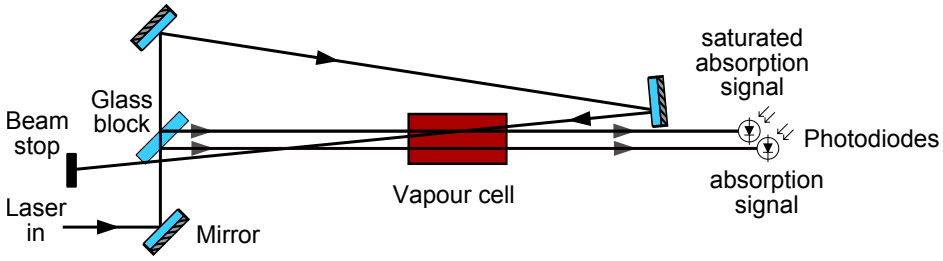

Fig. 4.15: Doppler free saturated absorption spectroscopy setup with the addition of a second probe beam. The Doppler broadened signal from this second probe beam is subtracted from the saturated absorption signal to remove the Doppler broadened features from the line shapes.

Figure 4.16 shows the line profile of the of the Doppler free saturated absorption spectroscopy. The absorption dip on the Doppler broadened background is shown and the Doppler free signal is obtained by subtracting the absorption signal from the second probe beam.

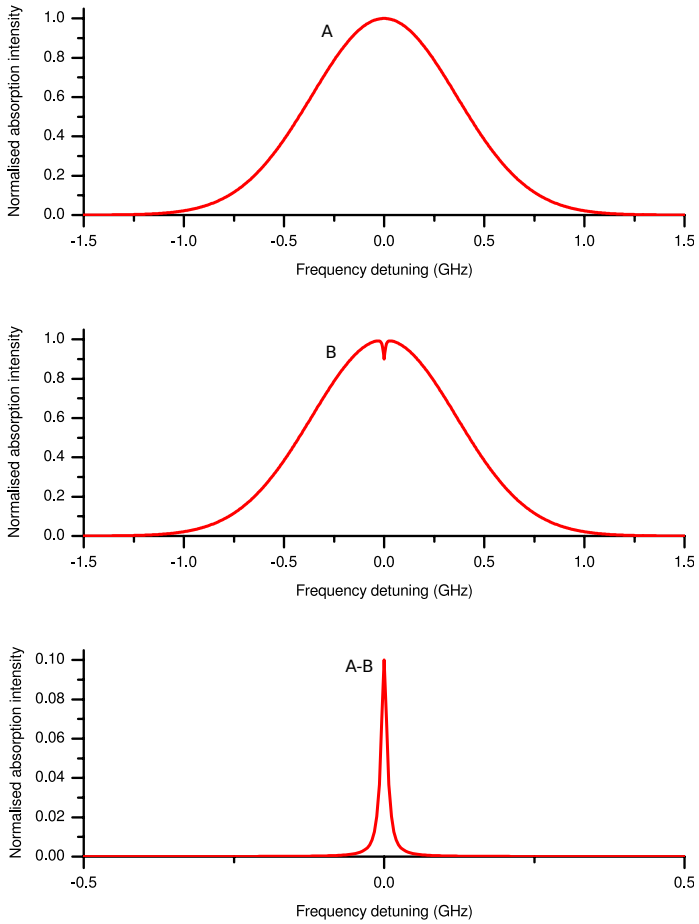

Fig.4.16: Line profile calculated for a single transition in potassium at 360 K in saturated absorption spectroscopy: Graph (a) shows the Doppler broadened absorption profile for a transition (FWHM ~850 MHz) in a thermal atomic vapour. The first graph shows the expected Doppler broadened absorption profile for a sample under saturated absorption conditions. The second graph the absorption profile due to the intersecting probe and pump beam. The third graph is the inverted Doppler free profile, generated by subtracting Graph (B) from Graph (A). This is the signal that is used to lock the laser.

The setup used to lock the laser in this experiment is shown in figure 4.17, and is similar to figure 4.15 except that, with the inclusion of a non-polarizing beam splitter, the pump beam now completely overlaps the probe beam over the whole length of the vapour cell, resulting in a considerably stronger saturated absorption signal. The probe beam has an intensity of ≈ 2 mW/cm^2 and that of the pump beam is ≈ 20 mW/cm^2, which is significantly more than the saturation intensity of 1.77 mW/cm^2 for potassium.

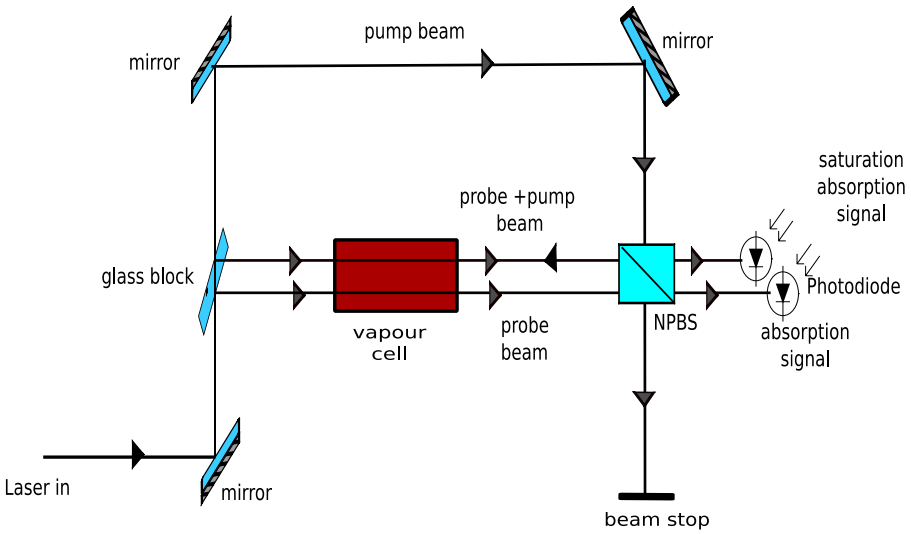

Fig. 4.17: Doppler free saturated absorption spectroscopy setup with the addition of a second probe beam overlapping the pump bean over the entire vapour cell. The Doppler broadened signal from this second probe beam is subtracted from the saturated absorption signal to remove the Doppler broadened features from the line shapes.

The saturated absorption signal obtained with the original setup (with only one probe beam) [21], as reproduced in figure 4.18, shows the absorption signal over the Doppler broadened background for potassium.

The result was obtained by scanning the laser frequency over the potassium transition around 766.7 nm. The left hand peak corresponds to the overlapped upper ground state $^2S_{1/2}$ (F=2) → $^2P_{3/2}$ F' =3 transitions at 766.7011 nm while the right hand peak corresponds to the lower ground state $^2S_{1/2}$ (F =1) → $^2P_{3/2}$ (F' = 2) transition at 766.7002 nm. The central peak is a crossover resonance due to transitions from both hyperfine ground states F =1,2 → F'. It occurs when the laser frequency is half way between the resonance frequencies of the two ground states.

When the pump beam interacts with F = 1 atoms and pumps them to F' = 2, they can then decay to F = 2. This means there are more atoms for the probe beam to interact with and so the probe beam is absorbed more strongly. This gave rise to the inverted crossover dip shown in Figure 4.18. Since the F=2→ F'=3 transition is used to trap potassium in this

experiment, the laser is locked to the left hand peak corresponding to the F=2→ F'=1,2,3 transitions. The probe and pump beams are circularly polarized in order to pump the system towards a two level system containing only the F=2→ F'=3 transition. In this way the left hand peak is narrowed to a FWHM of only 13.6 MHz [21], which provides a sharper peak to lock the laser to.

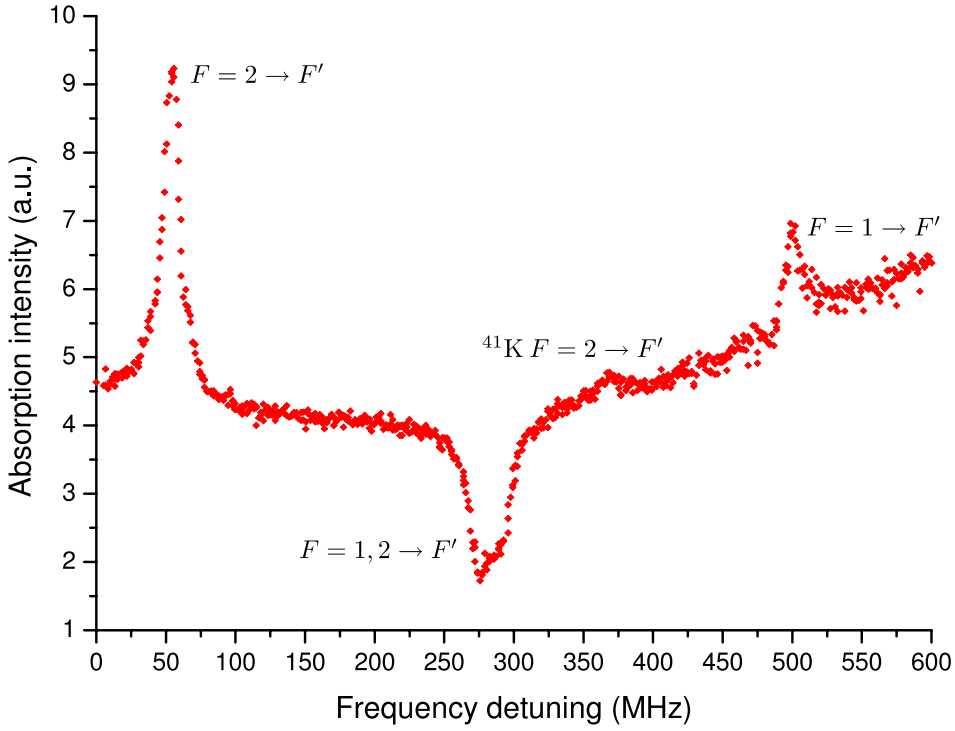

Figure 4.18: Doppler free saturated absorption signal for potassium. The left hand peak and right-hand peak correspond to transitions from the F = 2 and F = 1 ground states respectively, while the central peak corresponds to the crossover resonance which is exactly half way between these two peaks. The left hand peak from the F=2 transition is used to lock the laser in the experiment. A right-handed (σ^+) circularly polarized laser beam with intensity of $\sim 1.4\ mW/cm^2$ *was used as the probe beam. The small peak at ~350 MHz corresponds to the F = 2 → F'= 3 transition of* ^{41}K*. The shift between this transition and the* $F = 2 \rightarrow F' = 3$ *transition is* $\sim 308 MHz$ *[21]. The zero of the frequency scale corresponds to the laser frequency at the start of scan which was below the* $F = 2 \rightarrow F' = 0$ *transition.*

The above procedure in conjunction with applied magnetic fields (both DC and AC) was used to lock the laser in these experiments. The AC (sinusoidal) magnetic field was applied to the cell in order to oscillate the atomic resonance transitions. This dithering of the resonances through Zeeman modulation provided the error signal (which is proportional to the laser frequency drift from the desired frequency) to lock the laser (see details below). The DC magnetic field offset was used to provide the appropriate detuning to the laser by Zeeman shifting the energy levels of the atoms, for effective cooling and trapping of the atoms.

4.5.1 Locking System Setup

To effectivly lock the laser to the F=2→ F'=1,2,3 transition absorption peak, the laser frequency is monitored as it scan across this absorption peak. There are two ways of monitoring the drifting of the laser frequency from the central frequency of the transition accurately: (a) by rapidly scanning the laser frequency either side of the transition by a few MHz; and (b) by employing an AC magnetic field to oscillate the resonance frequency of the atoms in the vapour by Zeeman shifting their energy levels. Scanning the laser rapidly as in method (a) will oscillate the output frequency of the laser thus disturbing the trapping process. Hence in the experiments described here, the AC magnetic field method was adopted. A Similar technique was used to detune the laser from resonance, by applying a DC magnetic field. This causes hyperfine sub-levels to be Zeeman shifted so that the locking frequency of the laser is then offset from the natural resonance. This was to provide the effective detuning of the laser required for the trapping experiments. The optics and electronic layout of the locking system is shown in figure 4.19.

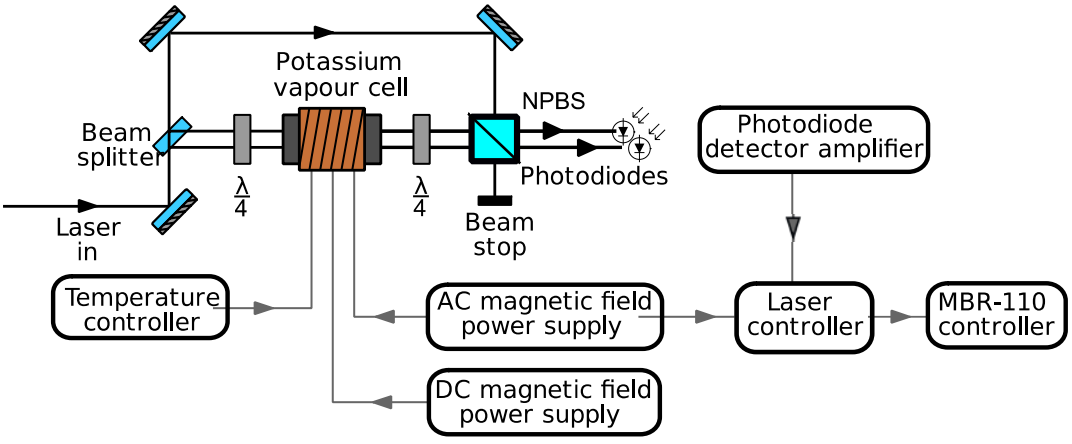

Fig 4.19: The layout of the optics and electronics required for the laser locking system. The laser controller provides a feedback signal to keep the laser locked.

The electronics setup includes a temperature controller to keep the potassium vapour at a set temperature of $\sim 360\ K$, the power supply for the AC and DC magnetic fields and the laser locking controller which uses the signal from the absorption photodiode to generate feedback control signals for the laser. The AC magnetic field was generated by a solenoid wound around the vapour cell, while a second solenoid surrounding the cell provides the DC magnetic field. Detailed design specifications for the locking system electronics can be found in [11]

4.5.1.1 The Vapour Cell

The vapour cell is placed in an aluminium case and surrounded with Thermocoax heating wires [28] which is used to heat the cell to $\sim 360\,K$, as shown in figure 4.20. A thermocouple is attached to the body of the aluminium case to monitor the temperature and provide a feedback to the temperature controller. The temperature controller is a simple proportional controller, which is accurate enough to maintain the cell to within $\pm 1K$. Two solenoids are wound over the heating cables to provide the AC and DC magnetic field needed to Zeeman shift the energy levels of the atoms in the vapour cell.

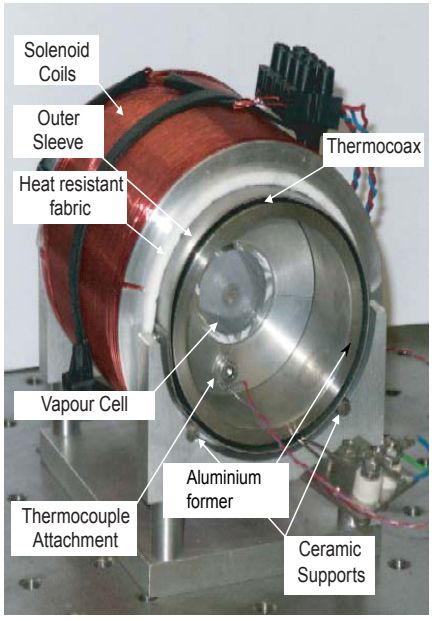

Fig. 4.20: The potassium vapour cell setup. The cell was heated by the Thermocoax heating cables wounded on an Aluminum former. This is insulated from the surrounding layers by ceramic support rods. Around this are wound two solenoids; one to generate an AC- magnetic field used to provide the locking signal and the second coil generates the DC offset magnetic field used to detune the laser frequency.

4.5.1.2 The Vapour Cell Solenoid Power Supply

The solenoid power supply shown in figure 4.21, generates a 75 Hz sinusoidal signal with a peak-to-peak voltage of ±12 V. The AC solenoid contains ~ 6100 turns per meter, so that when driven by the power supply, the magnetic field generated inside the cell is $\sim \pm 35$ Gauss peak to peak. This causes a Zeeman shift of $\sim \pm\ 50\ MHz$, which is larger than the linewidth of the absorption peak. It is then sufficient to scan across the absorption peak for laser locking. The 0.1 Ω resistor acts as a current to voltage converter for input to the laser controller. A phase shift stage was added to the laser controller electronics, so as to compensate for the inherent phase shift between the drive voltage and the magnetic field and thus bring the B-field in phase with the power supply.

The DC magnetic field power supply is a constant current power supply with output ranging from 0 A to 1 A. This creates a field of up to 150 Gauss through the vapour cell, thus causing a Zeeman shift of up to 210 MHz for the F= 2, (M_F = 2) → F' =3, ($M_{F'}$ = 3) transition.

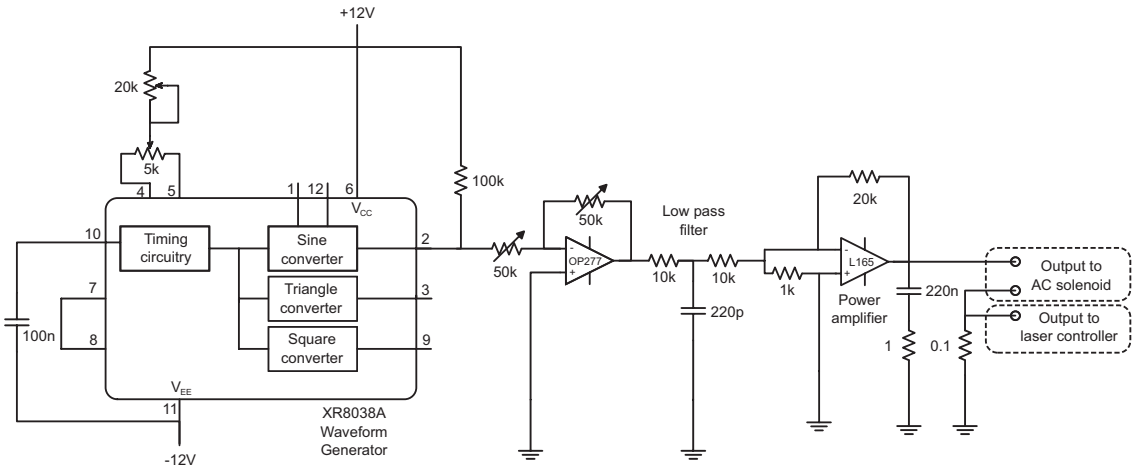

Figure 4.21: The AC solenoid power supply. This generates a 75 Hz sinusoidal signal with ±12 V peak to peak. With this signal through the AC solenoid, the AC magnetic field generated inside the vapour cell has a peak-to-peak value of ~± 35 Gauss.

4.5.1.3 The Laser Control Electronics

The laser control circuitry shown in figure 4.22 provides a feedback voltage signal to the MBR-110 laser, by examining the absorption of the probe beam together with the AC magnetic field.

The circuitry is divided into five stages. Stage one amplifies the photodiode signals and subtracts one signal from the other, leaving only the Doppler free saturated absorption signal. In stage two, the absorption signal and the magnetic field are monitored and are differentiated and digitized into logic signals, with 1 for positive gradients and 0 for negative gradients. This was achieved by passing the signal through a gain stage. In the high gain stage, the output of the amplifier goes into saturation, thereby digitizing the signal making a 1 to corresponds to +8 V and 0 corresponds to -8 V. As mentioned in section 4.5.1.2, the AC magnetic field monitor is passed through a phase shifter before being digitized to compensate for the phase shift between the magnetic field and the drive voltage. An exclusive OR (XOR) logic gate (logic comparator) in stage three compares the differentiated and digitized AC magnetic field signals with that of the absorption signal.

The difference between the signals gives a measure of how much the laser has drifted from the resonance frequency, which can be used in a feedback loop to adjust the laser system settings that control the laser frequency, until a zero error is achieved. Sending the output signal from the XOR, which is a square wave to the laser control servo, will result in the oscillation of the servo loop, which will distort the laser output. To avoid this oscillation, the output of the XOR is passed through an integrator circuit in stage four, which averages it, and then produces an error signal with information of how much the laser frequency has drifted from the resonance frequency of the transition. Stage five produces the feedback signal, which is sent to the external scan input of the MBR-110 laser controller, to effect appropriate compensation to the laser system. In this way, the laser frequency is locked to the F=2→ F'=1,2,3 transition peak.

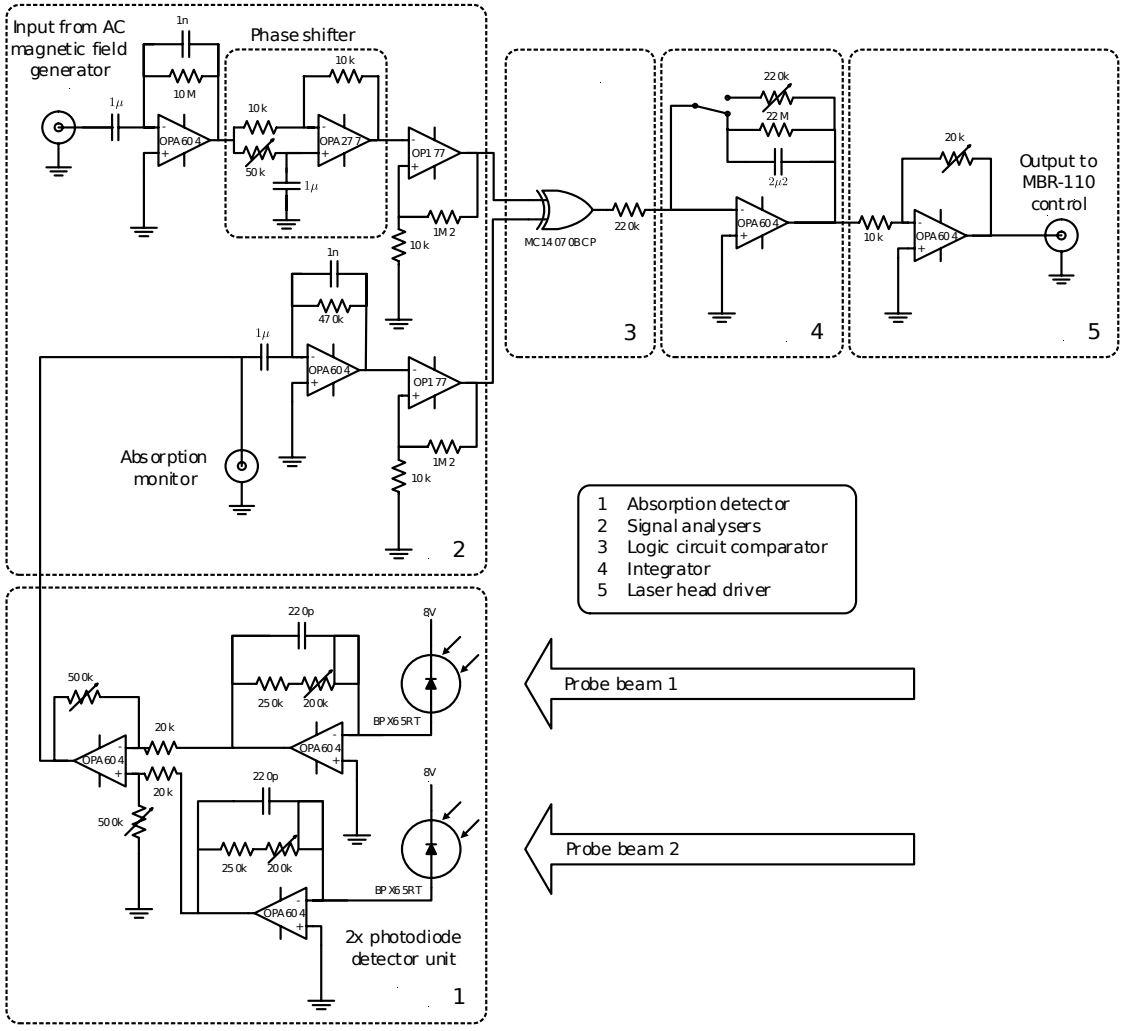

Figure 4.22: The locking system laser controller electronics showing the different stages. In stage one, the photodiode signals are amplified and the signal difference is obtained. The photodiode signal and the AC magnetic field monitor signal are differentiated and digitized in stage two. In stage three, the digitized signals are compared with an XOR gate. Stage four then integrates the resulting signal to provide a feedback signal and stage five amplifies this so that it can be used to drive the MBR-110 laser controller

4.5.1.4 Understanding The Locking System Logic

Figure 4.23 shows the differentiated AC magnetic field signal compared with the differentiated absorption signal. If the laser is on resonance as in case 1, the output of the XOR gate will spend as much time in logic 1(+8 V) as in logic 0 (-8 V). When this signal is integrated, the average of 0 V will be sent to the laser controller. If the laser is off resonance as in the second case, the output of the XOR gate spends more time as 1 than as 0. Integrating this, a positive voltage will be sent to the laser, which will drive it back to resonance with the saturated absorption peak. If the output of the XOR gate spends more time as 0 than as 1, a negative voltage will be sent to the laser to equally drive the laser back to resonance.

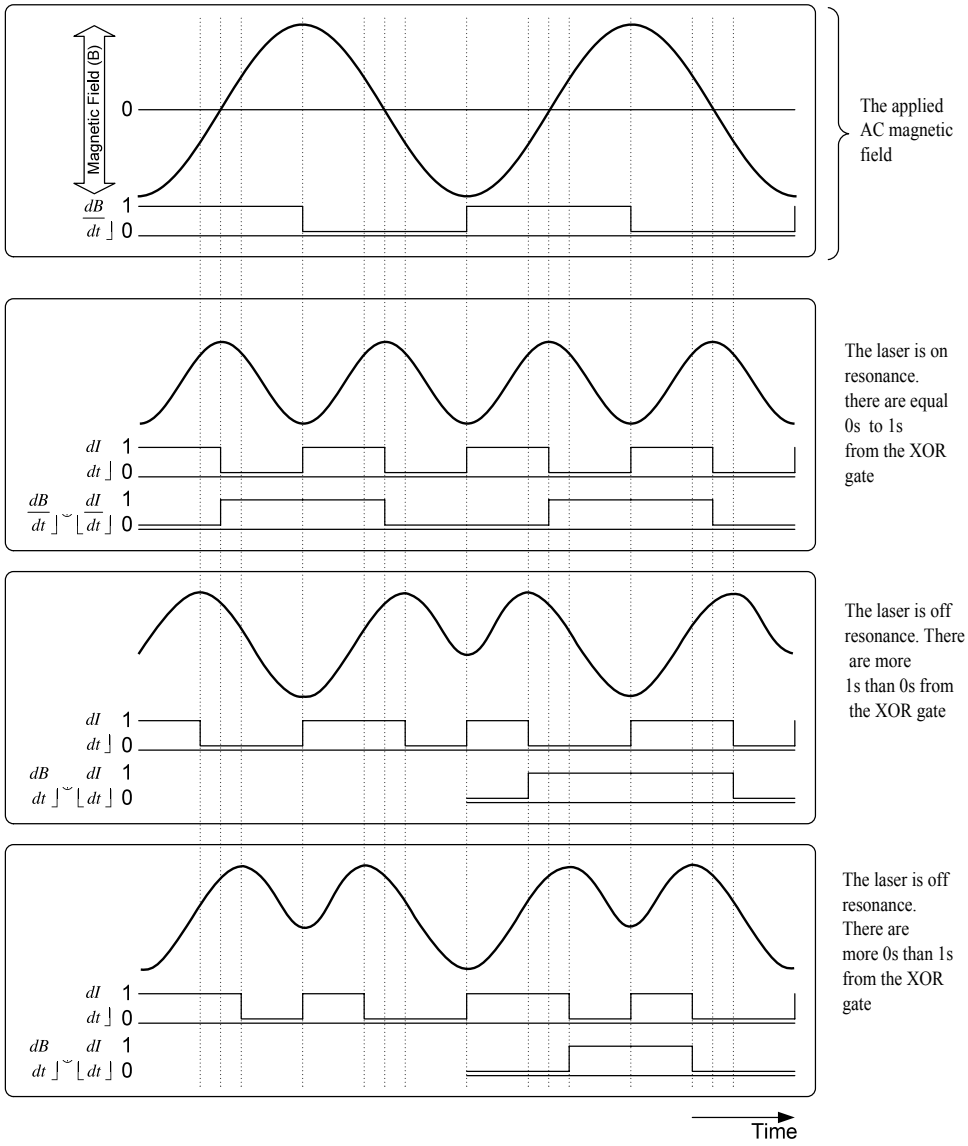

Figure 4.23: The logic output from the laser locking XOR gate. The XOR gate compares the digitised gradients of the AC magnetic field and absorption signal. When the laser is on resonance, the XOR output spends equal amounts of time as 0 and 1 and so the output of the integrator is then zero.

4.5.1.5 Detuning the locking system

Trapping potassium requires the trapping laser to be slightly detuned from resonance. This is achieved by applying a DC offset magnetic field to the vapour cell. This Zeeman shifts the F= 2, (M_F = 2) → F' =3, ($M_{F'}$ = 3) transition to which the laser is locked. The tunability of the locking system can be estimated by calculating the Zeeman shift of the atomic transition. A DC magnetic field of up to 150 Gauss can be applied, which corresponds to a shift of up to 210 MHz for this transition. To accurately know the amount of detuning in terms of laser frequency, the locking system detuning was calibrated by measuring the laser frequency at different current settings of the locking system using a WS-UL Highfinesse wavelength meter [29]. The relationship between the applied DC current and the laser frequency shift was found to be linear, but was found to be almost the same for red and blue detuning as shown in figure 4.24, and was therefore used as a calibration curve for the laser detuning system.

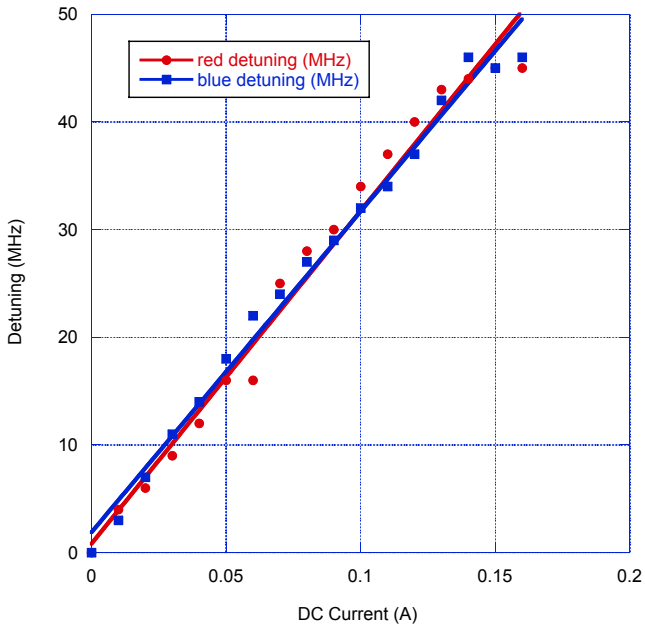

Fig.4.24: Laser detuning curve. Detuning was achieved by a DC magnetic field to the vapour cell.

A measurement of the laser locking systematic offset [21] revealed that probing the atomic beam at the defining aperture with a retro-reflected, circular polarized laser of total intensity of 3 mW/cm^2, a maximum fluorescence signal from the F = 2→ F' = 3 excited state was observed when the laser was blue detuned by ~5 MHz. Similar results have been reported [23], and is attributed to the closely spaced hyperfine structure of the upper excited state of potassium. This offset therefore introduces ~5 MHz uncertainty in determining the resonance frequency of the laser.

4.6 The Optical Setup

In this section, a brief description of how all the necessary laser beams with the correct frequencies needed to both slow potassium atoms in the Zeeman slower and trap the atoms in the AC driven magneto-optical trap (AC-MOT) are obtained is given. The output of the MBR-110 laser was used to provide all the beams necessary to cool and trap potassium in this experiment. The additional optical setup for the excitation and photoionization experiments are described in chapters 6 and 7.

4.6.1 The Re-Pump Laser Beam

The excited state hyperfine structure of potassium means the energy of different transitions is close compared to the natural line-width. This implies that when these atoms are excited by absorption of light photons, they can decay through one or more decay channels to a non-resonant final state, thereby limiting the laser cooling and trapping process. As mentioned above, the cooling trapping laser is locked to the F = 2→ F' = 3 transition, which implies that some atoms that are in the F=1 ground state to start with, will without any mechanism of bringing them to resonate with the cooling and trapping laser, remain 'dark' to the experiment. Effective cooling and trapping of potassium is more difficult than it is for other alkali metals, because of the lack of a closed optical cycling transition, which is a consequence of the small nuclear magnetic moments of its isotopes leading to correspondingly small hyperfine splitting of the optical transitions. The use of circular polarized light eventually results in a two state system where the atoms cycle between the F =2 ground state and the F' = 3 excited state. As potassium atoms are excited from the $4^2S_{1/2}$ ground state to the $4^2P_{3/2}$ state i.e. F = 2→ F' = 3 transition, there are unavoidable excitation to the F' = 1 and F' = 2 excited states which can then decay to the F = 1 and F = 2 ground states. With the trapping laser resonant with the F = 2→ F' = 3 transition, atoms that decay to the F = 1 ground state are decoupled from the laser because of the hyperfine splitting of $\sim 462\ MHz$ between the F =1 and F = 2 ground state. Without some intervention, these transitions limit the efficiency of the resonant laser in cooling and trapping the atoms.

The solution to this problem requires a modulated laser beam made up two frequencies differing by the ground state hyperfine splitting; one resonant with the main trapping transition (F = 2→ F' = 3) and a second frequency (the re-pump frequency) which is resonant with the F = 1→ F' = 2 transition. Although the F =1 and F = 2 ground state are

separated by $\sim 462\ MHz$, the F' = 2 and F' = 3 excited state hyperfine splitting are separated by $\sim 21\ MHz$ (see the energy level diagram), hence the re-pump frequency was $\sim 441\ MHz$, higher than the main trapping frequency. This repump frequency is obtained by passing the laser beam through a $440\ MHz$ intraAction acouto-optical modulator (AOM) [30]. This AOM splits off a $+441\ MHz$ blue detuned re-pump beam which is then recombined with the main (unshifted) beam by passing both beams through a non-polarizing beam splitter (NPBS) in the recombination stage, as shown in figure 4.25. This produces two beams, each containing the main laser frequency and the re-pump frequency. Typically, the re-pump intensity is set to between 20% and 30% of the total laser intensity by changing the driving power through the AOM.

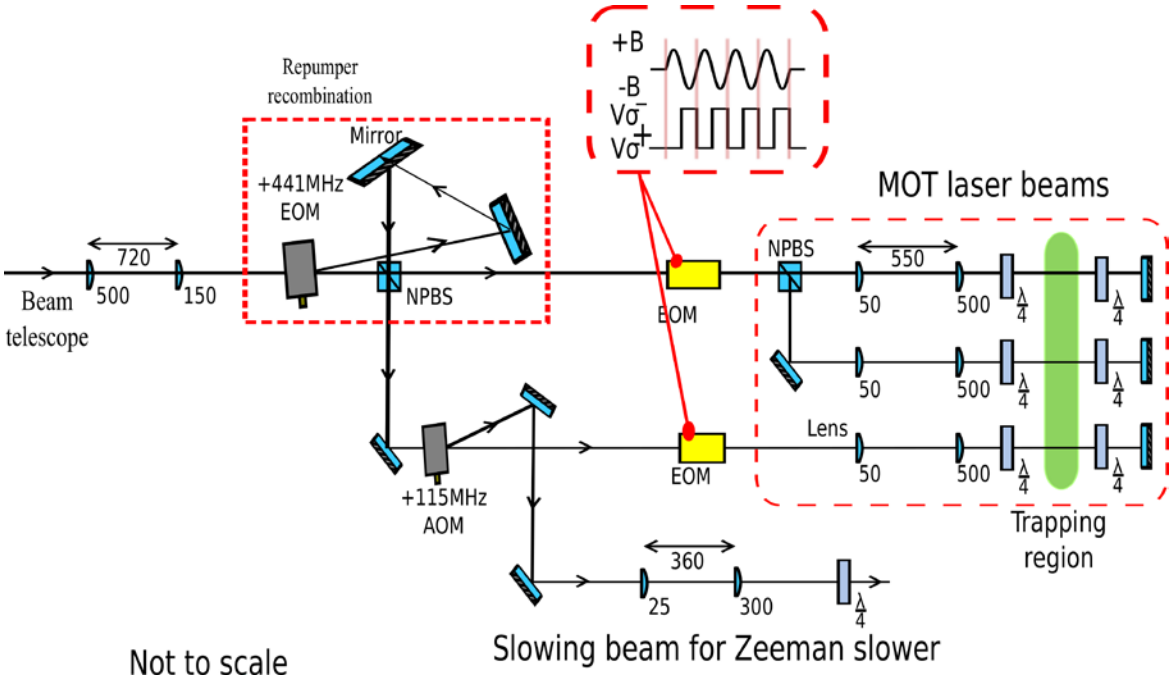

Fig 4.25: The optical setup used to generate all the necessary beams for Zeeman slowing and trapping the atoms in the AC-MOT. The two EOMs orientated so that their optical axes are 45° to the polarization axes of the laser beams are used to switch the polarization of the MOT laser beam in synchronicity with the alternating magnetic field. The voltage across the EOM crystals is switched at the frequency and phase of the AC drive current so that they act as half wave plates in order to rotate the polarization of the laser beams by 90° when the trapping magnetic field has switched sign. This is done by applying a square wave high voltage signal to the EOMs controlled by the LabVIEW computer system. The numbers represent the focal lengths of the lenses and the distances between them in mm. NPBS = non-polarizing beam splitter and $\frac{\lambda}{4}$ = quarter wave plate.

4.6.2 Trapping Beam And Zeeman Slower Beams

Atom trapping in a MOT requires six laser beams intersecting at the trapping region as well as a slowing laser beam for the Zeeman slower. As shown in figure 4.24, the laser beam is first passed through a beam telescope made of two plano-convex lenses to reduce

the beam waist and focus it to pass through the 440 MHz AOM which splits off the re-pump frequency. The beams then pass through the recombination stage where they recombine to produce two laser beams containing both frequencies. One of these two beams is passed through another NPBS to create two additional beams, which are expanded and collimated by two lenses and then retro-reflected after passing the trapping region to form four of the six MOT beams.

The other beam from the recombination stage is passed through a 110 MHz AOM to provide a +115 MHz blue shifted beam. This beam, of power ~ 30 mW forms the Zeeman slowing beam. It is blue detuned to prevent it interacting with atoms trapped in the MOT, as discussed above. The unshifted beam from the 110 MHz AOM is also expanded and collimated, and it is retro-reflected after passing the trapping region to form two more MOT beams. All beams are circularly polarized by passing them through quarter wave plates (QWP). A second QWP just before the retro-reflecting mirrors ensures that the retro-reflected beams have the correct handedness of circularly polarized light in all directions as shown in figure 4.26.

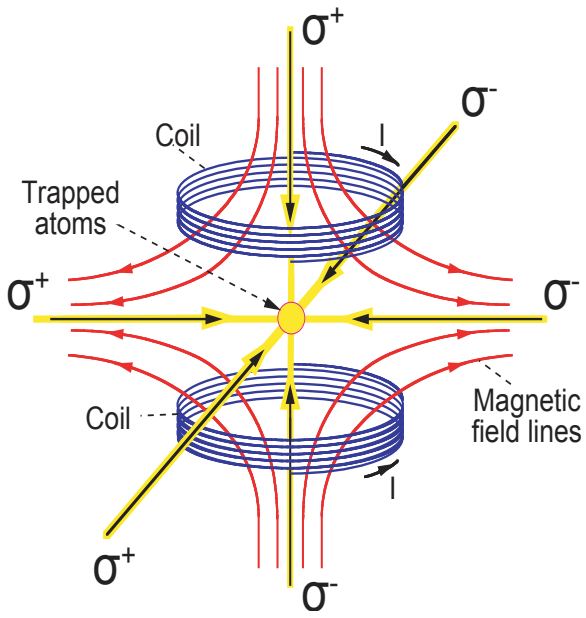

Fig 4.26: The magneto-optical trap consists of three pairs of counter- propagating, orthogonal laser beams centred on the trap region of an inhomogeneous magnetic field. The laser beams are circularly polarised and a pair of current carrying coils in an anti-Helmholtz configuration creates the magnetic field. The polarisation of the light and the direction of the magnetic field mean that atoms moving away from the centre of the MOT are more likely to scatter photons from a laser beam travelling in the opposite direction to their motion.

4.6.3 AC-MOT Laser Beam Polarization Switching

Since the magnetic field switches sign as the sinusoidal AC drive current oscillates, trapping atoms in both cycles of the AC-MOT requires a corresponding switching of the polarization of the trapping laser beams from σ^+ to σ^- in synchronicity with the AC-current as shown in figure 4.27. To accomplish this, one of the beams from the recombination stage and the unshifted beam from the 110 MHz AOM pass through two electro-optical modulators (EOMs) before they are expanded and retro-reflected to form the MOT beams.

Applying an electric field across an EOM changes the indices of refraction (both ordinary and extraordinary), given rise to an electric field dependent birefringence, which leads to change in the polarization of the laser beams. The electro optical crystals then act as variable wave plates, with a retardation that is linearly dependent on the applied electric field [31]. The EOM therefore, has a zero and a half wave plate voltage. When the AC current has the same sign as the DC-MOT, the zero wave voltage is applied to the crystal and when the AC-MOT field swaps sign, a half wave voltage is applied to the EOMs. The EOMs are orientated with their optical axes at 45˚ to the polarization axes of the laser beam in order to provide a 90˚ rotation of the laser beam polarization axis when the half wave voltage is applied.

Two Conoptics Inc EOMs; 360-80 and 360-81 EOMs were used in these experiments to switch the polarization of the trapping laser beams. The zero wave V_0 and half wave $V_{\lambda/2}$ voltages of the EOMs were found to be 15 V and 125 V respectively. The voltages across the crystals were driven with the same frequency and phase as the AC drive current signal that generates the trapping magnetic field.

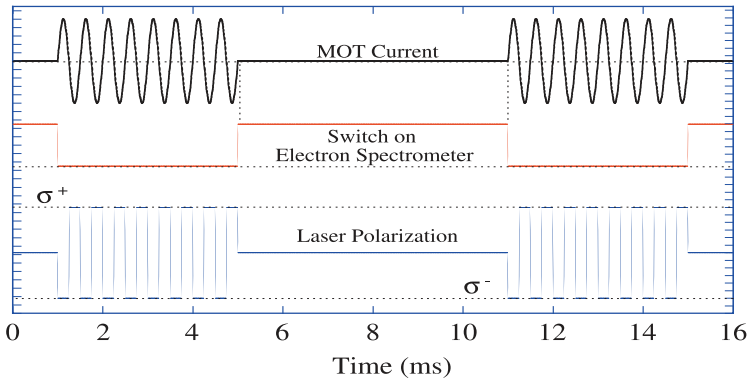

Fig 4.27: The switching configuration for the AC-MOT. The MOT is driven by an alternating supply, so that the net induced current in the conductors surrounding the MOT coils is zero. The polarization of the six trapping laser beams is switched at the same rate as the MOT current, so as to maintain trapping. Experiments using charged particles are conducted during the time the MOT current is zero.

4.6.3.1 The EOM Drive Signal

A TTL voltage signal from the DAQ card, which is used to switch the EOM voltages serve as input to the PA85 power amplifier circuit shown in figure 4.28. The PA85 amplifier is a high voltage, high power bandwidth MOSFET amplifier capable of delivering an output current of 200 mA and voltages of up to ±215 V. In the circuit in figure 4.28, it was configured as an inverting amplifier, where the non-inverting input is referenced to earth.

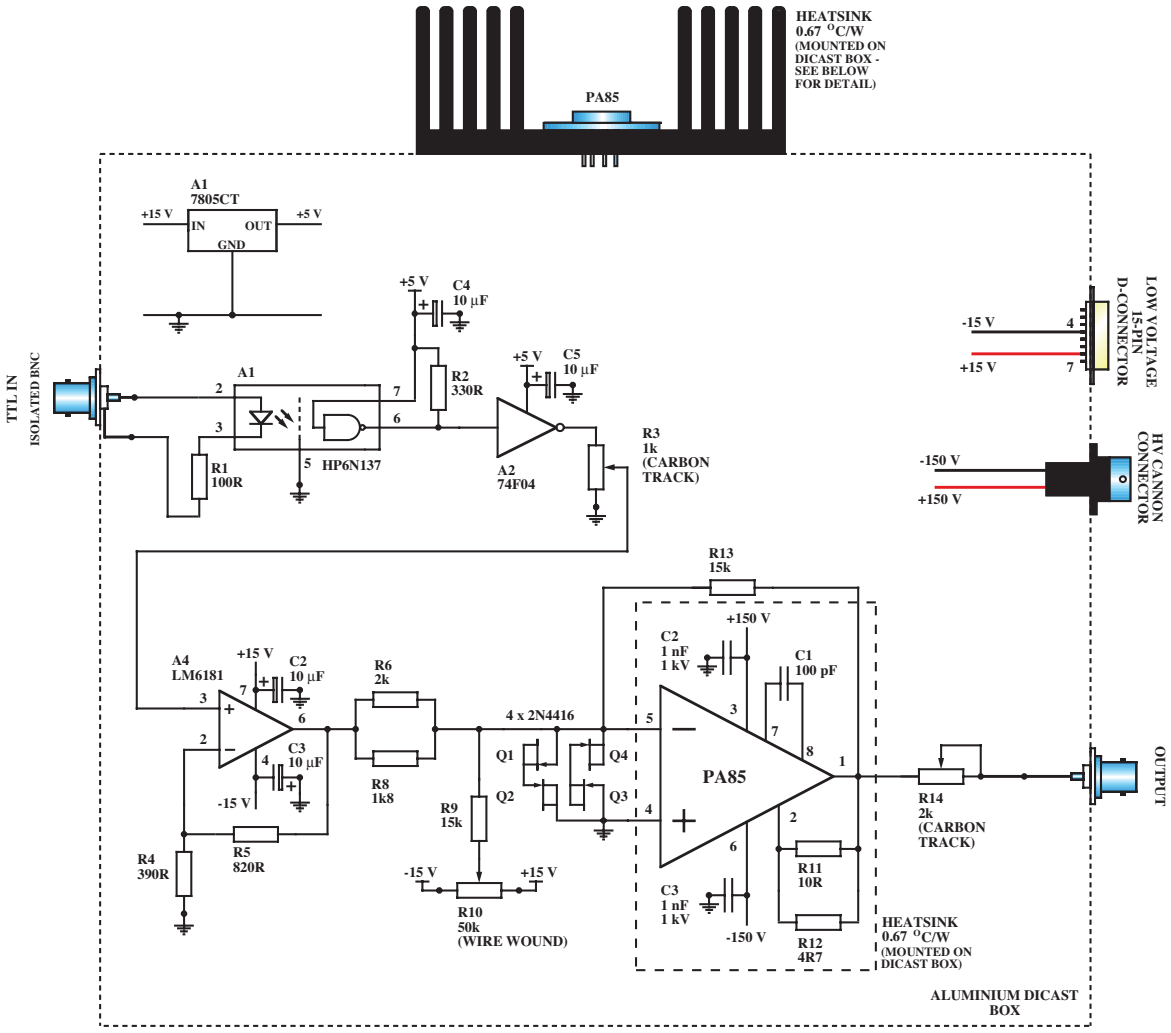

Fig 4.28: Schematic of the circuit used to generate the variable high voltage pulse for the EOMs. The circuit is based around a PA85 high voltage power amplifier which is capable of generating a negative pulse of ~ 140 V.

A detailed description of the design and workings of this pulsed high voltage switch is found in [32]. The output of the PA85 power amplifier is then a negative pulse. The PA85 power operational amplifier can be adapted to a number of applications requiring different output pulse shape by adjusting the values of the external compensation resistors and capacitors shown in figure 4.29. With these adjustments the high voltage output was set at

-125 V while the low voltage was at -15 V, and was used to drive the EOMs via a BNC cable connected to the monitor BNC shown in figure 4.29.

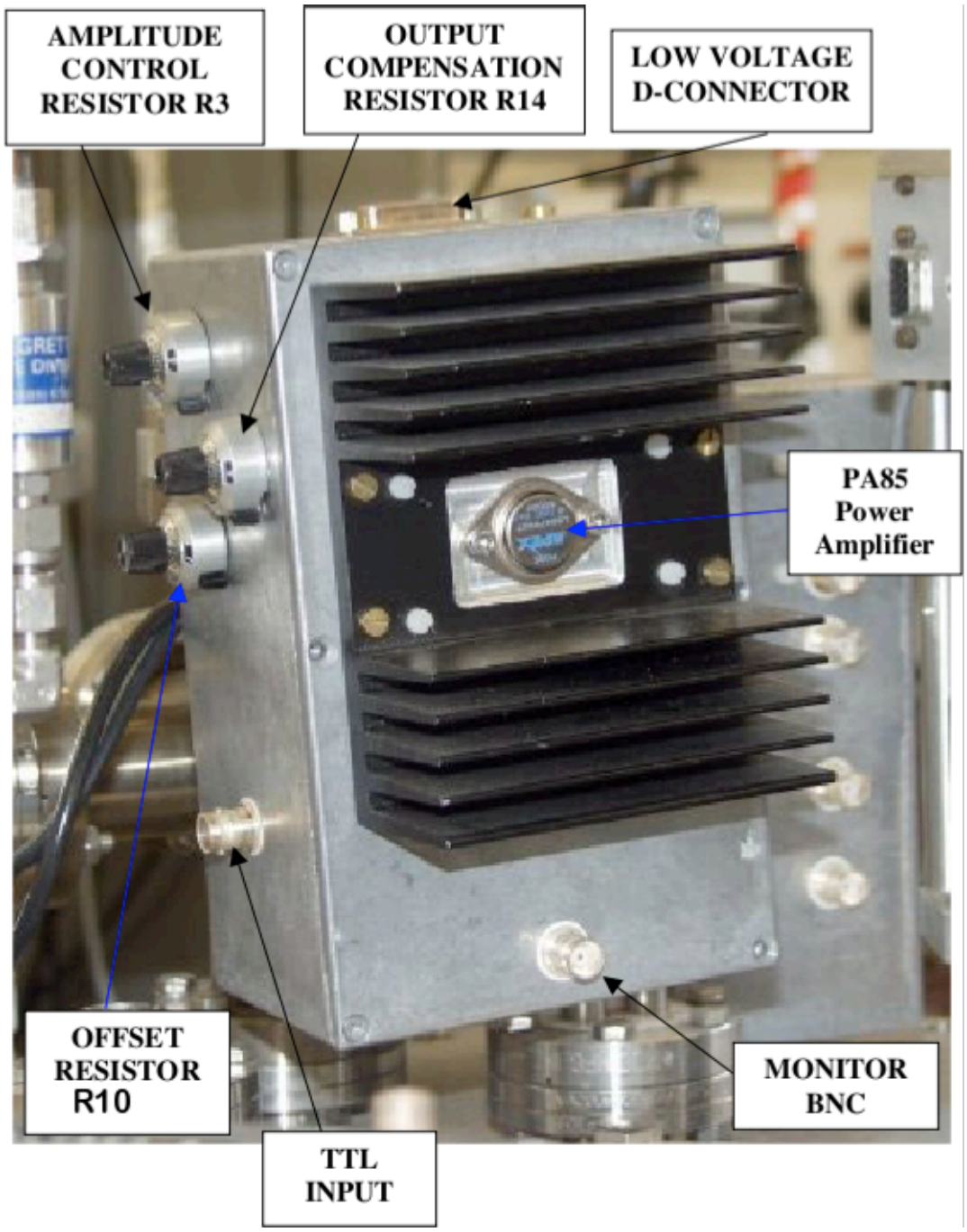

Fig 4.29: Photograph of the aluminium diecast box containing the PA85 amplifier circuit. The circuit is used to amplify the TTL signal of the same frequency as the AC-0MOT drive from the DAQ card into a variable amplitude negative voltage pulse (~ 0 V to – 140 V) for the EOMs. The PA85 is mounted on a 0.67° C W^{-1} heatsink to prevent overheating. The circuit is secured to the underside of the diecast lid using four nylon screws.

4.7 Conclusion

In this chapter, the major components used in the setup for trapping potassium atom in the AC-MOT have been described. These include the vacuum system and the techniques needed to produce the UHV condition required for the experiments. The atomic beam oven and its operating settings have been discussed. The Zeeman slower and the magnetic field profile needed to produce a beam of slow atoms for the MOT is detailed. The laser and the external locking systems, in addition to the optical setup used to create the different laser beams required to both slow and trap the atoms have been described. The additional apparatus used in the electron impact ionization, photoionization and high N – Rydberg studies are described in chapters 5, 6 and 7 respectively.

References

[1] Michael Lengden, Single-Colour and Two-Colour Laser Excitation of Atomic and Molecular Metastables Excited by Electron Impact, PhD thesis University of Manchester, 2006

[2] Pfeiffer vacuum Technology AG, Berliner Strasse 43, 35614 Asslar Germany

[3] Varian TV 301 Navigator ion pump http://www.chem.agilent.com/Library/usermanuals/Public/TV301%20Navigator%20Ops%20Man%20(M).pdf

[4] Varian Triscroll 300 backing pump http://www.chem.agilent.com/Library/usermanuals/Public/6999-04-265S%20TriScroll%20300%20Series%20Dry%20Scroll%20Vacuum%20Pump%20Installation%20and%20Operation%20Manual.pdf

[5] Varian VacIon pump, http://www.chem.agilent.com/Library/usermanuals/Public/VacIon%20Plus%20300%20pumps%20User%20Manual.pdf

[6] ThermoVacGenTi:Sub pump controller Manual http://www.thermovacgen.com/instructions.UI6200.pdf

[7] ThermoVacGen Ti:SubST22 cartridge operating instruction http://www.vgscienta.com/_resources/File/Manuals/Pumps_1/UI62494B_ST22%20Sub%20Pump.pdf

[8] Varian UHV-24 Ion gauge manual, http://www.chem.agilent.com/Library/usermanuals/Public/6999-05-505E%20UHV-24%20UHV-24p%20Ionization%20Gauge%20Instruction%20Manual.pdf

[9] Varian convector backing gauge manual, http://www.chem.agilent.com/en-US/products-services/Instruments-Systems/Vacuum-Technologies/ConvecTorr-Gauge-Tube/Pages/default.aspx

[10] Varian multigauge controller manual, http://www.chem.agilent.com/Library/usermanuals/Public/6999-08-091Y%20Multi%20Gauge%20Controller%20Instruction%20Manual.pdf

[11] Cooper P. S., *Magneto-Optical Trapping of Potassium from a Zeeman Cooled Collimated Atomic Beam* PhD thesis, University of Manchester, 2005

[12] Smee R.J. Design of a recirculating atomic beam. MPhys. Project Report, The University of Manchester, 2001.

[13] Patel K. Recirculating atomic beam source. MPhys. Project Report, The University of Manchester, 2001.

[14] D. Hickey. Project Report, The University of Manchester, 2001.

[15] R.E. Honig and D.A. Kramer, *Vapor Pressure Data for the Solid and Liquid Elements.* RCA Review 30 (1969): 285-305.

[16] Balykin, V. I., Letokhov, V. S., & Mushin, V. I. (1979). *Observation of the cooling of free sodium atoms in a resonance laser field with a scanning frequency.* Journal of theoretical and experimental Physics Letter, 29(10), 560-564.

[17] Phillips, W. D., & Metcalf, H. (1982). *Laser deceleration of an atomic beam.* Physical Review Letters, 48(9), 596.

[18] Schappe, R. S., Walker, T., Anderson, L. W., & Lin, C. C. (1996). *Absolute electron-impact ionization cross section measurements using a magneto-optical trap.* Physical review letters, 76(23), 4328.

[19] DuPont de Nemours International S.A., P.O. Box 50, CH-1218 Le Grand- Saconnex, Geneva, Switzerland,

[20] Vacuum Generators, Maunsell Road, Castleham Industrial Estate, St Leonards-on-Sea, East Sussex, TN38 9NN

[21] Matthew Harvey. PhD thesis, University of Manchester. 2009.

[22] Molenaar, P. A., Van der Straten, P., Heideman, H. G. M., & Metcalf, H. (1997). *Diagnostic technique for Zeeman-compensated atomic beam slowing: Technique and results.* Physical Review A, 55(1), 605.

[23] Prodan, J. V., Phillips, W. D., & Metcalf, H. (1982). *Laser production of a very slow monoenergetic atomic beam.* Physical Review Letters, 49(16), 1149.

[24] Coherent MBR-110Ti:Sapphire data sheet http://www.coherent.com/download/135/MBR-110-Ring-Laser-Data-Sheet.pdf

[25] http://www.coherent.com/download/6538/Verdi-Family-Data-Sheet.pdf

[26] Hänsch, T. W., Shahin, I. S., & Schawlow, A. L. (1971). *High-resolution saturation spectroscopy of the sodium D lines with a pulsed tunable dye laser.* Physical Review Letters, 27(11), 707.

[27] Mudarikwa, L., Pahwa, K., & Goldwin, J. (2012). *Sub-Doppler modulation spectroscopy of potassium for laser stabilization.* Journal of Physics B: Atomic, Molecular and Optical Physics, 45(6), 065002.

[28] http://www.thermocoax.com/pdf/E013_10_HE_English.pdf

[29] http://www.highfinesse.com/Brochure/LowRes/HighFinesseProductBrochure.pdf

[30] IntraAction Corp., 3719 Warren Avenue, Bellwood, Illinois 60104, USA.

[31] Lo, Y. L., & Hsu, P. F. (2002). *Birefringence measurements by an electro-optic modulator using a new heterodyne scheme*. Optical engineering, 41(11), 2764- 2767.

[32] Martyn Hussey. PhD thesis, University of Manchester, 2003

[33] Varcoe, B. T. H., Hall, B. V., Johnson, G., Johnson, P. M., MacGillivray, W. R., & Standage, M. C. (2000). *Long term laser frequency control for applications in atomic physics*. Measurement Science and Technology, 11(11), N111.

CHAPTER FIVE

Trapping ^{39}K in the AC-MOT

5.0 Introduction

The magneto-optical trap (MOT) is an important technique in the production of cold atomic ensembles. The low velocity of targets in cold atom collisions eliminates the complications associated with Doppler effects and makes experimental measurements more sensitive and effective [1]. With the trapped atoms as targets, the MOT opens up new research opportunities, these include the measurement of fundamental atomic properties such as electron impact [2] and photoionization cross sections [3], excited states lifetime measurements [4], and atom to atom interactions [5,6]. Cold atoms have been useful in the production of cold electrons [7], in the creation of Bose Einstein condensates (BEC) [8] and Fermi gases [9], and in the study of high-n Rydberg states of ultra-cold atoms [10].

The application of the MOT to studies involving collisions with charged particles has been hindered by the requirement in such interactions that any magnetic field is eliminated. This requires the trapping magnetic field to be switched off before such experiments can be reliably performed. Switching the MOT fields off (normally operated with a direct current, DC) off rapidly results in the production of eddy currents in the conductors in the vicinity of the trap. This generates further magnetic fields within the interaction region at the centre of the MOT, which also need to reduce to zero before experiments can be conducted. This requirement has prevented many experiments from being conducted with a DC-MOT.

One of the ways of determining the properties of atomic samples is to probe them with low energy electrons and ions, and investigate the dynamics of the resulting collision. Collision studies may involve the change in the momentum of the incident particle with no

change in the energy (elastic scattering), or may lead to the excitation or ionization of the target. In order to extract maximum information from the interaction, the incident charged particle must be of a well-defined momentum, and accurate measurement of the state and momentum of the outgoing products is necessary.

To employ the DC-MOT in collision studies requires the trapping magnetic field to be switched ON and OFF in a cycle, as illustrated in fig 5.1.

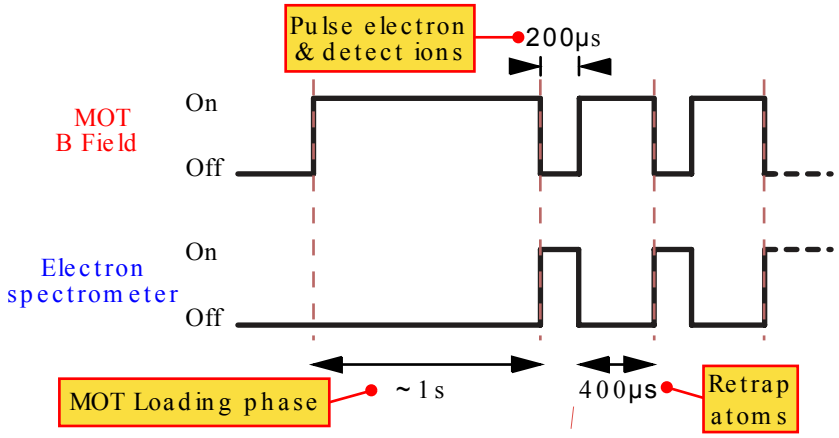

Fig 5.1: DC-MOT pulsing scheme for collision studies. The MOT B-field is pulsed for $200\mu s$ *after an initial loading time of* $1s$*. Since the fields can take up to 10ms to decay to acceptable levels, repetitive measurements are not possible since all the atoms will have drifted from the interaction region within a few cycles.*

While the DC-MOT traps atoms during the ON stage, collision studies cannot be carried out. According to Harvey et al [11], it takes the MOT magnetic field approximately 10 ms to reduce to less than 1 mGauss, as is necessary for most collision experiments with low energy electrons. This then restricts the rate of data acquisition to 50 Hz. Also within this time, a large fraction of the trapped atom will have escaped from the trap, and so this further reduces the number of atoms available for collision experiments. The decay time of the induced fields depends on several factors such as the resistivity, shape and proximity of the conducting material within the MOT chamber.

To address these limitations, which has hampered the wide spread adoption of cooled and trapped atoms as targets in collision studies, a new kind of MOT, driven with an alternating current was developed, the AC-MOT [11]. With the AC-MOT, it is possible to reduce the magnetic fields in the interaction region (including those due to eddy currents) to acceptable level in a time ≈ 500 times faster than with the conventional DC-MOT. In this way collision studies can be carried out with the trapped atoms in the MOT, without significant losses during the off time.

This chapter describes the procedure adopted in the trapping of ^{39}K in the AC-MOT. First, a brief description of the AC-MOT coils used to generate the trapping magnetic field is given. Secondly, the AC-MOT optical setup, including beam alignment procedures is discussed. Next the computer program used in the operation of the AC-MOT, and the real-time data acquisition system will be presented. This is followed by a brief discussion on the measurement techniques, with characteristics of the AC-MOT being described. Finally, results from electron impact ionization of the trapped atom will be presented showing the application of the AC-MOT to electron collision studies.

5.1 The AC-MOT Magnetic Field Coils

In most magneto-optical traps, the vacuum chambers are quite small and so the magnetic field coils can be located outside the vacuum chamber**.** In this configuration, the coils can be air-cooled and the outgassing of the coils does not contribute to the pressure in the vacuum chamber. The vacuum chamber used in this experiment has a diameter of 50 cm, and so the coils must be situated inside the chamber. The large vacuum chamber is needed to accommodate the charge particle spectrometer used during collision studies. The coil windings and the coil formers are therefore made from ultra-high vacuum compatible materials.

The MOT coils consist of a pair of circular coils arranged in an anti-Helmholtz configuration. In this arrangement (shown in figure 5.2), the coils carry equal but opposite currents and produce a field which is zero at the centre between the coils, but increases outwardly in all directions.

In the existing apparatus, each coil is made up of 184 turns of Kapton coated copper wire, wound around a former made from oxygen-free copper. As shown in figure 5.3, the formers are split to reduce the formation of eddy currents when current through the coils are switched on and off. The wires are covered with grounded molybdenum strips to prevent them electrostatically charging due to stray electrons during collision experiments. The coil geometry is chosen to ensure that the fields vary linearly within the interaction region which is defined by the six intersecting laser beams shown in figure 5.2.

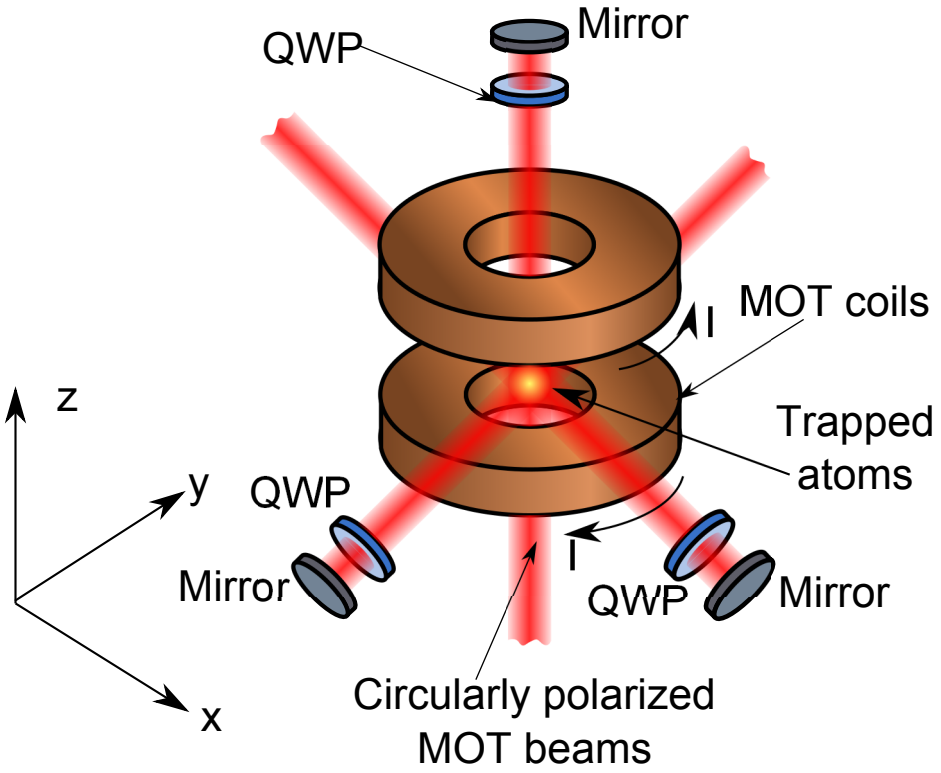

Fig.5.2: AC-MOT coils and circularly polarized trapping laser beams. Three orthogonal beams are retro-reflected by the mirrors to create the six MOT beams. Along each beam path is a quarter wave plate QWP, which gives the beam the correct circular polarization.

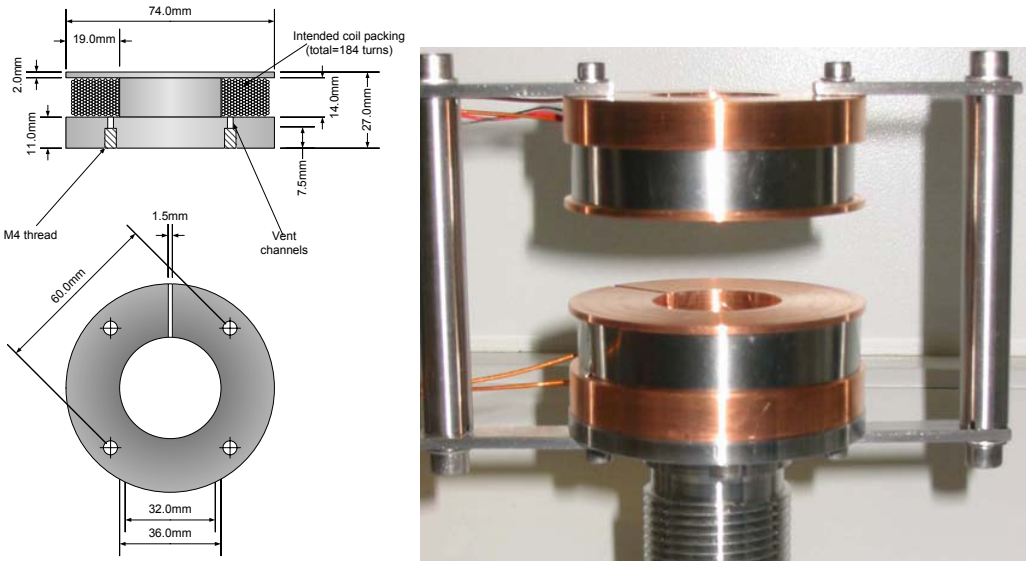

Fig 5.3: The AC-MOT coil design. The coils consist of 184 turns of Kapton coated copper wire covered with molybdenum strips to avoid electrostatic charging, wound on formers made from oxygen free copper. The formers are split to eliminate the formation of eddy currents within the copper.

5.1.1 AC-MOT Magnetic Field Profile

Consider a current carrying loop of radius R centered at $Z = Z_0$ and $\rho = 0$ in cylindrical polar coordinate as illustrated in figure 5.4. The components of the magnetic field along the longitudinal axis B_z and radial axis B_ρ are obtained by integrating the vector potential $\boldsymbol{A}$. Applying Maxwell's equation $\nabla \times \boldsymbol{A}$, the components are [12]:

$$B_z = \frac{\mu \mathrm{I}}{2\pi} \frac{1}{[(R+\rho)^2 + (z-z_0)^2]^{\frac{1}{2}}} \times \left(K(k^2) + \frac{R^2 - \rho^2 - (z-z_0)^2}{(R-\rho)^2 + (z-z_0)^2} E(k^2) \right), \tag{5.1}$$

$$B_\rho = \frac{\mu \mathrm{I}}{2\pi\rho} \frac{z-z_0}{[(R-\rho)^2 + (z-z_0)^2]^{\frac{1}{2}}} \times \left(-K(k^2) + \frac{R^2 + \rho^2 + (z-z_0)^2}{(R-\rho)^2 + (z-z_0)^2} E(k^2) \right), \tag{5.2}$$

where z and ρ are the longitudinal and radial displacements respectively, I is the current in the loop, and K and E are the elliptical integrals [13], whose argument is given by

$$k^2 = \frac{4R\rho}{(R+\rho)^2 + (z-z_0)^2} \tag{5.3}$$

Using equations 5.1 and 5.2, different models of the anti-Helmholtz coils with different number of turns, radii and coil separations were tested [14]. Each set of MOT coils used in this experiment were wound on a 36 mm diameter formers, and contained 16 layers of coils as shown in figure 5.3.

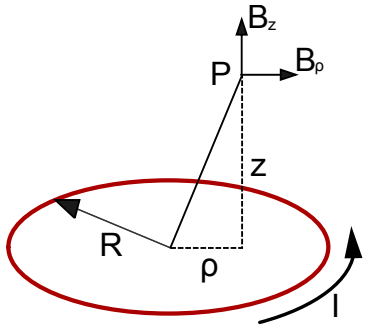

Fig.5.4: Illustrating the magnetic field component at a point p due to a current carrying loop. ρ is the radial displacement and z is the longitudinal displacement from the center of the coils.

The number of rows in each layer alternates between 12 and 11 rows making a total 184 winding on each former. Each of the MOT coils therefore contains 62.4 m of wire.

To create space for the trapping laser beams, the coils are separated by 24 mm. At this separation, the field gradient has a higher maximum value at the boundary of the interaction region than the maximum value obtained when the coils were separated by a distance $x = \sqrt{3}R$, (the ideal condition for a uniform gradient in Helmholtz coils), where R is the radius of the circular coils [14]. The longitudinal (on-axis) component of the field gradient is 25.1 Gauss/cm and 22.4 Gauss/cm at extremities of the trapping region; this is $\approx 90\%$ of the on-axis value and is therefore considered fairly uniform and sufficient for the trapping experiment.

The magnetic field in the ρz plane produced by this configuration is shown in figure 5.5, with a contour spacing of 5 Gauss/Ampere. As expected, the magnitude of the field is zero at the center between the coils and has a maximum value near the inner surface of each coil. At a typical AC-MOT operating current $I_{rms} = 0.68\,A$, the on-axis magnetic field gradient is 15 Gauss/cm and the coils reach a temperature of ~35℃. This temperature does not cause any significant outgassing during operation of the experiment.

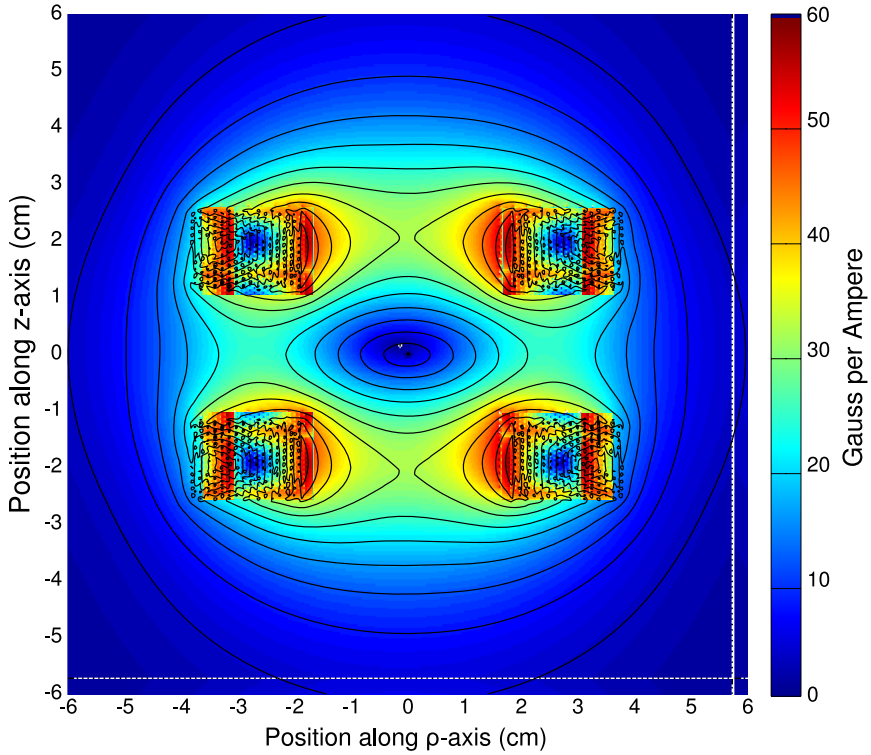

Fig.5.5: The magnetic field pattern produced by the AC-MOT coils along the ρz plane. The rectangular concentration of the contour lines indicates the points where the plane cuts through both MOT coils. The separation of the contour lines is 5 Gauss per Ampere.

5.2 Rapid Switching of the DC-MOT Current

As mentioned earlier, using a DC-MOT for collision studies requires the field to be pulsed to allow the magnetic field to decay to an acceptable level. This section discusses the implication of rapid switching (pulsing) of the DC-MOT magnetic field with a square wave voltage signal, and why the DC-MOT is not suitable for collision experiment involving charged particles.

Consider the MOT coils inside the MOT chamber as an inductive circuit with inductance L and resistance R. The response of the circuit is then described by the equation

$$V_s - IR - L\frac{dI}{dt} = 0 \tag{5.4}$$

where I is the current in the coils, and V_s is the voltage applied across the coils. If the voltage is abruptly switched to zero from a steady state value V_{ss}, then equation 5.4 will have a solution

$$I(t) = \frac{V_{ss}}{R} e^{-\frac{R}{L}t}\,, \tag{5.5}$$

Equation 5.5 indicates that the current will decay exponentially with a time constant $\tau = \frac{L}{R}$. Different fast switching methods were used to study the effect of switching a conventional DC-MOT field suddenly to zero [14], and measuring the magnetic field at various locations within the MOT chamber as the field decays. The results are shown in figure 5.6. This figure shows that the magnetic field at the MOT coils closely follows the current through the coils, while the field at other locations within the chamber had a much slower rise and decay time. This difference in rise and decay times is a result of eddy currents induced in the conductors in the chamber. These results show that it is not possible to pulse the MOT field using a square wave signal as illustrated in figure 5.1, because of the induced eddy current in the conductive components in the MOT chamber. The model described by equation 5.5, hence fails to take into account other conducting material in the vicinity of the MOT coils.

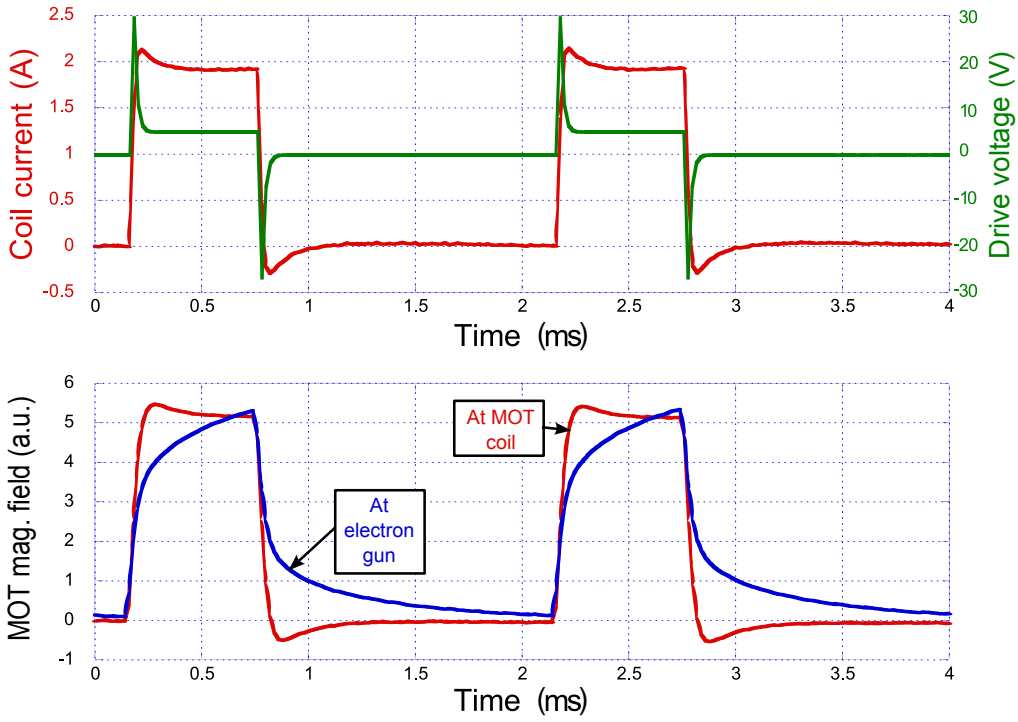

Fig 5.6: Current – field relation for a pulsed DC-MOT. (a) Shows the drive voltage and the current through the MOT coils. (b)The measured magnetic field near one of the coils, (red traces) and at the electron gun (shown in blue). The difference in the rise time at the two locations is due to eddy current induced in the surrounding conductors in the MOT chamber.

5.2.1 The MOT Coils Coupled Inductively to Other Conductors

Now consider the MOT coils inductively coupled with other conducting components in the MOT chamber including the ion detector, electron gun, MOT support and the metal vacuum chamber as shown in figure 5.7. The response of each conductor can then be described by the equation

$$V_s - I_M R_M - L_M \frac{dI_M}{dt} + \sum_i M_i \frac{dI_i}{dt} = 0 \tag{5.6}$$

where I_M is the current through the coupled components, and R_M and L_M are the resistance and inductance of these components respectively. The mutual inductance that represents the conductor couplings together with the resistance and inductance, and the current through each conductor are represented by M_i and I_i respectively.

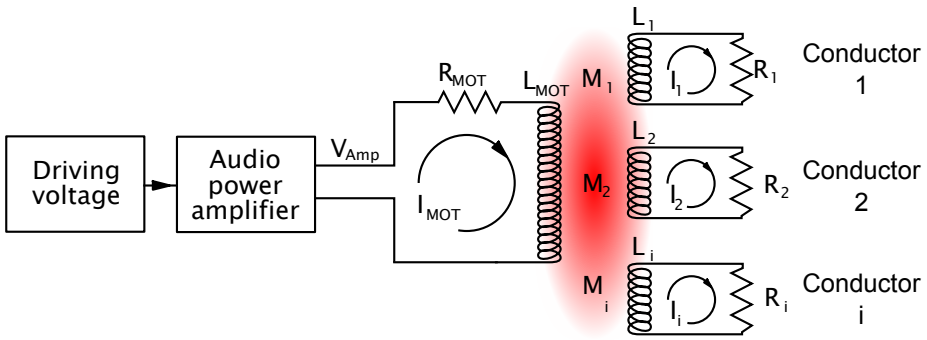

Fig 5.7: Model of the MOT coils coupled by mutual inductance to other conducting components in the MOT chamber.

In order to obtain an analytical solution to this problem, the equations are decoupled by assuming a weak mutual inductance between the conductors, so that equation 5.6 reduces to

$$V_s - I_M R_M - L_M \frac{dI_M}{dt} \approx 0 \tag{5.7}$$

where V_s the voltage is across the coils, I_M is the current through the coils, while R_M and L_M are the resistance and inductance of the coils respectively shown in fig 5.7.

Also from equation 5.6,

$$M_i \frac{dI_M}{dt} - I_i R_i - L_i \frac{dI_i}{dt} \Leftrightarrow V_{eq} - I_i R_i - L_i \frac{dI_i}{dt} = 0 \tag{5.8}$$

Where M_i is the mutual inductance between each conductor and the MOT coils, and I_i is the induced current in each conductor. L_i and R_i are the inductance and resistance of each conductor as shown in fig 5.7.

With the MOT coils now coupled with other conductors in the chamber, switching the current rapidly is again attempted. As described in [14], a metal oxide semiconductor field effect transistor (MOSFET) through a simple feedback loop was used to provide a current through the MOT coils. At switch off (the MOSFET was shut off), the resistance of the coils circuit is effectively increased, thereby reducing the time constant τ.

A system in steady state with $V_s = V_{ss}$ (constant current I_{ss}), will induce no eddy current in the conductors. Switching this to $V_s = 0$ at $t = 0$, will cause eddy currents to be induced. In this case, equation 5.7 will have the solution

$$I_M = I_{ss} e^{-t/\tau_M} \tag{5.9}$$

where $\tau_M = \frac{L_M}{R_M}$ and $I_{ss} = \frac{V_{ss}}{R_M}$.

To get an expression for the induced current I_i, equation 5.9 is substituted into equation 5.6, and simplified to give [13]

$$I_i = -\frac{M_i I_{ss}}{R_i}\left(\frac{1 - e^{-\frac{t}{\tau_i}}}{\tau_M - \tau_i}\right) \tag{5.10}$$

where the experimentally measured value of $L_M \approx 3mH$ has been used. This result is illustrated in figure 5.8, and shows that while the current through the MOT coils can be rapidly reduced to zero (blue trace), the induced eddy currents take a much longer time to decay (red trace). Switching off the current through the MOT coils rapidly from a steady state value does not lead to a rapid switch off of the eddy currents.

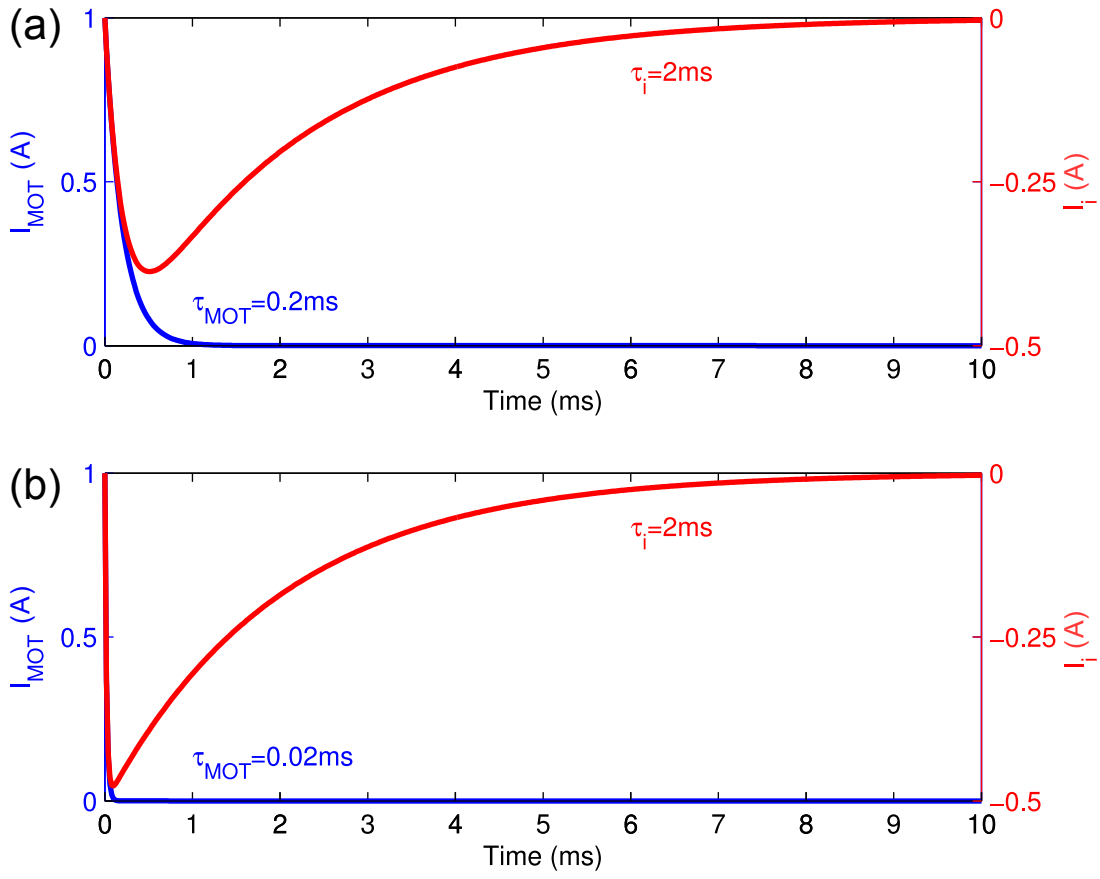

Fig 5.8: A plot of the current through the MOT coil I_{MOT} and the induced eddy current I_i at switch off for a DC supply. In (b) the resistance of the MOT coil was increased by a factor of ten. This is equivalent to a fast switching process using the MOSFET switch. This results in the MOT current decaying ten times faster, but it has no effect on the induced eddy current decay rate.

In the apparatus used in this experiment it is only after $\approx 10\,ms$ that this field is reduced to a level that allows electron collision experiments to be conducted. As noted above, most

of the atoms in the trap will have escaped during that time, making most collision experiments of high accuracy unfeasible.

5.3 Driving the MOT with a Sinusoidal Varying Voltage Signal - The AC-MOT

Suppose a sinusoidal varying voltage $V_s = V_0 \sin(\omega t + \varphi)$ (where $V_{0,} \omega \; and \; \varphi$ are the amplitude, frequency and phase of the drive voltage signal respectively) is adopted instead in equation 5.6. Following the above steps, and again assuming a weak coupling between the conductors and the MOT coils, an expression for the MOT current I_M and the induced eddy current I_i can be derive as detailed in [10];

$$I_M = \frac{V_0}{R_M}\left(\frac{\sin(\omega t + \varphi) - \omega\tau_M \cos(\omega t + \varphi) + e^{-t/\tau_M}(\omega\tau_M \cos\varphi - sin\varphi)}{1 + \omega^2\tau_M^2}\right) \qquad (5.11)$$

The induced eddy current in each of the conductors within the MOT chamber is then given by

$$I_i(t, \varphi)$$
$$\approx \frac{M_i V_0}{R_M R_i \tau_i}\left(\frac{\omega\tau_i \cos(\omega t + \varphi) + \omega^2\tau_i^2 \sin(\omega t + \varphi) - e^{-t/\tau_i}(\omega\tau_i \cos\varphi - \sin\varphi)}{1 + \omega^2\tau_i^2}\right) \qquad (5.12)$$

where it has been assumed that the response time of the MOT coils are much faster that the response time of the conductors i.e. $\tau_i \gg \tau_M \cong 0$.

For a phase angle φ such that

$$\omega\tau_i \cos\varphi = \sin\varphi \implies tan\varphi = \omega\tau_i \qquad (5.13)$$

the transient exponential term in equation 5.12 is eliminated, making the induced current purely sinusoidal, and so the induced current in the conductors follows the current through the MOT coils as shown in figure 5.9. At a typical operating frequency of 5 kHz, the phase angle needs to be set to 78° (as obtained from experiment). At this angle, the induced eddy current and the current through the MOT coils are perfectly in phase and so they both go to zero at the same time. Driving the MOT coils with a sinusoidal varying voltage signal therefore eliminates eddy currents and the corresponding magnetic fields due to switching transients once the drive current is set to zero.

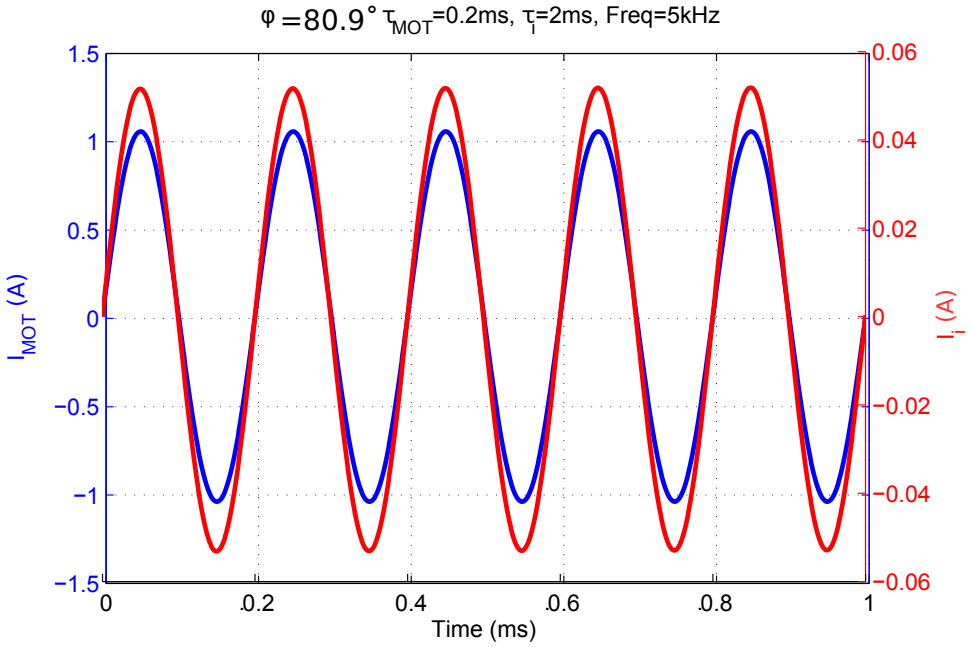

Fig 5.9: A plot of the current through the MOT coil I_{MOT} (blue trace) and the induced eddy current I_i (red trace) at switch off for an AC supply with a phase angle $\varphi = \arctan(\omega\tau_{MOT})$. The current through the coils and the induced eddy current both go to zero at the same time and so transient field at switch off are eliminated.

5.4 The AC-MOT Optical Setup

The optical setup for an AC-MOT differs from that of a DC-MOT. This section summarizes the AC-MOT optical setup, which includes the control, polarization and alignment of the MOT beams. The setup is shown in figure 5.10.

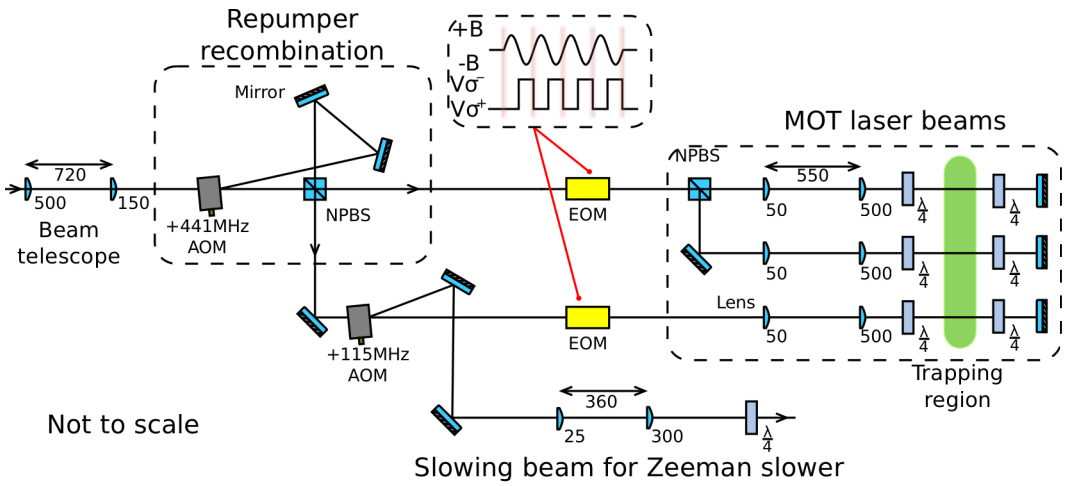

Fig 5.10: The optical setup of the AC-MOT. The EOMs are included to switch the polarization of the laser beams in synchronicity with the alternating trapping magnetic field in the AC-MOT.

5.4.1 The MOT Laser Beams

All the laser beam used in the trapping experiments, including the Zeeman slower beam were created from the output of a Coherent MBR-110 Ti:Sapphire (Ti:S) tunable ring laser

as was described in section 4.6. As shown in figure 5.10, the main beam from the laser system was focused down and collimated using two lenses in order to fit through the aperture of the 441 MHz acousto optic modulator (AOM). This AOM shifted off a +441 MHz repump beam from the main beam, which was then added to the unshifted beam in the recombination stage to produce two beams containing both frequencies that are required for the cooling and trapping of ^{39}K. Although the number of atoms in the trap increases with increasing power of the re-pump beam, it also leads to an increase in the temperature of the atomic cloud [14]. Hence to provide a compromise between the number of trapped atoms and their temperature, the repump beam was set to contribute about 30% of the total beam intensity by adjusting the driving power of the AOM. One of the beams from the recombination stage passed through electro optic modulator (EOM)1 to a non-polarizing beam splitter to produce two beams, which were then retro-reflected after going through the MOT chamber to create four of the MOT beams. The other beam from the recombination stage passed through another AOM (115 MHz AOM), which shifted off a 30 mW (shifted by +115 MHz) beam that formed the Zeeman slower beam. This beam was focused at the oven aperture using two lenses and was circular polarized by passing it through a quarter wave plate (QWP). The unshifted beam went through EOM2 and was then retro-reflected after passing through the interaction region to form the final two MOT beams. All the beams passed through QWPs to give them the appropriate circular polarization. The two lenses in the path of each of the MOT beams were used to expand and collimate the beams.

The EOMs are essential to the operation of the AC-MOT because they are used to switch the polarization of the trapping laser beams in synchronicity with the changing sign of the magnetic field in the MOT. The polarization switching is accomplished by the application of an electric field across the electro-optic (EO) crystal. This induces a change in the indices of refraction of the crystal resulting in a birefringence that depends on the applied electric field. This then changes the polarization state of the laser beam. Since the the EO crystal acts as a variable wave plate whose retardation depends linearly on the applied electric field [15], it therefore has a zero waveplate voltage V_0 and a half waveplate voltage $V_{\frac{\lambda}{2}}$.

The EOMs used in this experiment are Conoptics Coporation 360-80 and 360-81 EOMs, which have a $V_0 = -15V$ and $V_{\frac{\lambda}{2}} = -125V$. This half wave plate condition was achieved when the optical axis of the EO crystal was oriented at $45°$ to the polarization axis of the laser beams. The field direction, and the QWP settings determine which of these voltage is

applied across the EO crystal when the AC-MOT field is of the same sign as the DC-MOT, and when the field changes sign, the other voltage is applied across the crystals. In this way, the AC-MOT traps atoms during both half cycles of the AC field. The EOMs were driven with the same frequency as the AC-MOT drive signal as described in section 4.6.3.

5.4.2 MOT Beam Intensities and Alignment

The reflective losses associated with different optical components reduces the effective laser intensity at the interaction region. The beams lose 2.5% on the QWPs, 8.5% on each uncoated window of the chamber, 8.5% each lens, 1% on each infra-red mirror and 25% on any silver coated mirror. These losses were considered in the quoted MOT laser beam intensities. The intensity of the pair of counter-propagating laser beams along the y–axis (right hand side with respect to the wide window of the MOT chamber through which the trap is usually monitored) was $\sim 192\, mWcm^{-2}$, for the z-axis (vertical), the intensity was $\sim 120\, mWcm^{-2}$ and the intensity was $\sim 113\, mWcm^{-2}$ for the beams along the x-axis (left hand side beam wrt the same window) as illustrated in figure 5.2.

The MOT beams have a total intensity of $\sim 425\, mWcm^{-2}$ of which $\sim 127\, mWcm^{-2}$ is from the re-pump beam. The power of the left hand beams was balanced with the others, by placing a 2X neutral density filter before the beams enter the MOT chamber. This did not have significant effect on the brightness of the MOT, and so was removed.

Proper alignment of the MOT beams is crucial in the realization of the MOT, as it was observed that slight misalignment of any one of the MOT beams resulted in the loss of the MOT cloud. During alignment, the beams were made to pass through a 1 cm aperture placed centrally over the windows of the MOT chamber. They were then steered by mirrors until they passed through the centre of the window on the opposite side of the chamber, and the retro-reflected beam was then overlapped with the incident beam. Care was taken not to exactly retro-reflect the beams, as this sends light back into the laser system, which makes the laser unstable. Owing to fluctuations in the room temperature and the long path length from the laser table to the experiment, re-alignments of the beams was sometimes required to optimize the trapping conditions.

5.5 Operating the AC-MOT

Most aspects of the experiment were controlled by a computer based control system. The computer control system consisted of a Window 7 PC with an installed National Instrument PCI-6221 data acquisition card which has a sample rate of 500 kHz. The card has 24 digital I/O connections, 16 Analogue to Digital Inputs (ADCs) and 2 analogue output ports. All the waveforms signals required to control different aspects of the experiment, including the photoionization and high-n Rydberg studies, were generated by the DAQ card controlled by a LabVIEW program developed for this experiment. In addition to recording the signal from the photodiode, the DAQ card also recorded and stored time of flight ion signal data from both the photoionization and the high-n Rydberg studies. The program provided a graphic interface, which made it possible for the experiments to be monitored in real time. It could also be set to automatically trigger different processes, such as switching on the ionizing laser or pulsing the Zeeman slower field. Figure 5.11 shows the layout of the control system, and a screen shot of the user interface of the control program is shown in figure 5.12.

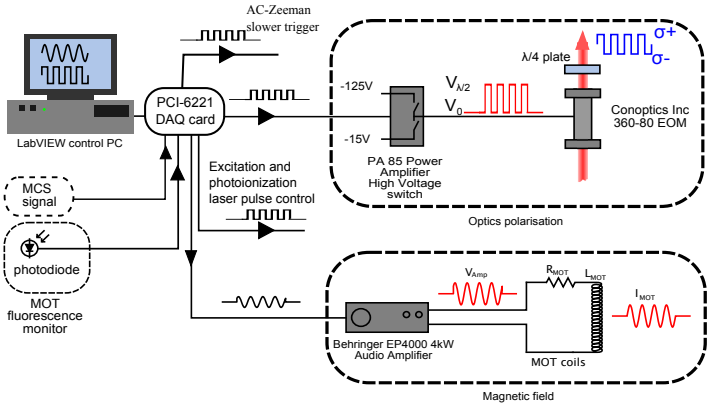

Fig 5.11: AC-MOT control setup. The PCI-6221 DAQ card generates all the waveforms required to control the experiment. Signals from the photodiode and multichannel scaler were acquired and displayed on the screen for real time monitoring of both the MOT intensity and the ionization signal during collision experiments.

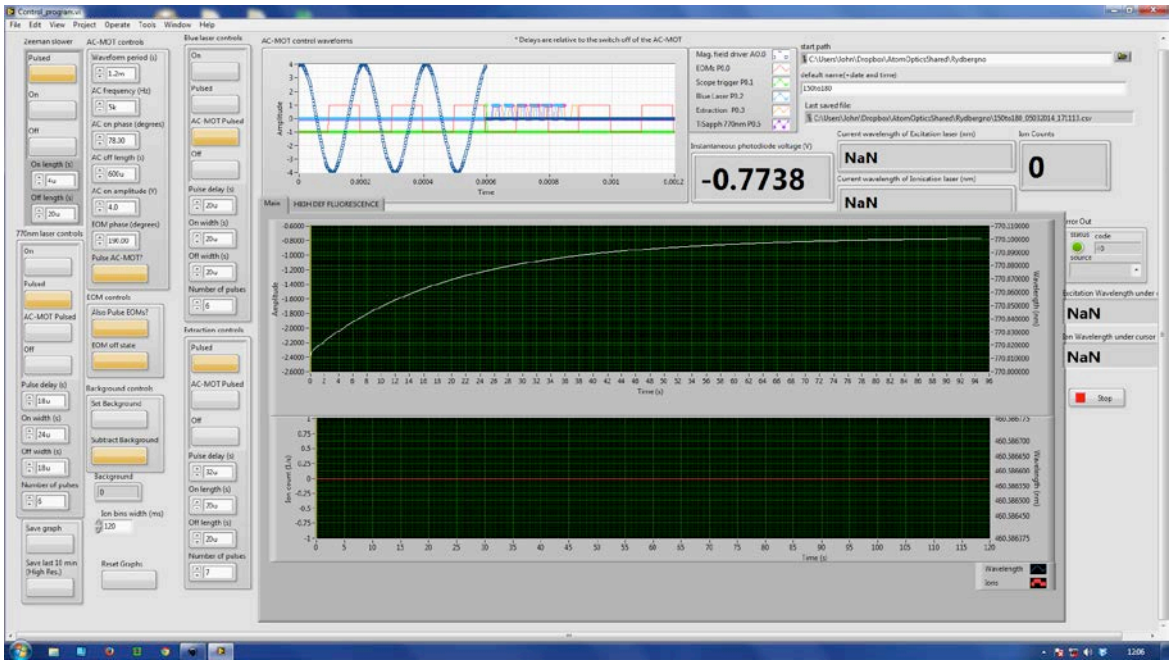

Fig 5.12: A screen shot of the front panel of the AC-MOT control program. This program generates the AC-MOT and the EOM drive signals (analogue signal out), and the digital signals which include the photoionization pulsing signals, as well as TTL pulses for the electron gun and extraction field and MCS trigger pulses (see chapter 6 and 7). The acquired signals from the photodiode and the ion detector were also displayed in both numeric and graphical forms on the front panel.

5.5.1 The AC-MOT Voltage Signal

The drive voltage signal for the AC-MOT was generated by the DAQ card and inputted into a Behringer EP4000 audio amplifier [16]. The output of the amplifier was connected in series with the MOT coils and a 0.1Ω resistor, which served as a sense resistor. The sense resistor was used to monitor the shape and magnitude of the current through the MOT coils. Monitoring the shape of the current through the coils was useful especially during the optimization of the drive waveform parameters in order to generate an integral number of half cycles, as required to eliminate transient behaviour.

As noted above, choosing a phase angle for the drive signal that gives an integral number of half cycles is a necessary condition to eliminate the effect of eddy currents when the current through the coils switches sign. The AC-MOT can be operated in continuous or pulsed mode. Since scattering experiments are carried out when the field is off, the AC-MOT was operated in pulsed mode during those experiments, as illustrated in figure 5.13.

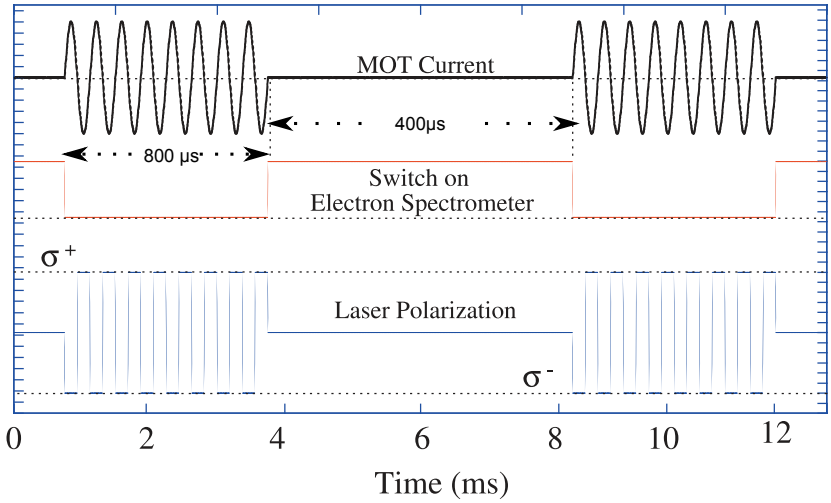

Fig 5.13: The AC-MOT pulsing scheme (not to scale). In every cycle the field was on for $800\ \mu s$ *and off for* $400\ \mu s$*, giving each cycles a period of* $1.2\ ms$*. All collision experiments, including photoionization and ion extraction experiments were synchronized to occur during the* $400\ \mu s$ *zero field regions.*

5.5.2 The EOM Drive Signal

The EOM drive signal is a TTL voltage signal with the same frequency and period per cycle as the AC-MOT drive signal. The signal was ~190° out of phase with the AC-MOT field because of the orientation of the quarter wave plates. This signal was used as input to the PA85 power amplifier as shown in figure 4.29, which then provided the zero and half wave voltages needed to switch the polarization of the trapping laser as was described earlier in chapter four.

5.5.3 The AC-MOT Settings

The AC-MOT was loaded from a precooled beam of atoms emitted by the Zeeman slower. The optimal Zeeman slower current settings used in these experiments are listed in table 4.3. Except where otherwise stated, the AC-MOT settings listed in table 5.1 were used

Oven operating temperature	$\sim 473\ K (200℃)$
Amplitude of AC-MOT drive voltage	$4V$
AC field frequency	5 kHz
AC field ON time	$800\mu s$
AC field OFF time	$400\mu s$
AC phase	78°
EOM phase with respect to MOT field	190°
Magnetic field gradient	$\sim 15\ Gcm^{-1}$
Typical pressure in MOT chamber	$\sim 6 \times 10^{-10} Torr$

Table 5.1: AC-MOT operational setting. The AC-MOT drive voltage stated here is the amplitude of the drive signal from the DAQ card, which serves as input to the audio amplifier. The actual current through the coils depends on the setting of the amplifier. The AC-MOT phase is set to ensure that the current through the coils is zero when the driving voltage is switched off so that eddy currents are not induced. At the current orientation of the quarter wave plates, the EOM signal was 190° *out of phase with the trapping field.*

5.6 Measurement Techniques

An important aspect of laser cooling and trapping experiment is the characterization of the trap. This involves the determination of the temperature of the trapped atoms, the atomic cloud density, the number of trapped atoms and the trap lifetime, amongst other properties. These characteristics depend on the AC-MOT parameters, which include the intensity, size and detuning of the trapping laser beams, the intensity of the re-pump beam and beam alignment. Other factors that may affect the MOT characteristics are the temperature of the atomic beam oven, the base pressure in the MOT chamber, and the Zeeman slower settings. Several techniques are therefore required to measure these properties. This section discusses the techniques adopted in the characterization of potassium atoms in the AC-MOT.

5.6.1 Imaging Technique

Some properties of the trap can be determined by the observation of the fluorescence from the excited atoms in the trap. These include the trap shape and size, lifetime measurements, temperature determination, estimation of the number of trapped atoms and the density of the atomic cloud. In these experiments, a charge coupled device (CCD) camera was used to monitor the size, shape and position of the MOT. This camera gives a real time observation of the MOT and was very useful during alignment of the MOT. For a three dimensional profile of the MOT, a Thorlab camera beam profiler BC106-VIS operating within a wavelength range of 350 – 1100 nm was used. The 2-D and 3-D images of the trapped atoms captured with the BC106-VIS beam profiler are shown (in arbitrary units just for illustrative purpose) in figure 5.14.

For a more quantitative monitoring of the behaviour of the MOT, the fluorescence from the MOT was focused with a lens onto an infrared photodiode. A 50 mm focal length lens of radius 20 mm was mounted in front of the main window of the vacuum chamber to project an image of the trapped atoms onto the photodiode. Assuming an isotropic emission of fluorescence from the MOT, the fraction of fluorescence from the MOT input to the photodiode F, is given by

$$F = \frac{\pi r^2}{4\pi R^2}\,, \tag{5.14}$$

where r is the radius of the lens and R is the separation between the lens and the MOT.

The lens was separated from the MOT by a distance of 27 cm, and so for this configuration, the fluorescence detection fraction was $\cong 0.137\%$ of the total fluorescence emitted by the MOT.

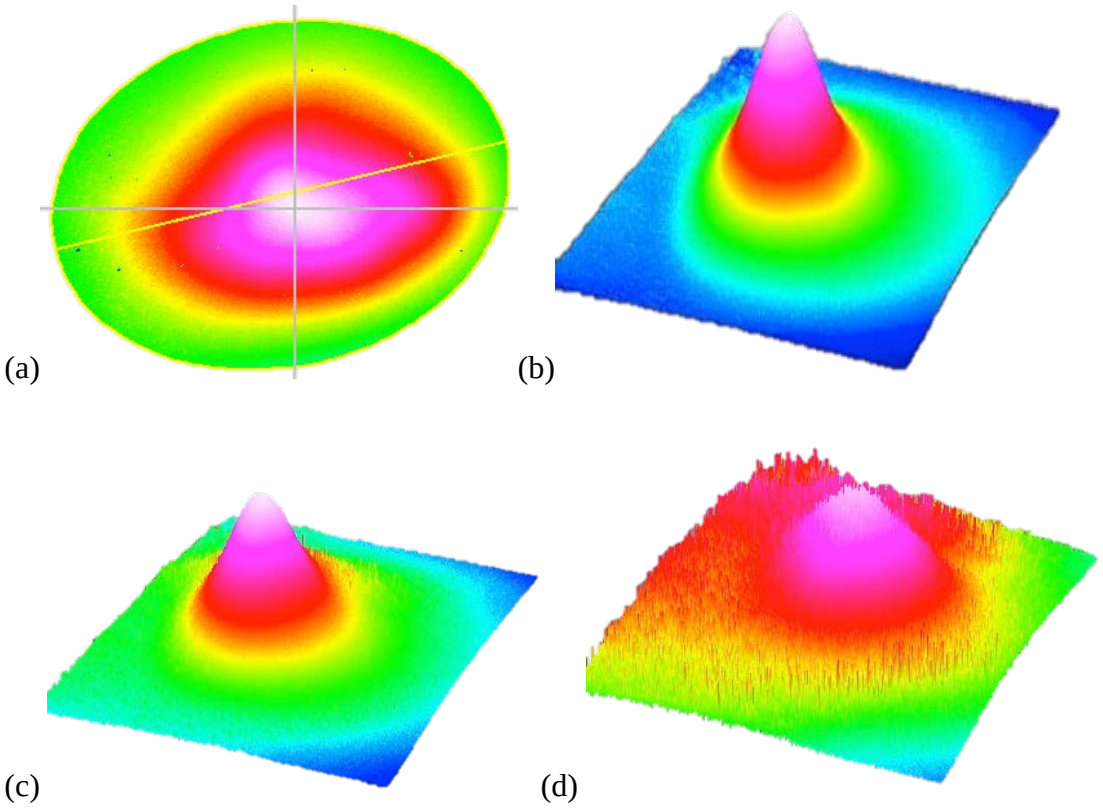

Fig5.14: Images of trapped atoms as captured by the beam profiler BC106-VIS. a & b shows a 2-D and 3-D image of the trap before decay, and c & d show the expanding atomic cloud as the trap decays.

The data from the photodiode provides a real time measurement of the MOT intensity, and was very useful during experiments to measure loading and decay lifetimes of the MOT. The photodiode signal was calibrated using a calibrated power-meter, and so the output of the photodiode was used in the estimation of the number of trapped atoms. During photoionization experiments as discussed in chapter six, the output of the photodiode was used to trigger the switching of the photo-ionizing laser, when a set threshold fluorescence level was reached. This was used to probe and ionize different parts of the MOT as a function trapping time.

5.6.2 Estimating the Number of Atoms in the MOT

Since the photodiode was calibrated, the signal was used to estimate the number of atoms in the trap. Assuming the trapped atoms emit radiation equally in all directions, and the effect of radiation trapping is neglected, the number of trapped atoms N is related to the power P of the emitted fluorescence measured at the photodiode by [17]

$$N = \frac{P}{\Gamma_p \hbar \omega F} \tag{5.15}$$

where F is the fluorescence detecting fraction of the imaging optics, $\hbar\omega$ is the energy of each emitted photon, and Γ_p is the scattering rate of photons from the MOT. For a two-level atom, the scattering rate is given by

$$\Gamma_p = \frac{\Gamma S_0/2}{1 + S_0 + (2\delta/\Gamma)^2} \tag{5.16}$$

where Γ is the natural line-width of the $4^2P_{3/2}$ excited state, S_0 is the on resonance saturation parameter, and δ is the detuning of the trapping laser from resonance. For a typical AC-MOT operating with a trapping laser of total intensity of $424\ mWcm^{-2}$, and red detuned by $\sim -4\Gamma$, the AC-MOT trapped $\approx 4.09 \pm 0.03\ \times 10^8$ atoms.

5.6.3 Estimating the Temperature of the MOT

There are several techniques that can be used to estimate the temperature of atoms trapped in a MOT, amongst which are the release and recapture method (R&R) [17] and the time of flight (TOF) [18] technique. The R&R method relies on the ballistic expansion of trapped atoms in the absence of the trapping laser beam. Atoms in the trap then move freely in all direction with a velocity that depends on their mean temperature, and given sufficient time the atoms can move out of the interaction region and be lost from the trap. In this experiment, the release and recapture (R&R) method was used to estimate the temperature of the MOT. In this technique, the atoms are momentarily set free from the optical molasses force by rapidly switching the trapping laser off for a time Δt (light-off time), and the atoms then move freely out of the trap with no damping force. The rate at which atoms escape from the MOT depends on their kinetic energy, which is then related to the temperature. The trapping laser was switched back on after Δt (in milliseconds) and all atoms within the capture region were then recaptured and trapped.

Since only atoms that have sufficient energy can escape the trap during the switch off period, the velocity (temperature) of the atoms can be inferred from the percentage of atoms remaining after the R&R cycle. The velocity of atoms necessary for atoms to escape the interaction region depends on the light-off time, and the size of the interaction region.

During the release, atoms with sufficient speed will reach the edge of the interaction region defined by the intersection of the trapping laser beams of beam width ~ 1 cm,

before the trapping lasers are switched on again. The atoms that are beyond the trapping lasers were therefore lost from the trap. The fraction of atoms remaining after the light was turned on again, as measured by the fluorescence signal, gives a measure of the temperature of the cloud. The expansion of the atomic cloud during this process is shown in figure 5.14. Assuming a Maxwell-Boltzmann distribution of velocities in the atomic cloud, the radius of the atomic cloud after the light-off time Δt would become

$$\sigma_1 = \sigma_0 + v_p * \Delta t \tag{5.17}$$

where σ_0 is the radius of the cloud in the steady state before the light was switched off. The most probable speed of the atoms v_p is given by

$$v_p(T) = \sqrt{\frac{2k_B T}{m}} \tag{5.18}$$

where k_B is Boltzmann's constant, m is the mass of the atoms and T is the temperature.

Using equations 5.17 and 5.18, and assuming a uniform cloud density, the temperature of the atomic cloud can be expressed as [19]

$$T = \frac{m}{2k_B}\left[\frac{\sigma_0}{\Delta t} * \left\{\left(\frac{N_0}{N_1}\right)^{1/3} - 1\right\}\right]^2 \tag{5.19}$$

Where N_0 is the number of atoms before light-off and N_1 is the number of atoms remaining in the trap after the light was switched on again.

Since only a maximum of 50% of atoms can be in the excited state, (photons are emitted on average once in two lifetimes), and the number of atoms N is proportional to the detected fluorescence signal, equation 5.19 can be modified as

$$T = \frac{m}{2k_B}\left[\frac{\sigma_0}{\Delta t} * \left\{\left(2\frac{U_0}{U_1}\right)^{\frac{1}{3}} - 1\right\}\right]^2 \tag{5.20}$$

where U_0 and $U_1$are the fluorescence signals before and after light-off time respectively. In using this technique in the experiment, the AC-MOT was loaded to a steady state condition, then the six trapping beams were switched off using a mechanical shutter for $\sim 5\, ms$. During this time, the atoms were free and so moved with their instantaneous velocity. Those with sufficient velocity then escaped from the trap. On switching the

trapping laser beams on again, a fraction of atoms were recaptured to the trap center as shown in figure 5.15. This was repeated for different light-off times.

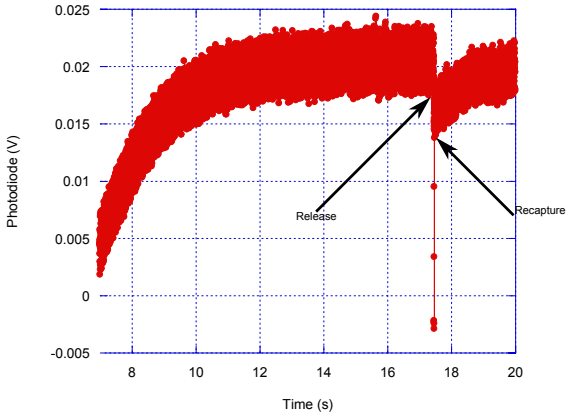

Fig 5.15: AC-MOT fluorescence signal during release and recapture. From the Fraction of atoms remaining with respect to a given light-off time, the average temperature of the atomic cloud was estimated.

Using the above procedure, the average temperature of the atoms in the AC-MOT operating with a trapping laser of total intensity of $424\, mWcm^{-2}$, and red detuned by $\sim -4\Gamma$, was $275 \pm 33\mu K$. This is the mean temperature calculated from three different light-off times; the quoted uncertainty is the standard deviation of the mean from these measurements.

5.7 The AC-MOT Characteristics

Different experiments were carried out to establish the characteristics of the AC-MOT. These included characterizing the AC-MOT behaviour under different amount of trapping laser detuning; measurement of the loading and decay lifetime of the MOT and the estimation of the size and temperature of the atomic ensemble in the AC-MOT.

5.7.1 The AC-MOT and Laser Detuning

In order to operate the MOT and create the required optical molasses, the trapping laser is red detuned from resonance with respect to the trapping transition.

Different amounts of laser detuning have been proposed by several researchers in order to create a sustainable MOT of ^{39}K [14, 20]. To determine the optimal detuning used in this

experiment, a measurement of the AC-MOT loading rate, decay lifetime and the number of trapped atoms in the AC-MOT was carried out with the AC-MOT operated with different amount of detuning.

5.7.1.1 AC-MOT Loading Rate

The AC-MOT just like any other MOT, traps only a finite number of atoms due to intrinsic losses in the MOT (the atomic cloud does not build up indefinitely). The AC-MOT is said to be fully loaded when there is a balance between the loading rate and the combined rate of losses due to different loss mechanisms in the MOT. The size of the trap and the number of trapped atoms is determined by different AC-MOT parameters, such as the trapping laser intensity, detuning and beam width, and the trapping magnetic field gradient.

The loading rate of the AC-MOT for a given magnetic field gradient, laser intensity and detuning, depends on the flux of atoms from the Zeeman slower and the loss rate due to collisions with background gasses. This collisional rate depends on the background pressure in the MOT chamber and on inter-atom collisions between trapped potassium atoms. The capture rate also depends on the laser beam intensity and alignment. The time evolution of the number of trapped atoms in the AC-MOT is here described by the rate equation [21]

$$\frac{dN(t)}{dt} = L - \gamma N(t) \tag{5.21}$$

With a solution given by

$$N(t) = N(0) + \frac{L}{\gamma}(1 - exp(-\gamma t)) \tag{5.22}$$

where $N(0)$ is the background level at $t = 0$. This term accounts for the light scattered by various components in the MOT chamber as detected by the photodiode ($at\ \ t = 0$). L is the trap loading rate and γ is the loss rate due to collisions.

With all other MOT parameters set and running, the AC-MOT was loaded by opening the gate valve, thus letting atoms pass through the Zeeman slower into the MOT chamber. The evolution of the trap as was detected by the photodiode is shown in figure 5.16 for different amount of detuning.

From a fit of equation 5.22 to the loading curve in figure 5.16, the loading and loss rate, and the number of atoms in the trap in the steady state of the AC-MOT for different laser detunings were determined. The results presented in figures 5.17a and 5.17b, clearly show the dependence of the loading and loss rate as well as the number of trapped atoms on the laser detuning. The loading rate, loss rate and the number of atoms in a steady state do not significantly vary for laser detuning between -3Γ and -5.5Γ, however they fall sharply at -2.5Γ and -6Γ.

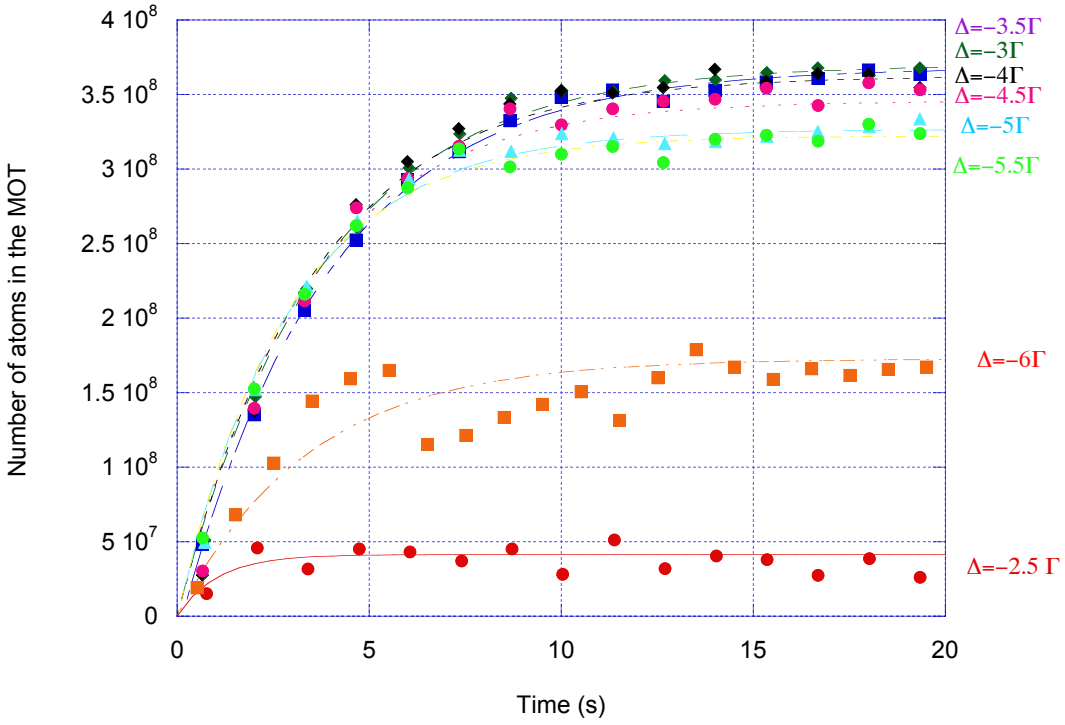

Fig.5.16: AC-MOT loading curve for different laser detuning. The AC-MOT operates well at trapping laser detuning between -3Γ and -5.5Γ. At 1.5Γ the laser is very close to resonance, and so cooling is less efficient. The trap has a shallow depth at -6Γ detuning, and so atoms were easily knocked out of the trap by background collisions.

These results were helpful in optimizing the MOT for maximum efficiency before collision experiments were performed.

The highest loading rate of $1.13 \pm 0.004\times10^{8} atoms/s$ was obtained when the AC-MOT was operated at a laser detuning of -5.5Γ, with a corresponding loss rate of $0.35 \pm 0.01\ s^{-1}$. The lowest loading rate of $4.0 \pm 0.28\times10^{7} atoms/s$, was found at a detuning of -6Γ, with a loss rate of $0.95 \pm 0.07\ s^{-1}$, where $\Gamma = 6.035$ MHz is the natural line-width of the transition. The maximum number of atoms in the trap in a steady state condition N_{max}, is limited by the intrinsic loss of atoms through various mechanisms that remove

atoms from the trap. The AC-MOT reaches a steady state when the loading process is balanced by the loss mechanisms, as noted above.

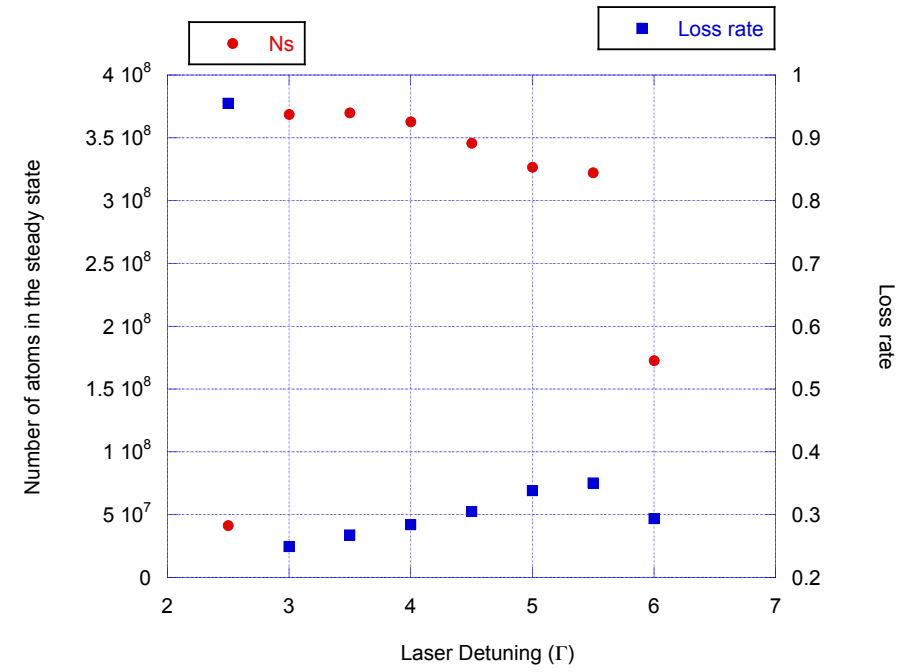

(a)

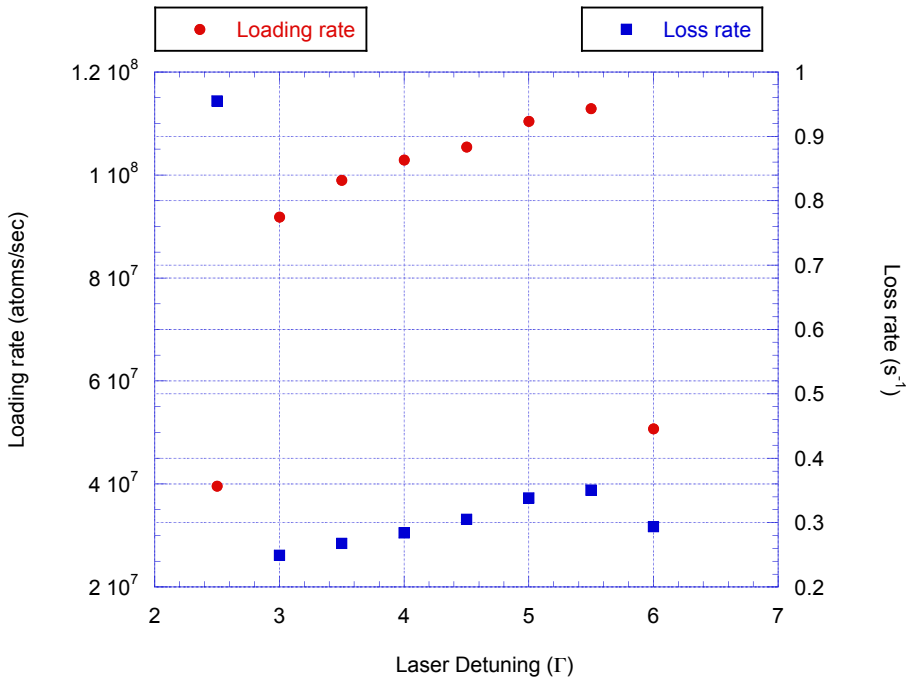

(b)

Fig 5.17: AC-MOT behaviour at different trapping laser detuning. (a) Maximum number of atoms (N_{max}) in the AC-MOT and the loss rate. N_{max} was highest for the AC-MOT operated with the trapping laser detuned by $\sim -3.5\Gamma$. (b) Loading rate and loss rate.

After a background correction (subtracting the fluorescence level in the MOT with gate valve closed and no atom was emitted into the MOT chamber), the maximum number of atoms in a steady state N_{max} is then given from equation 5.22 as

$$N_{max} = \frac{L}{\gamma} \tag{5.23}$$

From figure 5.17a, the highest value of $3.70\times10^{8} \pm 3.1\times10^{5} atoms$ for N_{max} was obtained with the AC-MOT trapping laser detuned by -3.5Γ with the corresponding loading rate of $1.0\times10^{8} \pm 2.7\times10^{5}\ atoms/s$ and a loss rate of $0.27 \pm 0.001\ s^{-1}$.

The AC-MOT operating at -2.5Γ $(\sim -15\ MHz)$ laser detuning, which is close to resonance with the $F = 2 \rightarrow F' = 3$ transition, and $\sim 1\Gamma$ blue detuned with respect to the $F = 2 \rightarrow F' = 2$ transition resulted in a smaller number of trapped atoms in the steady state. This is attributed to the increased photon scattering rate which possibly causes the overall losses, and due to some heating effects from atoms in the $F' = 2$ sub-level at this detuning, therefore leading to higher losses. Similarly, when the trapping laser was red-detuned by $\sim 6\Gamma$ $(-36\ \text{MHz})$, this produced an unstable MOT and a low number of trapped atoms in the steady state. At this detuning, the laser is detuned below the F'=0 excited state and is a long way from the F'=3 sub-level, and so atoms experience only a weak damping force in the trap. This results in an easy escape of atoms from the trap and a reduction in the number of trapped atoms in the MOT. These results were obtained at fixed trapping laser intensity of $\sim 424\ mWcm^{-2}$.

5.7.1.2 AC-MOT Decay Rate

As noted above, the number of atoms trapped in the AC-MOT was limited due to different loss mechanisms which are inherent in the MOT, but reaches a steady state condition when there is a balance between the capture rate and the rate of losses in the MOT. There are several different ways that the AC-MOT population can decay. These include switching off the trapping field, turning the trapping laser off, turning the Zeeman slower field off, interrupting the slowing laser, or stopping atoms from entering the Zeeman slower. Further the interaction of trapped atoms with electrons or photons of sufficient energy can cause the AC-MOT population to decay due to ionization or electron collision.

Several different processes contribute to the decay of the MOT when no external interactions are present. These include: collisions with background gasses in the chamber (the rate then being proportional to the number of atoms in the trap N, as well as the

background pressure), and collisional losses between trapped atoms. The lifetime of the MOT (the time it takes the MOT to decay), therefore depends on several factors, including the method used to cause the MOT to decay. The results of MOT decay through three of the methods mentioned above namely: stopping atoms from entering the Zeeman slower, turning the Zeeman slower field off, and interrupting the slowing laser beam, are shown in figure 5.18. The figure shows that the AC-MOT has a longer lifetime (shorter decay rate) when atoms were stopped from entering the Zeeman slower while the trapping field and the trapping laser beams remained on, and other AC-MOT operational conditions were maintained. This was a result of the reduced losses from collisions between trapped atoms and hot atoms that entered the MOT.

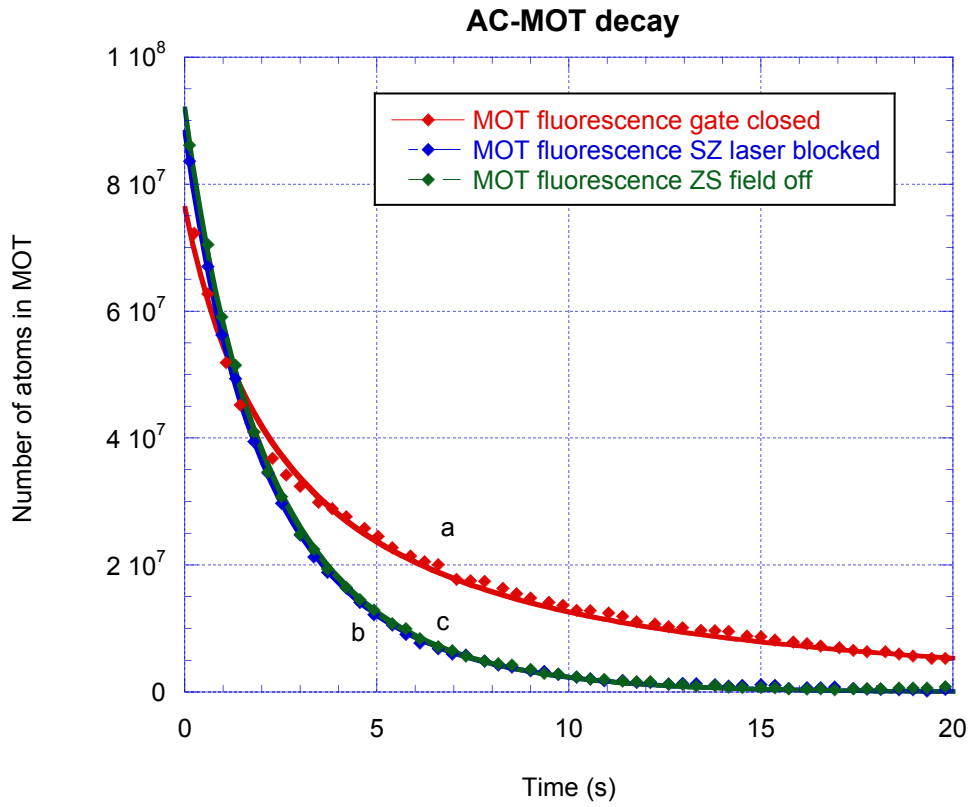

Fig 5.18: AC-MOT decay. (a) The gate valve was closed and so atoms were stopped from entering the Zeeman slower. (b) The magnetic field of the Zeeman slower (ZS) was suddenly switched off, and (c) the Zeeman slower cooling laser was blocked.

Since the lifetime of the AC-MOT depends amongst other factor on the cause of the decay, it is possible to obtain information on the method that influences the MOT decay (which determines the prevailing loss mechanisms in the MOT), from the decay lifetime of the MOT. It is also possible to deduce properties of the trapped atoms from the decay rate, as is shown in chapter six where the photoionization cross section of potassium was determined from the lifetime of the AC-MOT modified due to photoionization.

If the atomic beam is stopped by closing the gate valve, then the capture rate will be zero and so rate equation 5.21 becomes

$$\frac{dN(t)}{dt} = -\gamma N(t), \tag{5.24}$$

which has a solution

$$N(t) = N_0 \exp(-\gamma t) \tag{5.25}$$

where N_0 is the number of atoms in the MOT just before the gate valve was closed. A fit of equation 5.25 to the decay curve shown in figure 5.19a indicates that this is not a good fit. It was observed that the MOT decays with a rate which varied as the number of atom in the MOT decreased. This is indicative of two-body collisional losses due to collisions amongst trapped atoms at high atomic cloud density.

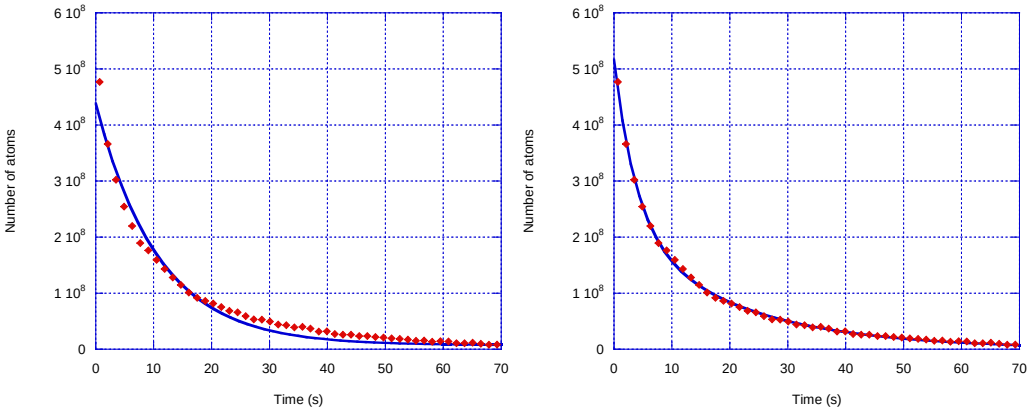

(a) (b)

Fig 5.19: The AC-MOT decay curves illustrating the effect of two-body losses. (a) The thick line shows the least squares fit of equation 5.25 through the data points. (b) This shows the same result fitted with equation 5.30, which includes inter-atom collisions in the MOT.

To quantify the contribution of the different loss mechanisms, the rate equation describing the decay of the AC-MOT is hence modelled as [20]

$$\frac{dN(t)}{dt} = -\alpha N(t) - \beta \int n^2(r,t) d^3r \tag{5.26}$$

Where α is the decay coefficient due to collisions with background gasses (the one-body collision), and so is proportional to the number of atoms in the trap N. β is the two-body decay coefficient due to collisions between trapped atoms, which is proportional to N^2. Hence n is the density distribution of the atomic cloud. For a spherical distribution of trapped atoms in the cloud, the density distribution may be described by an isotropic Gaussian function given by

$$n(r,t) = \frac{N(t)}{\pi^{3/2}\sigma^3(t)} \exp\left(-\frac{r^2}{\sigma^2(t)}\right) \tag{5.27}$$

where σ is the $1/e$ radius of the atomic cloud. This can be obtained from a Gaussian fit to the atomic cloud imaged by a CCD camera as shown in figure 5.14.

The effective diameter of the atomic cloud increases as the AC-MOT decay, as illustrated in figure 5.14. The average density n_{av} therefore varies with time and is given by [22, 23]

$$n_{av}(t) = \int \frac{n(r,t)}{N(t)} n(r,t) d^3r = \frac{N(t)}{V} \tag{5.28}$$

where V, is the effective volume corresponding to the average density, and is defined for an isotropic cloud as $V = (2\pi)^{3/2}\sigma^3(t)$ [22, 24].

Using equation 5.28, the rate equation can be rewritten as

$$\frac{dN(t)}{dt} = -\alpha N(t) - \frac{\beta}{V} N^2(t) \tag{5.29}$$

which has a solution of the form

$$N(t) = \frac{N_0 \alpha}{\left(\alpha + \frac{\beta}{V} N_0\right) \exp(\alpha t) - N_0 \frac{\beta}{V}} \tag{5.30}$$

Here N_0 is the number of atoms in the MOT at $t = 0$. The parameters obtained from a fit of equation 5.30 to the decay curves shown in figure 5.20 are tabulated in table 5.2. These fits indicate that for detuning between -3Γ to -6Γ the decay coefficients α ranges from $0.034 \pm 0.0002\ s^{-1}$ to $0.054 \pm 0.0004\ s^{-1}$, whereas the loss rate due to two-body collisions $\frac{N_0\beta}{V}$ ranges between $0.070 \pm 0.003\ s^{-1}$ to $0.240 \pm 0.001\ s^{-1}$. Figures 5.21 and 5.22 show the plots of the different loss coefficients.

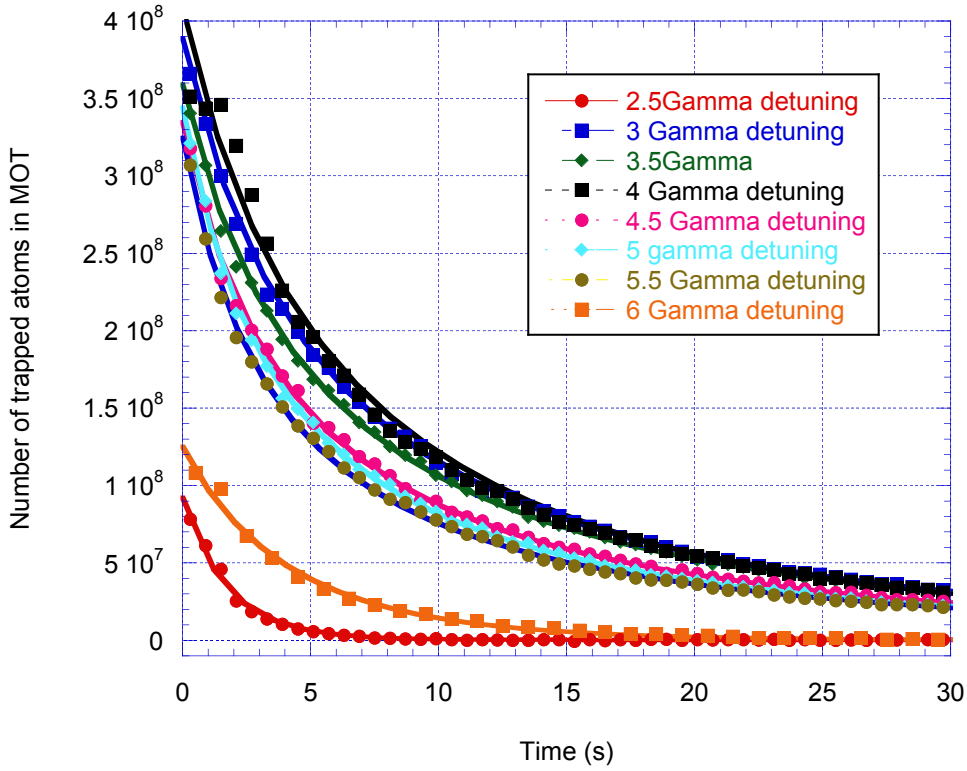

Fig 5.20: AC-MOT decay curve for different trapping laser detuning. The points indicate the data and the thick lines are from the fit of equation 5.30.

Detuning (Γ)	Number atoms in MOT in steady state ($\times 10^8$ atoms)	Loss coefficient α (s^{-1})	Two-body Loss coefficient $\frac{N_0\beta}{V_{eff}}$ (s^{-1})
2.5	0.857 ± 0.002	0.717(3)	0.315(7)
3.0	3.890 ± 0.002	0.040(1)	0.154(1)
3.5	3.600 ± 0.002	0.035(1)	0.163(1)
4.0	3.63 ± 0.001	0.054(4)	0.128(1)
4.5	3.35 ± 0.002	0.036(1)	0.199(3)
5.0	3.440 ± 0.002	0.039(1)	0.228(4)
5.5	3.240 ± 0.002	0.034(2)	0.243(1)
6.0	1.250 ± 0.002	0.192(1)	0.070(3)

Table 5.2: The AC-MOT loss coefficients.

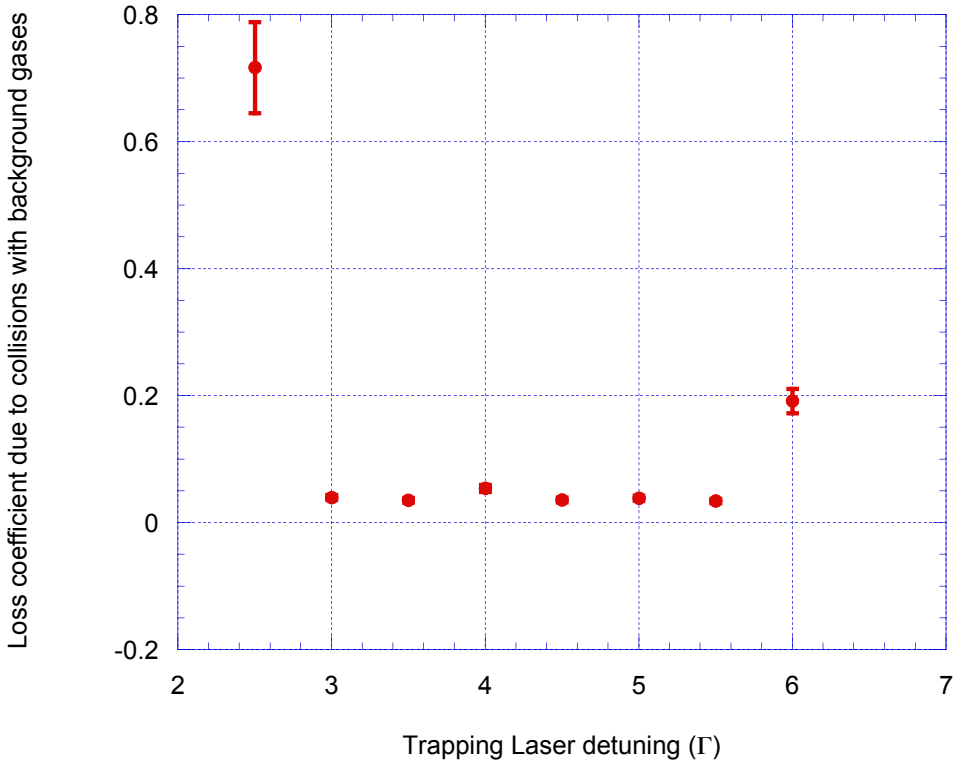

Fig 5.21: A plot of loss rate due to collision with background gases at approximately the same background pressure in the MOT chamber and for the same trapping laser intensity. The rates are fairly unchanging except for laser detuning of ~ -2.5 *and* $\sim -6\Gamma$. *At both of these detunings, the AC-MOT was very unstable.*

The one body loss rates from collisions with background gases are fairly constant for detuning from -3Γ to -5.5Γ. This loss rate rises sharply for detunings of $\sim -2.5\Gamma$ and $\sim -6\Gamma$, possibly because the trap depth is shallow at this detunings, and so atoms were easily knocked out of the trap. For detunings from -3Γ to -5.5Γ, the two-body loss coefficient was fairly linear except at -3Γ where it dropped, before rising again to a value of 0.240 ± 0.001. at 5.5Γ. The highest two-body loss rate was recorded at $\sim -2.5\ \Gamma$, and a much lower value was obtained at $\sim -6\Gamma$ detuning as shown in figure 5.22. These results are possibly due to the low number of trapped atoms, and the instability of the trap.

These results therefore show the dependence of the stability of the trap on the number of atoms in the trap and on the different loss mechanisms due to detuning of the trapping laser beams.

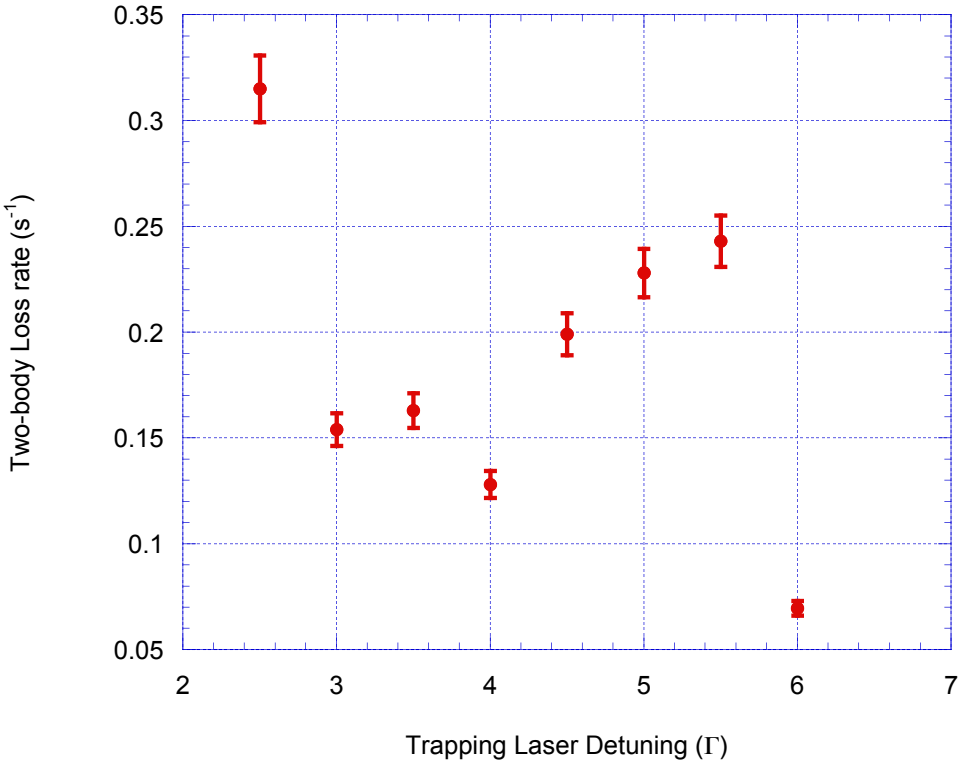

Fig 5.22: Plot of two-body loss coefficient at the same background pressure in the MOT chamber for the same trapping laser intensity

5.7.2 The Effect of Re-pump Frequency on the AC-MOT Fluorescence Intensity

In order to produce and sustain a magneto optical trap of potassium, two laser frequencies are required as discussed in chapter two. In this experiment, the re-pump frequency laser beam was created by passing the laser beam through an AOM operated at 440 MHz. This then produced two laser beams, one with the same frequency as the incident beam and the other shifted in frequency by that of the applied acoustic wave from a radio frequency signal generator. The second beam was then recombined with the unshifted beam to form the trapping laser beams.

To ascertain the dependence of the number of atoms trapped in the MOT on this second laser beam frequency, the intensity of the AC-MOT fluorescence signal was measured for different re-pump frequencies. In this experiment, the AC-MOT was operated with the trapping laser red detuned by $\sim -4\Gamma$, where $\Gamma = 6.035$ MHz is the natural line-width of the excited state. Other settings were as stated above. A plot of the fluorescence intensity of the AC-MOT for different frequencies of the re-pump beam is shown in figure 5.23. The result shows that the applied re-pump frequency is critical in the production of a sustainable MOT. The maximum AC-MOT fluorescence intensity was obtained with the

re-pump frequency of 440.7 MHz, and the fluorescence signal falls sharply around this frequency. Hence to produce the most stable potassium MOT, the re-pump laser frequency was set at 441 ± 1 MHz.

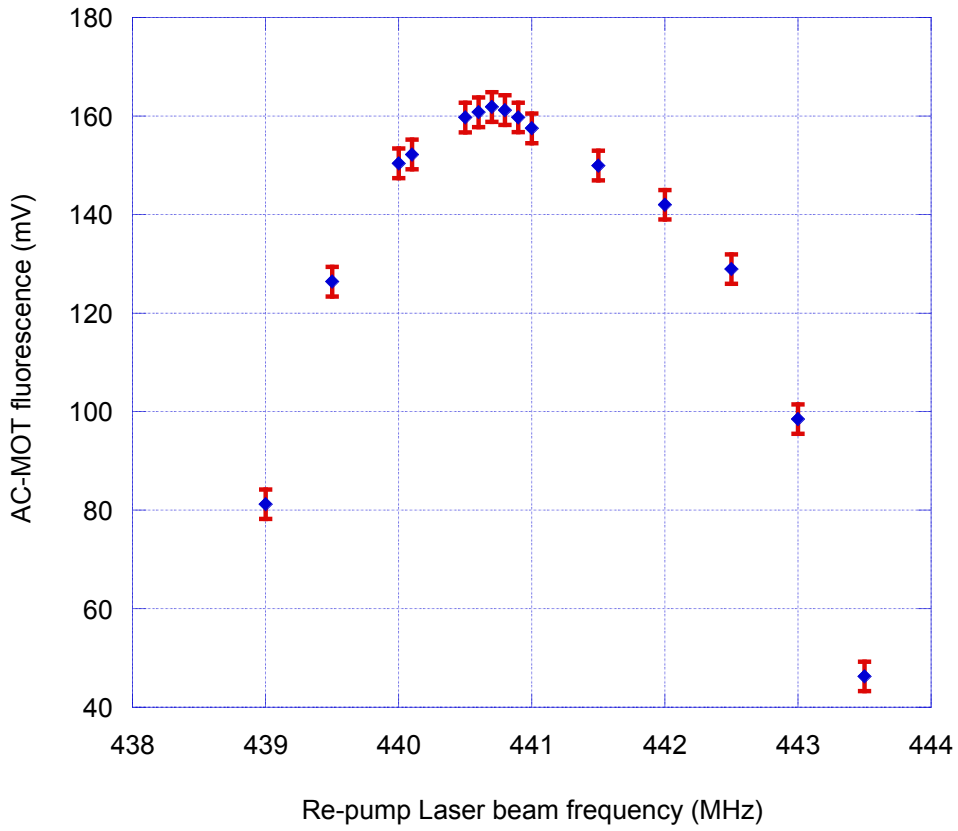

Fig 5.23: Variation of AC-MOT fluorescence intensity with re-pump frequency. Each data point is the mean of fifteen measurements, and the error bars are the standard deviation of the mean. The horizontal axis is referenced from the $F = 2 \rightarrow F' = 3$ transition, (391,016,011 MHz).

5.7.3 Summary of Typical AC-MOT Characteristics during Experiment

The characteristics of the AC-MOT depend on several different AC-MOT parameters and operation setting, and so may vary from one experiment to the other. In the experiments reported here, the AC-MOT magnetic field gradient was kept constant at 15 G/cm, and the Zeeman slower settings given in table 4.3 were used. The trapping laser intensity was fixed at $\approx 424\, mWcm^{-2}$, out of which the re-pump laser beam contributed about 30%. The AC-MOT was then characterized as follows:

- Loading rate $\approx 1.03 \pm 0.01 \times 10^{8}\ atoms/s$
- Number of trapped atoms $\approx 3.63 \pm 0.02 \times 10^{8} atoms$
- Mean trap density $\approx 2.14 \pm 0.02 \times 10^{11}\ atoms/cm^{3}$
- Mean trap temperature = $275 \pm 33\ \mu K$
- Doppler temperature limit for cooling potassium $= 146\ \mu K$
- One-body loss rate $= 0.05 \pm 0.01\ s^{-1}$
- Loss rate due to background collision = $8.12 \pm 0.01 \times 10^{6}\ atoms/s$
- Two body loss coefficient $\frac{\beta}{V} N_0 = 0.13 \pm 0.01 s^{-1}$

The above results were obtained for the AC-MOT operating with the trapping laser beam red-detuned by $\mathbf{23\ MHz}$ (~$\mathbf{4\Gamma}$). The measured temperature was about a factor of two higher than the Doppler temperature. During subsequent experiments (photoionization and Rydberg excitation, the AC-MOT characteristics may change due to variation in the MOT parameters.

5.8 Electron Impact Ionization

A preliminary electron scattering experiment was carried out to test for the suitability of the AC-MOT for low energy collision studies, with electron energies ranging from a few electron volts to a hundred electron volts. The resulting data showed the development of the first (K^{+}) and the second (K^{++}) ionization states of potassium [14]. The setup illustrated schematically in figure 5.24 consisted of a source of electrons (the electron gun) and a charge particle detector, in this case a channel electron multiplier (channeltron). A brief description of the electron gun and the channeltron are given below. The experiment described in this section was carried out to check the condition of the ion detector inside the MOT chamber in preparation for future ionization experiments.

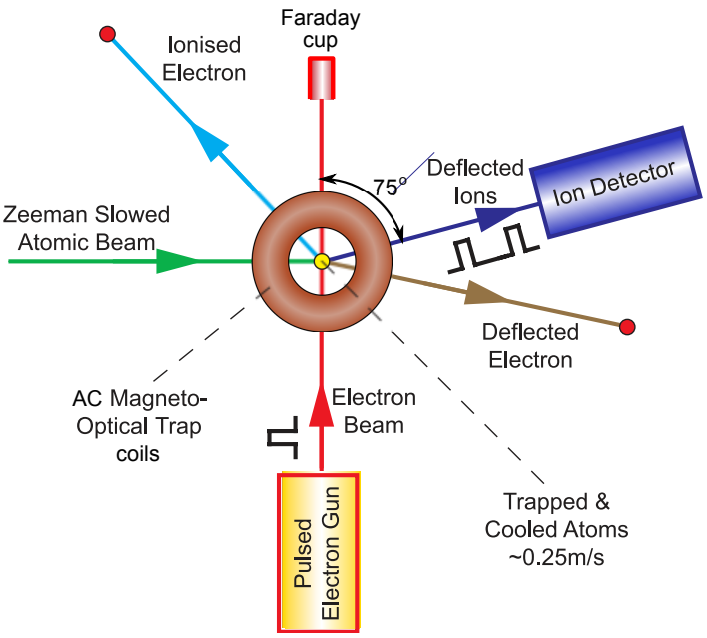

Fig 5.24: Schematic diagram of the electron impact ionization setup. The electron gun produced electrons with energies between 2eV and 100 eV. In this setup, the position of the ion detector was fixed and oriented at 75° *from the electron beam.*

5.8.1 The Electron Gun

The electron gun was designed to produce a collimated beam of electrons in the energy range 2eV to 100eV, at a beam current of 12μA. The gun is made up of an electron source and collimation electrostatic optics, which were used to focus the beam onto the trapped atoms in the interaction region. The gun was mounted directly onto a 19 pin Conflat CF70 electrical feed-through, as shown in figure 5.25. In order to be non-magnetic and UHV compatible, the gun was constructed from 310-grade stainless steel. Also, all surfaces within the gun were lined with molybdenum to provide a uniform surface potential [25].

The source of electrons is a Pierce triode [26] comprising a filament, a grid and an anode. The filament is an Agar AO54 hairpin tungsten filament, and the grid is a Pierce electrode with a 3 mm aperture. Passing a current of $\approx 2A$ through the filament heats it up and electrons are emitted. The filament was biased with a negative voltage to set the gun energy with respect to ground. This is the energy with which the electron beam exits the gun.

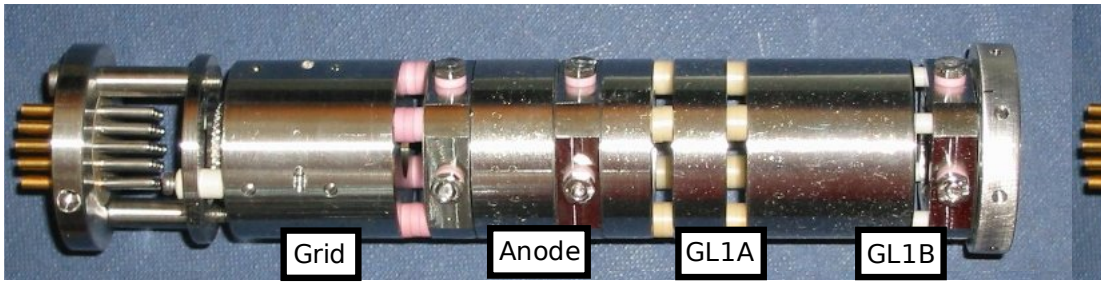

(a)

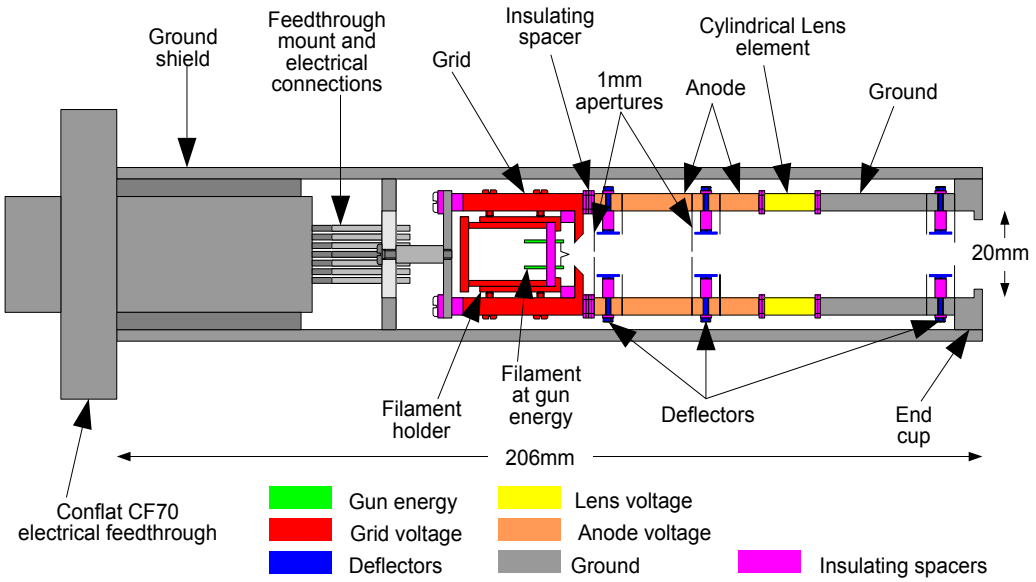

(b)

Fig 5.25: The electron gun showing the configuration of different components.

The grid voltage was kept slightly negative relative to the gun energy, and the anode voltage was positive so as to partly collimate the electron beam from this region of the gun. The electrons were then accelerated out of the grid into the anode region. To ensure that the electron beam was directed into the trapped atoms in the interaction region, the beam was focused with a lens element (GL1A) located after the anode. The last lens element (GL1B) was held at ground potential, as illustrated in figure 5.26.

Two Lambda LPD-425-FM-V1 0-250 V high voltage dual power supplies were used to set the gun energy and the voltages for the anode and lens elements. The anode supply and the lens element voltage (created with two supplies connected in series to provide 0-500 V) were referenced to the gun energy voltage, while the gun energy was referenced to ground. To compensate for any misalignment within the gun and to steer the electron beam onto the interaction region, three sets of x-y electrostatic deflectors were used. Each pair of deflectors was made of two parallel plate electrodes oriented at 90° to each other. The first

two sets of deflectors were referenced to the anode voltage, and the last set was referenced to ground. The deflectors were controlled by applying voltages ranging between $\pm\ 10\ V$ to the plates. In order to eliminate the influence of any external magnetic field (e.g. from the earth's magnetic field or the magnetic field from the Zeeman slower), on the trajectory of the charged particles within the chamber, it was essential to cancel the these magnetic field during this experiment. This was done by applying appropriate currents to the three set of Helmholtz coils mentioned in chapter four.

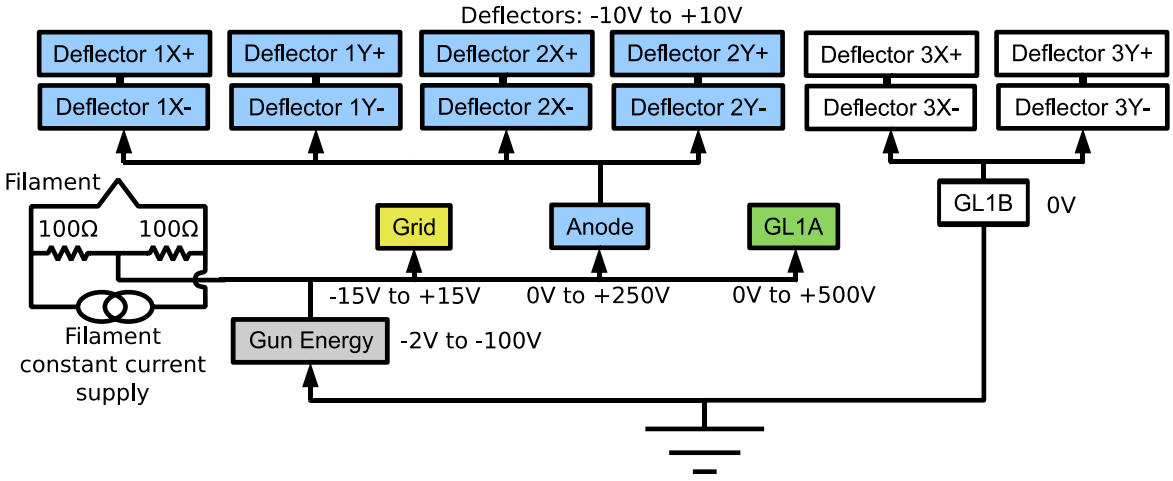

Figure 5.26: Schematic diagram illustrating the voltage relationships between various components of the electron gun.

In this experiment, the electron gun was operated in a pulsed mode using the pulse control scheme shown in figure 5.12, which allows time of flight data to be taken. The electron gun grid voltage was biased to emit electrons during the $400\ \mu s$ AC-MOT off time, so that electrons were fired at the trapped atoms only during the AC-MOT field off regime.

5.8.2 The Time of Flight (TOF) Ion Detector

To monitor the electron impact ionization process, a time of flight (TOF) ion detector was installed within the MOT. The TOF detector consists of a channel electron multiplier (channeltron) and a bias mesh plate. The channeltron has a recovery time of $\sim 5\ \mu s$ between detection events, and this limits the maximum sampling rate to $\sim 100\ kHz$ in order to reduce dead time effects. The front face of the channeltron was biased at a negative high voltage (-2.0 kV to -3.0 kV) so as to detect ions, while the output was terminated by a 50Ω resistor to ground as shown in figure 5.27. The negative electric field from the channel electrons multiplier accelerates ions towards the front face of the

detector. Ions striking the inner surface of the channeltron induce the production of secondary electrons that in turn impinge on the inner surfaces to produce more secondary electrons. This avalanche effect produces an increased signal in the final measured current pulse so that individual ions could be detected.

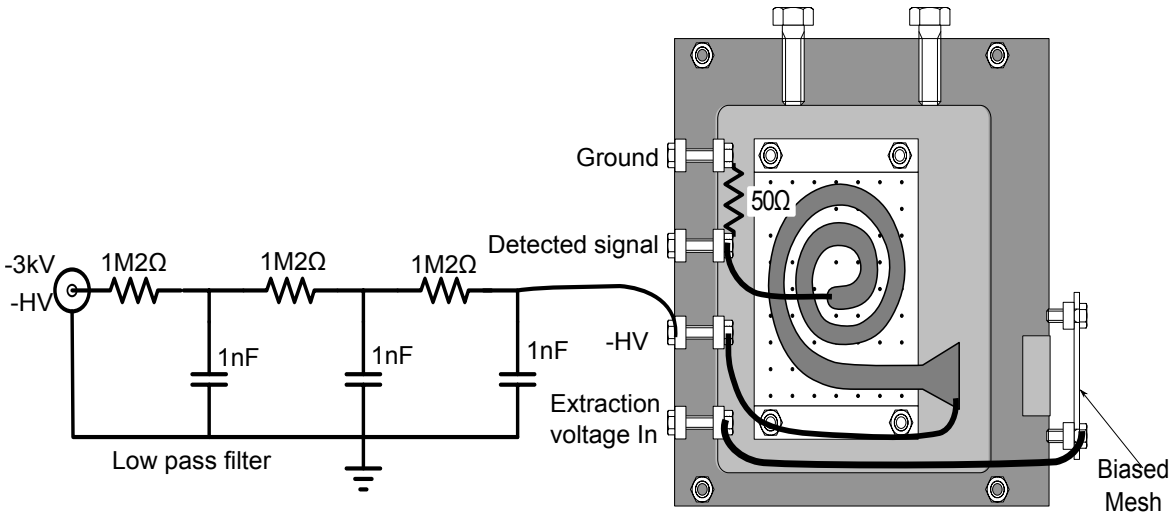

(a)

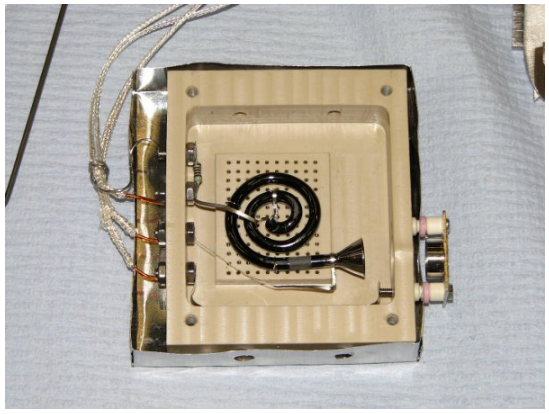

(b)

Fig 5.27: The Channel electron multiplier.(a) The channeltron showing the biasing voltages.(b) A photograph of the channeltron. With the low pass filter, high frequency signals are isolated from the detector. Ions were extracted by applying a negative voltage (the extraction voltage) to the bias mesh. The detected signal was amplified before being sent to the acquisition system.

To prevent high frequency noise from the HV power supply affecting the channeltron signal, the channeltron is connected to the HV power supply by a low pass filter. More details on the wiring of the channeltron are found in [14].

The detected ionization signal from the channeltron was amplified using a wideband amplifier (Phillips Scientific model 6954-wideband amplifier), which has a gain of 100.

This amplified signal was then sent to an Ortec 473 constant fraction discriminator. The output of the discriminator was then sent to an Ortec 541 rate meter and Ortec Turbo-multi-channel scaler (Turbo-MCS), which recorded and displayed the ionization events as a function of time. This MCS stored the recorded signal as a histogram in channels with a dwell time ranging from $5\,ns$ to $500\,ns$. The trigger pulses for the electron gun, extraction field and the MCS were generated by the AC-MOT computer control DAQ card.

5.8.3 Time Of Flight Ion Signal

During electron impact ionization experiments, electrons from the electron gun were fired onto the cold atom target, resulting in ionization of the atoms. Since electrons are released from the atoms, this ionization process results in a change in the momentum and energy of the incident electron, and the creation of an ion and an ionized electron. Electrons with incident energies between $10\,eV$ and $100\,eV$ were directed onto the trapped atoms. The ions created by this process were extracted, detected and recorded as described above, and the time of flight ion signal displayed by the MCS.

The AC-MOT was operated with the typical settings listed in table 5.1, and at a detuning of $\sim -4\Gamma$. The electron gun filament current was set at 2 A. the emission of electron was triggered with the application of a $+10\,V,\ 4\,\mu s$ wide pulse to the gun grid. The gun was triggered $20\,\mu s$ after the AC-MOT field was switched off, to ensure a zero magnetic field in the interaction region. Ions were extracted by applying a $-45\,V$, $140\mu s$ wide extraction voltage to the bias mesh $10\mu s$ after the electron pulse. The electrostatic deflectors of the electron gun were re-adjusted each time the electron gun energy was changed, to optimize the flux of electrons into the interaction region. The data was accumulated for 500,000 electron gun pulses by the Turbo-MCS, and stored in 500 channels which each had a dwell time of $500\,ns$.

To obtain the 3D ionization signal, the electron energy was fixed while scanning the time of flight (TOF) of the generated ions. This was repeated for different electron energies to build up the 3D ionisation profile. The resulting time of flight spectra is shown in figure 5.28. The result compares well with spectra reported in [11], and shows the evolution of the first ($^{39}K^{+}$) and second ($^{39}K^{++}$) ionization cross-sections as a function of the incident electron energy. The K^{+} and K^{++} spectra are not well resolved due to the poor timing resolution compared to that reported in [11], however the result was reasonable as these

experiments were setup to test the charge particle spectroscopy, especially the ion detector and data acquisition system, which were then used during the photoionization and high-n Rydberg experiments described later in this thesis.

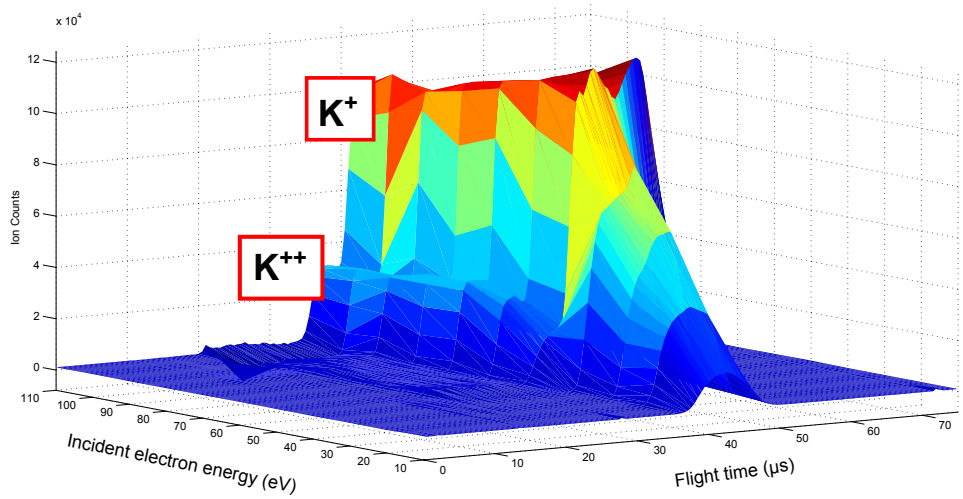

Fig 5.28: Time of flight ion spectra from trapped atoms in the AC-MOT. The first and second ionization cross section are shown. Because of poor timing resolution, the spectra are not well resolved. The small dip in the K^+ spectrum was due to saturation of the detector at high-count rates.

5.9 Conclusion

This chapter has detailed the characterization of the AC-MOT. The basic operation of the AC-MOT and its use in the trapping of ^{39}K, including some of the MOT characteristics, has been discussed. The dependence of the loading and decay rates of the AC-MOT on the detuning of the trapping laser was presented. As a test to ascertain the condition of the charge particle optics in the MOT chamber, results from the electron impact ionization of trapped atoms have also been presented.

References

[1] Hall, J. L., Zhu, M., & Buch, P. (1989). *Prospects for using laser-prepared atomic fountains for optical frequency standards applications. JOSA B, 6(11), 2194-2205.*

[2] Schappe, R. S., et al. *Absolute electron-impact ionization cross-section measurements using a magneto-optical trap*. Physical Review Letters 76.23 (1996): 4328.

[3] Dinneen, Timothy P., et al. *Use of trapped atoms to measure absolute photoionization cross sections*. Optics letters 17.23 (1992): 1706-1708.

[4] Fox, R. W., Robinson, H. G., Gilbert, S. L., Hollberg, L., & Marquardt, J. H. (1993). Optical probing of cold trapped atoms. *Optics letters*, *18*(17), 1456-1458.

[5] Wang, H., P. L. Gould, and W. C. Stwalley. *Long-Range Interaction of the K-39 (4S)+ K-39 (4P) Asymptote by Photoassociative Spectroscopy. 1. The OG (-) Pure Long-Range State and the Long-Range Potential Constants*. Journal of Chemical Physics 106.19 (1997): 7899-7912.

[6] Weiner, J., Bagnato, V. S., Zilio, S., & Julienne, P. S. (1999). *Experiments and theory in cold and ultracold collisions*. Reviews of Modern Physics, 71(1), 1.

[7] McCulloch, A. J., Sheludko, D. V., Saliba, S. D., Bell, S. C., Junker, M., Nugent, K. A., & Scholten, R. E. (2011). *Arbitrarily shaped high-coherence electron bunches from cold atoms*. Nature Physics, *7*(10), 785-788.

[8] Anderson, M. H., Ensher, J. R., Matthews, M. R., Wieman, C. E., & Cornell, E. A. (1995). *Observation of Bose-Einstein condensation in a dilute atomic vapor*. science, *269* (5221), 198-201.

[9] DeMarco, B., & Jin, D. S. (1999). Onset of Fermi degeneracy in a trapped atomic gas. *Science*, *285*(5434), 1703-1706.

[10] Tong, D., Farooqi, S. M., Stanojevic, J., Krishnan, S., Zhang, Y. P., Côté, R., & Gould, P. L. (2004). *Local blockade of Rydberg excitation in an ultracold gas.* Physical Review Letters, 93(6), 063001.

[11] Harvey, M., & Murray, A. J. (2008). *Cold atom trap with zero residual magnetic fields: The ac magneto-optical trap*. Physical Review Letters, 101(17), 173201.

[12] Bergeman, T., Erez, G., & Metcalf, H. J. (1987). *Magnetostatic trapping fields for neutral atoms.* Physical Review A, 35(4), 1535.

[13] Good, R. H. "Elliptic integrals, the forgotten functions." *European Journal of Physics* 22.2 (2001): 119.

[14] M Harvey, *Low energy electron scattering from a pulsed AC-MOT*; PhD thesis, University of Manchester. 2009

[15] Hecht, E. *Optics*, 1987. Addison-Wesely Publishing Co., Inc., Menlo Park, CA, 281-286.

[16] http://www.behringer.com/assets/EP2000_P0A38_M_EN.pdf

[17] Chu, S., Hollberg, L., Bjorkholm, J. E., Cable, A., & Ashkin, A. (1985). *Three-dimensional viscous confinement and cooling of atoms by resonance radiation pressure.* Physical Review Letters, 55(1), 48.

[18] Lett, P. D., Watts, R. N., Westbrook, C. I., Phillips, W. D., Gould, P. L., & Metcalf, H. J. (1988). *Observation of atoms laser cooled below the Doppler limit.* Physical Review Letters, 61(2), 169.

[19] Arora P., Chowdhury S., Agarwal A., Pant K., and Gupta A. S. *Characterization of cold atomic clouds in a magneto-optical trap.* Indian J Pure & Applied Phys, Vol 49. 2011.

[20] Williamson, R. S., and T. Walker. *Magneto-optical trapping and ultracold collisions of potassium atoms*. Journal of Optical Society of Amaerica B 12.8 (1995): 1393-1397.

[21] Götz, S., Höltkemeier, B., Amthor, T., & Weidemüller, M. (2013). *Photoionization of optically trapped ultracold atoms with a high-power light-emitting diode*. Review of Scientific Instruments, 84(4), 043107.

[22] Browaeys, A., Poupard, J., Robert, A., Nowak, S., Rooijakkers, W., Arimondo, E., & Aspect, A. (2000). *Two body loss rate in a magneto-optical trap of metastable He.* The European Physical Journal D, 8(2), 199-203.

[23] Tol, P. J., Herschbach, N., Hessels, E. A., Hogervorst, W., & Vassen, W. (1999). *Large numbers of cold metastable helium atoms in a magneto- optical trap.* Physical Review A, 60(2), R761.

[24] Bradley, C. C., McClelland, J. J., Anderson, W. R., & Celotta, R. J. (2000). *Magneto-optical trapping of chromium atoms.* Physical Review A, 61(5), 053407.

[25] Woolf M.B.J, *e-2e Measurement in the perpendicular plane*. PhD thesis, University of Manchester 1989.

[26] Pierce, J. R. *Theory and design of electron beams*. New York, Van Nonstrand 1954.

CHAPTER SIX

Measurement of the Absolute Photoionization Cross Section of Potassium from the $4^2P_{3/2}$ Excited State

6.0 Introduction

The ability of light of sufficient energy and frequency to ionize an atom is the basis for photoionization spectroscopy. With the development of high intensity laser systems with narrow line-width and tuneable frequency, it became possible to selectively excite and ionize various states of atomic species, and so the photoionization cross section of the state could be determined. The determination of the photoionization cross section has a wide range of applications in different areas of science such as laser designing and radiation protection, space science, astronomy and plasma physics. Determination of photoionization cross-sections of different atomic species from the ground state has been extensively studied [1, 2]. Since the report of the first measurement of photoionization cross-section of potassium from the 4^2P excited states by Nygaard et al in 1977 [3], many measurement of photoionization cross sections from different excited states of potassium have been reported [4-7].

Several techniques have been adopted by different authors in the determination of photoionization cross-section from various excited states, see reference [4]. The method that is adopted depends mainly on the photo energy (photoionization potential) of the state in question. With the development of laser cooling techniques and the magneto optical trap, which has the capability of producing a high density of cold atoms, Dinneen et al in 1992 [8] reported the first determination of photoionization cross sections of rubidium from cold atoms trapped in a MOT. Trapped atoms if ionized, escape from the trap leading to a reduction in the detected fluorescence signal from the trap, thus photoionization introduces a new loss mechanism to the MOT. The induced loss rate is then a measure of

the rate of photoionization. While photoionization cross-sections of different alkali metals in the MOT have been reported [8-11], the same cannot be said of potassium.

In this technique, the photoionization cross section is determined by measuring and comparing the population dynamic of the trap with and without the ionizing laser, through the detection of the fluorescence from the excited atoms in the trap. With this technique, it is not necessary to know the density of the atomic sample since it measures the rate of ionization per atom. The rate of ionization is measured by fluorescence detection, meaning the detection of ions or photoelectrons is not required. Another advantage of this technique is its sensitivity to very low ionization rates, since the atoms are confined, eliminating the uncertainties associated with the Doppler effect. In this case low ionizing laser intensities can be utilized.

This chapter presents the results of direct photoionization (resonant ionization) of cold-trapped ^{39}K atoms in the AC-MOT, and reports for the first time the measurement of absolute photoionization cross-sections from the $4^2P_{3/2}$ excited state of ^{39}K atoms in the AC-MOT. This will includes the effects of the ionizing laser intensity and detuning to the rate of ionization. Since the trapping laser is slightly detuned from resonance with the $4^2P_{3/2}$ excited state, some atoms will still be in the ground state, and so cannot be directly ionized by the ionizing laser used in this experiment. An attempt to excite this group of atoms prior to photoionization with the addition of a second laser beam resonant with these atoms will be discussed. These experiments will further demonstrate the applicability of the AC-MOT to collision physics.

6.1 The Setup

Potassium has a first ionization potential of 4.34 eV [12] from the ground state. In this experiment, a two-step excitation technique was used. The AC-MOT was operated with a 766.7 nm trapping laser which was red detuned by 23 MHz with respect to the $4^2P_{3/2}$ excited state, and so atoms were excited to the $4^2P_{3/2}$ state by this laser. This provided the first step of excitation, raising the energy of the atoms by 1.62 eV. A second laser then is needed to provide the additional energy of at least 2.72 eV that is required to ionize the atoms, as illustrated in figure 6.1.

The experimental arrangement is similar to that used for electron impact ionization described in chapter five, except that instead of electrons, the ionizing laser is directed at the trapped atoms.

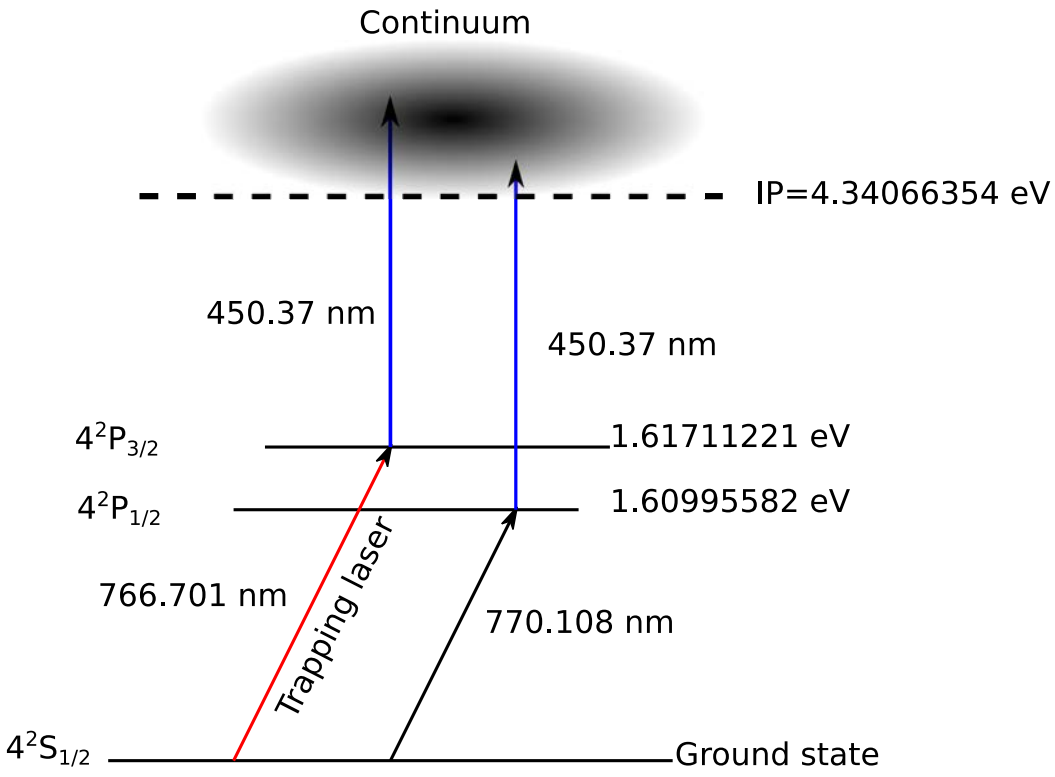

Fig 6.1: Two-step photoionization scheme. The trapping laser excites the atoms to the $4^2P_{3/2}$ state. The 770.108 nm laser provides the excitation of ground states atoms to the $4^2P_{1/2}$ excited state. The addition of the 450.37 nm blue laser provides the extra energy required to ionize the atoms.

6.1.1 The Ionizing Laser

To provide the energy required to directly photo-ionize potassium atoms into the continuum, a 450 nm diode laser was used. The layout of the 450 ionizing diode laser system is shown in figure 6.2.

The ionizing laser was produced by a blue laser diode LD-445-1000 MG (Roithner lasertechnik) with an output power of up to 1 W.

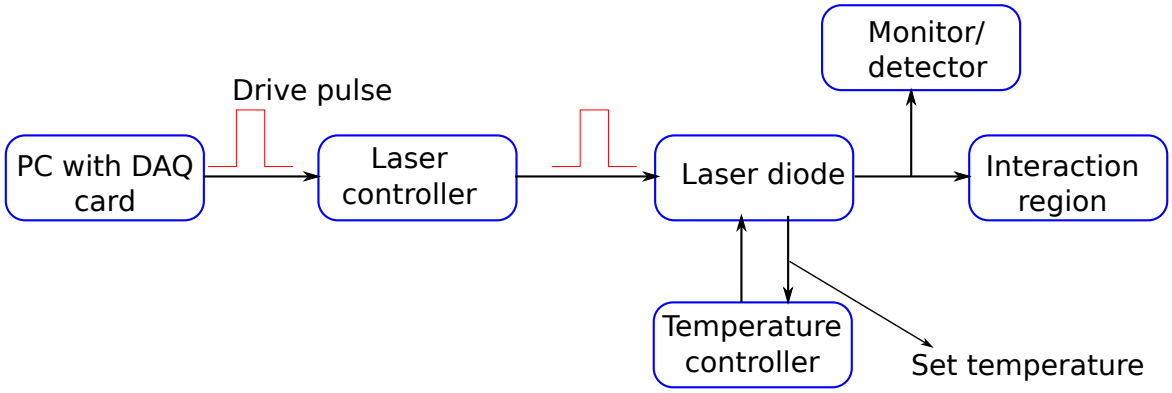

Fig 6.2: Layout of the ionising laser system. The drive signal is generated from the DAQ card. Part of the beam is directed to a photo diode for real time observation of the ionizing laser pulse. This allows for optimal settings and power measurements to be made.

Figure 6.3 shows the spectrum of the emitted light measured with an Oceanoptics US 4000 fibre optics spectrometer, which has a resolution 1.5 nm (FWHM). The emitted light has a peak wavelength of 450.37 nm. As illustrated in figure 6.1, a threshold wavelength of $\approx 455\ nm$ (from 4.34eV-1.61eV) is required to ionize potassium atoms from the first excited states, and in this case 100% of the spectral distribution of the laser is above the threshold energy required to photo-ionize potassium atom.

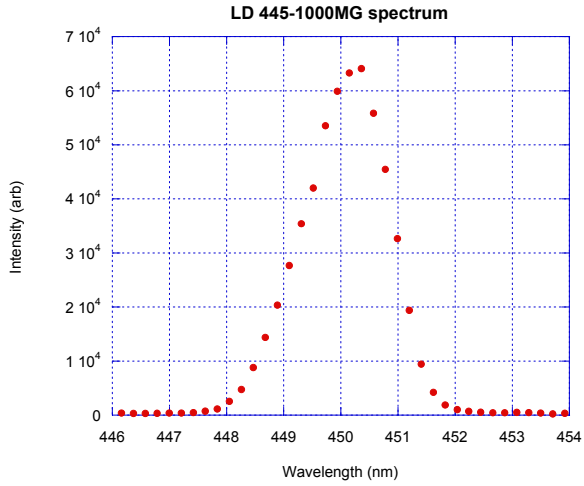

Fig 6.3: The spectrum of the 445 nm blue laser operating at drive current of 583 mA and a temperature of 10℃. *Although stated to be a 445 nm laser by Roithner, the wavelength is closer to 450 nm, which is still above the threshold required to photo ionize potassium atoms.*

Since the laser diode must be cooled, it was mounted on a temperature-controlled mount (Newport mount model 700), and the temperature was controlled by a Seastar temperature controller. At a given drive voltage, the peak wavelength varies linearly with temperature. Fig 6.4 shows the variation of the peak wavelength with temperature at a laser drive current of $\approx 600\ mA$.

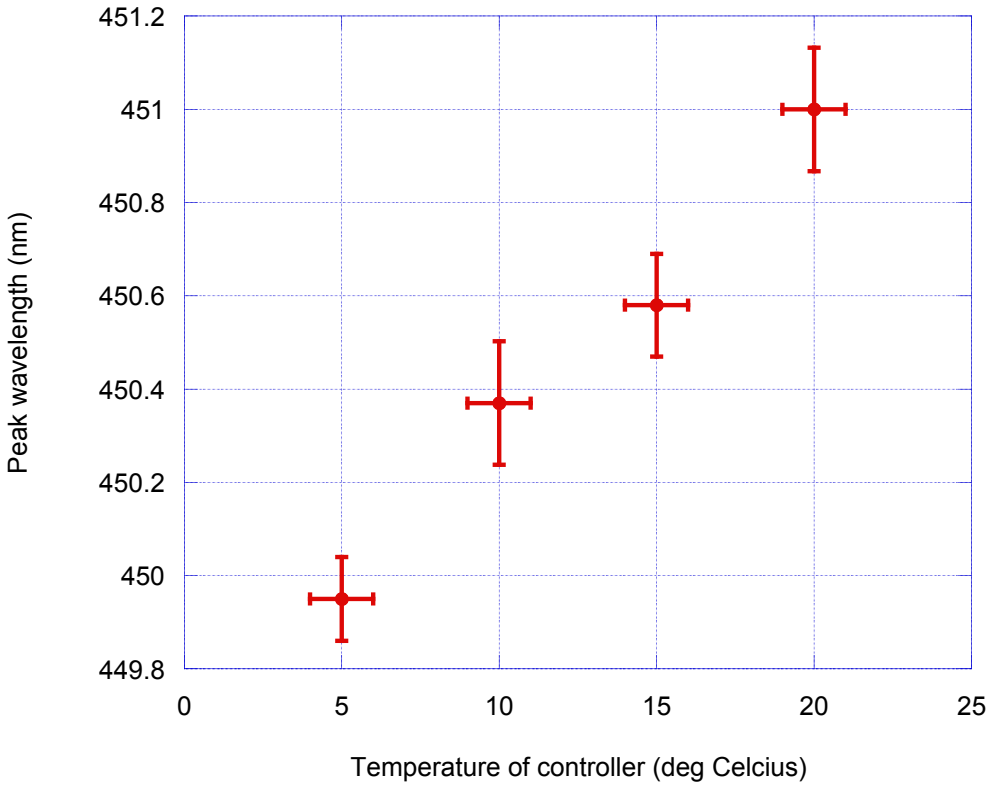

Fig 6.4: Variation of peak wavelength of the LD-445-1000MG laser diode operating at a drive current of $\sim 600\ mA$.

During normal operation, the laser diode was kept at a temperature of 10˚C.

The laser diode was operated by varying the current setting of the laser controller. Although blue light is emitted even with the smallest possible current from the controller, the laser diode starts to lase only after the threshold current of 145 mA is reached, which corresponds to a dc drive voltage of $\sim 1.5\ V$ as shown in figures 6.5 (a) and (b). In most cases, the laser diode was operated via the computer based AC-MOT control program described in chapter five, by sending a signal of known voltage and pulse-width to the external input of the laser controller. In this way, it was possible to adjust the intensity (drive voltage) and temporal width of the laser beam, so that the laser could be operated in either continuous or pulsed mode. To relate the intensity of the laser output to the drive voltage, a power calibration of the laser diode was carried out as shown in figure 6.5.

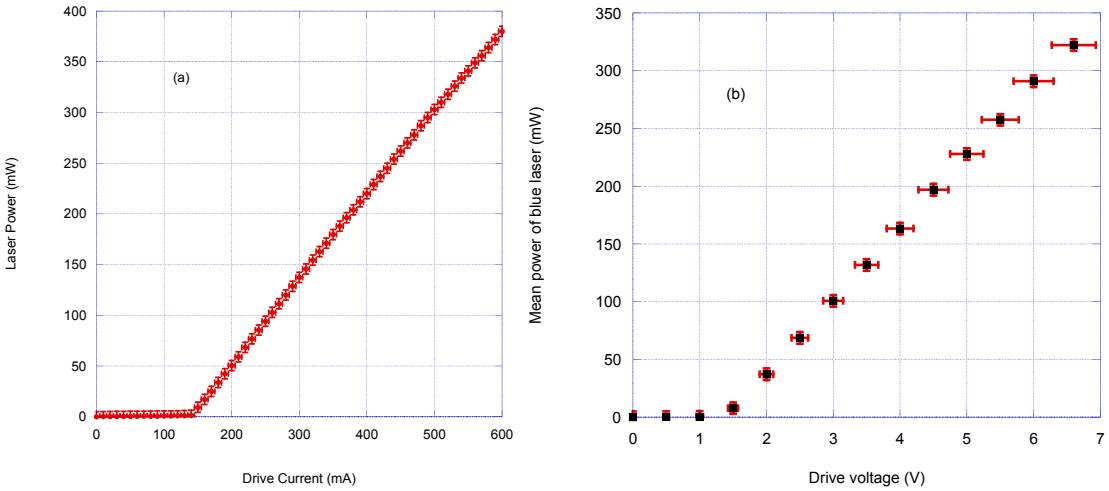

Fig 6.5: (a) Current-Power relation of the diode laser. The laser power varied linearly with applied current after the threshold current of ~145 mA. (b) Laser power against drive voltage. During normal operation the laser power was varied by changing the drive voltage via the control program.

A beam profiler (Thorlab camera BC106-VIS) was used to capture the profile of the ionizing beam at the interaction region, shown in figure 6.6. The beam has a fairly rectangular profile with an uneven power distribution. The ionizing beam was steered onto the trapped atoms using mirrors, while monitoring the fluorescence signal to maximize the overlap with the atom cloud. To ensure maximum interaction with the trapped atoms, during alignment, the laser was operated in continuous mode with a drive voltage of 4 V (~26 mW /mm^2).

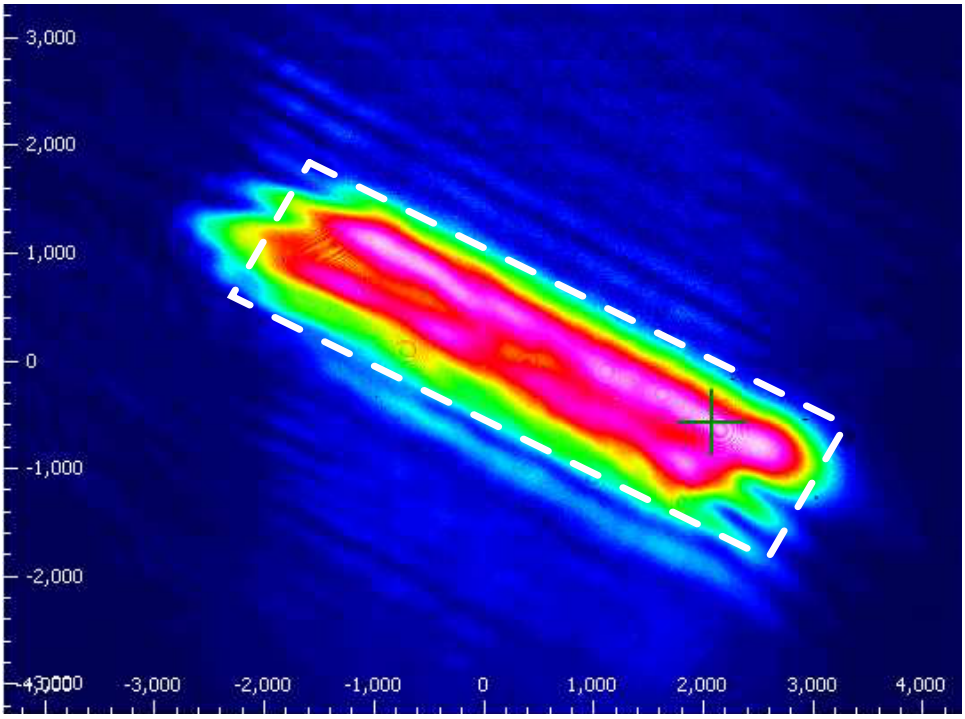

Fig 6.6: A 2-dimensional beam profile of the 445 nm blue laser diode captured with a beam profiler. The profile is fairly rectangular with an area of ~8 mm^2.

At optimal alignment, there was a high rate of ionization and so most of the atoms were removed from the trap due to photoionization, resulting in the depletion of the trap as shown in figure 6.7. The figure shows the MOT fluorescence intensity monitored with a photodiode, when laser beam of different intensities were directed on the trapped atoms. It therefore shows the effectiveness of the ionization process with this laser. For each of the ionizing laser intensities, the AC-MOT was loaded to the steady state condition before the ionizing laser was directed on the trap; this caused the MOT to decay rapidly to a new steady state level. In new steady state, the number of atoms depends on the filling rate as well as the intensity of the ionizing laser, and so gives a measure of the photoionization rate.

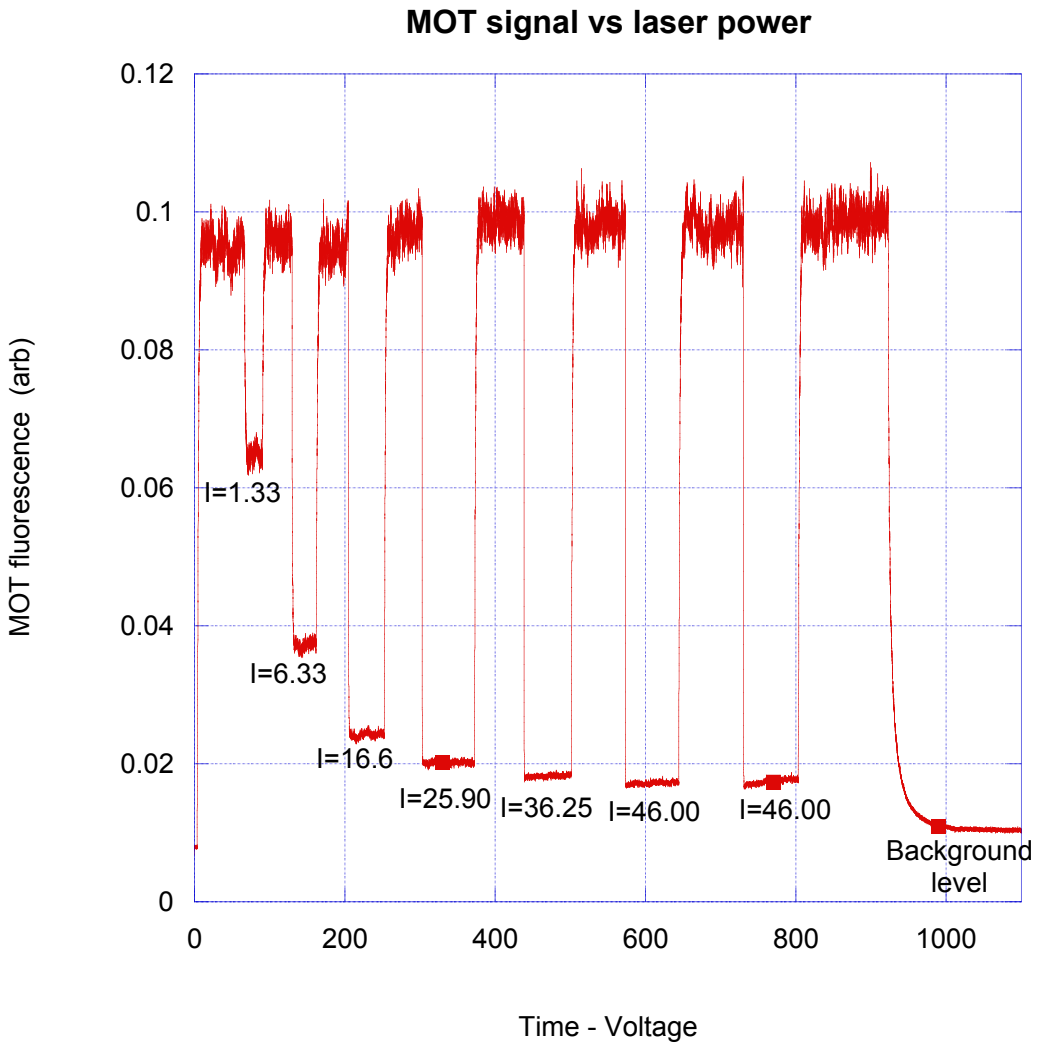

Fig 6.7: AC-MOT steady state fluorescence level for different ionizing laser intensities I (mWmm^{-2}) measured in CW mode. The plot shows the depletion of the trap due to intense ionization of trapped atoms by the ionizing laser.

6.2 Estimating the Rate of Photoionization

As noted in chapter five, different loss mechanisms inherent in the MOT determine the number of trapped atoms in the MOT, and so the evolution of the number of atoms in the trap can be described by the rate equation [14]

$$\frac{dN(t)}{dt} = L - \gamma N(t) - \frac{\beta}{V_{eff}} N^2(t) \tag{6.1}$$

where L is the loading rate, γ is the trap loss rate due to collisions with background vapour, and N is the number of atoms in the trap. The last term represents the two-body loss due to collisions between trapped atoms, where V_{eff} is the effective volume of the atomic cloud and β is the two-body loss coefficient. Equation 6.2 has a solution of the form

$$N(t) = \frac{L(1 - \exp(-2\alpha t)}{\alpha\,(1 + \exp(-2\alpha t)) + \gamma(1 - \exp(-2\alpha t)} \tag{6.2}$$

Where L is the loading rate, and α is defined as

$$\alpha = \sqrt{\gamma^2 + \frac{4L\beta}{V_{eff}}}, \tag{6.3}$$

This is a combined loss coefficient obtained by solving equation 6.1.

For $t = \infty$, (i.e. in the steady state),

$$N(\infty) \approx N_{ss} = \frac{L}{\alpha + \gamma} \tag{6.4}$$

Using equation 6.4 and 6.3, equation 6.2 can be written as

$$N(t) = N_{ss} \frac{(1 - \exp(-2\alpha t))}{1 + \frac{2N_{ss}^2 \beta}{V_{eff} L} \exp(-2\alpha t)} \tag{6.5}$$

The introduction of an ionizing laser will introduce a new loss mechanism which modifies the loss rate to γ'. Assuming a constant loading rate and that the two-body collisional term is independent of the ionizing laser, the combined loss rate becomes

$$\alpha' = \sqrt{(\gamma_0 + \gamma_{PI})^2 + \frac{4L\beta}{V_{eff}}} \tag{6.6}$$

and $\gamma' \rightarrow \gamma_0 + \gamma_{PI}$.

where γ_0 is the loss rate due to background collisions in the absence of the photo-ionizing laser, and γ_{PI} represent the loss rate due to photoionization.

Equation 6.5 is therefore modified to give

$$N(t) = N_{ss}\frac{(1-\exp(-2\alpha' t))}{1+\frac{2N_{ss}^2\beta}{V_{eff}L}\exp(-2\alpha' t)} \tag{6.7}$$

From the measurement of these loss rates both in the presence of the ionizing laser, and without the ionizing laser, the rate of photoionization can be deduced. The rate of photoionization and the absolute cross section is related to the intensity of the ionizing laser by the expression [8]

$$\gamma_{PI} = \frac{I_{eff}}{E_p}\sigma f, \tag{6.8}$$

where I_{eff} is the effective intensity of the photo-ionizing laser, E_p is the photon energy of the ionizing laser, σ is the photoionization cross section, and f is the excited state fraction. The excited state fraction f is a function of the trapping laser intensity and detuning, and for a two level system is given by

$$f = \frac{I_t/I_s}{2\,I_t/I_s + 4\left(\delta/\Gamma\right)^2 + 1} \tag{6.9}$$

where the saturation intensity $I_s = 1.77 mW/cm^2$ and Γ is the natural line-width of the excited state (6.035 MHz). In the experiments discussed here, the trapping laser detuning was $\delta = -23\ MHz$ and $I_t = 289 mW/cm^2$. This gives an excited state fraction of ≈ 0.4. The photon energy is given by

$$E_p = \frac{hc}{\lambda} \tag{6.10}$$

where h is Planck's constant, c is the speed of light, and λ is the wavelength of the ionizing laser.

6.2.1 Determination Of The Absolute Photoionization Cross Section From The AC-MOT Loading Curve

This section describes the experiment performed to determine the absolute photoionization cross-section from the loading process of the AC-MOT. From the measurement of the loading rate, loss rate and the number of atoms in the steady state, the absolute photoionization cross-section was then estimated.

The AC-MOT operated with the trapping laser detuned by $\sim -23MHz$ and with a total intensity of $\sim 289\, mW/cm^2$. The base pressure in the MOT chamber was $7.4 \times 10^{-10} Torr$, and other AC-MOT and Zeeman slower settings were as stated in chapter 5. With the laser diode drive voltage constant at $4\, V$, (equivalent to a laser intensity measured in a continuous wave (CW) mode of $\sim 26\, mW mm^{-2}$), the AC-MOT was first loaded with no ionizing laser. Subsequently, the AC-MOT was then loaded to steady state in the presence of the ionizing laser. The ionizing laser was operated in a pulsed mode, emitting one laser pulse in each AC-MOT cycle of $1.2\, ms$. This experiment was performed with different temporal widths (Δt) of the ionizing laser pulse, with the laser on only during the $400\, \mu s$ AC-MOT field off time (zero field regimes). The temporal width of the ionizing laser was set by adjusting the duty cycle of the input drive signal to the laser diode controller.

Since the ionizing laser is operated in pulsed-mode, the effective intensity I_p is proportional to the temporal width Δt of the ionizing laser, and is given by

$$I_{eff} = \frac{\Delta t}{1.2 \times 10^{-3}} * I_{cw} \tag{6.11}$$

where Δt is the temporal width of the laser pulse, and I_{cw} is the ionizing laser intensity measured in CW mode. The factor 1.2×10^{-3} is the period of the AC-MOT cycle, and so equation 6.8 can be rewritten as

$$\gamma_{PI} = \frac{\Delta t * I_{cw}}{E_p * 1.2 \times 10^{-3}} \sigma f, \tag{6.12}$$

Figure 6.8 shows the time-evolution of the number of atoms in the trap under different ionizing laser intensities.

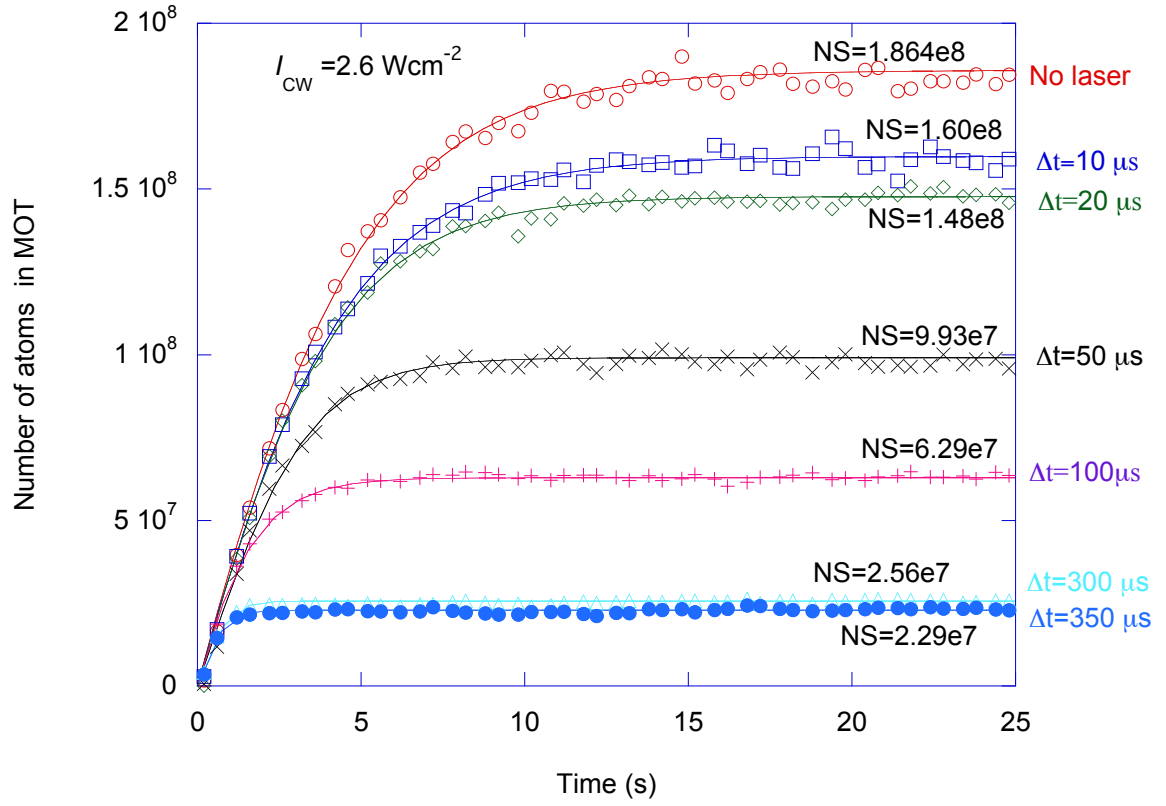

Fig 6.8: AC-MOT loading curve at different temporal widths of the ionizing laser. The number of atoms in the MOT in the steady state decreases with an increase in the ionizing laser intensity due to a higher rate of photoionization. NS *is the number of atoms in the steady state. The lines are from a fit of equation 6.7 to the data.*

The plot in figure 6.8 shows the variation in the number of trapped atoms in the MOT in the steady state with the intensity of the ionizing laser. The thick lines represent a fit of equation 6.7 to the data using a Kaleidagraph fitting routine, with a correlation coefficient greater than 0.95 for each curve. From these fits, the total loss rate γ' were deduced. In the presence of the ionizing laser, γ' is a combination of the intrinsic loss in the MOT and the loss due to photoionization. The number of atoms in the trap was measured by detecting the fluorescence from the trapped atoms. From a fit of equation 6.2 to the MOT loading curve in the absence of the ionizing laser using the same fitting routine, values for $\alpha, \gamma_0, L,$ and $\frac{\beta}{V_{eff}}$, were obtained. Using these values as initial values (for $L,$ and $\frac{\beta}{V_{eff}}$ independent of the ionizing laser), the loss rates due to photoionization γ_{PI} that corresponds to the measured number of atoms in the steady state N_{ss} were calculated from equation 6.2 and 6.6, for each ionizing laser intensity. Again using equation 6.12, the photoionization cross-section was calculated for each value of Δt. The photoionization cross section that was obtained from the data was found to be between 1.19 Mb and 1.59 Mb, with an average value of 1.49 ± 0.13 Mb.

6.2.2 Determination of the Ionization cross section from the AC-MOT decay rates.

In the previous section, the photoionization cross section was determined by measuring the loss rate due to photoionization at different ionizing laser intensities during the AC-MOT loading process. In this section, the effect of the ionizing laser on the decay rate (the AC-MOT lifetime) and the determination of the photoionization cross section from these measurements are discussed.

In this procedure, the AC-MOT was loaded to a steady state condition, and was then made to decay by closing the gate valve to stop atoms from entering the MOT chamber. This method was chosen since this resulted in a longer decay lifetime of the MOT because of reduced losses due to collision with hot atoms entering the MOT from the Zeeman slower. As noted in chapter five, the decay of the AC-MOT has two parts; a fast decay attributed to collisions between trapped atoms which dominate at high density of the atomic cloud, and a slower decay due to background gas collisions, which becomes dominant at lower densities. To reduce the contribution of the fast decay mechanism and hence obtain a more accurate analysis of the photoionization effect on the decay of the MOT, the AC-MOT was first allowed to decay to a chosen threshold before the ionizing laser was injected into the trapped atoms in the AC-MOT.

A typical AC-MOT operating with the trapping laser detuned by $\sim -23\ MHz$, has a fast decay lifetime of about 6 seconds and a slow decay lifetime of about 24 seconds as noted in chapter five, and so after two fast decay lifetimes, the AC-MOT has lost about 87% of the atoms. After this time, the effect of the fast decay mechanism was deemed to be negligible. In the results presented here, the ionizing laser was hence triggered on when the MOT had decayed to a threshold level of $\sim 1.0 \times 10^6 atoms$. The AC-MOT control program was hence set to automatically inject the ionizing laser when the MOT has decayed to this level.

The AC-MOT decay can then be described to a good approximation by the simpler rate equation

$$\frac{dN(t)}{dt} = -\gamma' N(t) \tag{6.13}$$

with a solution

$$N(t) = N_0 e^{-\gamma' t} \tag{6.14}$$

where N_0 is the number of atoms in the MOT when the ionizing laser was injected, and γ' is the modified decay rate defined to be

$$\gamma' = \gamma_0 + \frac{I_P}{E_p}\sigma f \tag{6.15}$$

Here, γ_0, is the AC-MOT decay rate in the absence of the ionizing laser, and the second term defined by equation 6.6 is the loss rate due to photoionization. The AC-MOT decay curve for a 300 μs wide ionizing laser pulse for different equivalent CW mode intensities is shown in figure 6.9.

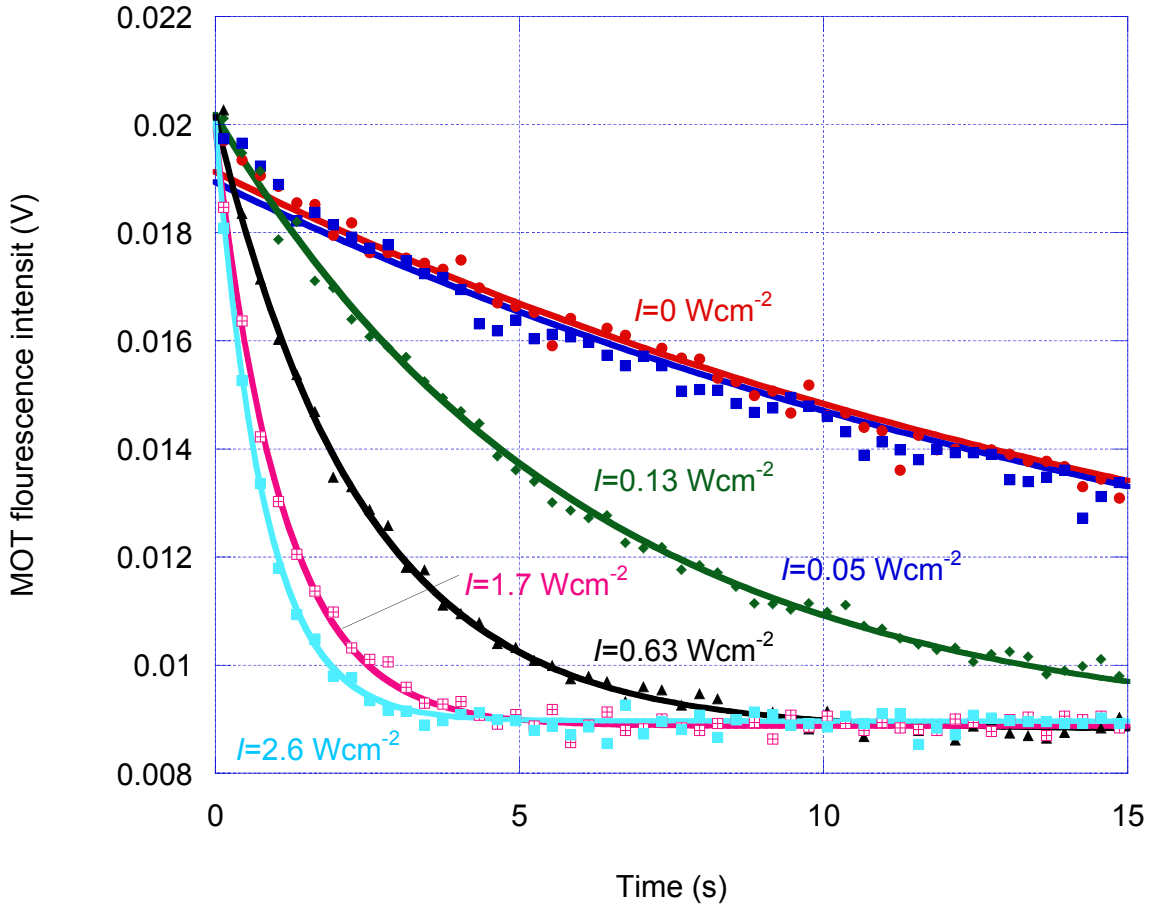

Fig 6.9: AC-MOT decay curve at different ionizing laser intensity for a 300 μs *ionizing laser pulse turned on at each AC-MOT cycle. The lines are from a fit of equation 6.15 to the data.*

This experiment was repeated for different temporal widths of the ionizing laser beam. For each ionizing laser pulse width, the decay rate was measured for different intensities. From the fit of equation 6.14 through the data, the overall decay rate was deduced and plotted against the ionizing laser intensity measured in CW mode, as shown in figure 6.10.

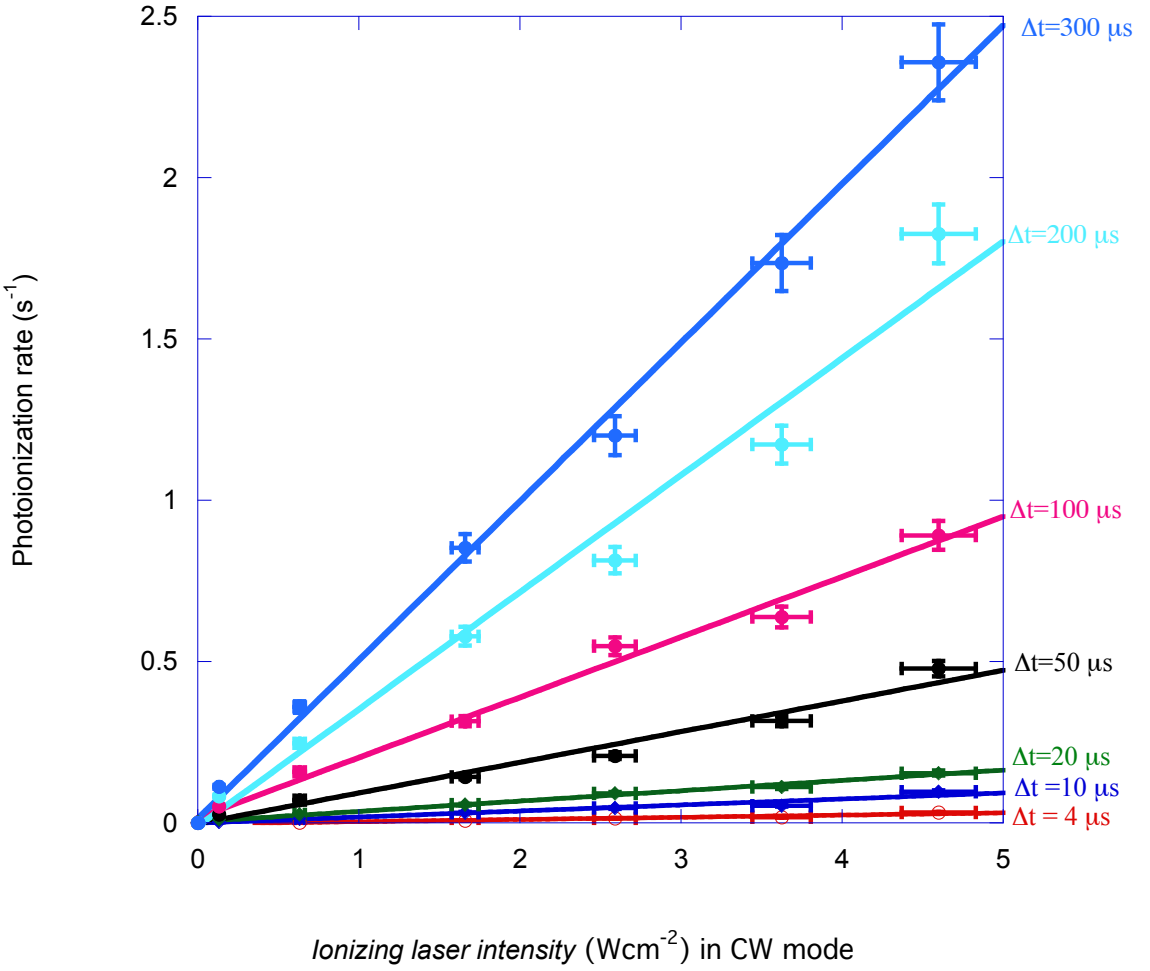

Fig 6.10: Rate of ionization for the ionizing laser of different temporal widths and intensity in a CW mode. The effective ionizing intensity is then proportional to the temporal width of the laser pulse for each set of data.

From the slope of each of the curves in figure 6.10, the absolute photoionization cross section of ^{39}K from the $4^2P_{3/2}$ excited state using the 450.4 nm ionizing laser was determined. The values obtained from these data lies between 2.12 ± 0.06 Mb and 2.65 ± 0.26 Mb, with an average value of 2.38 ± 0.18 Mb.

6.2.3 Discussion

From the above experiments, the absolute photoionization cross-section for ^{39}K from the $4P_{3/2}$ excited state by direct ionization of cold potassium atoms in the AC-MOT was calculated. At an ionizing wavelength of 450.4 nm the absolute cross section obtained from the measurement of the loss rate during the AC-MOT loading phase under photoionization was 1.49 ± 0.13 Mb. From lifetime measurement during AC-MOT decay, the mean cross-section was 2.38 ± 0.18 Mb.

These values are about a factor of 3-4 times smaller than previous values of 6.8 Mb reported by I.D Petrov et al [6] at an ionizing wavelength of 453 nm, and 7.2 ± 1.1 Mb [4] and 7.6 ± 1.1Mb by C.E.Burkhardt et al [5] from the $4P_{3/2}$ excited state of potassium with an ionizing laser of 355 nm.

In the results presented here there was good agreement between the experimental data and the lines of best fit. For all the procedures above, the rate of photoionization γ_{PI} maintained a fairly linear relationship with the ionizing laser intensity I_{eff} as predicted by equations 6.8. Fuso et al [9] showed that a deviation from the linear dependence of γ_{pi} on I_{eff} could be an indication of the occurrence of recombination of photoelectrons and ions, and charge diffusion processes in the photoionization of Cs and Rb. In the direct ionization experiment reported here, the ionizing wavelength was significantly higher than threshold, and so the emitted electrons had an excess energy of ≈ 33 meV. Therefore the difference between the results presented here and those reported in references [4-7], is unlikely to be attributable to recombination of cold plasma.

As noted above, the results from the two methods differ significantly from theoretical values [7] and from other reported experimental results [4, 5]. In calculating the loss rate due to photoionization from the AC-MOT loading process, the loading rate and the two-body loss coefficient were assumed to be independent of the ionizing laser. It has been reported that the photoionization could affect the loading rate [13], due to ionization of some background atoms before they enter the MOT. Also in an experiment to measure the rate coefficient for collisions among trapped atoms β from the loading curve of a MOT [14], it was observed that the spatial distribution of the atomic cloud deviated from a pure Gaussian function, which implies a variation in the assumed effective volume of the trap during the loading phase. These variations in both the loading rate and the effective volume, may have affected the results obtained from the loading curve.

There were several possible sources of systematic uncertainties in the experiment. A two-level system has been assumed, and the effect of radiation trapping was ignored in the estimation of the fraction of atoms in the excited state. Potassium has a complex structure, and these assumptions may result in an overestimation of the excited state fraction, since the occurrence of radiation trapping cannot be ruled out. A -23 MHz detuning with respect to the $F = 2 \rightarrow F' = 3$ transition brings the trapping laser close to resonance with the $F' = 2$ sub-level. Fluorescence from atoms in this state therefore accounted for most of the detected fluorescence, and the estimated fraction of atoms in the excited state.

Three of the MOT beams were produced by retro-reflection, and so accurate determination of the total trapping intensity was difficult. This will also contribute to the uncertainties in the estimated excited state fraction. The ionizing laser has a profile as shown in figure 6.6, and so it was difficult to get a well-collimated beam onto the interaction region. Therefore a complete overlap between the ionizing laser and the atomic cloud was not guaranteed. This also introduces some uncertainties in the measured effective ionizing intensity. The polarization of the ionizing laser in relation to the field direction was also not considered. Uncertainties due to the rise time in the ionization pulse of about $5\,ns$ were deemed negligible.

In a similar experiment carried out on cold Rubidium atoms in a MOT [15] the absolute cross-section obtained for different excited states were lower than the theoretical values [16] once again by about a factor of four. The difference between the values reported by previous authors (for both theoretical and experiment) and the values reported here is outside experimental uncertainties, and cannot be explained by recombination of emitted electrons with ions. Further investigation is therefore necessary in order to understand the origin of these differences.

6.3 Resonance Enhanced Excitation and Ionization from the $4^2P_{1/2}$ State

In the previous sections, the determination of the photoionization cross-section of ^{39}K in the AC-MOT from the $4^2P_{3/2}$ excited state has been discussed. These atoms were excited to this state by the -18 MHz detuned trapping laser. As mentioned above, ~ 40% of the atoms were in this excited state, leaving $\approx 60\%$ still in the ground state. The following section discusses the ionization of atoms from *resonant* excitation of the $4^2P_{1/2}$ excited state with the $450.4\,nm$ blue diode laser. This was aimed at enhancing the photoionization process in the AC-MOT, in order to increases the production of cold ions and electrons.

6.3.1 The Resonant Excitation Laser System

The ~ $770.1\,nm$ laser needed to excite ground state atoms to the $4^2P_{1/2}$ excited state was provided by a Spectra-Physics Matisse Ti: Sapphire (Ti:Sa) tuneable ring laser [17]. The Ti:Sa ring laser was pumped by a Spectra-Physics millennia Pro s- series $15\,W$ $Nd:YVO_4$ diode-pumped continuous wave solid state laser [18], operating at $532\,nm$. The ring laser

is capable of producing up to 3W at wavelengths ranging from 700 $nm\ to$ 1000 nm, and has a line-width of 10 kHz. A block diagram of the laser system and the AOM pulsing system used to switch the 770.1 nm light into the experiment are shown in figure 6.11.

The output of the pump laser was coupled to the ring laser via mirrors which steered and focused the 532 nm radiation onto the Ti:Sa crystal (the gain medium). The Ti:sapphire laser was stabilized with a reference cavity. The reference cavity is external to the laser and contains the reference cavity itself and the optics for a Pound-Drever-Hall (PDH) frequency stabilization scheme [19, 20]. The PDH technique works by measuring the reflected light from the reference cell. When the laser is on resonant with a cavity mode, no reflected light is measured and so the reflected light from the cavity can be used to lock the laser to the reference cavity.

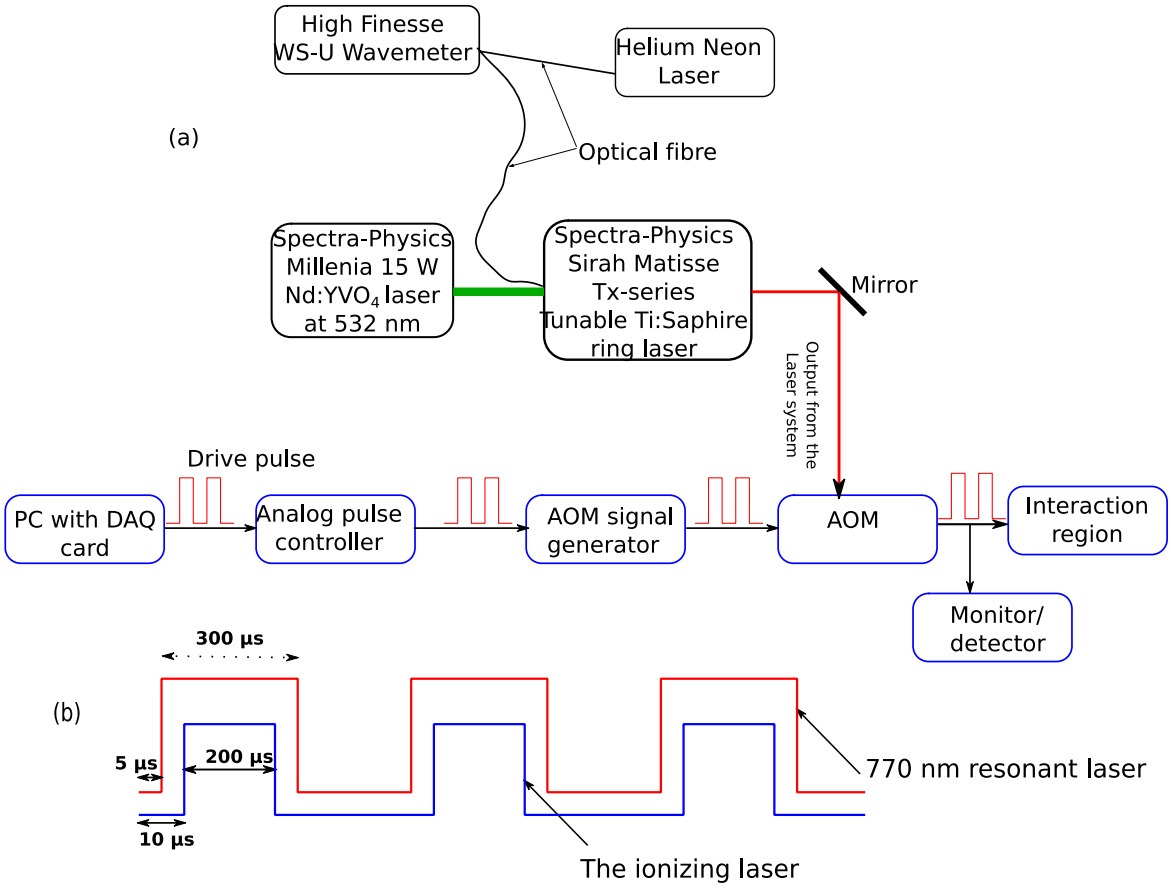

Fig 6.11: (a) The layout of the resonant laser system and the pulsing arrangement. (b) The resonant (red) and ionizing (blue) laser pulse. The ring laser was pumped by a Spectra- Physics millennia laser. The frequency of the Ti: Sapphire laser was monitored in real time using the WS-U wavemeter. The wave meter was re-calibrated every five minutes using the stabilized HeNe laser.

A detailed description of the laser system and the PDH frequency stabilization scheme are available in [17,21]. The Matisse ring laser was controlled via computer software called

Matisse Commander, and the frequency/wavelength was monitored in real time by a High Finesse WS-U wave meter.

In order to produce a pulsed beam at the interaction region, the laser beam was passed through an acousto-optic modulator (AOM), which produces two beams, one shifted in frequency by $\sim 70\ MHz$. The AOM was driven by a pulsed signal generated by the AC-MOT control program via an analogue pulse controller that modulated the radio frequency (RF) signal generator, thereby controlling application of the RF signal to the AOM. In this way the shifted beam from the AOM was switched on and off accordingly. The pulsed laser beam was then sent via an optical fibre to the interaction region

6.3.2 Exciting Atoms to the $4^2P_{1/2}$ Excited States

Due to the hyperfine structure of ^{39}K, there are four possible transitions from the $4^2S_{1/2}$ ground state to the $4^2P_{1/2}$ excited state as shown in figure 6.12.

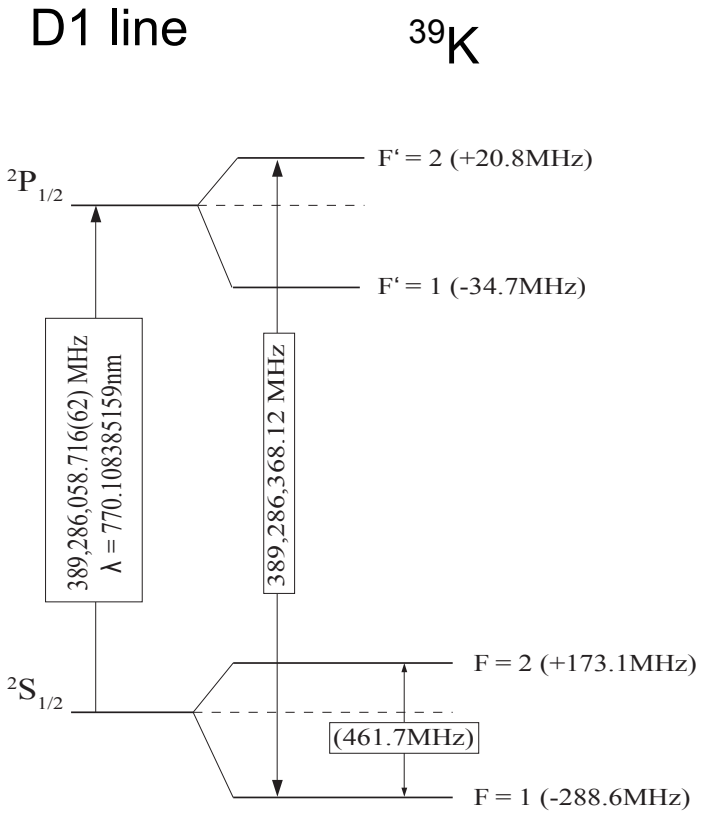

Fig. 6.12:The D1 line of ^{39}K. Atoms can be excited to the $^2P_{1/2}$ state via any of the four possible transitions namely $F = 1 \rightarrow F' = 1 = 389{,}286{,}312.6\ MHz$, $F = 1 \rightarrow F' = 2 = 389{,}286{,}368.1\ MHz$, $F = 2 \rightarrow F' = 1 = 389{,}285{,}850.9\ MHz$ and $F = 2 \rightarrow F' = 2 = 389{,}285{,}906.4\ MHz$.

To ensure an optimal interaction with the atomic cloud in the AC-MOT, the 770.1 nm resonant beam was aligned along the same path as the ionizing laser. The resonant laser and the ionizing laser were delayed by $5\,\mu s$ and $10\mu s$ respectively after the AC-MOT field was switched off, as illustrated in figure 6.11b. This was to ensure that atoms have been excited before the ionizing laser was switched on.

The AC-MOT fluorescence and time of flight ion signals were both monitored as the resonant laser was scanned through the four transitions mentioned above. It was expected that as the laser scanned through these transitions, there would be an enhanced fluorescence and ionization signal as a result of excitation of atoms from the $4^2S_{1/2}$ ground state to the $4^2P_{1/2}$ excited state. In contrast to these expectations, a sharp *decrease* in both fluorescence and ionization signals was found as the resonant laser scans through the four transitions. The time of flight (TOF) ion signal that was obtained is shown in figure 6.13.

The white feature on the blue background shows the ionization signal due to photoionization by the blue laser. When the 770 nm laser was not in resonance with any of the transitions, the ion signal was a maximum due to ionization of the $4^2P_{3/2}$ excited atoms. As the 770 nm laser scanned through the transitions there was a significant loss of atoms (ions), as indicated by the dips. Figure 6.13 (i) shows the TOF signal when the resonant laser operated in CW mode with peak power of $\sim 7.3\,mW$ scanned up in frequency and then down hence going through the transitions twice. In figure 6.13 (b), the same laser was operated at the same peak power but in pulsed mode with a temporal width $\Delta t = 300\,\mu s$. Scanned in the same manner as in 6.13 (i). As observed in figure 6.13(ii), only the $F = 1 \rightarrow F' = 2$ transition, which has the highest energy resulted in significant loss of atoms (ions) during the $300\mu s$ interaction time. These show that the magnitude of the observed dips increases with the intensity of the resonant laser and the interaction time.

The dips in the time of flight ion signal and the corresponding loss in fluorescence signal indicates a loss of atoms from the trap, however this is not found to be due to photoionization. To establish this, the ionizing laser was switched off while the 770 nm resonant laser scanned through the transition. In this case no ionization signal was observed. By contrast, the fluorescence signal obtained is shown in figure 6.14. This figure shows the AC-MOT fluorescence signal as the $770\,nm$ laser was scanned through the transitions. These results indicate that the depletion of the trap was not due to photoionization, but was rather due to the interaction of the 770 nm resonant laser with the trapped atoms.

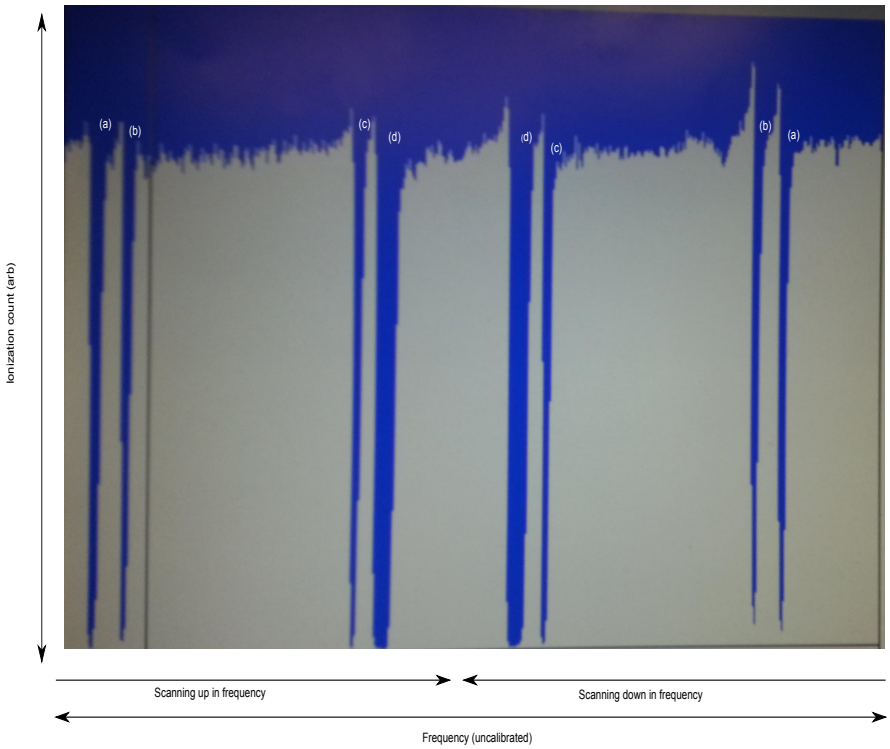

Fig 6.13 (i)

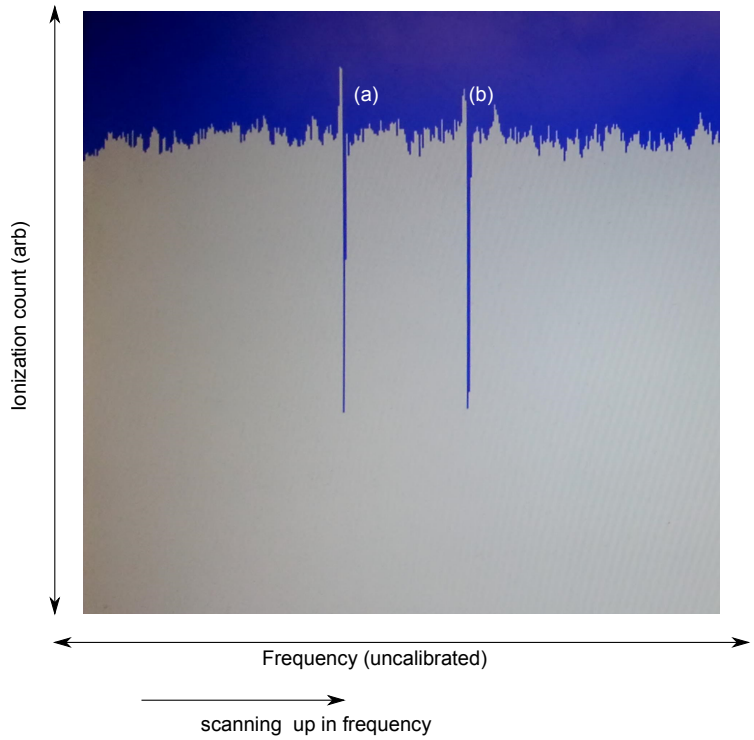

Fig 6.13 (ii)

Fig 6.13: Time of flight ion signal captured as the 770 nm scanned through the transitions, (i) CW mode at a peak power of 7.3 mW, (ii) pulsed mode with $\Delta t = 300\ \mu s$ *In (i) the dips correspond to scan through the four resonant transitions; (a)* $F = 2 \rightarrow F' = 1$, *(b)* $F = 2 \rightarrow F' = 2$, *(c)* $F = 1 \rightarrow F' = 1$, *and (d)* $F = 1 \rightarrow F' = 2$. *The four transitions are well resolved. In (ii) only the* $F = 1 \rightarrow F' = 2$ *transition has sufficient energy to result in significant loss of atoms within the interaction time of* $300\mu s$.

It is not clear why most atoms were lost from the trap at these transitions (even at low laser intensities). The 770 nm laser is not resonant with atoms in the $4^2P_{3/2}$ excited state, and consequently will not directly affect the number of atoms in that state. These results indicate that there is a mutual interaction between the atoms, and that the behaviour of the MOT signals are modified by the second laser field. Since there was no enhancement in both fluorescence level and ionization signal, it was hence concluded that the 770 nm laser impacted sufficient energy to the trapped atoms to drive them from the trap.

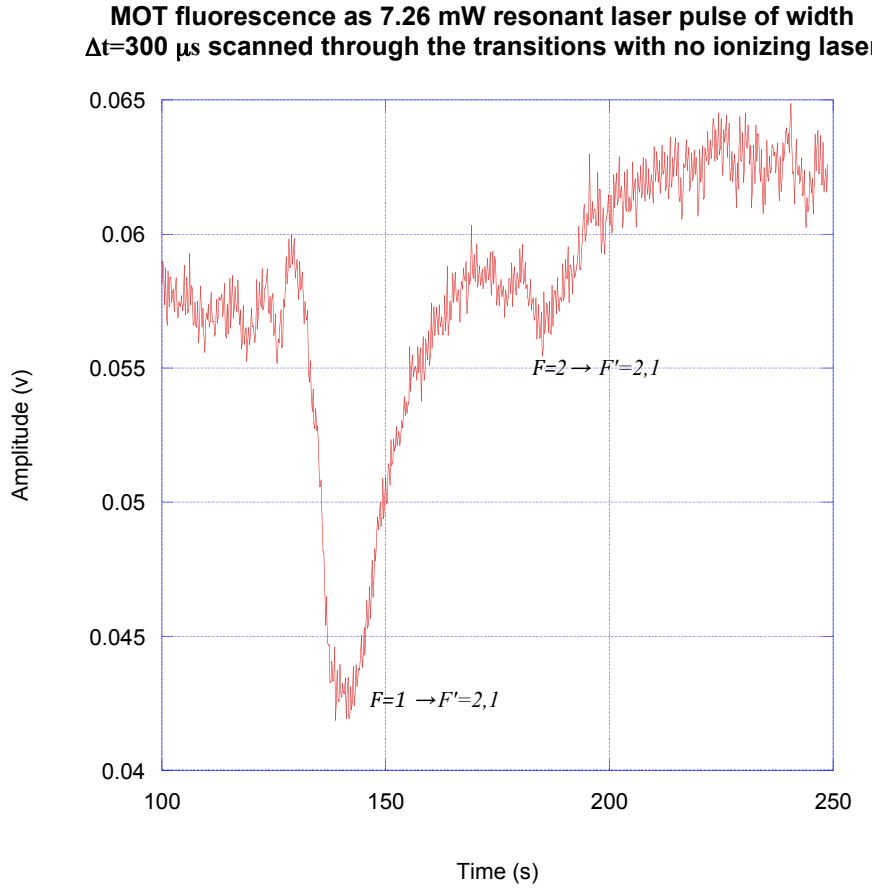

Fig 6.14: AC-MOT fluorescence signal as a $7.3\ mW$ *770 nm resonant beam was scanned in time through the* $4S_{1/2} \rightarrow 4^2P_{1/2}$ *transitions from a frequency of* $389.2865761\ THz \rightarrow 386.2857673\ THz$. *As the laser scanned through the various transitions, atoms were lost from the trap as indicated by the dips. Since the ionizing laser was switched off during this scan, the depletion of the MOT could not be due to photoionization.*

To further study this, consider an atom in the $4^2P_{1/2}$ excited state which has a lifetime $\tau = 26\ ns$. The maximum scattering force on the atom is then $F = \hbar\frac{k\gamma}{2}$, where $\gamma = 1/\tau$. The application of this force moves the atom from equilibrium. During the AC-MOT off regime, atoms in the MOT will be drifting, and so the application of the 770 nm laser radiation (which was on for $300\ \mu s$), then gives the atoms extra kinetic energy. For atoms of mass m at rest, the distance moved under the influence of this force is given by

$$s = \frac{1}{2}\left(\frac{Force}{m}\right)t^2 = \hbar\frac{k\gamma}{4 * m}t^2 = \frac{\hbar k}{4m\tau}t^2 \qquad (6.17)$$

A graph of this expression for potassium is shown in figure 6.15, and shows that atoms will have move $\approx 11.5\ mm$ in $300\ \mu s$ under the influence of this driving force.

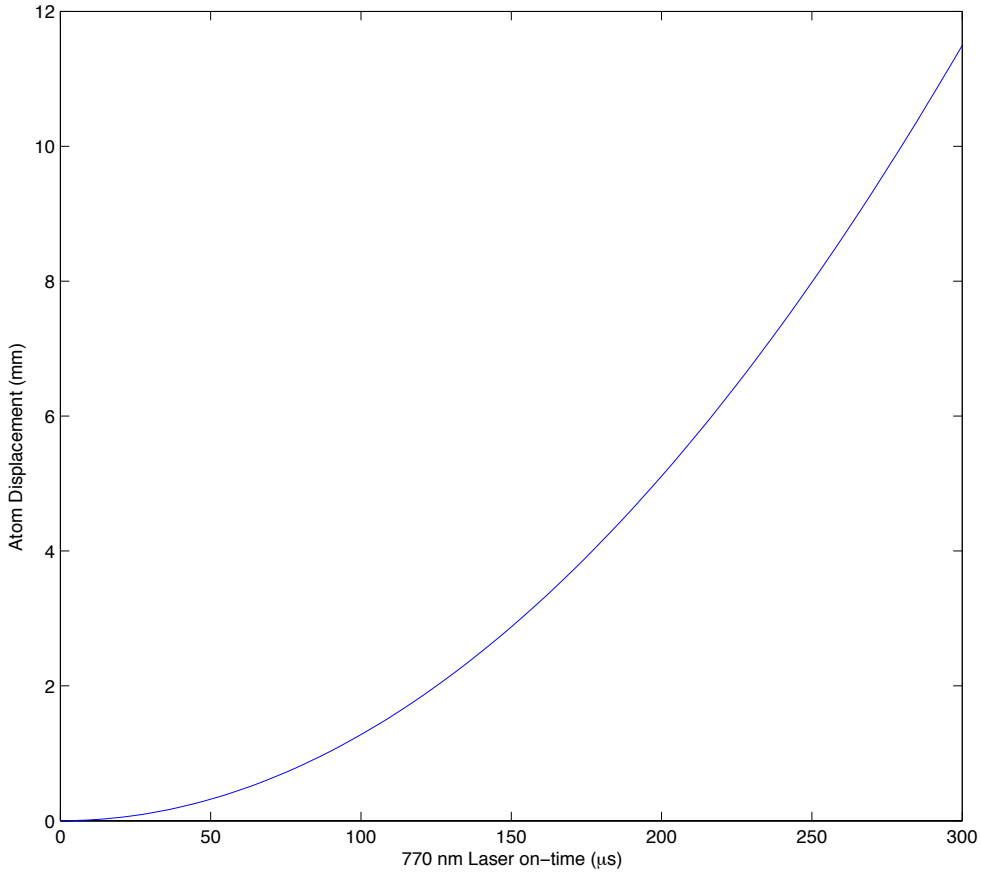

Fig 6.15: A plot of the distance moved by an atom due to the scattering force from the $770\ nm$ *resonant laser pulse of temporal width of* $300\ \mu s$, which is directed along a single direction through the MOT.

Application of the 770 nm laser does not create an optical molasses, since it only travels along one direction. This model may explain why a significant number of ground state atoms are pushed out of the trap. An investigation into the detailed dynamic of these processes is clearly desirable.

6.4 Conclusion

In this chapter, experiments on the direct photoionization of cold trapped ^{39}K atoms in the AC-MOT using a 450 nm high power light emitting diode were detailed. The profile of the ionizing laser beam and the technique adopted to produce a pulsed ionizing laser beam were also discussed. From the experiments, the absolute photoionization cross- section of potassium from the $4^2P_{3/2}$ excited state was calculated. The value obtained by measuring the loss rate during the AC-MOT loading process was $1.49 \pm 0.13\, Mb$. From measurements of the AC-MOT decay rate during the decay process, the absolute photoionization cross section was found to be 2.38 ± 0.18 Mb. The result of an attempt to ionize atoms from the $4^2P_{1/2}$ excited state by adding a second laser resonant with this transition to excite ground state atoms to this state prior to ionization has also been presented. In this case it was found that the 770 nm laser beam produced significant depletion of the trap due to the scattering force, when the laser was switched on for few tens of microseconds. In the next chapter, a stepwise spectroscopy of ultra-cold Rydberg atom will be presented, which further demonstrate the applicability of the AC-MOT to cold collision studies.

References

[1] Moskvin, Yu V. *Photoionization of atoms and recombination of ions in the vapors of alkali metals*. Optica. Spectroscopy.(USSR)(English Transl.) 15 (1963).

[2] Zatsarinny, O., and S. S. Tayal. *Photoionization of potassium atoms from the ground and excited states.* Physical Review A 81, no. 4 (2010): 043423.

[3] Nygaard, Kaare J., Robert J. Corbin, and J. Daniel Jones. *Two-step photoionization of potassium atoms*. Physical Review A 17, no. 4 (1978): 1543.

[4] Amin N., Mahmood S., Haq S.U., Kaiyar M.A., Rafiq M., and Baig M.A. *measurement of photionization cross section from the 4p, 5d, and 7s excited states of potassium.* Journal of quantitative spectroscopy &radiation transfer 109 (2008).

[5] Burkhardt C.E., Libbert J.L., Jian Xu, Leventhal J.J, and Kelley J.D. *absolute measurement of photoionization cross section of excited atoms: application to determination of atomic beam densities.* Physical Review A.38 1988.

[6] Petrov I D, Sukhorukov V L, Leber E, and Hotop N. *Near threshold photoionization of excited alkali atoms Ak(np) (Ak=Na, K, Rb, Cs; n=3-6).* Eur Phys J D 10(1) 2000.

[7] Aymar, M., E. Luc-Koenig, and F. Combet Farnoux. *Theoretical investigation on photoionization from Rydberg states of lithium, sodium and potassium*. Journal of Physics B: Atomic and Molecular Physics 9.8 (1976): 1279.

[8] Dinneen, T. P., Wallace, C. D., Tan, K. Y. N., & Gould, P. L. (1992). *Use of trapped atoms to measure absolute photoionization cross sections*. Optics letters, 17(23), 1706-1708.

[9] Fuso, F., D. Ciampini, E. Arimondo, and C. Gabbanini. *Ion processes in the photoionization of laser cooled alkali atoms.* Optics communications 173, no. 1 (2000): 223-232.

[10] Wippel, V., C. Binder, W. Huber, L. Windholz, M. Allegrini, F. Fuso, and E. Arimondo. *Photoionization cross-sections of the first excited states of sodium and lithium in a magneto-optical trap.* The European Physical Journal D-Atomic, Molecular, Optical and Plasma Physics 17, no. 3 (2001): 285-291.

[11] Lowell, J. R., T. Northup, B. M. Patterson, T. Takekoshi, and R. J. Knize. *Measurement of the photoionization cross section of the $5S_{1/2}$ state of rubidium.* Physical Review A 66, no. 6 (2002): 062704.

[12] Lorenzen, C. J., Niemax, K., & Pendrill, L. R. (1981). *Precise measurements of ^{39}K nS and nD energy levels with an evaluated wavemeter*. Optics Communications, 39(6), 370-374.

[13] Maragò, O., Ciampini, D., Fuso, F., Arimondo, E., Gabbanini, C., & Manson, S. T. (1998). *Photoionization cross sections for excited laser-cooled cesium atoms*. Physical Review A, 57(6), R4110.

[14] Browaeys, A., Poupard, J., Robert, A., Nowak, S., Rooijakkers, W., Arimondo, E., & Aspect, A. (2000). *Two body loss rate in a magneto-optical trap of metastable He*. The European Physical Journal D, 8(2), 199-203.

[15] Gabbanini, C. *Assessments of lifetimes and photoionization cross-sections at 10.6 μm of nd Rydberg states of Rb measured in a magneto-optical trap.* Spectrochimica Acta Part B: Atomic Spectroscopy 61.2 (2006): 196-199.

[16] Aymar, M., O. Robaux, and S. Wane. *Central-field calculations of photoionisation cross sections of excited states of Rb and Sr+ and analysis of photoionisation cross sections of excited alkali atoms using quantum defect theory.* Journal of Physics B: Atomic and Molecular Physics 17.6 (1984): 993.

[17] http://www.sirah.com/wp-content/uploads/pdfs/Matisse-2-TS.pdf

[18] Spectra-Physics, *Millenia Pro s-Series diode-pumped, cw visible laser sys- tems user's Manual*, 2006.

[19] Black, E. D. (2001). *An introduction to Pound–Drever–Hall laser frequency stabilization.* American Journal of Physics, 69(1), 79-87.

[20] Drever, R. W. P., Hall, J. L., Kowalski, F. V., Hough, J., Ford, G. M., Munley, A. J., & Ward, H. (1983). *Laser phase and frequency stabilization using an optical resonator*. *Applied Physics B*, *31*(2), 97-105.

[21] Knight-Percival A S. *Low Energy Super-Elastic Scattering from Laser Excited Calcium.* PhD Thesis University of Manchester 2012.

CHAPTER SEVEN

Potassium Rydberg Atoms

7.0 Introduction

The study of Rydberg atoms dates back to the late nineteenth century with the observation of the Balmer series of atomic hydrogen. These atoms, in energy states of high principal quantum number n, have since been the subject of intense studies, and have become an invaluable way of testing fundamental quantum mechanical problems. It became obvious after the formulation of Bohr's atomic theory that Rydberg atoms would exhibit unusual properties. Most of these properties are a consequence of the exaggerated orbital radius r, which scales according to n^2. Rydberg atoms are highly sensitive to their environment due to the close spacing between their energy levels and their large electron orbit [1].

Being highly excited, Rydberg atoms have very low binding energies (scaling as $1/n^2$), which gives rise to their high diamagnetic susceptibility [2]. The shift in energy levels and hyperfine splitting of atoms due to diamagnetic interaction between atoms known as the diamagnetic energy shift [2] is proportional to their geometric cross-section, and so scales according to n^4. Therefore, the detection of the diamagnetic effect is more obvious in Rydberg atoms than in ground state atoms [2]. The formation of Rydberg atoms is common in plasmas due to the recombination of electrons and positive ions; low energy recombination results in the formation of fairly stable Rydberg atoms, while formation of auto-ionizing Rydberg atoms results from high-energy recombination [3]. Their susceptibility to perturbations and ionization by electromagnetic fields is also employed in the determination of the properties of plasmas [3].

The long lifetime of Rydberg atoms makes possible the observation of radiation from outer space at a frequency of 2.4 GHz, which corresponds to the transition of a hydrogen atom from the $n = 109 \rightarrow n = 108$ [4]. This confirms the formation of Rydberg atoms in interstellar space. There is also a strong interaction between Rydberg atoms because of

their large electric dipole moment. The ability to control these interactions and their longevity makes them suitable candidates for quantum information processing [5] and for the realization of quantum computers [6, 7].

There has been renewed interest in the study of Rydberg atoms following the development of high-powered, tuneable laser systems. Using these lasers, it becomes possible to selectively excite atoms into different Rydberg states. With the development of laser cooling techniques such as the magneto-optical trap, which has the capability of producing an ensemble of cold atom with virtually no Doppler effect, attention has been shifted to the study of cold Rydberg atoms [8] by laser-exciting cold, trapped atoms. With cold atoms as a target, collective effects [9, 10], and the suppression of Rydberg excitations [11], have been observed. Other quantum mechanical and non-linear optical processes resulting from the interaction of Rydberg atoms with light are also being studied [12-15]. The study of cold Rydberg atoms has numerous significance in different areas of science, such as the formation of anti-matter [16], the formation of frozen gases of Rydberg atoms [17,18] and quantum computing [6,7].

In this chapter, new experiments demonstrating the use of the AC-MOT in Rydberg atom spectroscopy are described. First, the theory of quantum defects, Rydberg atom wave functions and the production and detection of Rydberg atoms will be discussed. Next, a detailed description of the experimental setup and procedures are presented. Finally the energy level measurements of Rydberg states from the $4^2P_{1/2}$ excited states of cold potassium in the AC-MOT are presented.

7.1 The Theory of Quantum Defects

By definition, Rydberg atoms have a highly excited valence electron, which means that the electron spends significant time far from the inner core of the atom. This electron therefore “feels” only a central Coulombic force, and so one electron Rydberg atoms such as alkali metals, can be described reasonably well by the model of a hydrogen atom. This is strictly true as long as the electron never gets close to the core, as for circular Bohr orbits. Assuming the electron is in a highly elliptic and low orbital angular momentum ($l \leq 3$) [1] as illustrated in figure 7.1, the Rydberg electron will at some point during its orbit come close to the core.

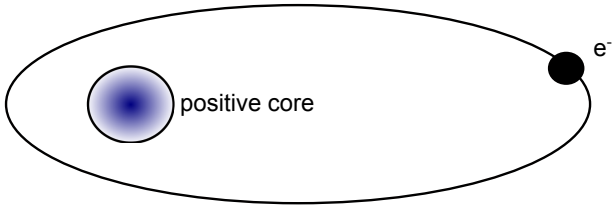

Fig 7.1: An illustration of a Rydberg atom. The electron orbits around the atomic core. For hydrogen the core is a point charge, for other one electron Rydberg atoms, the core is made up of Z nuclear charges and $Z-1$ inner shell electrons, where Z is the atomic number. In states with high angular momentum l, the one electron Rydberg atom can be represented as a hydrogen atom. In states with low l, the electron penetrates and polarizes the inner shell of the core, and so perturbations will occur.

While for hydrogen the electron sees a point charge at the nucleus, non-hydrogenic atoms will be exposed to the positive ionic nuclear charge due to core penetration and polarization. This results in an increase in the binding energy, and so reduces the energy of the Rydberg state. The deviation of Rydberg atoms from a purely hydrogenic model is known as the *quantum defect*.

7.1.1 Rydberg atom wave-functions

Potassium like other alkali metals, has to a good approximation one valence electron orbiting around an ionic core, made up of a nuclear core of charge $+Ze$ shielded by a cloud of electrons of charge $-(Z-1)e$, where Z is the atomic number and e is the electronic charge. The valence electron can hence be described by the Schrödinger wave equation

$$\left(-\frac{\hbar^2}{2m}\nabla^2 - V(r)\right)\psi(r,\theta,\phi) = E\psi(r,\theta,\phi) \tag{7.1}$$

Where $V(r)$ is the potential of the system. For a hydrogen atom, $V(r) = \frac{1}{4\pi\epsilon_0 r}$, where ϵ_0 is the permittivity of free space. E is the energy and r is the distance between the electron and the ionic core. For alkali metals, the potential is an l-dependent core potential $V_c(r)$, given by [19]

$$V_c(r) = -\frac{Z_{nl}(r)}{r} - \frac{\alpha_c}{2r^4}\left(1 - e^{-\left(\frac{r}{r_c}\right)^6}\right) \tag{7.2}$$

where the first term describes the Coulomb potential for a radial charge $Z_{nl}(r)$, which accounts for core penetration. The second term describes the long range potential due to

the induced core polarization of the valence electron, where α_c is the core polarizability, which increases with the number of electrons in the core, and r_c is the core radius.

Equation 7.1 can be expressed in spherical polar co-ordinates, and is then separable into radial and angular parts, such that $\psi(r,\theta,\phi) = R(r)Y_l^{ml}(\theta,\phi)$. The angular equation and its solution for a one electron Rydberg atom is the same for that of a hydrogen atom, with solutions described by the spherical harmonic eigenfunctions $Y_l^{ml}(\theta,\phi)$, which depends on the orbital angular momentum l of the Rydberg state.

For a hydrogen atom, the Coulomb potential is due to the point charge of a proton, however for a one-electron Rydberg atom the point charge is replaced by a finite-sized ionic core. When far from the core, the electron feels a Coulomb potential identical to that due to the point charge of a proton. At a small orbital radius, it feels a potential different to the Coulomb potential of a proton, due to electron penetration of the core and due to polarization of the electron cloud. Consequently the wave function of a one electron Rydberg atom differs from that of a hydrogen atom because of the modified potential given by equation 7.2 [1]. As stated above, the valence electron "sees" a lower potential at small r, which results in an increase in the kinetic energy of the electron and a decrease in the wavelength of the radial wave function when compared to hydrogen. This therefore imposes a new boundary condition at a distance $r > r_0$, where r_0 is the radius of the non-hydrogenic ion core. In this region the wavefunction of the non-hydrogenic Rydberg atoms is shifted in phase to that of hydrogen, and is given by [1]

$$\psi_{ryd}(\theta,\phi,r) = \frac{Y_l^{ml}(\theta,\phi,r)[f(E,l,r)\cos\pi\delta_{nlj} - \mathrm{g}(E,l,r)\sin\pi\delta_{nlj}]}{r} \tag{7.3}$$

And the allowed energies are then given by

$$E = -\frac{R_y}{\left(n-\delta_{nlj}\right)^2} \tag{7.4}$$

In equation 7.3, $Y_l^{ml}(\theta,\phi,r)$ are the spherical harmonics, $f(E,l,r)$ and $\mathrm{g}(E,l,r)$ are oscillatory functions which are 90° out of phase, and are referred to as the regular and irregular Coulomb potentials respectively [20, 21]]. The phase shift δ_{nlj} is known as the quantum defect, n is the principal quantum number and R_y is the Rydberg constant for the atom which is given by [1]

$$R_y = \frac{Z^2 e^4 m_e}{16\pi^2\epsilon_0^2\hbar^2} \tag{7.5}$$

For potassium, the Rydberg constant is $109735.774\ cm^{-1}$ [22]

Equation 7.4 can be written as

$$E = -\frac{R_y}{n^{*2}} \tag{7.6}$$

where $n^* = n - \delta_{nlj}$ is known as the *effective* quantum number. The properties of alkali metals like potassium are determined by the effective quantum number n^*. The quantum defect δ_l has an empirical form given by the Rydberg-Ritz formula [1]

$$\delta_{njl} = \delta_0 + \frac{\delta_2}{(n-\delta_0)^2} + \frac{\delta_4}{(n-\delta_0)^4} + \frac{\delta_6}{(n-\delta_0)^6} + \cdots, \tag{7.7}$$

Where δ_0, δ_2 ..., are the Ritz coefficients which depend on the orbital angular momentum l and the total angular momentum j.

7.2 Methods of Production and Detection of Rydberg Atoms

The renewed interest in the study of Rydberg atoms is partly attributed to the development of new techniques of producing these atoms, especially with the availability of tuneable lasers. In early studies of Rydberg atoms, techniques like electron impact excitation [23, 24] and charge exchange [25] were widely used. Although simple to implement, one of the drawback in the use of these techniques is that they were inefficient for selective excitation, resulting in the production of an entire spectrum of Rydberg states. Following the development of tuneable lasers with narrow line-width, optical excitation methods are now mostly used to produce Rydberg atoms. In optical excitation, it is possible to selectively excite atoms to different n-Rydberg states by choosing the appropriate photon energy. In each of the methods mentioned above, the cross section for excitation to a Rydberg state scales according to n^{-3} [1]. The combination of collisional and optical excitation [26] is another effective method of producing Rydberg atoms, especially for atoms whose transition from the ground state requires light of a shorter wavelength than is possible to produce with laser systems.

In the experiments described here, optical excitation was used to produce high-n (up to $n{\sim}200$) Rydberg states of potassium in the AC-MOT, and so these will be discussed in more detail. A brief discussion on the techniques used in the detection of Rydberg atoms is also presented.

7.2.1 Optical Excitation

One of the fundamental differences between optical excitation and other methods of creating Rydberg states is that the exciting photon is absorbed by the target atom. The Rydberg state that is produced is then specified by the energy of the absorbed photon. Figure 7.2 shows different optical excitation mechanisms that can be used to excite alkali metals to Rydberg states. In B, a single photon is absorbed by the ^{2}S ground state and the atom is excited to the n^2P Rydberg state. Different vales of n are chosen by varying the wavelength of the laser. Although this single photon mechanism is simple and only one laser is required, only the ^{2}P states can be prepared due to the restriction imposed by the selection rule for dipole transition that $\Delta l = \pm 1$. In A and C, known as two-photon excitation, two photon of the same wavelength are absorbed simultaneously by the target atom. In this mechanism, only one laser is required and both ^{2}S and ^{2}D states can be prepared since these transitions are permitted by the selection rules.

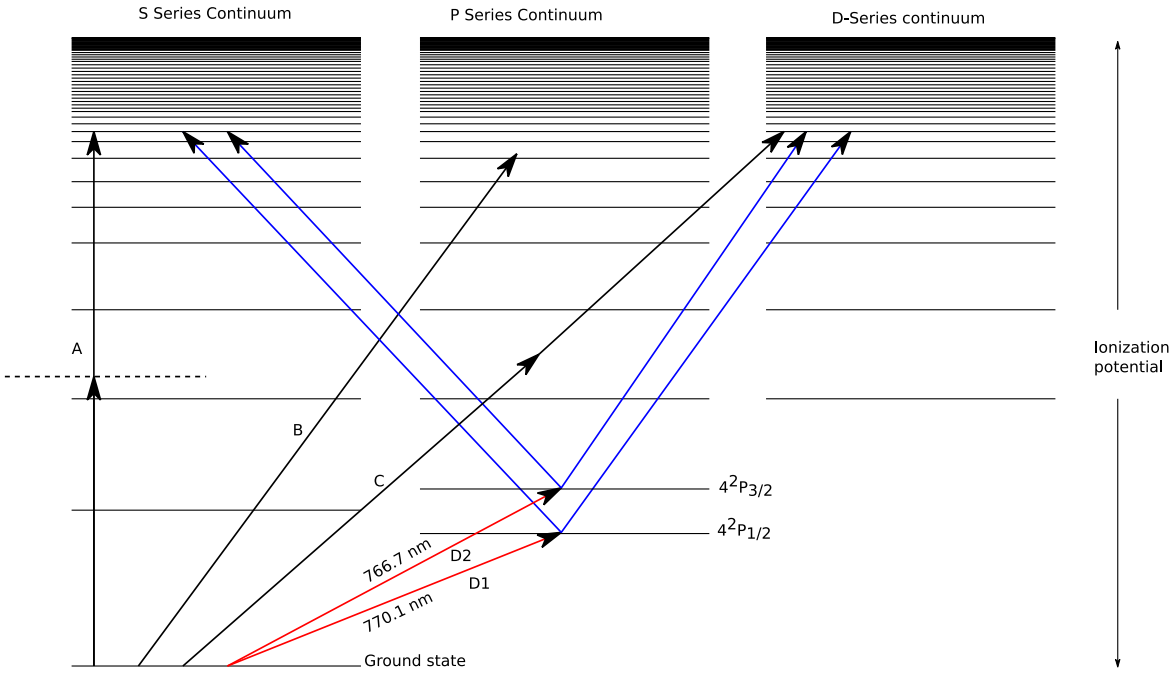

Fig 7.2: Optical excitation mechanisms. A. Two-photon excitation to n^2S state. B. One photon excitation to the P state. C. Two-photon excitation to n^2D state. D1 and D2. Stepwise excitation to n^2S and n^2D states. The step-wise excitation methods D1 and D2 were used in the experiments detailed in this thesis.

The probability of two-photon transitions is about four to five orders of magnitude smaller than that of dipole transitions [27], and is proportional to the square of the photon flux. High laser intensity is hence required to produce a significant number of Rydberg atoms. In the step-wise photo excitation mechanism represented by D1 and D2, two or more photons are used to excite an atom to Rydberg states. In potassium and other alkali atoms, the first laser excites atoms to the low-lying ^{2}P state, which has a large oscillator strength.

The second laser then excites the atom from the p-state to n^2S or n^2D states. Although at least two lasers are required, this step-wise mechanism has a high efficiency of producing Rydberg atoms, because of the large transition probability and the availability of high power lasers at the particular wavelengths involved. Since both the S and the D states may be excited, it is therefore possible to investigate the dependence of Rydberg atom collisions on the state of the atom. In the following experiments with trapped atoms, this step-wise photon excitation process was used to excite cold atoms to different n^2S and n^2D states, ranging from $n = 18$ up to $n{\sim}200$.

In optical excitation, the resolution of the measurement is limited by the Doppler Effect and the finite line-width of the laser. Since these experiments were performed with cold-trapped atoms, which virtually eliminate any Doppler effect, the resolution of the measurements was limited by the line-width of the excitation laser, which is assumed to be larger than the line-width of the Rydberg states.

7.2.2 Methods of Detecting Rydberg Atoms

The size and polarizability of Rydberg atoms plays an important role in their detection. Some of the methods of detecting Rydberg atoms are as follows:

A. **Optical Absorption method:-** The radiative decay of Rydberg atoms to lower lying states is accompanied by the emission of a photon with a characteristic wavelength. This is one of the oldest means of detecting Rydberg atoms. It was in fact the detection of these photons in the Balmer series of atomic hydrogen that led to the discovery of the Rydberg constant. Due to the small coupling between the Rydberg state and other states, only a small amount of light can be absorbed by the atom, and so high laser intensity is required to make the detection by this means more sensitive.

B. **Electromagnetically induced transparency (EIT):** - This is a non-destructive method of detecting Rydberg atoms. It exploits the strong dipole-dipole coupling between Rydberg atoms. In this method, there is no absorption or the associated rapid variation in the dispersion due to the atoms [28, 29], and hence it is possible to detect the desired Rydberg state without significant dispersion. Since the detected atoms are reusable from this technique, the EIT method is the preferred method of detecting Rydberg atoms for application in quantum information experiments.

C. Field Ionization: - This is the ionization of Rydberg atoms by the application of an electric field. Rydberg atoms have very low ionization potentials, and so only a moderate electric field is needed to ionize them. The ions or electrons that are produced can then be detected by charged particle detectors like channel electron multipliers (CEM), or Micro-channel plates (MCP). From the characteristics of the detected ions or electrons, the respective Rydberg states can be isolated. Since the magnitude of the field required to ionize the Rydberg atoms depends on the principal quantum number n and scales as $1/n^4$, it is therefore possible to select the Rydberg state that is to be detected.

D. Collisional Ionization: - The large diameter of Rydberg atoms makes them susceptible to collisions with neutral atoms or other Rydberg atoms. Since the valence electron of Rydberg atoms are in a weakly bound orbit, such collisions result in the ionization of the Rydberg atom. As in field ionization, the resulting ion or electron can be detected by a charged particle detector. Since no electric field is required in this experiments, all available Rydberg state in the system can be detected, with different states being identified from the characteristics of the detected electrons or ions.

7.3 Step-Wise Spectroscopy of Ultra-cold Potassium Rydberg Atoms in the AC-MOT

Following the successful direct photoionization of cold potassium atoms in the AC-MOT using the $450\ nm$ diode laser as described in chapter six, a newly commissioned blue tunable dye laser was used in an attempt to ionize the trapped atoms at several different photon energies (wavelengths). In the process of scanning the laser through different wavelengths, ionization signals from different Rydberg states of potassium were observed. In this section, a description of the step-wise spectroscopy of the Rydberg states of ultra-cold potassium atoms trapped in the AC-MOT is given. Although the experimental procedures for excitation from both the $4^2P_{1/2}$ and $4^2P_{3/2}$ states of ^{39}K are described, only energy level data obtained for Rydberg states from $18D$ to $\sim 200S$ excited from the $4^2P_{1/2}$ states of ^{39}K are presented here.

7.3.1 The Experimental Setup

The AC-MOT trapping laser from a Ti:Sapphire laser operating at $\sim 766.7\, nm$ red-detuned by $\sim 23\, MHz$ provided the stepwise excitation route from the ground state to the $^2P_{3/2}$ state. Atoms in the $^2P_{3/2}$ state were then excited to different high-n Rydberg states by radiation from the blue tunable dye laser. To excite the atoms from the $^2P_{1/2}$ state, the atoms were stepwise-excited by a second Ti:Sapphire laser operating at $\sim 770\, nm$, followed again by radiation from the blue dye laser. Collisions from the cold Rydberg atoms resulted in significant ionization of the excited targets, and the Rydberg states were detected from the ionization signal as measured using a time of flight detector configured to detect ^{39}K ions. The energy levels of potassium relevant to this experiment are shown in figure 7.3.

In figure 7.4, a schematic diagram of the experimental setup is shown. It shows the cooling and trapping laser for the D2 line, the laser system used to excite ground state atoms to the D1 line, and the blue dye laser used for the excitation to high Rydberg states. The diagram also shows the AC-MOT beam and coil configurations, and the frequency stabilization setup used to lock the cooling and trapping laser produced by the Coherent MBR-100. The Coherent Ti:Sapphire laser and its locking system, the Zeeman slower and AC-MOT have already been described in chapters 4 and 5. The additional components required for the high-n Rydberg state spectroscopy are now briefly described.

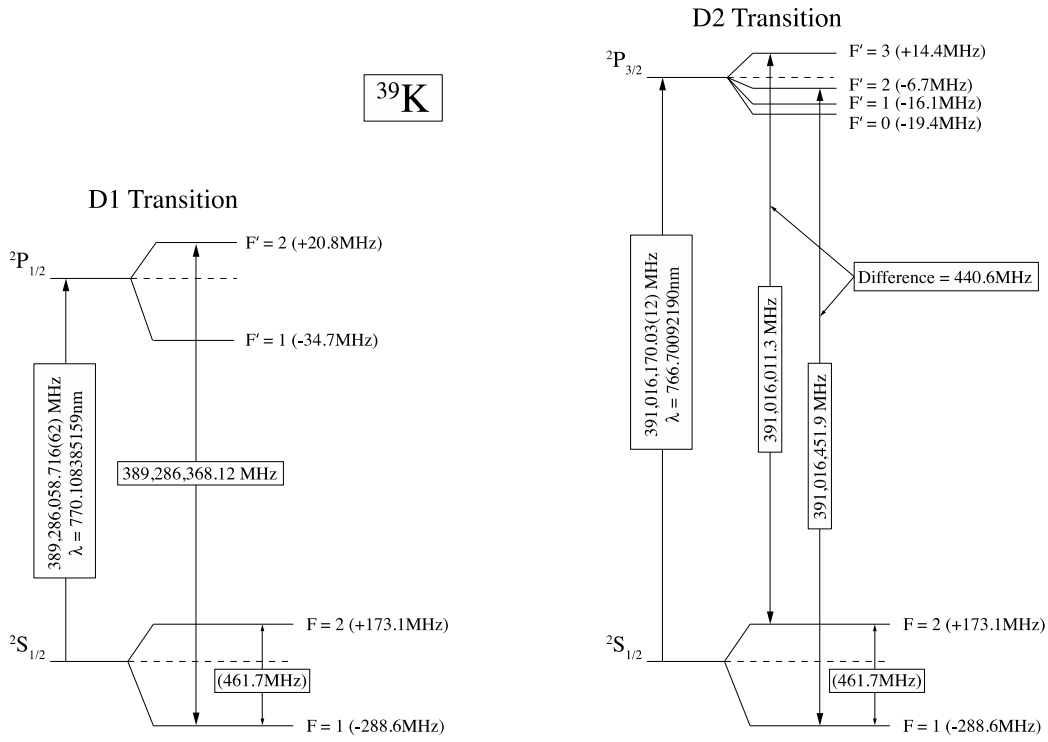

Fig 7.3: Energy level of potassium showing the hyperfine splitting of the ground state and the splitting for the first excited states. The cooling transition is resonant with the $^2P_{3/2}$ state and was using $\sim 766\ nm$ *radiation red-detuned by* $\sim -23\ MHz$ *from resonance, and so the cooling beam was at* $391{,}015{,}997.3\ MHz$*. A re-pump beam also was used that was blue detuned by* $+441\ MHz$ *from the cooling laser and so was at a frequency of* $391{,}016{,}438.3\ MHz$*. For transitions to the D1 state, radiation of* $\sim 770\ nm$ *was used to resonantly excite the* $F' = 2$ *transition from the ground state at a frequency of* $389{,}286{,}361.12\ MHz$ *before further excitation to the Rydberg state by the blue laser. The* $770\ nm$ *beam was switched on and off by an acousto-optic modulator (AOM) operating at* $-70\ MHz$*, so the laser was tuned to* $389{,}286{,}368.12\ MHz + 70\ MHz = 389{,}286{,}438.12\ MHz$*.*

7.3.2 The D1 Excitation Laser

The radiation for the stepwise excitation of atoms to the D1 state was produced by a Matisse TX-model Ti:Sapphire laser, which has a line-width of $\sim 10 kHz$. The excitation was accomplished by setting radiation from the Matisse Ti:Sapphire laser to the appropriate frequency of $f_1^{F=1\rightarrow F'=2} = 389{,}286{,}368.12\ MHz$. Since excitation of atoms was to occur when the AC-MOT magnetic field was off, the beam from this laser was rapidly switched on and off. This switching was accomplished by first passing the output of the laser through a gated AOM operating at $\sim -70\ MHz$. The Matisse laser was then returned to $389{,}286{,}368.12\ MHz + 70\ MHz = 389{,}286{,}438.12\ MHz$ in order to produce resonance with the $F = 1 \rightarrow F' = 2$ D1 transition in the trapped atomic cloud. This transition could be monitored by observing fluorescence from the AC-MOT.

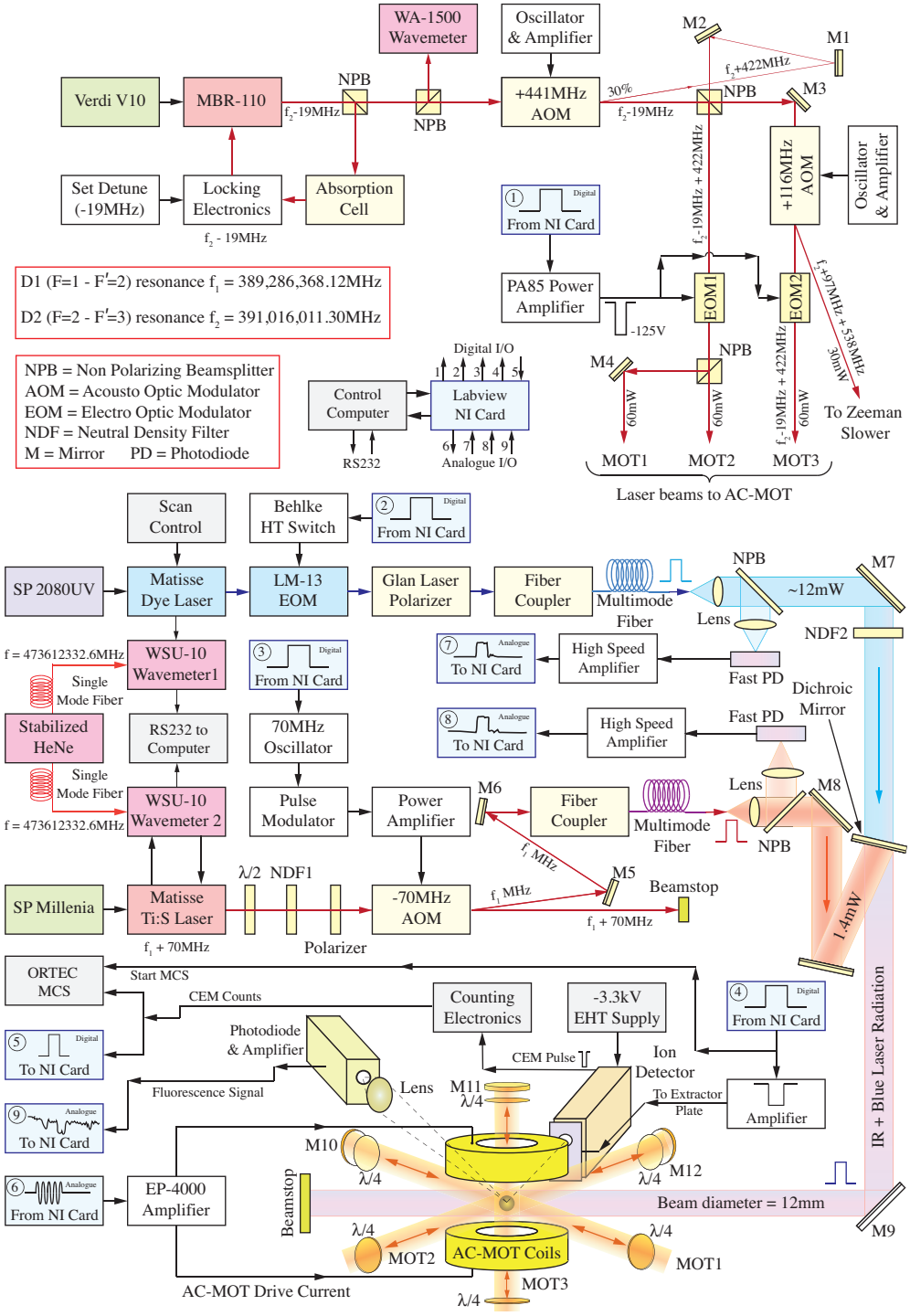

Fig 7.4: Schematic diagram of the apparatus, showing the laser systems and the detectors that were used during the experiment. The figure shows the cooling and trapping laser (MBR-100), the resonant excitation laser to the $^2P_{1/2}$ state (Matisse Ti:S laser), and the blue dye laser (Matisse dye laser) used to further excite the atoms to the high-n Rydberg states.

The Matisse Ti:Sapphire was set to the required frequency using a High finesse WSU-10 wave-meter, which was calibrated to a SIOS SL-02 stabilized Helium-Neon laser (HeNe) operating at an output frequency of 473,612,332.6 MHz. The wave-meter was re-calibrated every 5 minutes to this HeNe reference source. The output from the Matisse Ti:Sapphire laser with an output power of about 1.2 W at 770 nm, was initially passed

through a half wave plate ($\lambda/2$ plate), a neutral density filter (NDF1) and a linear polarizer in order to reduce the power to $< 120\,mW$ prior to entering the AOM. The primary beam from the AOM was not used in the experiment and so was dumped. The switched beam was sent to a fibre coupler that launched the light into 50m of multimode optical fibre, which had a core diameter of $50\,\mu m$. The output power of the pulsed beam was varied by adjusting the output from a Thurlby-Thandar oscillator operating at $70\,MHz$. The oscillator output was sent to a high-speed analogue gate that was controlled by a TTL pulse sent from the AC-MOT control program, after which it was passed to a mini-circuits 5W power amplify. The width of the gate (which set the temporal width of the laser pulse), the delay (with respect to a set master trigger pulse), and the pulse rate were all controlled using the AC-MOT control program.

Light exiting from the fibre was quasi-collimated and directed into the vacuum chamber using a series of dichroic mirrors and lenses to produce a beam with a diameter of $\sim 12mm$ at the interaction region. The peak power in each pulse was set to $\sim 1.4mW$, so that the intensity at the interaction region was about $18\mu W mm^{-2}$. The laser pulse from the fibre was monitored using a fast photodiode and amplifier, and the amplified signal sent as an analogue signal to the NI card connected to the computer. This signal was also monitored by the AC-MOT control programme.

7.3.3 The Blue Tunable Dye Laser

Excitation of either the $4^2P_{1/2}$ or $4^2P_{3/2}$ states to high-n Rydberg states was accomplished using radiation from a Matisse DS tunable dye laser, that was pumped by a Spectra-Physics 2080 UV Ar^+ laser operating at 4-5W. The Matisse dye laser has a tunable range from ~418 nm to ~470 nm using the selected dye (Coumarin-450), and the laser was found to be stable with an output power of ~150 mW over a period of two to three weeks when using this dye. The DS-dye laser has a line-width of ~500kHz. The Matisse dye laser frequency was again monitored using a High–Finesse WU-10 wave-meter, which was also calibrated using the stabilized HeNe laser every 5 minutes.

Since excitation to the high-n Rydberg states by the blue laser was required when the AC-MOT magnetic field was zero, the output of the blue dye laser was passed through a Linos LM-13 EOM phase modulator and Glan-laser polarizer. The EOM switched the polarization of the light by $\lambda/2$ using a high voltage pulse from an HTS-21-06-GSM Behlke switch. The combination of pulsed EOM phase modulator and polarizer, allowed

the blue laser to be switched on and off, with a contrast ratio of better than 65:1. This switching was again achieved by sending a gated pulse from the NI DAQ card to the Behlke switch that supplied the EOM voltage. The pulse-width and delay of the blue laser pulse was again set directly from the control program.

The pulsed blue laser output exiting the polarizer was sent to a fibre optic coupler that launched the light into a second 50m long multimode fibre that had a core diameter of $200\mu m$. The output from this fibre at the experiment was quasi-collimated and steered through one of the dichroic mirrors that were used to direct the 770nm light into the interaction region, as shown in figure 7.4. This was to ensure that the blue laser and the infrared laser beams from the two Matisse laser systems were co-linear along their paths. The diameter of the blue beam was also set to ~12 mm at the interaction region. The maximum power of the blue laser beam at the interaction region was between$\sim 12mW - 15mW$, depending on the age of the dye. This was further attenuated using a series of neutral density filters (NDF2 on figure 7.4) in the beam path, with attenuations of up to 32X used during the experiments. The intensity of the blue beam could hence be varied from $120\mu W mm^{-2}$ (no filter) to $\sim 4\mu W mm^{-2}$ (32X attenuation) at the interaction region.

The blue laser pulse was monitored prior to attenuation using a non-polarizing beam splitter (NPB) that directed some of the light to a fast photodiode and fast amplifier. As with the 770 nm pulsed laser beam, the output of the amplifier was sent to the NI card for monitoring. The photodiode amplifier output was also directed back to a monitoring system at the Matisse dye laser, so that the EOM could be adjusted to ensure maximum on/off contrast ratio in the pulsed laser beam as the wavelength was changed. During a scan of the blue laser, the EOM was periodically adjusted to maintain maximum contrast for the laser pulse at the interaction region.

7.3.4 Fluorescence Monitoring and Ion Detection

Fluorescence from the trapped atoms was imaged onto an additional photodiode external to the vacuum chamber, as was discussed in chapters 5 and 6. During studies of the high-n Rydberg states, the fluorescence signal from the MOT was used to determine when the laser beams were on resonance with a transition, by monitoring the changes in the trap density as the laser passed through different resonances in the cold atom ensemble.

As stated above, the collisions between the high-n Rydberg atoms resulted in significant ionization. These ions were extracted from the trapping region using a weak pulsed

extraction field whose duration and time delay was controlled by the Labview programme. The amplitude of the extraction field at the interaction region could be adjusted from $0\,Vm^{-1}\ to\ -30\,Vm^{-1}$ using a high-speed pulsed amplifier. The extraction plate was constructed from high transmissivity tungsten mesh (95% transmission) that was located just before the Channel Electron Multiplier (CEM), biased to detect ions using a $-3.3kV$ HT supply. The output current pulses from the CEM were input to a high speed pre-amplifier whose output was sent to an ORTEC 473A constant fraction discriminator (CFD). The output of the CFD was sent to the NI card for counting, and was also sent to an ORTEC Multi-Channel Scalar (MCS) that allowed the time signature of the ion pulses to be measured.

7.3.5 The Experimental Control

As mentioned above, the signals required to operate the experiment were derived from a national instruments PCI-6221 card located on the computer bus. Figure 7.5 shows a block diagram of the control signals from the card, as set by a Labview programme developed for this experiment. This control programme is similar to that described in chapter 5, with a few modifications. The Zeeman slower loaded AC-MOT operated in pulsed mode such that over the AC-MOT cycle of 1.2 ms set by the master clock, current was delivered to the MOT coils for $600\ \mu s$, followed by an AC-off time of $600\mu s$ where no current passed through the coils. The MOT laser beams remained on during the full AC-MOT cycle so as to provide a molasses force during the AC-MOT off period when the trapping magnetic field was zero. These trapping beams also provided the stepwise excitation of atoms to the $F' = 3,2,1,0$ excited states of the $^2P_{3/2}$ manifold. These atoms could then be further excited to high-n Rydberg states using radiation from the blue laser. Excitation of atoms to the $4^2P_{3/2}$ hyperfine manifold made it possible to directly excite atoms to the $n^2S_{1/2}$ $n^2D_{3/2}$ and $n^2D_{5/2}$ states.

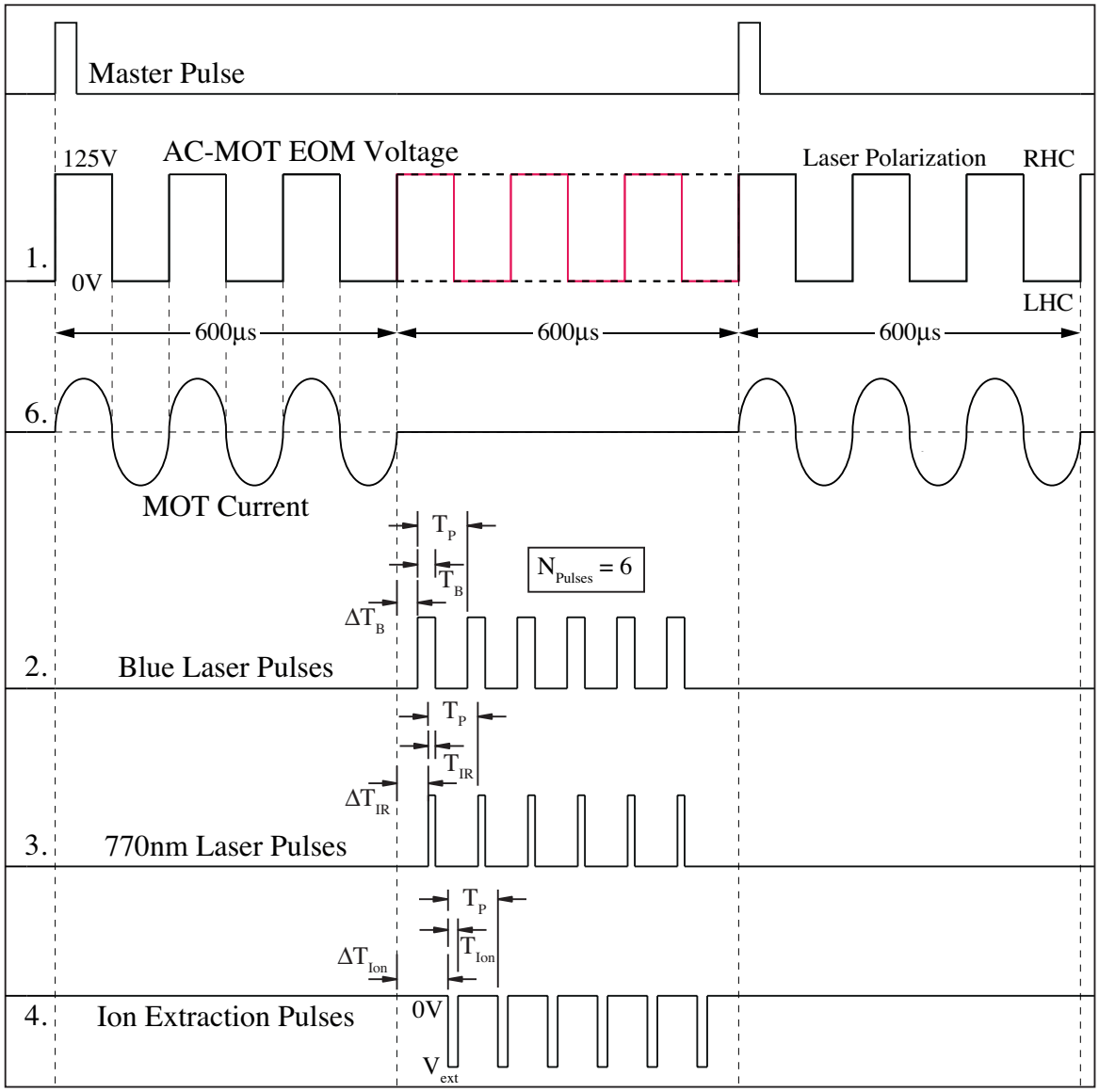

Fig 7.5: The experimental control signals. The master pulse has a duration of $1200\mu s$ *which is equivalent to the one AC-MOT cycle. The blue laser, the 770 nm laser as well as ion extraction occurred during the* $600\mu s$ *AC-MOT off regime. The time delay delays for each of the pulses were set relative to the AC-MOT current cycle.*

As shown in figure 7.5, excitation of the cold atoms in the AC-MOT using the blue and the on-resonance ~770 nm infrared pulse laser beams, as well as the extraction of ions were all carried out during the 600 μs period when the AC- **B**-field was off. From the $4^2P_{1/2}$ $(F' = 2)$ state the blue laser could only excite the $n^2S_{1/2}$ and $n^2D_{3/2}$ states due to restrictions imposed by the selection rule. In order to ensure that the **B**-field had fully returned to zero prior to laser excitation, a time delay was introduced for each of these events with respect to the end of the MOT current cycle. From the control programme, the initial time delays $(\Delta T_B, \Delta T_{IR})$, the ON time of each of the laser pules (T_B, T_{IR}), the time between pulses(T_P), and the number of pulses that were used during each cycle of the **B**-

field were set. In the example shown in figure 7.5, six pulses of both the blue and the 770 nm IR laser were used.

The extraction of ions was accomplished using the ion detector, which supplied a negative going pulse of voltage V_{ext} to the extraction plate as shown in figure 7.5. This signal was also controlled by the control programme, which set the initial time delay ΔT_{Ion}, the width of the extraction pulse T_{Ion}, the time between extraction pulses T_P and the number of extraction pulses N_{pulses}. This flexibility in timing allowed different experiments to be conducted. This included experiments where the extraction field overlapped with the laser excitation field in time and experiments where the extraction field was temporally separated from the laser excitation pulse as shown in figure 7.5. Typical extraction voltages of $V_{ext} = -2.5\ V$ were used during the experiments, except where the effect of the electric field of the extraction mesh was being investigated. This resulted in an extraction field at the interaction region of $\approx 2.5\ Vm^{-1}$ $(25 mV cm^{-1})$.

The PCI-6221 card was also useful in monitoring various analogue signals from the experiment. These included a direct measurement of the fluorescence from the MOT using analogue input (9) in figure 7.4. Signals from both the blue and infrared laser pulses were monitored using inputs (7) and (8) as shown. The slow NIM signals from the 473A constant fraction discriminator (CFD) derived from the Channel Electron Multiplier (CEM) pulses were input to the Labview programme through one of the digital input ports on the card. The fast signals from the CFD were sent to a dedicated ORTEC Multi-Channel Scalar (MCS), which allowed the time of flight of the ion signals to be determined with a temporal resolution up to 5ns. The X719BL CEM used in this experiment has a recovery time of ~ 5 to $10 \mu s$, and so any saturation of the CEM signal could be monitored by the MCS. This saturation of the detector, which occurs when more than one ion hits the surface of the CEM within its recovery time, was hence monitored.

7.5 Energy Level Measurements

Energy level measurements of potassium Rydberg states from both $^2P_{3/2}$ and $^2P_{1/2}$ states were carried out. Detailed description of the experiments is presented here, followed by the results. The measured energy levels were compared with theoretical values obtained using the Rydberg-Ritz formula. The accuracy of the WSU-10 wave meter used in measuring the resonant frequencies of the states was determined by comparing the measured energy level with the available energy level data from NIST.

7.5.1 Measurement from $^2P_{3/2}$ state

As noted above, excitation of the cold atoms to the high-n Rydberg state from the $^2P_{3/2}$ state followed a two-step excitation scheme. Figure 7.6 shows an illustration of the actual excitation scheme adopted. The process started with the formation of a magneto optical trap of potassium cooled to a temperature of about 300 μK.

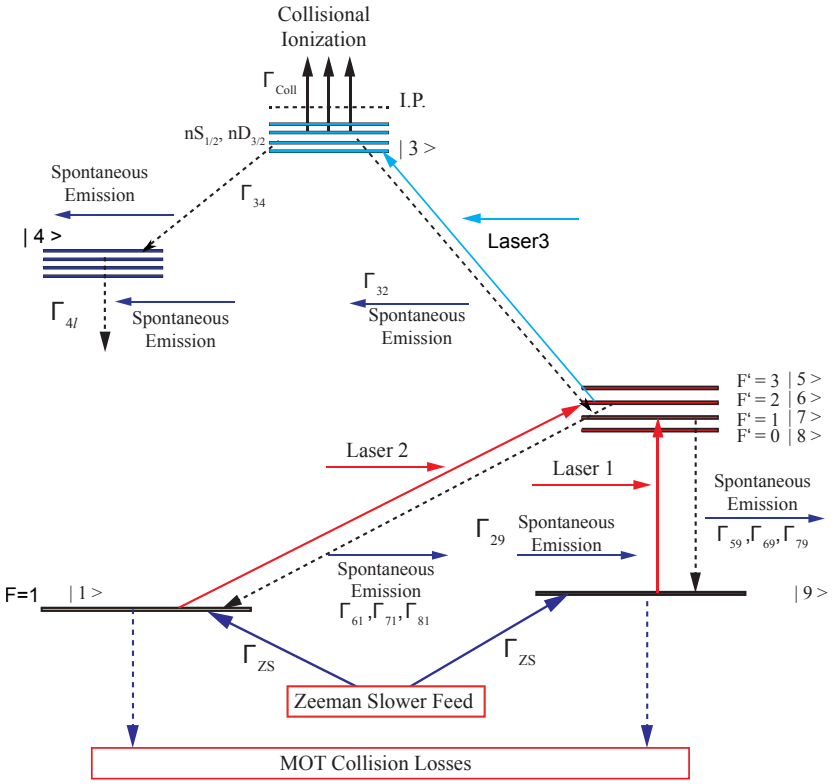

Fig: 7.6: Two-step excitation schemes to high-n Rydberg states for the $4^2P_{3/2}$ excited states. Excitation to different hyperfine sub-levels is shown with the various decay processes. The Zeeman slower prepared the atoms into the ground state hyperfine levels before being trapped in the AC-MOT. Lasers 1,2 (main trapping and re-pump laser beams) excited the atoms to different hyperfine levels, while excitation to the high-n Rydberg states was provided by laser 3.

The 766.7 nm MOT trapping laser, red-detuned by ~23 MHz relative to the $F = 2 \rightarrow F' = 3$ transition provided the first step of excitation to the $^2P_{3/2}$ state (D2 line). Subsequently radiation from the blue dye laser was directed onto the trapped atoms, while it scanned over the whole range of the wavelengths covering the Rydberg manifold from $18D \rightarrow \sim 200S$. During each AC-MOT cycle, the blue laser pulse with a peak intensity of $\sim 18\ \mu W mm^{-2}$ at the interaction region, was switched on for $\sim 10 \mu s$. As the blue laser scanned through different states, selective excitation to different Rydberg states occurred. Since excitation to the Rydberg states occurred during the AC-MOT off period (MOT magnetic field reduced to zero), and owing to the large orbits and sensitivity to their surrounding, collisions between Rydberg atoms resulted in significant ionization. The ions

that were generated were then extracted from the interaction region using the bias mesh and were detected by the channel electron multiplier (CEM). The resulting signal was displayed against the blue laser wavelength. In these experiments the extraction voltage pulse supplied to the mesh was -5V, and was $\sim 2\mu s$ wide.

To investigate the effect of the extraction field on the ion production, these experiments were repeated for cases where the extraction pulse and the blue excitation laser were overlapped in time, as well as when they were separated in time. The results are discussed later in this chapter.

7.5.2 Measurement from the $^2P_{1/2}$ state

Only about 40% of the trapped atoms in the AC-MOT were excited to the $^2P_{3/2}$ states by the trapping laser, leaving nearly 60% still in the ground state. For Rydberg excitation from the $4^2P_{1/2}$ state, the 770 nm infrared laser was directed along the same path as the blue laser onto the trapped atoms. This laser was tuned to be in resonance with the $F = 1 \rightarrow F' = 2$ excited state, and so provided the stepwise excitation of ground state atoms to the $4^2P_{1/2}$ state. This excitation scheme is illustrated in figure 7.7.

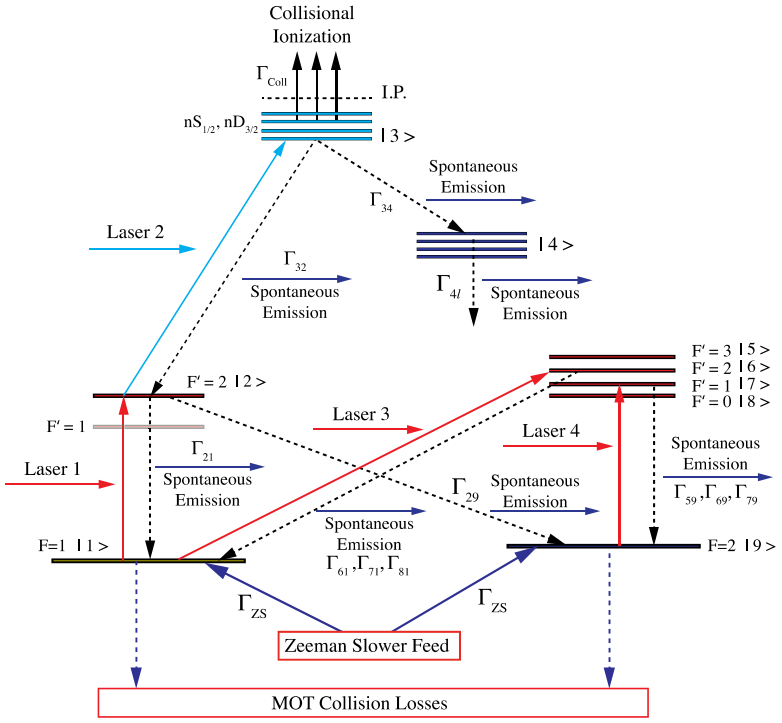

Fig: 7.7: Two-step excitation schemes to high-n Rydberg states for the $4^2P_{1/2}$ excited states. Excitation to different hyperfine sub-levels is shown with the various decay processes. The Zeeman slower prepared the atoms into the ground state hyperfine levels before being trapped in the MOT. Only about 40% of atoms were excited by the trapping laser, leaving nearly 60% still in the ground state Lasers 1,3 and 4 excited the atoms to different hyperfine levels, while excitation to the high-n Rydberg states was provided by laser 2.

With the 770 nm IR beam locked at this transition, the blue laser was scanned through the Rydberg series. The ionization signal was then detected as the laser scanned through various Rydberg states. An example of the observed spectra from the $4^2P_{1/2}$ state is shown in figure 7.8. From this state only the n^2S and $n^2D_{3/2}$ states could be excited, since transitions to the $n^2D_{5/2}$ state are forbidden because of restrictions imposed by angular momentum selection rules.

The excitation frequencies were extracted by fitting a Gaussian function to the ionization spectra. A typical fit is shown in figure 7.8, where the blue spectrum is the ionization spectrum and the red lines are from the Gaussian fit. From these fits the excitation frequencies corresponding to each observed peak, and the spectral width of the peaks were determined. In the following sections, only the energy level data for Rydberg states excited from the $4^2P_{1/2}$ are presented.

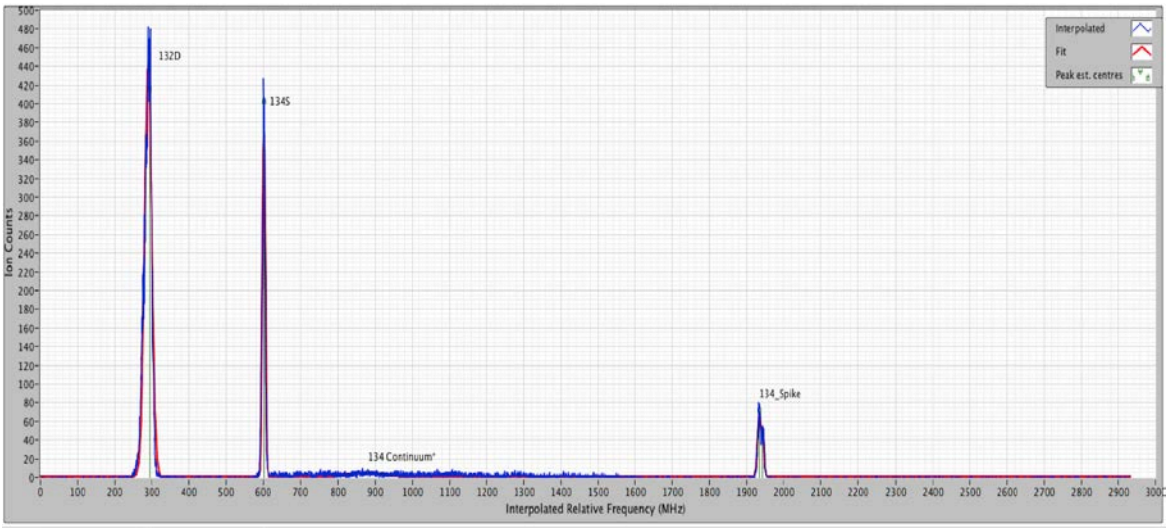

Fig 7.8: A typical ionization spectra in blue color, showing the excitation to the $132D_{3/2}$ and 134S Rydberg states. The additional features - the 'continuum' and 'spike' are discussed later in the chapter. From a Gaussian fit (indicated by the red line) to each peak, the frequency amplitude and width of each were determined.

7.5.3 Wave-Meter Frequency Offset Corrections

The accuracy of the measured frequencies from the High finesse WSU-10 wave-meter was calculated by comparing these frequencies to that of the available energy level data from NIST [30]. The difference between the measured frequency and NIST values for $n = 18$ to $n = 46$, for transitions from the $F = 1$ ground state (measured C0-NIST(F=1 GS) in Fig 7.9), were obtained and plotted for both S and D states, as shown in figure 7.9. From the combined plot (figure 7.9(c)), the average difference between the measurements from the wavemeter and the NIST values was $-3.59 \pm 0.83\ MHz$. This difference represents

the frequency offset of the wave-meter, and so +3.59 MHz was added to the measured values to obtain the correct excitation frequencies.

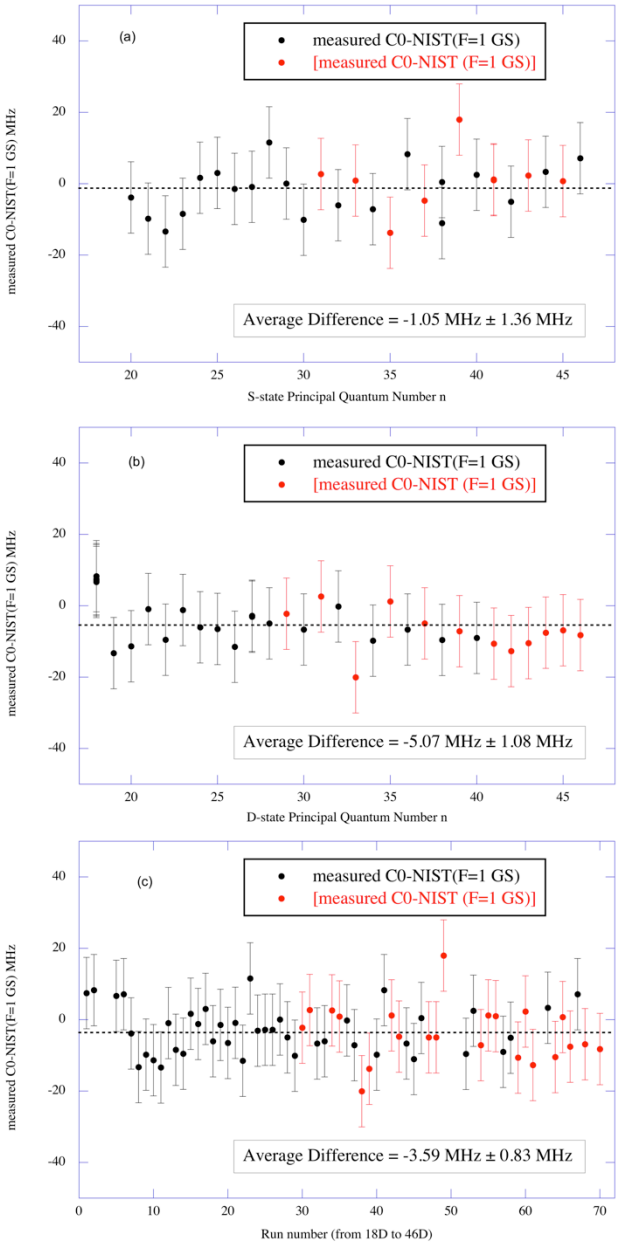

Fig 7.9: Frequency difference between the current measurements and values from NIST. The plot shows the difference from the S-state measurements (a), the D-state (b) and the combined plot of S- and D-state (c). An average difference of $-3.59 \pm 0.83\ MHz$ *was obtained. The black plots represent difference between the measured frequency and empirical data and the difference between the measured frequency and the extrapolated values from NIST are represented by the red plots.*

7.5.4 The Observed Energy Level Spectra

The measured energy level spectra of potassium Rydberg states with calibrated frequencies for $n = 18D$ up to $n = 200S$ are shown in figures 7.10- 7.14. The plots show

the spectra of the S-states from $n = 20$ to $n = 200$, and the D-states from $n = 18$ to $n = 167$. From around $n = 102$, two new additional features emerge, one adjacent to the S-state in the blue wing of the resonance (here called '*continuum*'), and a second feature at about half way between nS and $(n-1)D$ states, here referred to as '*spikes*'. To identify these additional features, the measured energy levels were compared with the theoretical values calculated using the extended Rydberg-Ritz formula;

$$E_{nl} = E_{IP} - \frac{R_{K^{39}}}{\left(n - \delta_0 + \frac{\delta_2}{(n-\delta_0)^2} + \frac{\delta_4}{(n-\delta_0)^4} + \frac{\delta_6}{(n-\delta_0)^6} + \frac{\delta_8}{(n-\delta_0)^8}\right)^2} \qquad (7.8)$$

where E_{nl} is the energy of the state, and E_{IP} is the ionization potential at limit. The values of the Rydberg constant $R_{K^{39}}$ and the Ritz coefficients $\delta_0,\ \delta_2,\ \delta_4,\ \delta_6\ and\ \delta_8$ were taken from [22], and are listed in table 7.1. Each of the calculated energies for $nS, nD_{3/2,}\ nP_{1/2}$, $nP_{3/2}, nF_J$ and $l \geq 4$ states could then be calculated.

$States$	δ_0	δ_2	δ_4	δ_6	δ_8
$n^2S_{1/2}$	2.1801985	0.13558	0.0759	0.117	−0.206
$n^2D_{3/2}$	0.2769700	−1.024911	−0.709174	11.839	−26.689
$n^2D_{5/2}$	0.2771580	−1.025635	−0.59201	10.0053	−19.0244
$n^2P_{1/2}$	1.713892	0.233294	0.16137	0.5345	−0.234
$n^2P_{3/2}$	1.710848	0.235437	0.11551	1.1015	−2.0356
n^2F_J	0.010098	−0.100225	1.56334	−12.685	0
$l > 3$	0	0	0	0	0

Table 7.1: Ritz coefficients for different states of ^{39}K taken from Lorenzen & Niemax (1983) [34].

From these parameters the energies of each of the Rydberg states were calculated up to n=200, for the allowed transitions to $^2S_{1/2}$, $^2D_{3/2}$, $^2D_{5/2}$ Rydberg states, and also to the *dipole- forbidden states* shown in the bottom four rows of table 7.1. In this way the energy of all the state in potassium for principal quantum numbers n up to 200 were estimated.

These parameters are for excitation from the *centre of gravity* of the ground state, which is +288.6 MHz above the F=1 ground state. The data from NIST is from the F=2 ground state, which is +466.1 MHz above the F=1 ground state. Hence the energy E_{PI} above the ionization potential is from the centre of gravity, so with respect to the F=1 ground state, $E_{IP} = 1{,}049{,}567{,}813.32\ MHz + 288.6\ MHz = 1{,}049{,}568{,}101.92\ MHz$. The Rydberg constant is unchanged and is given by $R_{K^{39}} = 109735.774\ cm^{-1} = 3{,}289{,}741.80\ MHz$.

Plots of the spectral lines of the states are shown in figures 7.10 - 7.14, with the estimated values from the Rydberg Ritz formula represented by the colored dots. From these plots, the measured energy levels are seen to be in good agreement with the theoretical predictions for $n \leq 130$. Above $n = 130$, the measured energy levels do not agree with the calculated values, resulting in a frequency shift (energy shift) which increases with principal quantum number n. It appears that the new feature adjacent to the S-state initially occurs where the higher angular momentum ($l \geq 3$) states are expected, whereas the spikes appear to correspond well to excitation of the dipole-forbidden ^{2}P-states. Similar structures have been observed in the Rydberg spectra of Rubidium at n~80 [31], however they were not identified. It is not yet clear whether excitation to the dipole-forbidden ^{2}P-states is due to S- and D-state admixtures induced by strong interaction between Rydberg atoms, or is due to mixing of states due to stray fields in the interaction region. However, since the field in the interaction region is very small, we believe that strong interactions between high-n Rydberg atoms are primarily responsible for both features.

The effective Rabi frequency Ω, for the transition to the Rydberg states is given by the simplified expression in rad/sec [37]

$$\Omega = 2\pi \sqrt{\frac{375}{4c\pi^3 h}} \sqrt{\lambda^3 \Gamma}\, \sqrt{I} \tag{7.9}$$

Where λ and I are the wavelength and intensity (in mW/mm^2) of the excitation laser respectively, Γ is the line-width of the transition, c is the speed of light and h is the Planck's constant. The line-width for the transition to Rydberg states (only up to 13s) are available on the NIST web page, which can be extrapolated to higher n. This shows that the line-width scales approximately as n^{-4} for the S-state, and n^{-5} for the D-state, as shown (in radians/sec) by equation 7.10a and 7.10b.

$$\Gamma = 9.74 \times 10^8 n^{-3.9092} \tag{7.10a}$$

for the S-state and

$$\Gamma = 3.8409 \times 10^{10} n^{-4.7426} \qquad (7.10b)$$

for the D-state. Using these equations, the line-width of the transitions to the 20S and 100S states were calculated to be $8141.71\, rad/sec$ and $15.23\, rad/sec$ respectively. Similarly, the line-width for transitions to the 20D and 100D Rydberg states are $25951.84\, rad/sec$, and $12.56\, rad/sec$ respectively.

With a laser intensity of $\approx 18 \mu W/mm^2$ (0.018 mW/mm^2) as used in this experiment, and using the appropriate laser wavelength, the Rabi frequency for excitation to 20S and 100S states are $0.93\, Mrad/sec$ and $0.0039\, Mrad/sec$ respectively. The Rabi frequency for excitation to 20D and 100D states is $0.166\, Mrad/sec$ and $0.0037\, Mrad/sec$. In this way, the Rabi frequency for any given Rydberg excitation can be calculated.

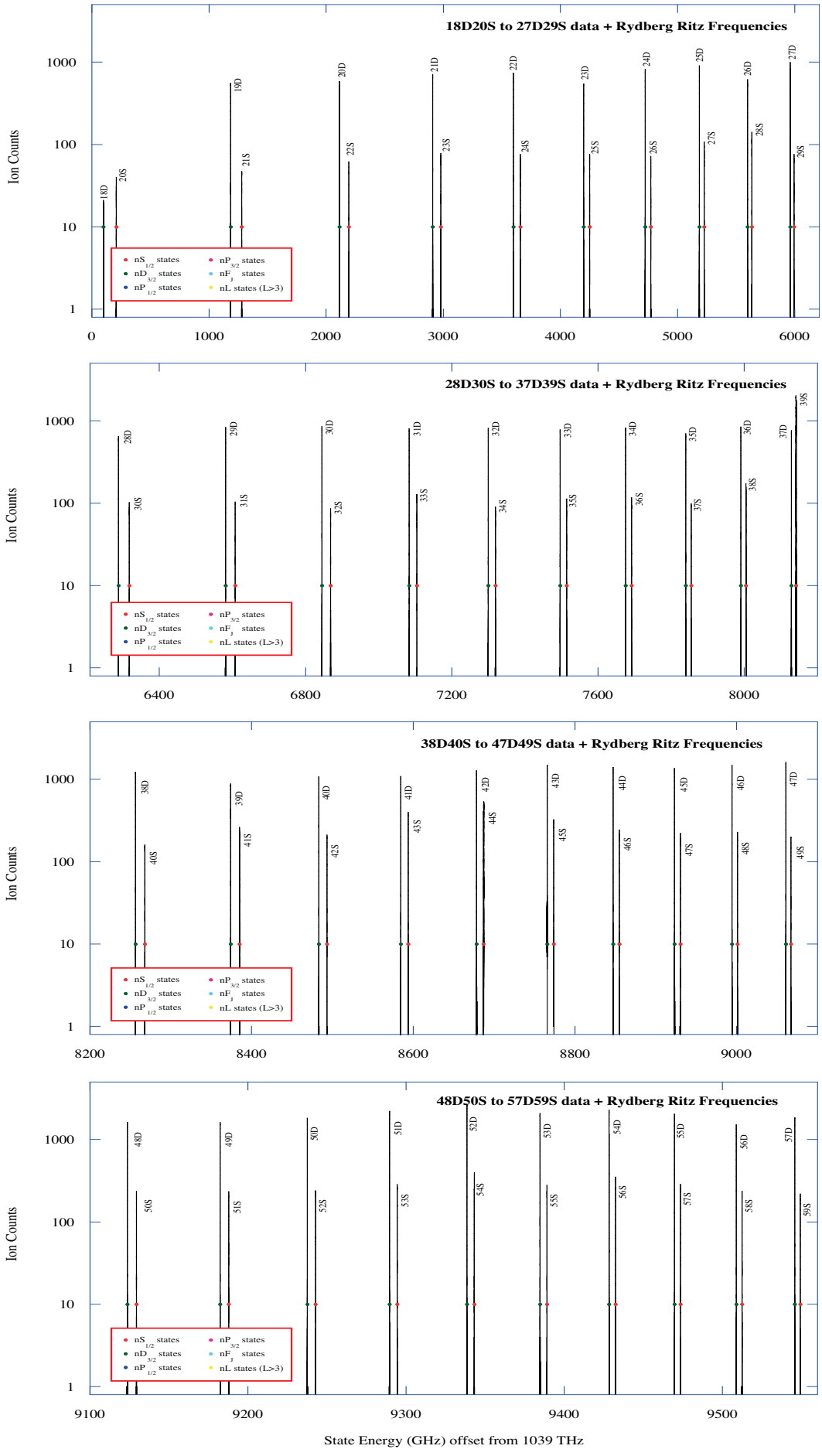

Fig 7.10: Measured energy level spectra for $18D_{3/2}$ to $59S_{1/2}$.

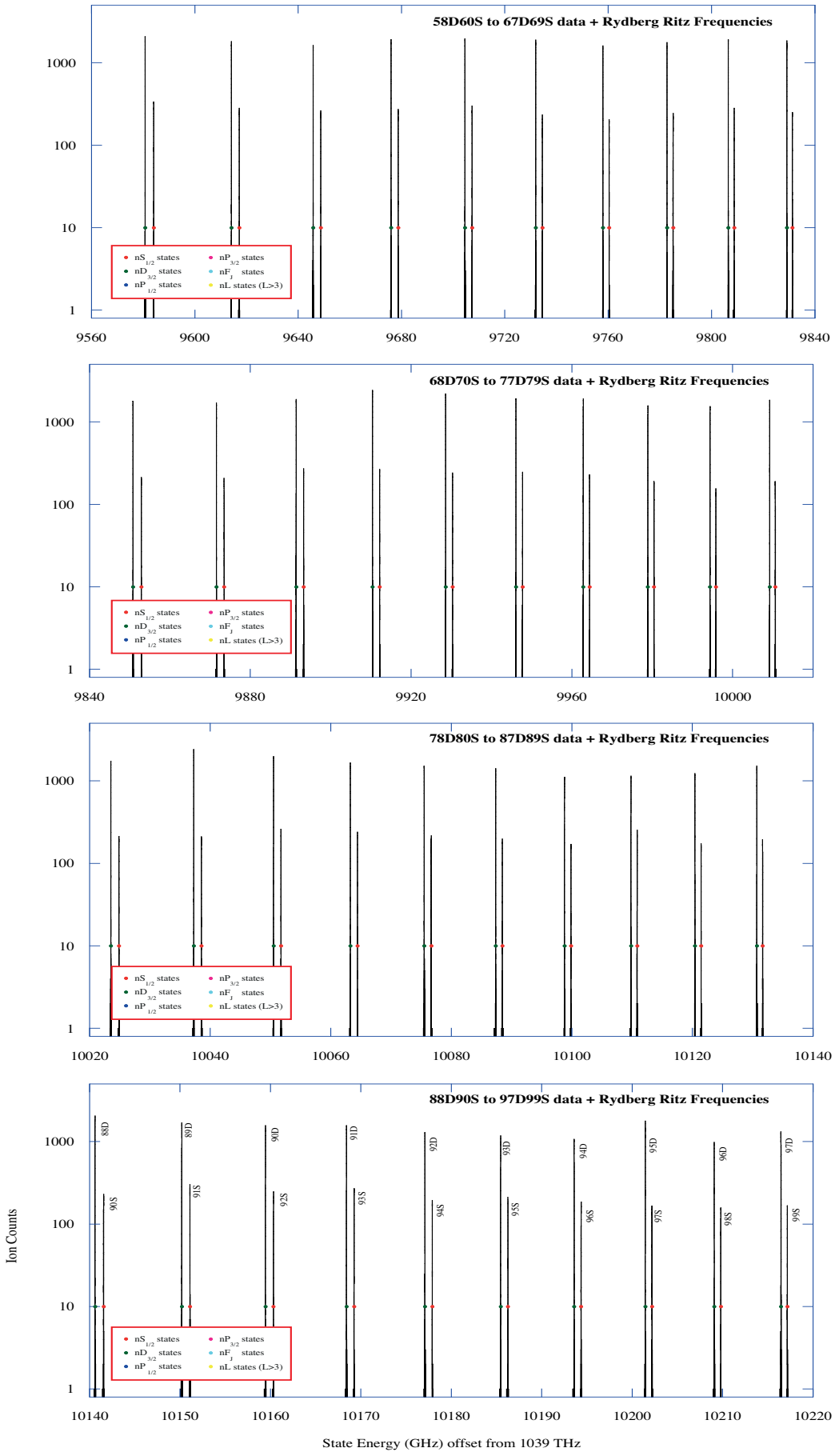

Fig 7.11: *Measured energy level spectra for* $58D_{3/2}$ *to* $99S_{1/2}$.

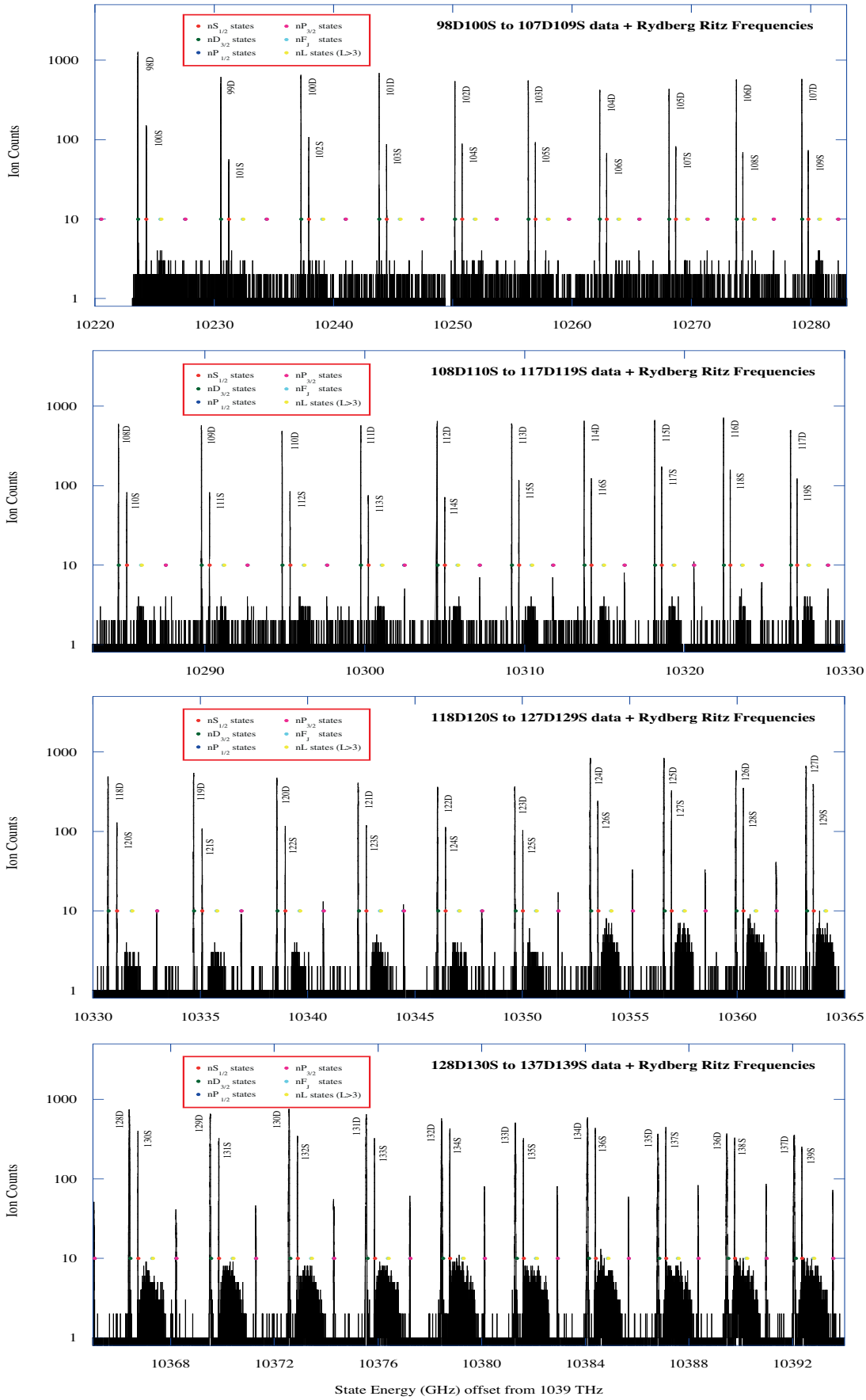

Fig 7.12: Measured energy level spectra for $98D_{3/2}$ to $139S_{1/2}$. From $n = 102$ new features (not labelled here) emerge. The structures adjacent to the S-state (here referred to as 'continuum') are possibly due to excitation of dipole-forbidden hydrogen like states with $l \geq 3$. The origin of the second feature –the 'spikes' appear to be due to excitation of the Dipole-forbidden ^{2}P-states.

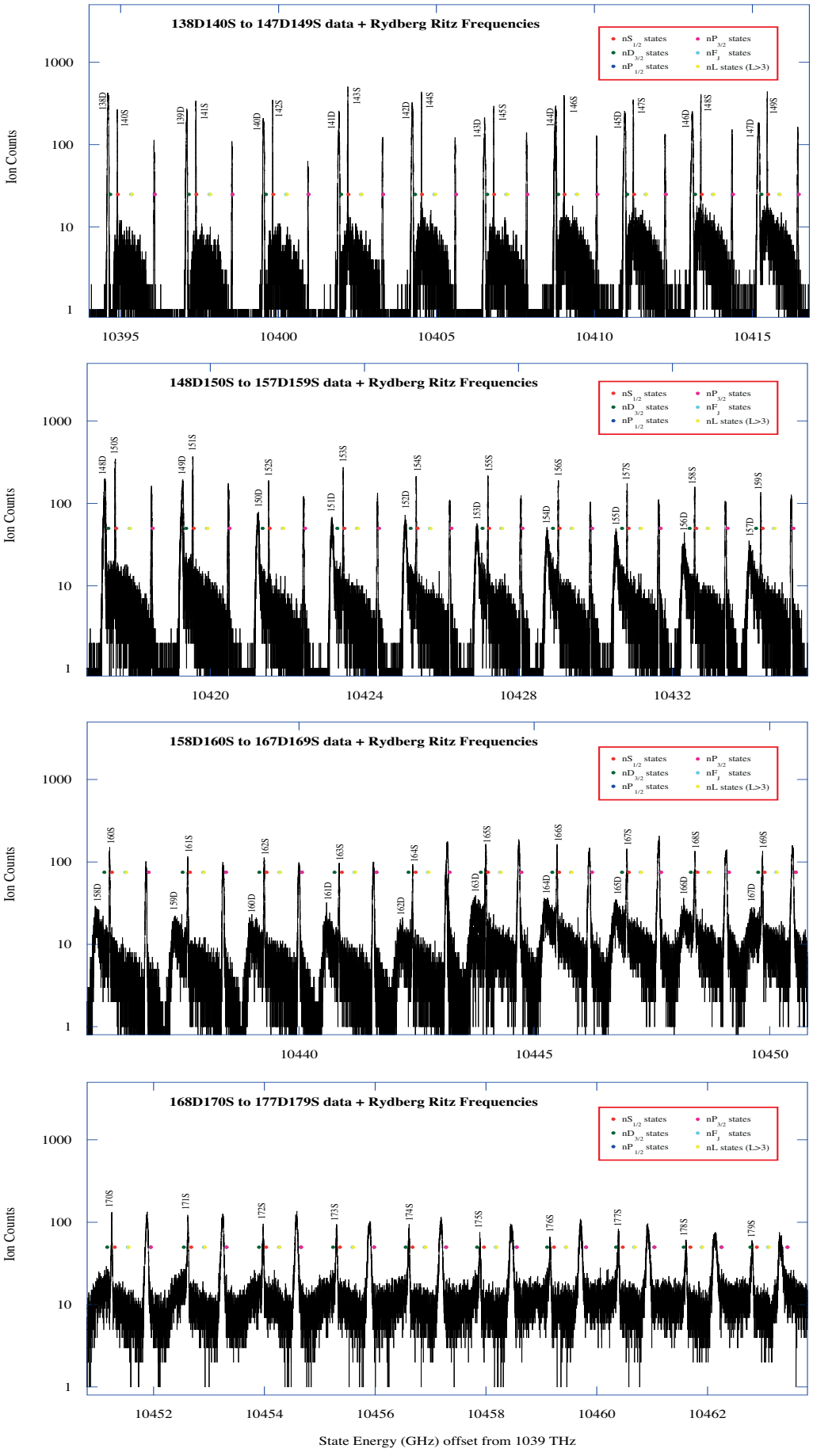

Fig 7.13: Measured energy level spectra for $138D_{3/2}$ *to* $179S_{1/2}$. *The new features mentioned above are enhanced and shift as* n *increases. For* $n > 167$ *the D-states intensities are very small and so were unresolved.*

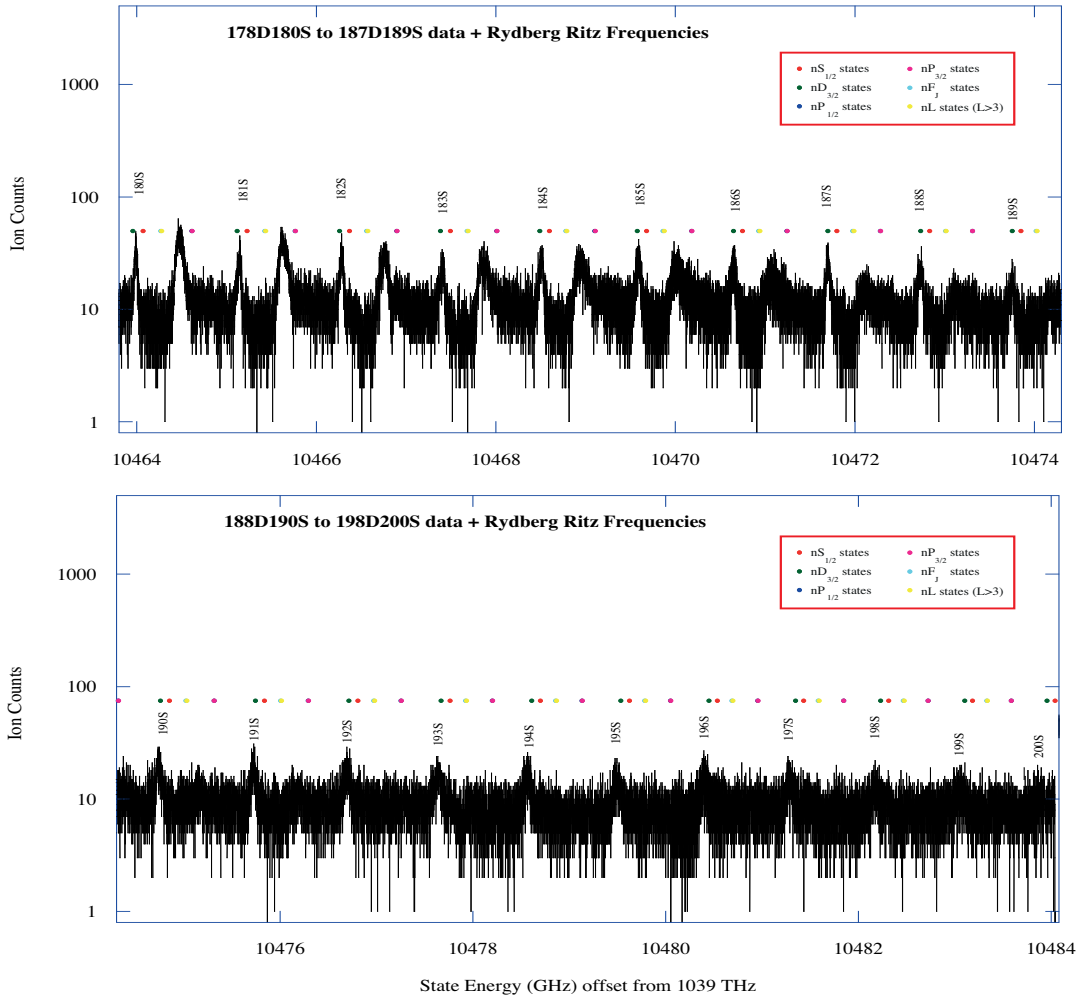

Fig 7.14: Measured energy level spectra for $178D_{3/2}$ *to* $199S_{1/2}$. *From* $n = 190$ *the new features are no longer resolved.*

The measured energy levels (in MHz) for excitation to both the $n^2S_{1/2}$ and $n^2D_{3/2}$ states from the $^2P_{1/2}$ state relative to $F = 1$ ground state, corrected for the excited state hyperfine structures splitting, are given in table A1 in Appendix A. Energy levels for excitation to the $n^2S_{1/2}$ and $n^2D_{3/2,5/2}$ from the $^2P_{3/2}$ state were also obtained, however these are still under analysis and so are not presented in this thesis.

7.5.6 Energy level shift

As mentioned in the previous section, the measured energy levels deviate from the calculated values estimated from the Rydberg Ritz formula as the principal quantum number n increases. Figure 7.15 shows results from experiments and calculation for the $n^2S_{1/2}$ state of potassium, from n=20 to n=200. Figure 7.15(a) shows the frequency of the transition offset from 1039 THz, whereas figure 7.15(b) shows the deviation of the measured energy levels from the calculation and the width of the peaks that were detected.

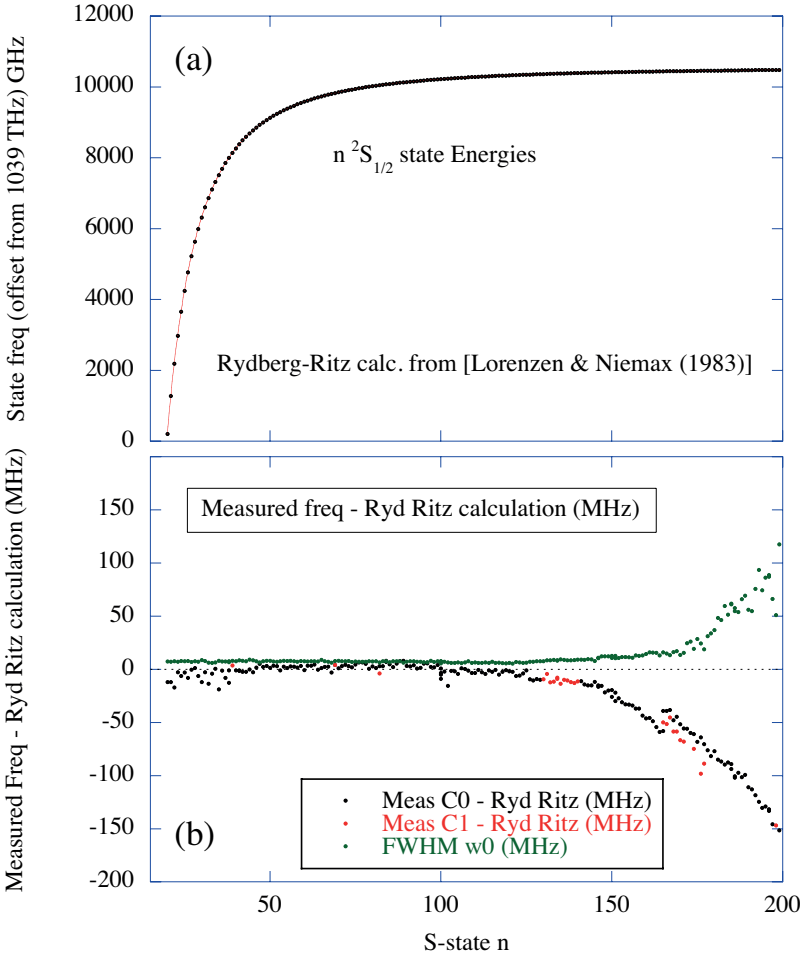

Fig 7.15: Energy level for the S-state versus a fit from Rydberg-Ritz formula, showing the variance between the measured energy levels and the calculated value as n increases, as well as the Full Width at Half Maximum (FWHM) of the peaks as n increases. At values of n~120, the data diverges from the calculation. The data shows the frequency of the main line that was calculated by fitting Gaussian peaks to the data. In some cases, more than 1 fit was required to emulate the data, and these are represented as C0 and C1 in the plots.

The two set of data sets in figure 7.15(b) for the deviation from the calculated value show the result from the experiment when more than one peak was found, the data indicating the main peak that was nearest to the estimated value in each case. The deviation from calculation occurred for values of n greater than ~120, and the width of the peaks also increases from this point. It is hence assumed that a fit of the Rydberg-Ritz formula to the S-state data given above $n = 130$ is not accurate.

Figure 7.16 shows results for the $n^2D_{3/2}$ states that are dipole-allowed from the $^2P_{1/2}$ state excited by radiation around 770 nm. Again figure 7.16(a) shows the transition frequency offset from 1039 THz, and figure 7.16(b) shows the deviation from the Rydberg-Ritz calculation. For the D-state, the deviation occurs for n greater than ~100, and the width of the peak also increases from this point.

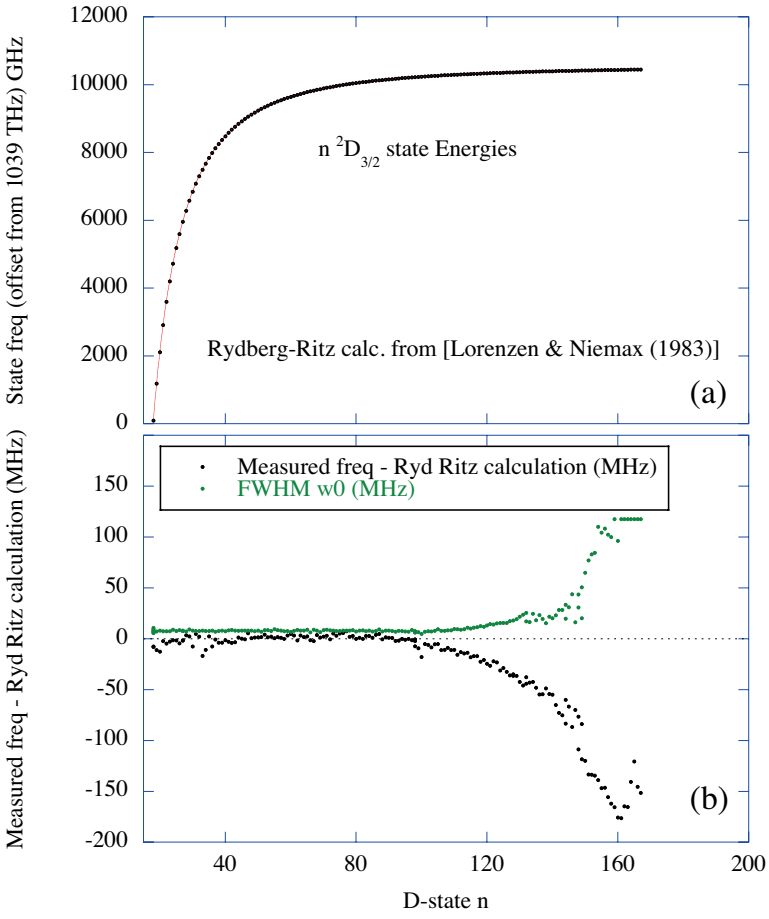

Fig 7.16: Energy level for the D-state versus a fit from Rydberg-Ritz formula, showing the variance between the measured energy levels and the calculated value as n increases, as well as the FWHM of the peaks as n increases. At values of n~100, the data diverges from the calculation.

The above figures also show the FWHM of the peaks for both nS and nD states. It appears the widths of the peaks increase at similar values of the quantum number n as is found for the frequency deviations. *This indicates that the process that produces the frequency shift also results in the increase in the width of the peaks*. These shifts in energy levels are believed to be due to interaction between the excited Rydberg atoms due to their large orbital diameter, polarizability and proximity in the AC-MOT. The proximity of the atoms can be established by considering the density of the MOT cloud, and the 'size' of the Rydberg atoms that are excited.

The size of the AC-MOT cloud inside the vacuum chamber was measured using a CCD camera. The camera monitored fluorescence from the AC-MOT that was imaged onto the CCD array using a 50mm diameter lens external to the vacuum chamber. The relative image size measured with the CCD array was determined using a calibration grid that was imaged onto the camera using the same set of optics as in the experiment. The AC-MOT cloud shape was found to approximate an oblate spheroid, with a major diameter of

~1.75mm and a minor diameter of $\sim 1.1mm$, yielding a volume $\sim 1.7mm^3$. The number of atoms in the MOT during the experiments was estimated from the fluorescence to be $\sim 2.5\times10^6$ atoms, so that the MOT density was at 1.5×10^7 atoms/mm^3. Assuming an equal distribution of atoms throughout the MOT cloud, the average distance between the atoms is then $\sim 4\mu m$.

For atoms in a Rydberg state with principal quantum number n, the approximate 'diameter' of the atom scales as n^2. Potassium has a calculated radius in the ground state of $\sim 0.486\ nm$ [33], and so if one assumes that this scaling rule holds for potassium, the diameter of the Rydberg atoms approximates that of the average spacing of atoms in the AC-MOT for $n\sim 96$. At higher values of n, it is therefore expected that Rydberg atoms in the AC-MOT that are in close proximity to each other will interact strongly. This will create a significant perturbation in their electronic structure, since their wavefunctions then have a greater probability of overlapping. This perturbation due to proximity, leads to the band structure in liquids and solids, and is due to the Pauli exclusion principle. The proximity of the excited Rydberg atoms in the AC-MOT also leads to other phenomena such as dipole-dipole interactions, due to their large polarizability. Dipole-dipole interactions are currently under study by a number of groups as it leads to dipole blockading [35-36], a phenomenon that is being used to produce coherent quantum systems that have possible use in quantum computing.

As the atomic diameter increases (i.e. for higher values of n), the overlap between the wavefunctions of the excited atoms increases rapidly, and so a measurement of the collective excitation of the atoms in the cloud (as in the current experiments) should show the effects of this. From these perturbations we would expect the peaks to increase in width, as is seen. From the dipole-dipole interactions, we would also expect the energy levels to shift in energy, as also is seen in the present data.

7.5.7 Fits of Rydberg-Ritz formula to the new experimental data

From the new energy level data, parameters for the Rydberg-Ritz formula were re-calculated using Maple. The Rydberg-Ritz coefficients reported Lorezen & Niemax in [34] were from their measurements reported in [22], which were from $n = 9$ to $n = 46$ for the $^2S_{1/2}$ state, and were from $n = 7$ for the $^2D_{3/2,5/2}$ states to $n = 40$ for the $^2D_{3/2}$ state, and $n = 46$ for the $^2D_{5/2}$ state. At lower values of n their fit diverges significantly from the measured values of the state energies.

Figure 7.17 shows the residuals from this fitting procedure from $n = 9$ to $n = 120$ for the $^2S_{1/2}$ state and for $n = 7$ to $n = 100$ for the $^2D_{3/2}$ states, where the new fit is shown compared to that generated from Lorenzen & Niemax [34]. The new fit calculated here is clearly giving much better residual values than the previous values.

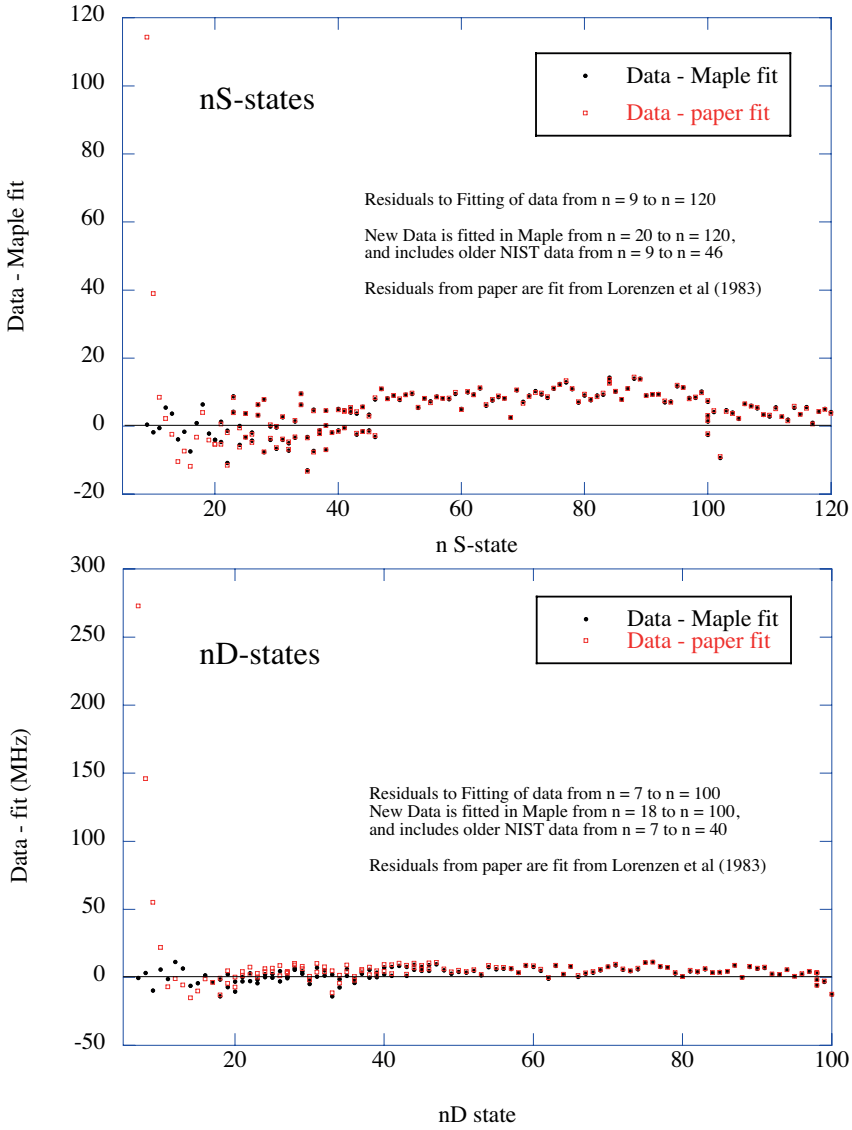

Fig7.17. Residuals from fitting the S- and D-state data to the Rydberg Ritz formula, showing the variance between the data and fit as n increases for n from 9 to 120 for S-states, and from n=7 to 100 for the D-states. The new fits are greatly improved on that of the work of Lorenzen et al (1983) [34], who only fitted the data up to n ~ 40.

From these data a new set of parameters for the Rydberg Ritz formula have been calculated, as shown (in bold characters) in table 7.2 for both the $^2S_{1/2}$ states and the $^2D_{3/2}$ states. The main improvement can be seen for the lower values of n, where the residuals from the new fit produce a marked improvement on the calculated values compared to the data. The parameters for the other states in table 7.2 have not changed as they were not measured.

$States$	δ_0	δ_2	δ_4	δ_6	δ_8
$n^2S_{1/2}$	$\mathbf{2.18019651}$	$\mathbf{0.13719839}$	$\mathbf{-0.133673}$	$\mathbf{8.7146620}$	$\mathbf{-125.9007}$
$n^2D_{3/2}$	$\mathbf{0.276944679}$	$\mathbf{-1.0128677}$	$\mathbf{-2.349888}$	$\mathbf{93.638996}$	$\mathbf{-1432.3923}$
$n^2D_{5/2}$	0.2771580	−1.025635	−0.59201	10.0053	−19.0244
$n^2P_{1/2}$	1.713892	0.233294	0.16137	0.5345	−0.234
$n^2P_{3/2}$	1.710848	0.235437	0.11551	1.1015	−2.0356
n^2F_J	0.010098	−0.100225	1.56334	−12.685	0
$l > 3$	0	0	0	0	0

Table 7.2. New parameters for the Rydberg-Ritz formula for the different states of potassium derived from the data taken with the cold potassium source, in combination with the data from NIST. The parameters have been re-calculated to derive the energies from the F=1 ground state.

7.5.4 Effect of the Extraction Field on Ion Production

As noted earlier, excitation to the high-n Rydberg states occurred during the AC-MOT off period, and so there was no magnetic field present during excitation and ionization of the Rydberg atoms. The only significant source of electric field during the Rydberg excitation and ionization process was the extraction voltage applied to the bias mesh used to extract ions. In the experiments, the bias mesh was pulsed with an extraction voltage between $-2.5\ V$ and $-5\ V$ in order to accelerate ions toward the channeltron after they have been produced. To determine the magnitude of the field in the interaction region due to this applied voltage, an ion optic program SIMION was used to simulate the field. This program calculates the electric field for conductors with defined voltages and position, and calculates the trajectories of ions under the influence of these fields. Figure 7.18 shows the calculated field components along the Cartesian coordinates x, y and z for an extraction voltage of $-1V$ at the interaction region, shown for a cubic region of side length 6mm (used here to emulate the AC-MOT trapping region). The direction of motion of the ions was chosen to be along the z-axis (perpendicular to the plane of the extraction plate), and the calculated field scales directly with the extraction voltage.

The calculated maximum field at the interaction region due to a $-1\,V$ extraction voltage was $\approx 1Vm^{-1}$, as shown in the figure. At a typical extraction voltage between $-2.5V$ and $-5\,V$ used in the experiments, the penetrating field at the interaction region was hence between $2.5Vm^{-1}$ *and* $5Vm^{-1}$. From the work of Gallagher [1] the field required to efficiently ionize potassium Rydberg targets scales as n^{-4}, and is given by the approximate formula $E_n^{FI} \sim 3.4\times10^{11}n^{-4}\ Vm^{-1}$. From this formula a field of $\sim 3.4kVm^{-1}$ is hence required to directly field ionize potassium in the n=100 state, which is several orders of magnitude larger than the field used in the current experiments. The penetrating field that is used here is hence far too small to cause significant field ionization of the Rydberg atoms, and so serves the purpose of extracting the ions that are produced due to atom-atom collisions.

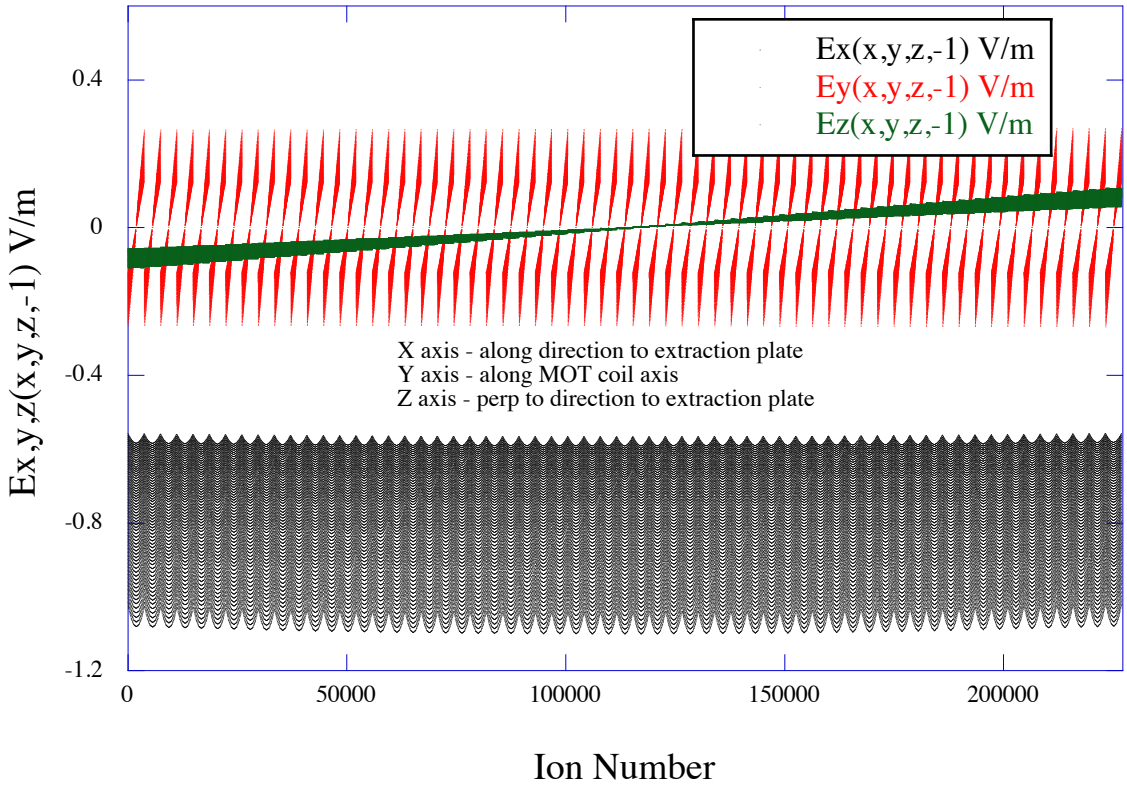

Fig 7.18: Electric field components at the interaction region due to field penetration from the extraction plate. A maximum field of $1Vm^{-1}$ *along the x-axis perpendicular to the extraction plate was found from the model. The ion number shown on the x-axis maps to the location point inside the* $6\times6\times6\ mm$ *cube.*

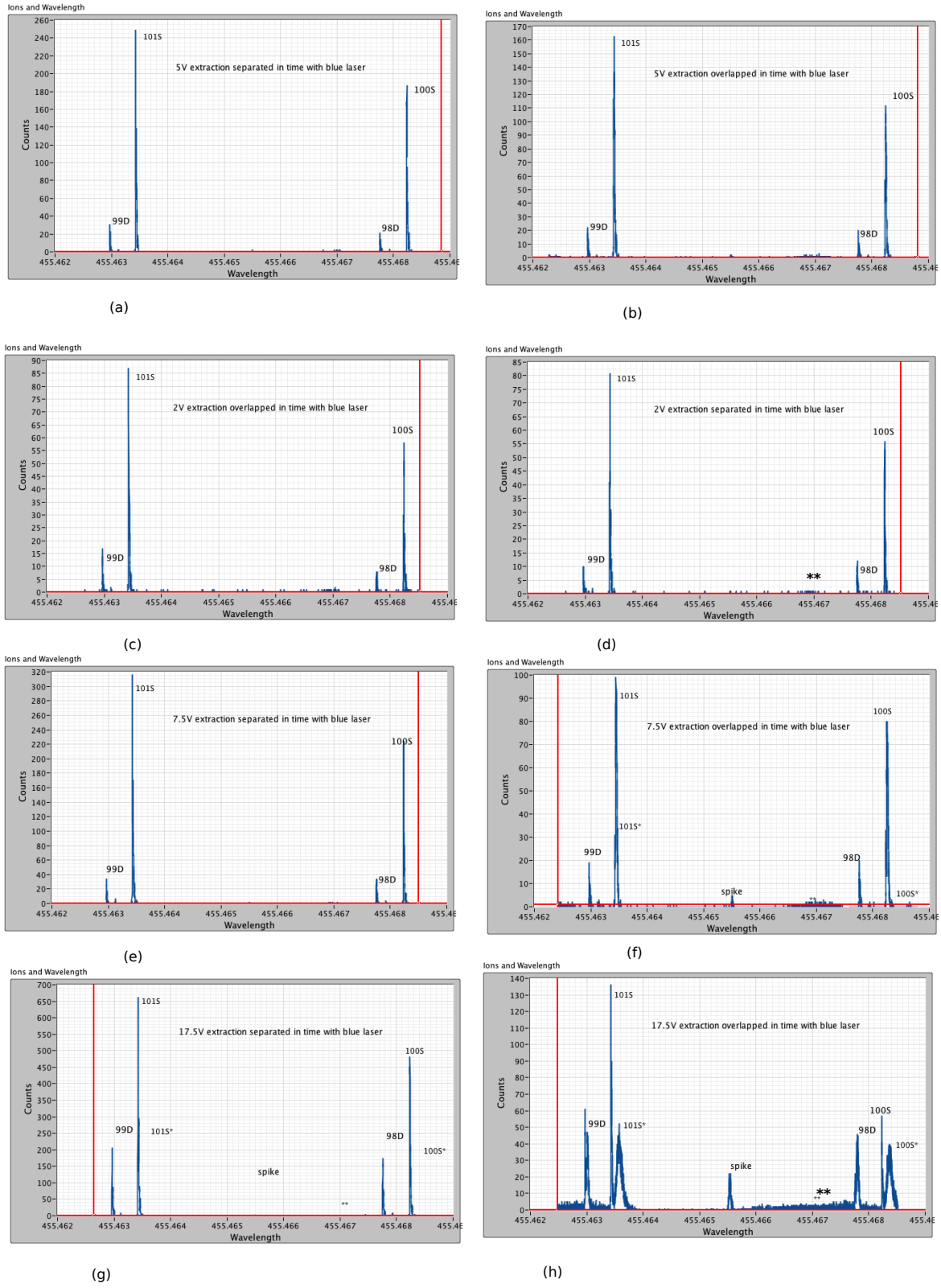

Fig 7.19: the effect of a penetration field on the ionization yield obtained for a scan through the 98D/100S - 99D/101S Rydberg states. (a), (c), (e) and (g), shows the result where the extraction field and blue laser were separated in time. (b), (d), (f), and (h), show result when the extraction field and the blue laser overlapped in time. There is no significant difference in the ionization spectra when the extraction voltage was $\leq 5V$ *(a)-(d). At extraction voltages* $\geq 7.5\,V$ *(e)-(h), additional structures emerge, denoted here as 101S* 100S*, spike and nD**.*

Ionization spectra obtained when the extraction field and the blue excitation laser were overlapped in time, and when they were separated are shown in figure 7.19. This figure shows ionization spectra following the excitation to Rydberg states 99D and 101S to 98D and 100S, as the blue laser was scanned up in wavelength. There are two set of data for each extraction voltage, one with the extraction field and the blue laser separated in time (a, c, e and g), and the other with the extraction field and the blue laser overlapped in time (b, d, f and h). The AC-MOT settings and other experimental conditions were the same for all cases, except for the extraction pulse and blue laser pulse delay times. While no significant difference is observed for extraction voltages $\leq 5V$, the effect of the penetrating field from the extraction plate becomes significant as the extraction voltage increased beyond $\sim 7.5\ V$, as evident by the emergence of new features seen in figure 7.19 (e)-(h). These results illustrate the importance of electric field interactions with Rydberg atoms, especially for states with high quantum numbers. Figure 7.19 (g) shows that even at extraction fields as high as 17.5V/m, there is no influence of any stray field on the spectra when the extraction field and blue laser were separated in time. This leads to the conclusion that the new features in the spectra presented in figures 7.10 to 7.14 (the continuum and spike) are probably not due to stray fields, since the measurements were made with the extraction field and the blue laser separated in time and at an extraction field of only $\sim 5\ V/m$.

7.6 Conclusions

A detailed description of the Rydberg states of cold potassium atoms in the AC-MOT has been presented. This included an overview of Rydberg atom spectroscopy, methods of producing Rydberg atoms and some applications of Rydberg atoms in different areas of science and technology. A concise experimental procedure has also been detailed. In this procedure a stepwise excitation from the first ($4^2P_{3/2}$, and $4^2P_{1/2}$) excited states was used, followed by excitation to the Rydberg states using a tunable blue dye laser. The data acquisition techniques and the procedures used to extract the transition frequency to each of the Rydberg states were also described. The results of excitation from the $4^2P_{1/2}$ state were presented. In this thesis energy level data for principal quantum numbers $n = 18$ up to $n = 200$ have been reported for the first time. For $n = 18$ to $n = 46$, the measured energy levels were in good agreement with the results obtained by Lorenzen et al [22], which are available on the National Institute of Standards and Technology (NIST) list of atomic spectral lines. The measured atomic transition energy level for $n = 47$ up to

$n = 200$ have therefore been detailed for the first time. Shifts in the energy levels for excitation to both the $^2S_{1/2}$ and $^2D_{3/2}$ at principal quantum number n greater than 100 were seen. These shifts are attributed to strong interaction between Rydberg atoms in close proximity. From a fit of the Rydberg-Ritz formula to the measured energy level data, new values for the parameters in the Rydberg-Ritz formula were calculated and presented.

Finally, the effects of penetrating electric field from the ion extraction plate were briefly discussed which shows the importance of the field on the interactions for these highly excited Rydberg targets.

References

[1] Gallagher, T. F. (2005). *Rydberg atoms* (Vol. 3). Cambridge University Press.

[2] J. Neukammer et al. (1984). *Diamagnetic shift and singlet-triplet mixing of 6snp Yb Rydberg states with large radial extent*. Physical Review A **30** (2): 1142–1144.

[3] Vitrant, G., Raimond, J. M., Gross, M., & Haroche, S. (1982). *Rydberg to plasma evolution in a dense gas of very excited atoms*. Journal of Physics B: Atomic and Molecular Physics, 15(2), L49.

[4] Stebbings, R. F., and F. B. Dunning, eds. *Rydberg states of atoms and molecules*. Cambridge University Press, 1983.

[5] Lukin, M. D., Fleischhauer, M., Cote, R., Duan, L. M., Jaksch, D., Cirac, J. I., & Zoller, P. (2001). *Dipole blockade and quantum information processing in mesoscopic atomic ensembles.* Physical Review Letters, 87(3), 037901.

[6] Nielsen, M. A., & Chuang, I. L. (2000). *Quantum computation. Quantum Information.* Cambridge University Press, Cambridge.

[7] Jaksch, D., Cirac, J. I., Zoller, P., Rolston, S. L., Côté, R., & Lukin, M. D. (2000). *Fast quantum gates for neutral atoms*. Physical Review Letters, 85(10), 2208.

[8] Tong, D., Farooqi, S. M., Stanojevic, J., Krishnan, S., Zhang, Y. P., Côté, R., ... & Gould, P. L. (2004). *Local blockade of Rydberg excitation in an ultracold gas.* Physical review letters, 93(6), 063001

[9] Heidemann, R., Raitzsch, U., Bendkowsky, V., Butscher, B., Löw, R., Santos, L., & Pfau, T. (2007). *Evidence for coherent collective Rydberg excitation in the trong blockade regime.* Physical review letters, 99(16), 163601.

[10] Raitzsch, U., Bendkowsky, V., Heidemann, R., Butscher, B., Löw, R., & Pfau, T. (2008). *Echo experiments in a strongly interacting Rydberg gas*. Physical review letters, 100(1), 013002.

[11] Singer, K., Reetz-Lamour, M., Amthor, T., Marcassa, L. G., & Weidemüller, M. (2004). *Suppression of excitation and spectral broadening induced by interactions in a cold gas of Rydberg atoms. Physical review letters, 93(16), 163001*.

[12] Day, J. O., Brekke, E., & Walker, T. G. (2008). *Dynamics of low-density ultracold Rydberg gases.* Physical Review A, 77(5), 052712.

[13] Brekke, E., Day, J. O., & Walker, T. G. (2008). *Four-wave mixing in ultracold atoms using intermediate Rydberg states.* Physical Review A, 78(6), 063830.

[14] Pritchard, J. D., Maxwell, D., Gauguet, A., Weatherill, K. J., Jones, M. P. A., & Adams, C. S. (2010). *Cooperative atom-light interaction in a blockaded Rydberg ensemble.* Physical review letters, 105(19), 193603.

[15] Mohapatra, A. K., Bason, M. G., Butscher, B., Weatherill, K. J., & Adams, C. S. (2008). *A giant electro-optic effect using polarizable dark states*. Nature physics, 4(11), 890-894.

[16] Hessels, E. A., Homan, D. M., & Cavagnero, M. J. (1998). *Two-stage Rydberg charge exchange: An efficient method for production of antihydrogen.* Physical Review A, 57(3), 1668.

[17] Mourachko, I., Comparat, D., De Tomasi, F., Fioretti, A., Nosbaum, P., Akulin, V. M., & Pillet, P. (1998). *Many-body effects in a frozen Rydberg gas.* Physical review letters, 80(2), 253.

[18] Anderson, W. R., Veale, J. R., & Gallagher, T. F. (1998). *Resonant dipole-dipole energy transfer in a nearly frozen Rydberg gas.* Physical review letters, 80(2), 249.

[19] Marinescu, M., H. R. Sadeghpour, and A. Dalgarno. *Dispersion coefficients for alkali-metal dimers*. Physical Review A 49.2 (1994): 982.

[20] Fano, U. *Quantum defect theory of l uncoupling in H 2 as an example of channel-interaction treatment.* Physical Review A 2, no. 2 (1970): 353.

[21] Seaton, M. J. *Quantum defect theory*. Reports on Progress in Physics 46.2 (1983): 167.

[22] Lorenzen, C-J., K. Niemax, and L. R. Pendrill. *Precise measurements of $^{39}K\,nS$ and nD energy levels with an evaluated wavemeter.* Optics Communications 39.6 (1981): 370-374.

[23] Schiavone, James A., Susan M. Tarr, and Robert S. Freund. *Electron-impact excitation of the rare-gas atoms to high-Rydberg states.* Physical Review A 20, no. 1 (1979): 71.

[24] Wing, W. H., & MacAdam, K. B. (1978). *The Microwave-Optical Resonance Method.* In Progress in Atomic Spectroscopy (pp. 491-527). Springer US.

[25] Bayfield, J. E., and P. M. Koch. *Multiphoton ionization of highly excited hydrogen atoms.* Physical Review Letters 33.5 (1974): 258.

[26] Stebbings, R. F., Latimer, C. J., West, W. P., Dunning, F. B., & Cook, T. B. (1975). *Studies of xenon atoms in high Rydberg states*. Physical Review A, 12(4), 1453.

[27] Zollars B G. *A study of low energy electron-molecule and ion-molecule collisions using Rydberg atoms.* PhD thesis Rice University, 1986

[28] Boller, K-J., A. Imamolu, and Stephen E. Harris. *Observation of electromagnetically induced transparency.* Physical Review Letters 66.20 (1991): 2593.

[29] Mohapatra, A. K., Jackson, T. R., & Adams, C. S. (2007). *Coherent optical detection of highly excited Rydberg states using electromagnetically induced transparency*. Physical review letters, 98(11), 113003.

[30] Kramida, A., Ralchenko, Yu., Reader, J., and NIST ASD Team (2014). *NIST AtomicSpectra Database* (ver. 5.2), [Online].
Available: http://physics.nist.gov/asd [2014, November 26]. National Institute of Standards and Technology, Gaithersburg, MD.

[31] Singer, K., Reetz-Lamour, M., Amthor, T., Marcassa, L. G., & Weidemüller, M. (2004). *Suppression of excitation and spectral broadening induced by interactions in a cold gas of Rydberg atoms*. Physical review letters, 93(16), 163001.

[32] Constantine E. Theodosiou, Mitio Inokuti, Steven T. Manson, *Quantum defect values for positive atomic ions,* Atomic Data and Nuclear Data Tables, Volume 35, Issue 3, November 1986, Pages 473-486, ISSN 0092-640X.

[33] Clementi, E. T., and D-L Raimondi. Atomic screening constants from SCF functions. The Journal of Chemical Physics 38.11 (1963): 2686-2689.

[34] Lorenzen, C. J., and K. Niemax. Quantum Defects of the n2P1/2, 3/2 Levels in 39K I and 85Rb I. Physica Scripta 27.4 (1983): 300.

[35] Urban, E., Johnson, T. A., Henage, T., Isenhower, L., Yavuz, D. D., Walker, T. G., & Saffman, M. (2009). *Observation of Rydberg blockade between two atoms*. Nature Physics, 5(2), 110-114

[36] Saffman, M., & Mølmer, K. (2009). *Efficient multiparticle entanglement via asymmetric Rydberg blockade*. Physical review letters, 102(24), 240502.

CHAPTER EIGHT

Summary

8.0 Introduction

The applicability of the AC-MOT to collision and photo-ionization studies has again been demonstrated. A high density of ^{39}K atoms was cooled and trapped in the AC-MOT loaded from a Zeeman slowed atomic beam, and the trap was then characterized. With the trapped atoms in the AC-MOT, direct photoionization of the atoms was carried out, leading to the determination of the absolute photoionization cross-section of potassium from the $4^2P_{1/2}$ excited state. A stepwise excitation of trapped potassium to high-n Rydberg states was also conducted. Energy level data of Rydberg states from both $4^2P_{1/2}$ and $4^2P_{3/2}$ states for principal quantum numbers n from 18 to 200 were obtained. These results have increased the precise experimental energy level data from $n = 46$ to $n \approx 200$, for excitation from the first excited state. Energy level shifts and spectral broadening at high principal quantum numbers were also observed, and were considered to be due to perturbation from the high density of the Rydberg atoms.

In this chapter, a summary of the work carried out in the course of this study is presented. This is followed by some suggestions for future investigations.

8.1 Theory

The experiments carried out in this thesis were based on the manipulation of atoms with light. The theory behind these studies is a consequence of the interaction of light with matter, with particular attention on the light interaction with neutral atoms. The interaction of light with matter results in several different processes, including excitation and ionization. A quantum electrodynamic (QED) model has been used to describe the interaction of atoms in a laser field. In this model, both the laser field and the atomic

system are treated as quantum systems, and so the laser-atom interaction is described by an interaction Hamiltonian containing both atomic and field operators. From the QED treatment of potassium in a laser field it was found to be necessary to use a laser beam containing two frequencies in order to create a sustainable trap of potassium atoms.

Laser cooling and trapping of neutral atoms relies on the momentum transfer from the field to the atoms, which follows the absorption and emission of photons. So over many absorption and emission processes, the velocity of the atom can be reduced significantly due to the optical molasses force that is then created. In the atom trap described here, the molasses force was not sufficient to confine the atoms in space, and hence a magnetic field was introduced to provide a restoring force and thereby keep the atoms trapped. The magnetic field exploits the dipole moment of the atom to shift their energy levels due to Zeeman effect.

8.2 The AC-MOT and Trapping of ^{39}K

The AC-MOT loaded from a Zeeman slowed atomic beam was used to produce a trap of potassium atoms of high density. The MOT operated with a trapping laser red-detuned between -3Γ $(-18\,MHz)$ and -5Γ $(-30\,MHz)$ from the $F = 2 \rightarrow F' = 3$ transition. The dependence of the trap lifetime on detuning and the process of MOT decay have been studied. A typical AC-MOT operating with the trapping laser red-detuned by -3Γ was characterized by the following properties:

- Loading rate $\approx (1.0 \pm 0.01) \times 10^8\ atoms/s$
- Number of trapped atoms $\approx (3.63 \pm 0.02) \times 10^8 atoms$
- Mean trap density $\approx (2.14 \pm 0.02) \times 10^{11}\ atoms/cm^3$
- Mean trap temperature $\approx 275 \pm 33\ \mu K$
- Single-body loss rate $\approx 0.05 \pm 0.01\ s^{-1}$
- Loss rate due to background collisions = $(8.12 \pm 0.01) \times 10^6\ atoms/s$
- Two body loss coefficient $\frac{\beta}{V} N_0 = 0.13 \pm 0.01 s^{-1}$

The number of atoms in the trap and the trap lifetime did not vary significantly for laser detunings between -3Γ and -5Γ, but reduced significantly for detuning of $-2.5\,MHz$ and -6Γ.

In preparation for photoionization experiments with the trapped atoms, the condition of the ion detector that was inside the MOT chamber was ascertained by performing electron scattering experiment using the trapped atoms, and the result of these experiments showed that the detector was operating in a satisfactory way, as indicated by the time of flight ion signals that were obtained.

8.3 Direct Photoionization of Trapped Potassium Atoms

Direct photoionization of the cold potassium atoms from the first excited state was carried out using radiation from a blue diode laser operating at 450.4 nm. Fluorescence from the trap was monitored when the ionizing radiation was directed onto the trapped atoms. By measuring the trap lifetime in the presence of the ionizing laser of various intensities, the rate of photoionization was determined. Using the measured rate of photoionization, the absolute photoionization cross-section was calculated. From the loss rate obtained during the AC-MOT loading process, and the trap lifetime measured during the AC-MOT decay process, the calculated absolute photoionization cross-section was found to be 1.49 ± 0.13 Mb and 2.38 ± 0.18 Mb respectively. These values are about a factor of 3-4 times smaller than previously reported cross-sections, however this was the first measurement of photoionization cross-section of potassium from the first excited state using trapped atoms in the AC-MOT. Clearly additional experiments are required in the future to ascertain the cause of these differences.

8.4 Rydberg atom spectroscopy

Stepwise excitation of the trapped atoms to high-n Rydberg states from both $4^2P_{1/2}$ and $4^2P_{3/2}$ states of potassium were also conducted. The $\sim 766.7\ nm$ AC-MOT trapping laser red-detuned by ~ 23 MHz with respect to the $F = 2 \rightarrow F' = 3$ transition provided the stepwise excitation from the ground state to the $4^2P_{3/2}$ excited state. This was then followed by excitation to high-n Rydberg states with principal quantum number n from 18 to 200, using radiation from a blue tuneable dye laser. Excitation to $n^2S_{1/2}$, $n^2D_{3/2}$ and $n^2D_{5/2}$ were observed. Collision between Rydberg atoms resulted in significant ionization, and the resulting ions were detected using a Channel Electron Multiplier (CEM). Energy

level data for excitation from the $4^2P_{3/2}$ is still being analysed, and so has not been reported in detail in this thesis.

Since the trapping laser was detuned by -4Γ from resonance, the majority of atoms in the AC-MOT were in the ground state. Using radiation from a second Ti:S laser operating at around 770.1 nm, and tuned to be resonant with the $F = 1 \rightarrow F' = 2$ transition, these ground state atoms were excited to the $^2P_{1/2}$ state. Following this excitation, atoms in the $4^2P_{1/2}$ state were subsequently excited to high-n Rydberg states with n from 18 to 200. From the $^2P_{1/2}$ state, excitation to the dipole-allowed $n^2S_{1/2}$ and $n^2D_{3/2}$ Rydberg states is possible, and additional new features were observed. The new features are thought to be as a result of interactions between Rydberg atoms in the MOT. From a Gaussian fit to the acquired ionization spectra, excitation frequencies to the Rydberg states and the spectral widths were derived. The measured energy levels are in good agreement to theoretical valued calculated using the Rydberg-Ritz formula for n not greater than 130 for the $^2S_{1/2}$ states and n not greater than 100 for the $^2D_{3/2}$ states. Atoms excited to states higher than these values clearly showed a deviation from the expected values.

Again from around these principal quantum numbers (130 for the S-state, and 100 for the D-state), broadening of the spectral widths of the Rydberg states was observed, and this broadening was found to increase with increasing n. This shift in energy level and the broadening of the spectral widths are believed to be due to strong interactions between Rydberg atoms, which are in close proximity. With these new energy level measurements the available spectral line data for excitation from the first excited state of potassium obtained from experiments has now been increased from $n = 46$ to $n \approx 200$.

8.5 Suggestions for future work

The results from photoionization and Rydberg atom spectroscopy have again demonstrated the applicability of the AC-MOT to collision and ionization studies, and therefore provide a platform for several possible future investigations. The calculated absolute cross-sections were about 2-3 times smaller than the theoretical predictions and previously reported experimental values. There were several possible sources of uncertainty as was discussed in chapter 6. Similar experiments are therefore suggested using several different high-powered diode lasers to ascertain the validity of these results. This experiment could be repeated with radiation from the blue tuneable dye laser at a fixed wavelength of $\sim 450\, nm$, since this produces a well-collimated beam through the

interaction region. The results of the Rydberg atom spectroscopy demonstrate that the AC-MOT can be used for various experiments involving Rydberg atoms.

8.5.1 Coherent Many-body processes in Rydberg atoms

One of the outstanding properties of Rydberg atoms is their high polarizability which scales as n^7, where n is the principal quantum number. This makes Rydberg atoms highly sensitive to electric fields, and leads to long-range dipole-dipole interactions. The study of coherent many-body processes in Rydberg atoms using atomic beams and vapour cell has been limited by the thermal motion and low density of the atomic ensemble. The AC-MOT can produce a high-density atomic ensemble with virtually no Doppler effect, and so trapped atoms are candidates for the study of coherent many-body processes in Rydberg gases. The energy level shift and spectral widths broadening as was observed in the results presented here are attributed to interactions between Rydberg atoms. An example of a coherent phenomenon that is currently being studied is *Rydberg-excitation blockade* [1-2]. This is where the excitation of an atom to a Rydberg state inhibits or suppresses the excitation of neighbouring atoms in a localized volume, due to energy shifts induced by strong Rydberg-Rydberg interactions. In the present setup, cold potassium Rydberg atoms in the AC-MOT can be used to study this phenomenon.

The possibility of the formation of new crystalline states of Rydberg atoms by causing a rapid change in the frequency (chirping) of the excitation laser has also been proposed [2-4]. Other many-body processes include the formation of ultra-cold plasmas enabled by spatial correlation of Rydberg atoms prior to their ionization, and the entanglement between neutral atoms due to the Rydberg blockade effects [6-8]. Recently, the use of ensembles of cold Rydberg atoms in the development of a cold-atom based processor for the realization of quantum computation [9], and coherent control of mesoscopic atomic ensembles based on adiabatic passage and Rydberg blockade [10], has been proposed. The present setup can be adapted in these studies for a wide range of principal quantum numbers, and so should provide a platform for rich body of study in the future.

References

[1] Urban, E., Johnson, T. A., Henage, T., Isenhower, L., Yavuz, D. D., Walker, T. G., & Saffman, M. (2009). *Observation of Rydberg blockade between two atoms*. Nature Physics, 5(2), 110-114.

[2] Gaëtan, A., Miroshnychenko, Y., Wilk, T., Chotia, A., Viteau, M., Comparat, D., ... & Grangier, P. (2009). *Observation of collective excitation of two individual atoms in the Rydberg blockade regime.* Nature Physics, 5(2), 115-118.

[3] Pohl, T., Demler, E., & Lukin, M. D. (2010). *Dynamical crystallization in the dipole blockade of ultracold atoms.* Physical review letters, 104(4), 043002.

[4] Schachenmayer, J., Lesanovsky, I., Micheli, A., & Daley, A. J. (2010). *Dynamical crystal creation with polar molecules or Rydberg atoms in optical lattices.* New Journal of Physics, 12(10), 103044.

[5] Van Bijnen, R. M. W., Smit, S., Van Leeuwen, K. A. H., Vredenbregt, E. J. D., & Kokkelmans, S. J. J. M. F. (2011). *Adiabatic formation of Rydberg crystals with chirped laser pulses*. Journal of Physics B: Atomic, Molecular and Optical Physics, 44(18), 184008.

[6] Zhang, X. L., Isenhower, L., Gill, A. T., Walker, T. G., & Saffman, M. (2010). *Deterministic entanglement of two neutral atoms via Rydberg blockade*. Physical Review A, 82(3), 030306.

[7] Saffman, M., & Mølmer, K. (2009). Efficient multiparticle entanglement via asymmetric Rydberg blockade. *Physical review letters*, *102*(24), 240502.

[8] Wilk, T., Gaëtan, A., Evellin, C., Wolters, J., Miroshnychenko, Y., Grangier, P., & Browaeys, A. (2010). Entanglement of two individual neutral atoms using Rydberg blockade. *Physical review letters*, *104*(1), 010502.

[9] Mansell, C. W., & Bergamini, S. (2014). A cold-atoms based processor for deterministic quantum computation with one qubit in intractably large Hilbert spaces. *New Journal of Physics*, *16*(5), 053045.

[10] Beterov, I. I., Saffman, M., Zhukov, V. P., Tretyakov, D. B., Entin, V. M., Yakshina, E. A., Ryabtsev I. I.,Mansell C.W., MacCormick C., Bergamini S., & Fedoruk, M. P. (2014). Coherent control of mesoscopic atomic ensembles for quantum information. *Laser Physics*, *24*(7), 074013.

APPENDIX A

Compliment to Chapter 7

Measured Energy Level Data

The measured energy levels values in MHz of the $n^2S_{1/2}$ and $n^2D_{3/2}$ relative to $F = 1$ ground state corrected for the excited state hyperfine structures splitting are given in table A1 together with the calculated values from the Rydberg-Ritz formula . The accuracy of the measured energy levels was limited by the uncertainty associated with the WSU-10 wave meter, which was $\pm 5MHz$. The $n^2D_{3/2}$ states were unresolved for principal quantum number n greater than 167 in the present experiment.

n	$n^2S_{1/2}$ state		$n^2D_{3/2}$ state	
	Calculated (MHz)	Measured (MHz)	Calculated (MHz)	Measured (MHz)
18	-	-	1039098443.6	1039098436.2
19	-	-	1040186424.6	1040186413.6
20	1039207528.6	1039207516.7	1041113266.6	1041113253.8
21	1040279373.6	1040279361.7	1041909281.6	1041909279.2
22	1041193094.6	1041193077.5	1042597973.6	1042597968.9
23	1041978334.6	1041978331.9	1043197798.6	1043197796.0
24	1042658097.6	1042658091.4	1043723412.6	1043723411.2
25	1043250464.6	1043250461.7	1044186567.6	1044186566.1
26	1043769798.6	1043769790.7	1044596780.6	1044596776.1
27	1044227631.6	1044227631.3	1044961822.6	1044961821.1
28	1044633303.6	1044633304.9	1045288088.6	1045288092.1
29	1044994447.6	1044994441.4	1045580881.6	1045580884.1
30	1045317349.6	1045317337.7	1045844629.6	1045844622.1
31	1045607225.6	1045607222.8	1046083048.6	1046083053.3
32	1045868430.6	1045868417.2	1046299282.6	1046299284.8
33	1046104622.6	1046104618.7	1046495999.6	1046495982.8
34	1046318898.6	1046318899.3	1046675480.6	1046675469.8
35	1046513887.6	1046513868.7	1046839680.6	1046839683.1
36	1046691836.6	1046691835.5	1046990286.6	1046990279.0
37	1046854674.6	1046854666.8	1047128758.6	1047128757.9
38	1047004065.6	1047004053.1	1047256366.6	1047256362.9

n	$n^2S_{1/2}$ state		$n^2D_{3/2}$ state	
	Calculated (MHz)	Measured (MHz)	Calculated (MHz)	Measured (MHz)
39	1047141450.6	1047141474.8	1047374217.6	1047374213.7
40	1047268082.6	1047268081.8	1047483280.6	1047483279.3
41	1047385054.6	1047385053.6	1047584409.6	1047584406.7
42	1047493325.6	1047493323.3	1047678354.6	1047678350.6
43	1047593736.6	1047593734.2	1047765781.6	1047765778.3
44	1047687030.6	1047687030.6	1047847278.6	1047847279.8
45	1047773865.6	1047773862.9	1047923370.6	1047923370.8
46	1047854823.6	1047854825.3	1047994525.6	1047994525.2
47	1047930422.6	1047930427.9	1048061159.6	1048061165.0
48	1048001126.6	1048001129.1	1048123650.6	1048123651.2
49	1048067348.6	1048067352.0	1048182333.6	1048182334.9
50	1048129460.6	1048129462.0	1048237510.6	1048237512.2
51	1048187793.6	1048187797.2	1048289457.6	1048289459.3
52	1048242650.6	1048242653.7	1048338420.6	1048338424.7
53	1048294300.6	1048294299.6	1048384624.6	1048384626.1
54	1048342988.6	1048342991.2	1048428272.6	1048428274.8
55	1048388938.6	1048388939.9	1048469549.6	1048469550.2
56	1048432350.6	1048432353.5	1048508623.6	1048508625.3
57	1048473408.6	1048473411.2	1048545650.6	1048545651.5
58	1048512280.6	1048512282.3	1048580769.6	1048580769.5
59	1048549117.6	1048549120.9	1048614109.6	1048614112.9
60	1048584059.6	1048584058.9	1048645788.6	1048645793.4
61	1048617235.6	1048617239.2	1048675916.6	1048675919.9
62	1048648760.6	1048648764.2	1048704591.6	1048704590.0
63	1048678744.6	1048678749.3	1048731905.6	1048731908.8
64	1048707284.6	1048707284.3	1048757944.6	1048757946.3
65	1048734472.6	1048734473.9	1048782785.6	1048782788.1
66	1048760392.6	1048760394.9	1048806501.6	1048806500.4
67	1048785121.6	1048785124.2	1048829158.6	1048829156.4
68	1048808732.6	1048808729.6	1048850820.6	1048850824.2
69	1048831292.6	1048831296.7	1048871543.6	1048871544.8
70	1048852860.6	1048852861.7	1048891380.6	1048891382.8
71	1048873495.6	1048873498.7	1048910382.6	1048910385.7
72	1048893250.6	1048893254.9	1048928595.6	1048928595.2

n	$n^2S_{1/2}$ state		$n^2D_{3/2}$ state	
	Calculated (MHz)	Measured (MHz)	Calculated (MHz)	Measured (MHz)
73	1048912174.6	1048912177.7	1048946061.6	1048946066.7
74	1048930313.6	1048930315.7	1048962822.6	1048962825.7
75	1048947710.6	1048947715.2	1048978914.6	1048978919.8
76	1048964404.6	1048964411.2	1048994373.6	1048994379.2
77	1048980434.6	1048980441.3	1049009231.6	1049009239.0
78	1048995833.6	1048995839.0	1049023520.6	1049023522.4
79	1049010636.6	1049010637.2	1049037268.6	1049037271.4
80	1049024871.6	1049024874.4	1049050501.6	1049050501.7
81	1049038568.6	1049038569.9	1049063246.6	1049063247.7
82	1049051753.6	1049051756.6	1049075526.6	1049075526.7
83	1049064452.6	1049064455.7	1049087363.6	1049087366.4
84	1049076688.6	1049076695.7	1049098778.6	1049098781.5
85	1049088483.6	1049088488.3	1049109792.6	1049109793.7
86	1049099859.6	1049099861.8	1049120422.6	1049120426.6
87	1049110835.6	1049110841.0	1049130687.6	1049130692.4
88	1049121430.6	1049121438.4	1049140603.6	1049140603.1
89	1049131660.6	1049131668.9	1049150186.6	1049150188.2
90	1049141543.6	1049141547.0	1049159449.6	1049159450.7
91	1049151095.6	1049151098.3	1049168409.6	1049168410.5
92	1049160328.6	1049160332.4	1049177077.6	1049177075.5
93	1049169259.6	1049169260.4	1049185465.6	1049185463.9
94	1049177899.6	1049177901.0	1049193587.6	1049193587.5
95	1049186262.6	1049186268.0	1049201453.6	1049201452.8
96	1049194358.6	1049194364.4	1049209074.6	1049209074.6
97	1049202200.6	1049202203.0	1049216459.6	1049216458.4
98	1049209798.6	1049209800.6	1049223619.6	1049223612.3
99	1049217161.6	1049217165.8	1049230563.6	1049230554.3
100	1049224300.6	1049224301.5	1049237298.6	1049237280.7
101	1049231223.6	1049231221.5	1049243834.6	1049243829.6
102	1049237939.6	1049237924.0	1049250179.6	1049250173.4
103	1049244456.6	1049244455.3	1049256339.6	1049256331.1
104	1049250782.6	1049250780.8	1049262321.6	1049262316.3
105	1049256925.6	1049256921.3	1049268133.6	1049268128.5
106	1049262890.6	1049262891.6	1049273781.6	1049273770.5

n	$n^2S_{1/2}$ state		$n^2D_{3/2}$ state	
	Calculated (MHz)	Measured (MHz)	Calculated (MHz)	Measured (MHz)
107	1049268686.6	1049268686.9	1049279271.6	1049279260.9
108	1049274319.6	1049274318.5	1049284609.6	1049284600.8
109	1049279794.6	1049279791.4	1049289800.6	1049289789.5
110	1049285117.6	1049285114.2	1049294849.6	1049294838.9
111	1049290294.6	1049290294.1	1049299763.6	1049299747.9
112	1049295330.6	1049295327.8	1049304545.6	1049304532.6
113	1049300231.6	1049300227.5	1049309201.6	1049309187.3
114	1049305001.6	1049305000.8	1049313734.6	1049313721.0
115	1049309644.6	1049309642.5	1049318149.6	1049318131.5
116	1049314166.6	1049314166.3	1049322450.6	1049322433.5
117	1049318570.6	1049318565.7	1049326642.6	1049326625.7
118	1049322861.6	1049322859.3	1049330727.6	1049330705.1
119	1049327041.6	1049327040.9	1049334709.6	1049334688.7
120	1049331116.6	1049331114.8	1049338591.6	1049338567.0
121	1049335088.6	1049335086.5	1049342378.6	1049342352.1
122	1049338962.6	1049338956.3	1049346071.6	1049346049.5
123	1049342739.6	1049342733.8	1049349675.6	1049349652.5
124	1049346424.6	1049346420.8	1049353192.6	1049353161.6
125	1049350019.6	1049350018.6	1049356624.6	1049356595.9
126	1049353528.6	1049353519.2	1049359975.6	1049359943.1
127	1049356952.6	1049356942.1	1049363247.6	1049363211.5
128	1049360295.6	1049360286.5	1049366443.6	1049366408.8
129	1049363560.6	1049363550.9	1049369564.6	1049369528.2
130	1049366748.6	1049366739.2	1049372613.6	1049372571.3
131	1049369862.6	1049369858.5	1049375592.6	1049375546.8
132	1049372904.6	1049372892.5	1049378504.6	1049378466.9
133	1049375877.6	1049375866.1	1049381351.6	1049381308.7
134	1049378782.6	1049378774.9	1049384133.6	1049384091.2
135	1049381623.6	1049381610.1	1049386855.6	1049386807.6
136	1049384399.6	1049384389.9	1049389516.6	1049389462.0
137	1049387115.6	1049387105.3	1049392118.6	1049392064.1
138	1049389770.6	1049389758.6	1049394665.6	1049394616.8
139	1049392367.6	1049392354.8	1049397156.6	1049397102.4
140	1049394908.6	1049394897.3	1049399595.6	1049399540.8

n	$n^2S_{1/2}$ state		$n^2D_{3/2}$ state	
	Calculated (MHz)	Measured (MHz)	Calculated (MHz)	Measured (MHz)
141	1049397394.6	1049397383.5	1049401981.6	1049401916.6
142	1049399828.6	1049399814.4	1049404317.6	1049404245.0
143	1049402209.6	1049402194.7	1049406604.6	1049406529.4
144	1049404541.6	1049404526.4	1049408844.6	1049408761.3
145	1049406823.6	1049406811.8	1049411037.6	1049410970.9
146	1049409058.6	1049409043.6	1049413186.6	1049413100.0
147	1049411247.6	1049411232.0	1049415290.6	1049415220.8
148	1049413391.6	1049413370.0	1049417352.6	1049417276.0
149	1049415491.6	1049415471.7	1049419373.6	1049419289.8
150	1049417549.6	1049417530.2	1049421353.6	1049421233.8
151	1049419566.6	1049419544.7	1049423294.6	1049423161.3
152	1049421542.6	1049421515.4	1049425196.6	1049425063.1
153	1049423479.6	1049423448.7	1049427062.6	1049426928.0
154	1049425378.6	1049425345.7	1049428891.6	1049428752.9
155	1049427240.6	1049427207.4	1049430685.6	1049430538.9
156	1049429066.6	1049429032.6	1049432444.6	1049432298.3
157	1049430856.6	1049430819.7	1049434170.6	1049434015.1
158	1049432612.6	1049432575.7	1049435863.6	1049435701.7
159	1049434335.6	1049434292.2	1049437524.6	1049437359.1
160	1049436024.6	1049435978.6	1049439154.6	1049438978.8
161	1049437683.6	1049437637.9	1049440753.6	1049440577.2
162	1049439310.6	1049439261.9	1049442323.6	1049442159.0
163	1049440907.6	1049440853.2	1049443865.6	1049443700.4
164	1049442474.6	1049442415.6	1049445378.6	1049445237.9
165	1049444012.6	1049443973.5	1049446863.6	1049446743.1
166	1049445523.6	1049445484.4	1049448322.6	1049448177.1
167	1049447006.6	1049446968.3	1049449755.6	1049449604.2
168	1049448462.6	1049448414.8	D-state Unresolved	
169	1049449892.6	1049449848.0		
170	1049451297.6	1049451246.0		
171	1049452676.6	1049452621.1		
172	1049454032.6	1049453976.8		
173	1049455363.6	1049455303.9		
174	1049456672.6	1049456611.7		

n	$n^2S_{1/2}$ state		$n^2D_{3/2}$ state
	Calculated (MHz)	Measured (MHz)	
175	1049457958.6	1049457890.4	D-state Unresolved
176	1049459222.6	1049459158.7	
177	1049460464.6	1049460394.3	
178	1049461685.6	1049461609.4	
179	1049462885.6	1049462804.0	
180	1049464065.6	1049463988.6	
181	1049465226.6	1049465141.7	
182	1049466367.6	1049466281.0	
183	1049467489.6	1049467400.1	
184	1049468593.6	1049468506.0	
185	1049469679.6	1049469590.6	
186	1049470746.6	1049470646.2	
187	1049471797.6	1049471700.3	
188	1049472831.6	1049472730.1	
189	1049473848.6	1049473749.5	
190	1049474849.6	1049474738.7	
191	1049475834.6	1049475721.6	
192	1049476804.6	1049476686.1	
193	1049477759.6	1049477634.9	
194	1049478698.6	1049478568.3	
195	1049479623.6	1049479494.8	
196	1049480534.6	1049480402.9	
197	1049481430.6	1049481284.9	
198	1049482314.6	1049482315.0	
199	1049483183.6	1049483032.1	

Table A1: Measured energy levels (in MHz) of potassium Rydberg states $n^2S_{1/2}$ and $n^2D_{3/2}$. For $n > 167$, the D-states were not detected.

The measured energy levels are in good agreement with the calculated values at lower principal quantum numbers ($n \leq 130$ for the S-state, and $n \leq 100$ for the D-states). At principal quantum numbers greater than these values, the measured energy levels deviated significantly from the calculated values. These deviations are attributed to the strong interaction between Rydberg atoms that are in close proximity.